
Multi-dimensional Resistivity Models of the Shallow Coal
Seams at the Opencast Mine 'Garzweiler I' (Northwest of
Cologne) inferred from Radiomagnetotelluric, Transient
Electromagnetic and Laboratory Data

INAUGURAL – DISSERTATION
ZUR
ERLANGUNG DES DOKTORGRADES
DER MATHEMATISCH–NATURWISSENSCHAFTLICHEN FAKULTÄT
DER UNIVERSITÄT ZU KÖLN

VORGELEGT VON
KARAM S. I. FARAG
AUS KAIRO (ÄGYPTEN)

KÖLN 2005

Berichterstatter: Prof. Dr. B. Tezkan
Prof. Dr. A. Junge

Tag der mündlichen Prüfung (Disputation): 02.02.2005

ABSTRACT

The entire Cenozoic unconsolidated fill of the Lower Rhine Embayment in Germany hosts the largest single lignite, or brown coal, deposit in Europe which covers an area of some 2,500 km² to the northwest of Cologne. Rhineland brown coal is mined in large-scale opencast mining and accounts for around one-quarter of the public electricity supply in Germany. The present study was devoted to carrying out radiomagnetotelluric (RMT) and transient electromagnetic (TEM) investigations over the shallow coal seams at the opencast mine 'Garzweiler I.' The main objectives of the survey were to highlight the applicability and efficiency of RMT and TEM methods in an area like brown coal exploration, and to image the vertical electrical resistivity structure of these coal seams. Therefore, the vertical and lateral resolution capabilities of such methods were as necessary as the ability to cover large areas. Consequently, a total of 86 azimuthal RMT and 33 in-loop TEM soundings were carried out along six separate profiles over two opencast benches at the 'Garzweiler I' mine. The local stratigraphy at the survey areas comprises a layer-cake sequence, from top to bottom, of Garzweiler, Frimmersdorf and Morken coal seams embedded in a sand background, consisting of Surface, Neurath, Frimmersdorf and Morken Sands. A considerable amount of clay and silt intervenes the whole succession.

The data were interpreted extensively and consistently in terms of one-dimensional (1D) RMT and TEM resistivity models, without using any complex multi-dimensional interpretation. However, the presence of thin, surficial clay masses (or lenses) broke down such interpretation scheme. In this case, to greatly improve the resistivity resolution for these surficial masses and the underlying coal seams, two-dimensional (2D) RMT and three-dimensional (3D) TEM interpretations have been carried out. They could be used effectively to study the local EM distortion on the measured data, where these surficial masses were found, as well as to cross-check the nearby-topography effect. Because the RMT data are usually skin-depth limited, they only provided a resolution depth between 25 and 30 m for the shallow resistivity structures. Whereas, the TEM data still have sufficiently early- to late-time information, and therefore resulted in a better resolution depth of about 100 m for the shallow to sufficiently-deep resistivity structures. The final 1D/2D RMT and 1D/3D TEM resistivity models displayed a satisfied correlation with both thicknesses derived from the stratigraphic-control boreholes and resistivities measured from direct-current (DC) and spectral induced polarization (SIP) laboratory techniques on 16 rock samples.

As demonstrated, the integrated use of azimuthal RMT and in-loop TEM soundings was highly successful and effective at mapping the major stratigraphic units at the survey areas, i.e. the shallowest conductive Garzweiler and Frimmersdorf Coals within their fairly resistive sand background. They could not distinguish between Neurath Sand and the underlying sand/silt or between Frimmersdorf Coal and the underlying organic clay. The deepest Morken Coal was beyond the depth-of-investigation of the present measurements. Finally, the resistivity models revealed that both coal seams gently dip in the southwesterly direction. This should be in fairly good agreement with the regional structural makeup of the Rhineland brown coal. However, they showed that Garzweiler Coal is gradually thinned northeastwards, while Frimmersdorf Coal still has almost a regular thickness.

KURZZUSAMMENFASSUNG

Die unverfestigten Ablagerungen des Känozoikums im unteren Rheingraben in Deutschland beherbergen das größte zusammenhängende Braunkohlevorkommen in Europa. Es befindet sich nord-westlich der Stadt Köln und umfasst eine Fläche von ca. 2.500 km². In Deutschland wird etwa ein Viertel des Bedarfes an elektrischer Energie durch Braunkohle gedeckt, die im Tagebau aus dem Rheinland gewonnene wird. In der vorliegenden Arbeit wurden die Kohleflöze des Braunkohletagebaues „Garzweiler I“ mit den Methoden Radiomagnetotellurik (RMT) und Transientelektromagnetik (TEM) untersucht. Hauptziel der Messungen war es, die Anwendbarkeit und Effizienz der Methoden RMT und TEM in der Braunkohleexploration aufzuzeigen und die vertikale Verteilung der elektrischen Leitfähigkeit von Flözen abzubilden. Zu diesem Zweck waren das vertikale und horizontale Auflösungsvermögen dieser Methoden genauso nötig wie die Möglichkeit große Flächen zu untersuchen. Infolgedessen wurden insgesamt 86 azimuthal RMT und 33 in-loop TEM Sondierung entlang sechs separater Profile auf zwei Strossen im Braunkohletagebau „Garzweiler I“ durchgeführt. Die lokale Stratigraphie am Ort der Meßgebiete entspricht gewöhnlich einer horizontalen Schichtung, bestehend aus den Garzweiler-, Frimmersdorf- und Morken-Kohlen, die in den Oberflächen-, Neurath-, Frimmersdorf- und Morken-Sand eingebettet sind und von unterschiedlich mächtigen Ton und Schlufflagen unterbrochen werden.

Die gemessenen RMT und TEM Daten wurden umfangreich und in Übereinstimmung mittels ein dimensionaler (1D) Widerstands-Modelle und ohne Hinzunahme von komplexeren 3D-Strukturen interpretiert. Lagen jedoch dünne Tonlagen oder Linsen vor, war diese Form der Interpretation nicht mehr möglich. In diesem Fall wurden zur Verbesserung des Auflösungsvermögens dieser Oberflächenschichten, zwei-dimensionale (2D) RMT und drei-dimensionale (3D) TEM Interpretationen durchgeführt. Anhand dieser Modellierungen konnte auf effektive Weise der Einfluss der Tonlinsen und der näheren Topographie auf die Messdaten untersucht werden. Durch die eingeschränkte Skin-Tiefe der RMT, konnten anhand der RMT-Daten nur die oberen 25 bis 30 m der Widerstandsverteilung im Boden aufgelöst werden. Die TEM-Daten hingegen besitzen genug Früh- bis hin zu Spätzeit Informationen und erlauben daher Aussagen über die Widerstandsverteilung bis in eine Tiefe von etwa 100 m. Die Mächtigkeiten der Schichten, die aus den Widerstandsmodelle für 1D/2D RMT und 1D/3D TEM abgeleitet werden können, stimmen mit den aus Bohrlöchern abgeleiteten Mächtigkeiten überein. Eine ähnlich gute Korrelation existiert mit den Widerstandswerten, die man aus Labor Messungen mit Gleichstrom Geoelektrik (DC) und spektraler induzierter Polarisation (SIP) für 16 Gesteinsproben abgeleitet hat.

Es wurde gezeigt, dass die kombinierte Anwendung von azimuthal RMT und in-loop TEM Sondierungen sehr erfolgreich und effektiv in der Kartierung der wichtigsten stratigraphischen Einheiten des Untersuchungsgebietes, wie zum Beispiel der in schlechtleitenden Sand eingebetteten oberen leitfähigen Garzweiler und Frimmersdorf Kohlenschichten, ist. Der Neurath Sand konnte nicht vom den tieferen Sand und Sluffe Schichten unterschieden werden. Die Frimmersdorf Kohle konnte nicht von tiefer gelegenen organischen Tonschichten unterschieden werden. Das am tiefsten gelegene Flöz Morken liegt unterhalb der Eindringtiefe der Sondierungen. Die Widerstandsmodelle zeigen, dass beide Kohleflöze leicht in Richtung SW abfallen. Dies ist in guter Übereinstimmung mit der regionalen Geologie für die Braunkohle des Rheinlandes. Außerdem konnte gezeigt werden, dass die Mächtigkeit der Garzweiler Kohle in Richtung NE leicht abnimmt, während die Frimmersdorf Kohle eine konstante Mächtigkeit zeigt.

CONTENTS

1	Introduction	1
1.1	Mining and Geophysics	1
1.2	Electromagnetic Methods	2
1.2.1	Frequency-domain Electromagnetic Methods	2
1.2.2	Time-domain Electromagnetic Methods	5
1.3	Scope and Objectives of the Present Work	8
1.4	Rhineland Brown Coal	9
1.5	Geological Background of Rhineland	10
1.6	Survey Areas	12
2	Inversion of Electromagnetic Data	15
2.1	General Statement	15
2.2	Inversion as Optimization	17
2.3	Marquardt-Levenberg Inversion Scheme	18
2.4	Occam's Inversion Scheme	19
2.5	Mackie's Inversion Scheme	20
2.5.1	Gauss-Newton Algorithm	21
2.5.2	Non-linear Conjugate Gradients Algorithm	21
2.6	SLDM Forward Modeling Scheme	23
3	Radiomagnetotelluric Resistivity Models	27
3.1	Radiomagnetotelluric Methods	27
3.1.1	Conceptual Background	27
3.1.2	Depth-of-investigation	30
3.1.3	Scalar CHYN RMT Equipment	30
3.1.4	Radio-transmitters	32
3.2	Data Interpretation	33
3.2.1	Data Viewing	33
3.2.2	Data Transformation	36
3.2.3	One-dimensional Inversion of Synthetic Data	37
3.2.4	One-dimensional Inversion of Field Data	41
3.2.5	Two-dimensional Inversion of Field Data	51
3.2.5.1	Mesh Design and Verification	51
3.2.5.2	The Regularization Parameter	52

3.2.5.3	2D Sensitivity	53
3.2.5.4	Inversion Results	55
3.2.6	Nearby-topography Effect	62
4	Transient Electromagnetic Resistivity Models	69
4.1	Transient Electromagnetic Methods	69
4.1.1	Conceptual Background	69
4.1.2	Depth-of-investigation	70
4.1.3	Zonge Nano/ZeroTEM System	71
4.1.4	Data Deconvolution	74
4.1.5	Data Transformation	78
4.2	Data Interpretation	78
4.2.1	Data Viewing	78
4.2.2	One-dimensional Inversion of Synthetic Data	80
4.2.3	One-dimensional Inversion of Field Data	82
4.2.4	One-dimensional Joint-inversion of RMT and TEM Field Data	94
4.2.5	Three-dimensional Modeling of Synthetic Data	98
4.2.5.1	Grid Design and Verification	98
4.2.5.2	Model Geometry and Results	100
4.2.6	Nearby-topography Effect	106
4.3	Correlation of Surface Electromagnetic with Laboratory-based Resistivity Models	110
4.4	Geological Implications inferred from Surface Electromagnetic Resistivity Models	112
5	Laboratory-based Resistivity Models	114
5.1	Electrical Resistivity of Coal	114
5.2	Laboratory Methods for Measuring Resistivity	116
5.2.1	Conceptual Background	116
5.2.2	Samples and Terminal-configurations	118
5.2.3	Direct-current Measurements	120
5.2.4	Spectral Induced Polarization Measurements	121
5.3	Results and Interpretation	121
5.3.1	Resistivity Magnitude and Phase Angle Spectra	121
5.3.2	Argand Diagrams	122
5.3.3	IP Measures	124
5.4	Discussion	126
6	Summary and Conclusions	128
A	Programs	136
B	Mining Results	138
	References	139
	Acknowledgment	147

CHAPTER 1

INTRODUCTION

1.1 Mining and Geophysics

Mining has been one of the oldest activities of man since times. As the human population increases and developing countries become more industrized, the search for new ore deposits will continue to grow. Evidence of the thoroughness and diligence with which this search was conducted in olden times can be found in many places, such as the ancient workings in the Egyptian Eastern Desert to find and extract the Pharaoh's Gold [Harrell, 2002]. One must look for more ore where ore has already been found and in districts with natural conditions similar to those in the known district. Invasive techniques, such as expensive drilling and direct-sampling, can provide very accurate one-dimensional information about the subsurface, but only for the sampling location and for a limited volume of the subsurface. Here the *geophysics* – the study of physics of the Earth, Earth's materials and surrounding atmosphere – enters the picture. A necessary condition for the detection of an ore body by geophysical (or non-invasive) methods is that the ore should differ sufficiently in physical properties (electric resistivity, magnetic susceptibility, bulk density, etc.) from that of the host background materials. The primary purpose of geophysics during the early stages in the life of a mine, i.e. during the prospecting and exploration stages, is to separate areas which appear to be barren from those which appear to hold a promise of ore [Parasnis, 1973]. Consequently, the success of a well-conducted geophysical method is not to be measured by the number of ore bodies discovered or by the number of recommended boreholes that struck ore, but by the time, effort and money which the survey has saved in eliminating ground which would otherwise have to be eliminated by more expensive methods.

Applied geophysics provides a wide range of very powerful methods which, when used correctly and in the right geological situations, will yield very useful information about the ground truth. Usually, multiple geophysical methods offer better answers than any individual method. During the last few decades, the hydrocarbon industry has exploited the geophysical exploration techniques to a far greater extent in terms of using the field data to quantify the value, size, and production capabilities of its resources. By contrast, the application of geophysical methods to mining industry, particularly to surface-mining, is not developed well in general [Nabighian and Asten, 2002]. Some possible reasons for this are:

- (1) Insufficient knowledge by mining managers, engineers, and operators of the existence of geophysical methods, coupled with a high tech–high cost perception of geophysics.
- (2) Perceived infrastructure and logistical difficulties in using geophysical methods due to the continuous mining activities.
- (3) Lack of knowledge of the physical properties of the ore and host background materials which may be exploitable in a mining environment.
- (4) Limited research effort applied to standard geophysical methods to develop higher-resolution acquisition or interpretation techniques applicable to mining problems.
- (5) Scarcity of geophysicists with access to mine difficulties or with sufficient knowledge of mining culture or operational requirements to champion the use of geophysical methods in this area.

1.2 Electromagnetic Methods

Electromagnetic (EM) methods are among some of the oldest geophysical techniques, which involve the measurement of one (or more) electric and magnetic field components, at the earth surface (or in borehole), induced in the subsurface by a primary field produced from a naturally occurred (passive) or artificially generated (active) source of EM field. There are two competing families of methods: one family satisfies the *diffusion equation*, which ignores displacement currents and non-linear effects to obey the EM induction regime and operates at frequencies less than 1 MHz. The other family satisfies the *wave equation*, which considers displacement currents and operates frequencies above 1 MHz. The latter is beyond the scope of this work and will not be discussed further. Commonly, the term 'EM methods' tends usually to refer only to 'EM induction methods.' Because of the large number of EM methods, there are many ways of classifying them for discussion. One common classification, which will be used here, is to group by whether the EM data are measured in the frequency-domain (FD) or the time-domain (TD).

1.2.1 Frequency-domain Electromagnetic Methods

In a typical FDEM survey, EM energy is introduced into the ground as continuous waves by a small transmitting-coil, comprising few turns of wire around permeable core and carrying alternating-current (AC) and primary magnetic field of a fixed (or swept) frequency oscillation. Satisfying the physical laws of EM induction, the primary field spreads out in a three-dimensional space both above and below the ground and results in an induced (or eddy) current pattern in the ground, and hence an associated secondary magnetic field which is added to the primary field. The induced currents flow in such a way that their primary field opposes the secondary field. The strength of the secondary field depends, among other factors, upon the ground resistivity and excitation frequency of the primary field. Therefore, its amplitude, direction and phase differ from that of primary field and can yield information on the ground resistivity-distribution. Normally, the primary field is nulled by a closely (or widely) spaced small receiving-coil so that the *in-phase* (real) and out-of-phase (*quadrature* or imaginary) components of the secondary field are directly measured. Alternatively, the resultant (vector sum) of both primary and secondary fields is measured and the secondary is computed separately. Both transmitting- and receiving-coils are usually identical and tuned to the same frequency for sensible measurements. Geometrically, they are not only described as horizontal (vertical magnetic-dipole) or vertical (horizontal magnetic-dipole), but also as coplanar, coaxial (maximally-coupled) or orthogonal (minimally-coupled). The effective

depth-of-investigation is dependent of the weighted-average resistivity of the subsurface earth, operating frequency, transmitter–receiver spacing and the overall signal-to-noise ratio (SNR).

Among the FDEM methods are the *magnetotelluric* (MT) methods which involve simultaneous orthogonal measurements of two horizontal electric and three horizontal and vertical magnetic field components induced in the subsurface by primary fluctuating ionosphere currents by means of two electric-dipoles and three magnetic sensors respectively [Tikhonov, 1950; Cagniard, 1953]. These currents are due to the complex interaction of the solar-wind with the magnetosphere, i.e. geomagnetic micropulsations. Typically, MT methods operate at the frequency range between 0.001 and up to 10 Hz. The variability in amplitude and/or direction of the geomagnetic micropulsations requires more stacking time for improvement of the SNR, thus making MT methods expensive and low-productive. The MT measurements made at the audio-frequency range from 1 Hz to 10 kHz, using EM energy from distant-lightening discharges (or spherics) due to global thunderstorm activity, are generally referred to as *audio-magnetotelluric* (AMT), or *controlled-source AMT* (CSAMT). Similarly, *audio-frequency magnetic field* (AFMAG) methods make use of this audio-frequency magnetic field, but the measured quantities are the azimuth and dip of the major axes of the polarization ellipse [Ward et al., 1968]. All these natural fields travel around the globe in the Earth's ionosphere waveguide cavity [Spies and Frischknecht, 1991], but are more frequent in equatorial regions such as Brazil, Central Africa and Malaysia. As the name implies, the *controlled-source* MT (CSMT) methods are those carry their own transmitters with prescribed characteristics, including loops, grounded dipoles or antennas.

Very low frequency (VLF) methods utilize EM radiation generated by remote powerful radio-transmitters which are distributed all around the world for the purpose of military communication and operate at frequency range from 10 to 30 kHz. These VLF transmitters emit continuously either superimposed frequency-modulated EM wave or occasionally chopped unmodulated 'Morse code' [Paal, 1965; Watt, 1967]. The VLF antenna mast is effectively a long vertical wire (or rod) carrying an AC current, i.e. vertical electric-dipole. The signal strength is roughly proportional to the amplitude of electric field component parallel to the mast and to the mast length. A radiated EM wave consists of coupled vertical electrical and concentric horizontal magnetic fields, perpendicular to each other and to the direction of propagation. It travels efficiently over long distances in the Earth's ionosphere waveguide cavity. Neither the ground nor the ionosphere is a perfect conductor and some EM energy is lost into space or penetrates the ground. Without this penetration, there would be neither naval communication with submarines nor geophysical uses. Because the VLF electric field near the ground surface is tilted, not vertical, it has also a horizontal component.

Induced currents in the ground by VLF magnetic field produce an opposite secondary magnetic field with the same frequency as the primary, but generally with a different amplitude and phase depending on the ground resistivity and excitation frequency of the primary field. The secondary magnetic field has also both horizontal and vertical components. Any vertical secondary magnetic field component is by definition anomalous, causing a tilted or elliptically polarized resultant field. A VLF magnetic field can be sensed by a small induction coil in which current flow in proportion to the core permeability, number-of-turns and the magnetic field component along its axis. Most VLF equipment compares vertical with horizontal magnetic fields either directly or by measuring the *tilt-angle* which is initially inferred from the in-phase and quadrature components.

In VLF work the profile direction is almost irrelevant, the critical parameter being the relationship between the known (or presumed) *geological strike* of a subsurface conductor and the azimuth (or bearing) of the radio-transmitter. A subsurface conductor which strikes towards the radio-transmitter is well-coupled, as the magnetic field is at right angle to it and current can flow freely. Otherwise, the current flow would be restricted, reducing the strength of the secondary field. The measuring procedure for a VLF survey is rather simple, carried out as follows: the VLF receiver (a small hand-held device) is tuned to a particular frequency of the selected radio-transmitter. The azimuth of the radio-transmitter is obtained by rotating a small induction coil around a vertical axis until the null position (i.e. minimum audibility) is found. The coil is then rotated around a horizontal axis at right angle to that azimuth, where the tilt-angle is noted at the null position. Measurements are then performed along the survey profile at right-angle to that azimuth using only a single, well-defined frequency. The asymmetry of the tilt-angle data along a profile can be used to obtain a qualitative estimate of the dip of a subsurface conductor, if present.

Very low frequency-resistivity (VLF-R) methods are hybrid forms of electrical and EM methods [Scott, 1975; Fischer *et al.*, 1983], but still similar in principles to the conventional VLF methods with two significant differences. First, the horizontal resultant electric field component is measured by the voltage drop between a pair of potential electrodes planted into the ground. Whereas, the horizontal resultant magnetic field component is sensed by a small vertical induction coil at the mid-point between electrodes. Second, the measured quantities are commonly expressed in terms of the apparent resistivity and impedance phase (the phase lag in time of the measured electric field relative to magnetic field) at the frequency range between 10 and up to 30 kHz. This allows a semi-quantitative interpretation to be performed. *Radiomagnetotelluric* (RMT) methods are extension of VLF-R methods to higher frequency range up to 1MHz, although the applicable frequency range of most RMT equipment is limited between 10 and 300 kHz [Turberg *et al.*, 1994; Turberg and Barker, 1996]. Recently, an impressive work was devoted by the Center of Hydrogeology Neufchâtel (CHYN) at the University of Neufchâtel in Switzerland to establishing a new VLF methodology known as *Very low frequency-resistivity EM gradient* (VLF-EM GRAD) methods [Bosch and Müller, 2001]. These techniques reveal high vertical and horizontal ground resistivity-resolution. The horizontal resultant magnetic field component is sensed simultaneously and continuously at two different altitudes, above the ground, with two attached vertical induction coils centrally-spaced 1 m apart. The signal differences in both in-phase and quadrature components between the upper and lower coils, which are based on their mutual coupling, are usually measured in percentage.

Slingram methods utilize two transmitting- and receiving-coils separated by a fixed distance, typically 30 to 350 m, and moved simultaneously over the survey area [Parasnis, 1973]. The ratio of the vertical secondary to primary magnetic field amplitudes is determined at several frequencies. This is initially done from measurements of both in-phase and quadrature components, which in turn are dependent on the mutual coupling between the two coils. Slingram is synonymous with the *horizontal loop EM* (HLEM) methods. *Ground conductivity meters* (GCM) are portable EM instruments which directly measure the terrain conductivity at shallow depths [McNeill, 1980; Frischknecht *et al.*, 1991]. They are essentially Slingram systems, but the operating frequency is sufficiently low, typically 0.5 to 10 kHz at each measuring inter-coil spacing, so that the skin-depth in the ground is always significantly

greater than this spacing. That means, the measurements must be made at low induction number (ratio of the inter-coil spacing to skin-depth). Virtually all response from the ground is in the quadrature phase of the received signal. So, quadrature component is taken to be a linear measure of the apparent conductivity of the ground. The in-phase component is measured in parts per thousand. The GCM devices can be deployed both horizontally and vertically. When used as a horizontal-coil system (vertical dipole mode), the device is quite sensitive to the relatively low-conductive steeply dipping subsurface structures. Whereas, as a vertical-coil system (horizontal dipole mode) the device is insensitive to such structures and gives fairly accurate measurement of ground conductivity in close proximity to them.

Sundberg methods utilize a horizontal dipole source as transmitter, typically an insulated-cable of few hundred meters to several kilometers long grounded at both ends or long rectangular loop, and a small receiving-coil. Phase reference is determined by a feeding coil located close to the transmitter cable or loop using a compensatory system. Measurements are usually made at the right angle to the cable or long-side of the loop [Parasnis, 1991]. *Turam* methods are further development of the Sundberg methods in which the feeding coil is not present, and therefore there is no need to carry phase reference information from the transmitter. Additionally, they utilize two mobile receiving-coils which are separated by, and deployed successively with, a fixed distance of about 10 to 20 m. The two coils provide a mean whereby the horizontal gradient of amplitude ratio of the vertical secondary field (or phase difference) at each two successive points can be determined. This is initially done from measurements of both in-phase and quadrature components, which in turn are dependent on the mutual coupling between the two coils. The major advantages from using such fixed-source methods over moving-source methods, i.e. Slingram and GCM, are that the topography has a less significant effect on their data, as well as the EM coupling between the cable (or loop) and the subsurface is maintained constant throughout the survey profile. Although in both fixed- and moving-source methods the receiving-coils are usually held horizontally, they can be deployed in three mutually perpendicular planes, and hence the EM field components can be measured completely.

Magnetometric resistivity (MMR) methods utilizes a commutated direct-current (DC) (alternating square-waveform) injected into the ground through a pair of widely separated electrodes. The anomalous resistivity is determined at the mid-point by measuring the secondary magnetic field arising from the non-inductive currents using an extremely sensitive low-noise magnetometer aligned perpendicular to the line between the electrodes [Edwards and Nabighian, 1991]. The electrode spacing may be held fixed or it may be increasingly varied to obtain much depth-of-investigation. They are used to explore beneath a highly-conductive surficial layer. Yet, they met with little success. Generally speaking, the claimed depth-of-investigation possible with the passive FDEM methods is much greater than that of the active FDEM methods.

1.2.2 Time-domain Electromagnetic Methods

In a typical TDEM survey, EM energy is introduced into the ground as transient pulses, instead of continuous waves, by a large transmitter-loop carrying steady¹ current and primary magnetic field. Satisfying the physical laws of EM induction, immediately after the current and primary field are suddenly turned-off, an associated secondary magnetic field resulting from an induced current pattern in the ground is sensed by a small receiver-loop and decays with time as the current gradually dissipates. The induced currents flow in such a way that

¹Either pure DC or commutated DC or low-frequency AC (typically 20 to 50 Hz) current.

their primary field opposes the secondary field. The strength of the secondary field depends, among other factors, upon the ground resistivity and sampling time of the transient-decay response. Therefore, its amplitude and shape yield information on the ground resistivity-distribution. Normally, the recorded signal by the receiver is the time-derivative of the decay of vertical secondary magnetic field as a *voltage*. The TDEM methods can be used in a number of different transmitter-receiver configurations. The most common loop-loop configurations are frequently described as in-loop (central loop), coincident loop, single (common) loop, separate loop, dual loop and fixed transmitter-/roving receiver-loop [Nabighian and Macnae, 1991]. The effective depth-of-investigation is dependent of the weighted-average resistivity of the subsurface earth, sampling time and transmitter-dipole moment (the effective area times output-current) and the overall SNR [Spies, 1989].

Long offset transient EM (LOTEM) is a subgroup of the TDEM methods in which carefully controlled electric current, usually several tens of amperes, is driven through the earth by means of a horizontal dipole source as transmitter, typically an insulated-cable of 1 to 2 km long grounded at both ends [Kaufman and Keller, 1983; Strak, 1992]. The transmitter is kept fixed, while many different mobile receivers about the survey area are used to measure two horizontal electric field components and the time-derivative of the vertical magnetic field component as *voltages*. The transmitter–receiver distance, called offset, is comparable to the depth-of-investigation, which is the reason for calling the method long offset TEM. It usually varies between 2 and 20 km, shorter or longer offsets are also possible, but are less often used. The LOTEM methods are now gaining recognition among geophysicists because of the possibility of overcoming typical EM noise problems as well as obtaining higher depth resolution with better transmitter signature.

For both FDEM and TDEM surveys, the primary field amplitude is decreased exponentially with depth and secondary field amplitude produced in the ground is similarly attenuated on its way to the surface, i.e. both surveys are *skin-depth* and *diffusion-depth* limited respectively. The TDEM surveys have principal advantages over the FDEM survey of that the primary magnetic field is not present during the measurement of the secondary magnetic field and that simultaneous voltage measurements of secondary field as a function of time are equivalent to quadrature component measurements over a very broad frequency range. Therefore, more depth-of-investigation would be expected in TDEM surveys, although the exact depth is not known. The absence of a primary field during TDEM measurements allows the receiver-loop to be positioned within the transmitter-loop, a technique which can be used in any FDEM work only with a very large transmitter-loop because of the strong coupling to the primary field. Furthermore, the TDEM surveys have a relatively low productivity because of long recording time. This is partly due to more stacking time for improvement of the SNR, especially at later-times. Contrary to FDEM, the TDEM measurements must be conducted over a longer period of time, causing the amplitude of the secondary field to vary much more. That means, the TDEM system must have a wide dynamic-range.

Like any other geoelectric methods, EM induction surveys can be conducted in the form of either *vertical sounding* or *horizontal profiling*. Assuming an uniform horizontally layered-earth, EM sounding is designed to determine variations in the ground resistivity with depth. Measurements are usually made at a number of frequencies or sampling times using a fixed transmitter–receiver spacing [Spies and Frischknecht, 1991]. Alternatively, measurements can be made at a single frequency or sampling time by varying the transmitter–receiver spacing. The first technique is sometimes called *parameteric* sounding, while the second is called *geometric* sounding. On the other hand, EM profiling is designed to determine variations in

the ground resistivity laterally. Measurements are also made at a single frequency or sampling time wherein a fixed transmitter–receiver spacing is moved progressively along a traverse to create a horizontal profile [Frischknecht *et al.*, 1991].

By comparison, most EM methods have a major advantage over the electrical methods, including DC resistivity, self-potential (SP) and induced polarization (IP), is that the induction process does not require direct (galvanic) electrode-contact with the ground. Consequently, the data can be acquired relatively more quickly than with electrical methods. The induction process also allows the EM methods to be conducted from the aircraft and ships, as well as down boreholes. Because EM soundings depend only on the longitudinal conductivity of an uniform horizontally layered-earth, whereas DC resistivity soundings, as an example, depend on both transverse and longitudinal resistivities [Spies and Frischknecht, 1991]. Thus, over an uniform horizontally layered-earth, DC resistivity soundings can provide better vertical resolution than EM soundings, especially for the resistive layers. However, over a laterally varied conductive (or fairly resistive) earth, EM soundings can generally provide better vertical and lateral resolution than DC resistivity soundings. Although modern EM equipment tends to be somewhat more costly, considering its sophistication, EM methods are still highly sensitive to the background natural EM and cultural noise [Spies and Frischknecht, 1991]. Whereas, electrical methods are less expensive and relatively insensitive to such background noise. Unlike the case for EM soundings, data processing and mutli-dimensional interpretation of electrical soundings are straight forward. Multi-dimensional EM interpretation may be used preferentially, but still require large amount of computing time and are limited by the computational difficulties in defining especially two- and three-dimensional models.

A much more comprehensive and detailed discussion of the various EM methods, with exception of the ground penetrating radar (GPR), has been produced by Misac Nabighian [1988, 1991] and *co-authors*. In the framework of present work, we shall come to touch on only two particular ground-based EM approaches that fall under the headings of *radiomagnetotelluric* (RMT) and *transient EM* (TEM) depth-sounding methods, and do not look deeper in other methods. The former is a passively FDEM method, whereas the second is an actively TDEM method. Both are among some of the robust near-surface exploration techniques that have been successfully used in areas as diverse as environmental [Zacher *et al.*, 1996; Tezkan *et al.*, 1996; Hördt *et al.*, 1999; Newman *et al.*, 2003], hydrogeological [Fitterman and Stewart, 1986; Christensen and Sørensen, 1998; Turberg *et al.*, 1994; Bosch and Gurk, 2000] and mineral investigations [Scott, 1975; Palacky, 1983; Asten, 1987; Helwig *et al.*, 1994].

Since the 1990's, the Institute of Geophysics and Meteorology (IGM) at the University of Cologne has continuously concentrated on the application and development of RMT/TEM methodology and interpretation schemes. Despite the reasons given in Section 1.1, which have always restricted the geophysical applications in the area of surface-mining, growing competition from other energy sources in Germany, such as imported hard coal, made it essential for RWE-Power AG to minimize costs, especially in field-work functions like expensive drilling and direct-sampling. Therefore, close cooperation of RWE-Power AG with experts, universities, institutions and associations was maintained for the purpose of continuously establishing cost-effective exploration strategies at the Rhineland opencast mines. On the other hand, there was an increasing interest of the IGM-Cologne to highlight the applicability, efficiency and reliability of RMT and TEM methods in an area like brown coal exploration. Both reasons greatly encouraged the field survey to get started.

1.3 Scope and Objectives of the Present Work

The present study was devoted to carrying out RMT and TEM investigations over the shallow coal seams at the opencast mine 'Garzweiler I', northwest of Cologne. It was hoped that such methods may image the vertical electrical resistivity structure of these seams, and hence define much better estimates of their boundaries and unexpected changes in their altitudes or thicknesses (faulting, dipping, thinning, etc.) which are usually considered as geological surprises for mining community, if present. For this purpose, the steps in planning the field campaign were as follows:

- (1) Collecting the available topographic, geological and geophysical information about the areas concerned to find out what type of rocks we are likely to encounter within them and how they are likely to be interrelated.
- (2) For deciding whether the RMT and TEM methods can be usefully undertaken within the survey areas or not, a two-day trial survey ought to be carried out before launching a large-scale field operations. Such a survey, together with a preliminary forward modeling, helped us to form some idea about the EM responses predicted from the various rocks within the areas, as well as those expected from nearby-topography. It also indicated some specific modifications necessary in the measurements for optimizing survey design, and hence obtaining the best possible results.
- (3) Staking the survey areas before starting the measurements to establish a coordinate system in which every sounding center was clearly and uniquely marked. This enabled us to reoccupy exactly the same sounding center with both RMT and TEM measurements so that a comparison of their resistivity models is rendered reliable. This was performed using a theodolit and differential GPS¹ readings, as well as using tap measures and some wooden sticks.
- (4) It was really a sound policy to procure some representative rock samples from the survey areas and measure their electrical properties in the laboratory to determine what can be interpreted reliably from surface RMT and TEM measurements.

This dissertation consists of six chapters and two appendices. Its structure is as follows: this chapter contains general introductory sections which state how the link between mining and geophysics comes into play, explain where RMT and TEM methods are placed in applied electromagnetics and discusses the scope and objectives of the present work. They also outline the importance and geological background of the Rhineland brown coal and describe the survey areas at the opencast mine 'Garzweiler I.' Chapter 2 gives an introduction to the inversion of EM data. Special attention is given to the one-dimensional (1D), two-dimensional (2D) and three-dimensional (3D) RMT/TEM inversion and modeling schemes which have been used in the present work. Chapter 3 explains the conceptual background of RMT methods and gives detailed description on how to acquire azimuthal RMT data sets in the field and to interpret them reliably in terms of 1D and 2D resistivity models. During the course of this chapter, the effect of nearby-topography on the RMT data is qualitatively assessed. Similar to RMT methods, the conceptual background of TEM methods and detailed description on how to acquire segmented in-loop Nano/ZeroTEM data sets in the field and to interpret them reliably in terms of 1D and 3D resistivity models are described in Chapter 4. The effect of nearby-topography on the TEM data is qualitatively assessed. It is an end intention of this chapter to correlate the final 1D/2D RMT and 1D/3D TEM earth models with laboratory-based resistivity models, which represent almost the whole vertical succession at the survey areas, and to give some useful geological implications inferred from these models.

¹Global positioning system.

Note that the final RMT and TEM resistivity models are visualized as two-dimensional section- or plane-views because the end objective of such investigation work is a practical guide for mining industry. Apart from the particular focus on the RMT and TEM methods, Chapter 5 illustrates two direct methods for measuring the electrical resistivity of rock samples in the laboratory, namely DC and spectral induced polarization (SIP) techniques. Like any other petrophysical analysis, the chapter first reviews the published resistivity ranges of coal among the most common sediments, ores and ore minerals. Then, it describes in details the studied rock samples and terminal-configurations used for both measuring techniques. Later on, the final results and interpretation, as well as a brief discussion are given. Finally, Chapter 6 summarizes the main concluding remarks that could be drawn from the whole research. A brief review about the programs used for data processing, inversion/modeling and visualizations are given in Appendix A. Mining results of the Garzweiler Coal Seam versus the interpreted 1D/2D RMT resistivity models, along profile I at the 'Coal-covered Area', are given in Appendix B.

1.4 Rhineland Brown Coal

The largest single lignite², or *brown coal*, deposit in Europe is found in Rhineland which covers an area of some 2,500 km² to the northwest of Cologne. Since lignite is the youngest variety of all coals, built in Early to Middle Miocene age [26.60 Ma], overlain by more recent sand, gravel, and clay, and thus closer to the surface, it is mined in large-scale opencast mining. Lignite seams also extend to a depth of around 500 m, while overburden thickness can be up to 300 m.

Cologne-based RWE-Power AG (formerly RWE-Rheinbraun AG) is responsible for mining of lignite in Rhineland with an annual production of around 100 million metric tons. It operates four large opencast mines, namely 'Inden I/II', 'Garzweiler I', 'Hambach I' and 'Bergheim.' The 'Garzweiler I' mine (Figures 1.1 and 1.2) accounts for one-third of total lignite output. The planned 'Garzweiler II' mine will replace capacity from 'Bergheim' mine, which is nearly worked out. Approximately one-quarter of the public electricity supply in Germany, generated by the coal-fired power plants of RWE-Energie AG, is based on the Rhineland brown coal [RWE AG Group, 1989].

Because of their depth below groundwater level (up to 500 m) and due to their horizontal extension (several kilometers wide and long), Rhineland opencast mines require extensive dewatering and flood control systems, both aimed at preventing in-mine flooding and guarantee dry mining. RWE-Power mining activities generally start with the central removal (or stripping) of overburden utilizing a fleet of giant bucket-wheel excavators. This is followed by mining the uppermost flat-laying lignite seams, then interburden to uncover further lignite seams separately. Once mined-out, lignite masses are entirely transported via conveyor belt systems or railways to the nearby refineries and, later on, to the coal-fired power plants. In an environmental move, RWE-Power AG carries out immediate reclamation of both outside waste dumps and mined-out areas of the opencast mines as part of its normal operations. Problems in recultivation are occurred due to minor ground-grade that makes reforestation difficult.

²A weakly-consolidated sedimentary rock, formed by the partial decomposition of woody plant debris (or peat), under moderately-high temperature and pressure, over geologic time. This low-rank (or low-carbonized) coal has a high inherent moisture content, sometimes as high as 45 percent, and a relatively low heat/energy content, from 9 to 17 million BTU (British thermal unit) per ton. It is used exclusively as fuel for steam-electric power plants [Matthes, 1990].

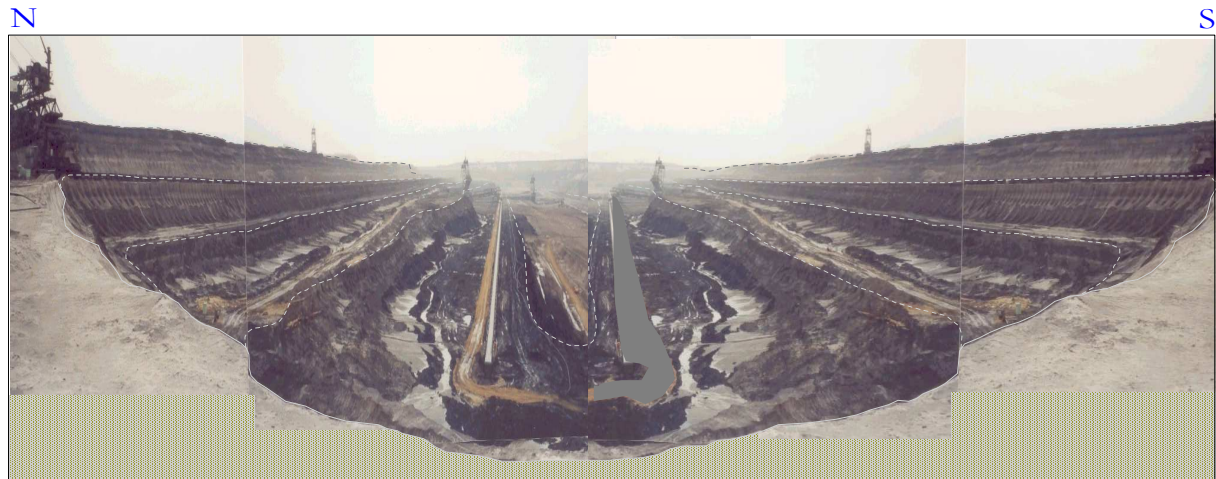


Figure 1.1: Field panorama of the opencast mine 'Garzweiler I', northwest of Cologne, viewed end-on from the western side.

1.5 Geological Background of Rhineland

The Cenozoic Dutch–German rift system transects the Rhenish Shield, that comprises the Rhenish Massif in the north and the Black Forest in the south, to form the 100 km long and 50 km wide Lower Rhine Embayment in Germany [Schäfer *et al.*, 1996; Wong *et al.*, 2001]. This asymmetrical basin (or graben) is subsided along NW–SE oriented faults (Figure 1.2a), forming several tectonic blocks: the Rur, Venlo, Erft, Krefeld and Köln blocks [Klett *et al.*, 2002]. The entire rift sedimentary section (Figure 1.2b) consists of the Tertiary and Quaternary unconsolidated fill of a maximum thickness of more than 1500 m and unconformably rests on a pre-existing Mesozoic to Paleozoic basement.

The tectonic–geological events which accompanied the formation of the Rhineland lignite merit special considerations. In the Paleocene, the area of the Lower Rhine Basin remained largely sediment-free. From the Early to Middle Oligocene the area was confined to tightly circumscribed sinking at differing speeds and depths. Furthermore, the old (Tertiary) North Sea could transgressed onto the basin with a huge carpet of floating peat, provided from the heights of the Rhenish Massif [Zagwijn, 1989]. This received fresh water from the south through a wide river, the old Rhine, and consequently caused the peat to sink into the rift trench. During the climax of the marine transgression in the Late Oligocene, the entire rift marine sediments were extensively deposited and covered by these accumulated organic masses that became the rich lignite seams since the Early Miocene regression of the North Sea. The extensive drift lignite horizons and the lateral change from lignite to sand represent a radical change in the depositional environment that resulted from short-lived transgressions of the North Sea onto the freshwater swamps [Schäfer *et al.*, 1996]. It is believed that the Rhineland coal seams, i.e. Garzweiler, Frimmersdorf and Morken seams, formed in this way. They join up in the center of the basin to form one 'Main Seam' which reaches a maximum thickness of about 100 m (Figure 1.2b). At the end of Late Miocene and during the Pliocene, thick and coarse-grained fluvial sediments followed the stepwise regression of the sea. Finally, the Pleistocene uplift of the Rhenish Massif increased the subsidence of the Lower Rhine Basin to form the early Rhineland plains.

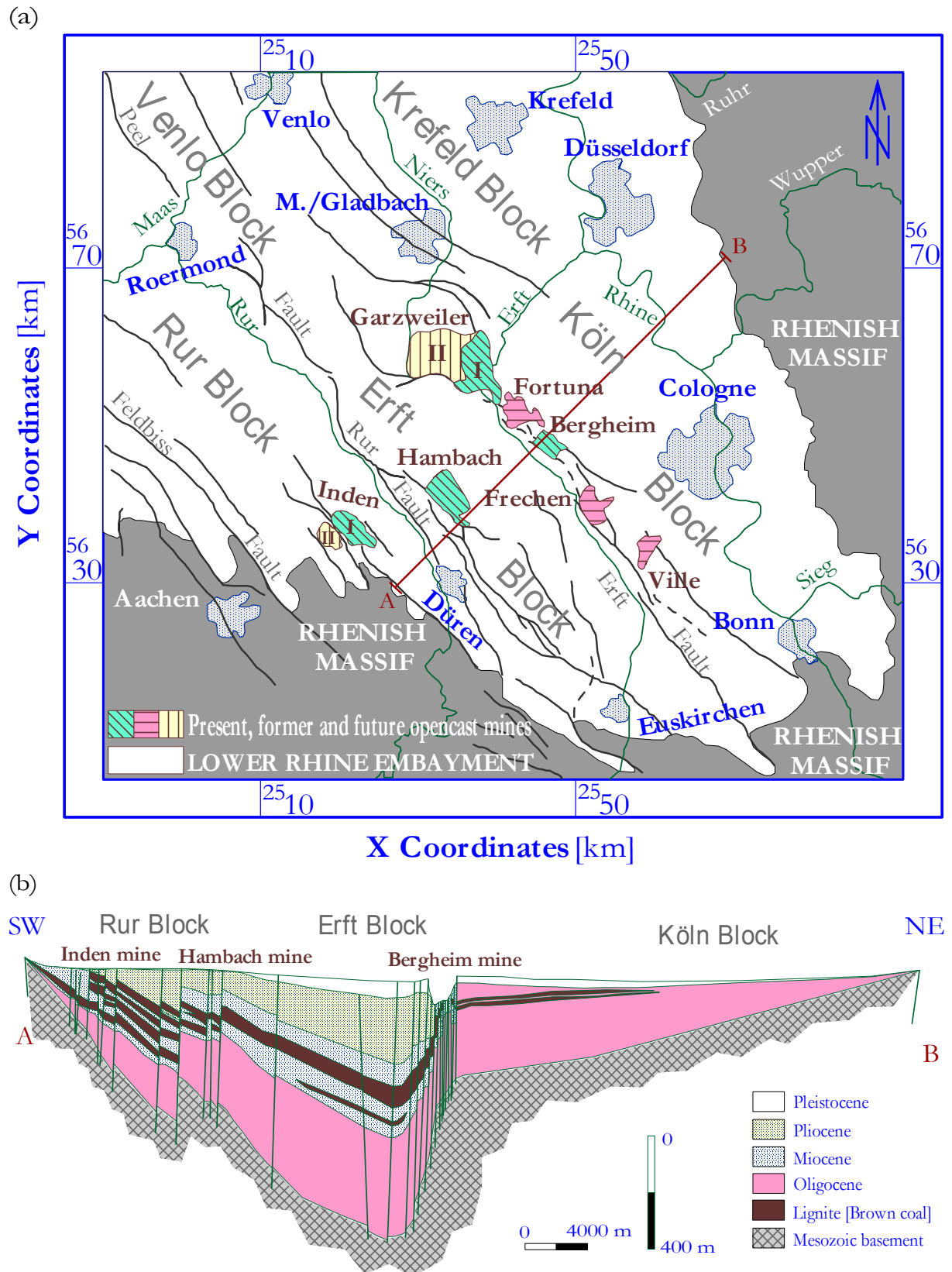


Figure 1.2: (a) Location of the opencast mine 'Garzweiler I', northwest of Cologne, within the Lower Rhine Embayment and (b) idealized geological cross-section running SW–NE through the Rur, Erft and Köln tectonic blocks with tentative Cenozoic stratigraphy. Some opencast mines are projected onto the section [redrawn after Klett et al., 2002]. Coordinates of the location map are given by the German national (Gauss–Krüger) coordinate system.

1.6 Survey Areas

A total of 86 *azimuthal* RMT and 33 *in-loop* TEM soundings were carried out along six separate profiles between April and May 2002 over two opencast benches (or terraces) at the opencast mine 'Garzweiler I', with a permanent crew of two persons. Throughout this dissertation, these small-scale benching areas are always referred to as 'Coal-covered Area' and 'Sand-covered Area.' The 'Sand-covered Area' is located at relatively higher altitude to the northeast of the 'Coal-covered Area' and bordered on the northerly side by a large hillock (about 22.8 m high) (Figure 1.3a). This hillock consists mainly of sand, gravel and loam. Profile I (about 350 m long) is conducted parallel to, and as far as possible from, that hillock and directed 90° N, while profile II (about 60 m long) is almost perpendicular to it. The topography along each profile is almost of very flat relief, where the elevation-difference does not exceed 0.45 m. Soundings RMT 1 and TEM 1 are close to the stratigraphic-control borehole 'WS 1452' and considered as *control soundings*.

The 'Coal-covered Area' is bordered on the northerly side by a small hillock (about 8 m high) and edged on the southerly side with a very steep cliff (about 26 m deep) to another subjacent mining bench (Figure 1.3b). This hillock consists of the uppermost (non-mined) Garzweiler Coal and Surface Sand. Profiles I and II (each about 500 m long) are conducted parallel to, and as far as possible from, both the hillock and the cliff and directed 79° N, while profiles III and IV (120 m and 32.5 m long respectively) are almost perpendicular to them. The area displays a slightly rugged topographic-relief, the elevation-difference varies between 0.05 and 3.5 m. Soundings RMT 32 and TEM 17 are close to the stratigraphic-control borehole 'WS 1380' and considered as control soundings.

Along the main parallel profiles, RMT soundings are performed at regular spacings, between centers, of about 12.5 m and 25 m for the 'Sand-covered Area' and 'Coal-covered Area' respectively, while TEM soundings are always spaced 50 m apart. Spacings along the complementary perpendicular profiles are a little irregular and shorter. Although profile locations were selected to fulfill the survey objectives, logistical difficulties due to the continuous mining activities and taking into account considerations of nearby-topography effect to minimize its distortion on the EM data, limited, to some extent, the number of profiles within each survey area.

The local stratigraphy at the survey areas typically comprises a layer-cake sequence, from top to bottom, of Garzweiler, Frimmersdorf and Morken Coals embedded in a sand background, consisting of Surface, Neurath, Frimmersdorf and Morken Sands (Figure 1.4). A considerable amount of clay and silt intervenes the whole succession. At the 'Coal-covered Area', the uppermost part of Garzweiler Coal (about 5 m thick) is already mined-out prior to the field measurements.

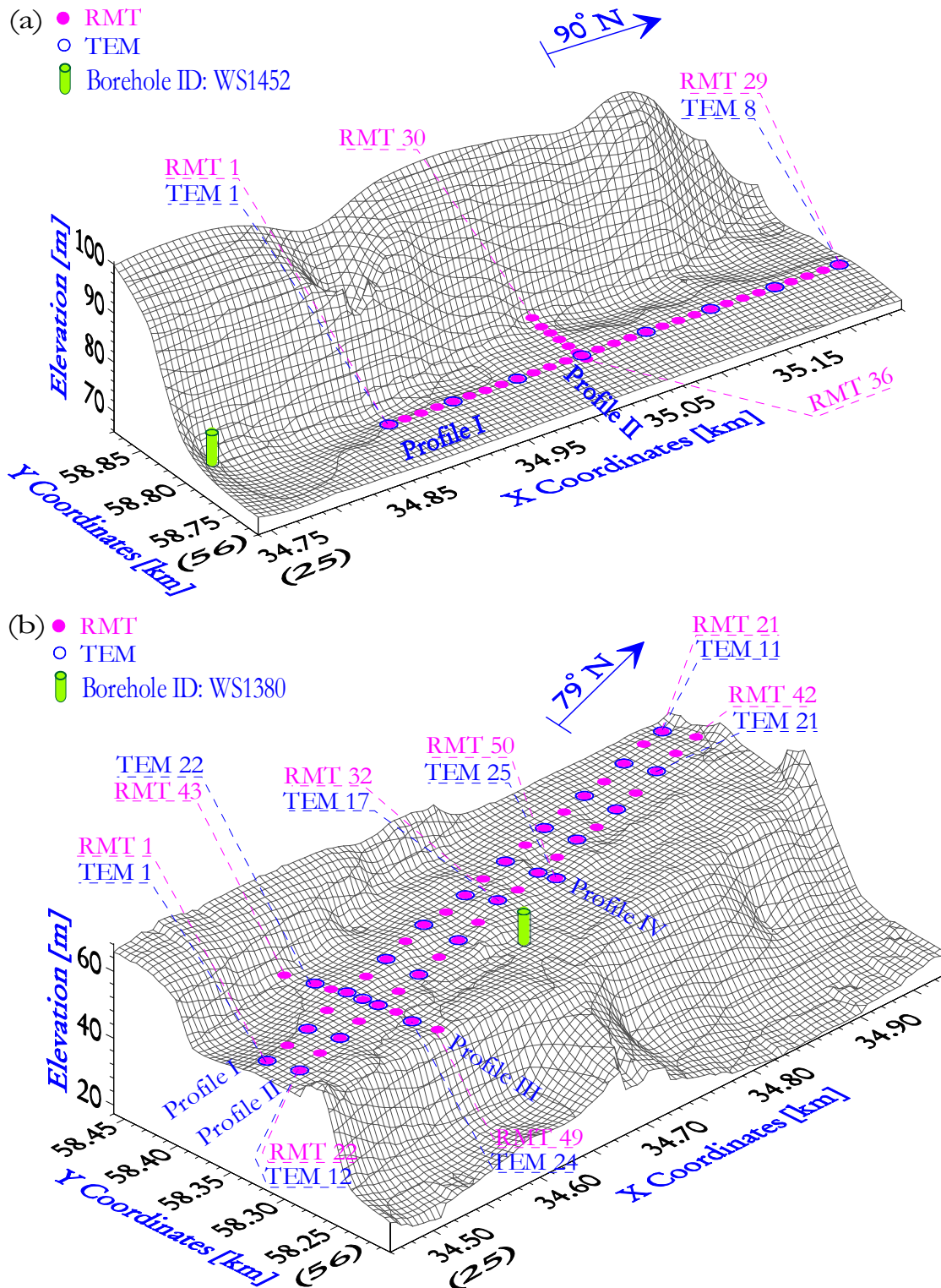


Figure 1.3: Topographic-relief models and locations of RMT/TEM soundings and stratigraphic-control boreholes at the survey areas: (a) 'Sand-covered Area' and (b) 'Coal-covered Area'. Coordinates are given by the German national (Gauss–Krüger) coordinate system.

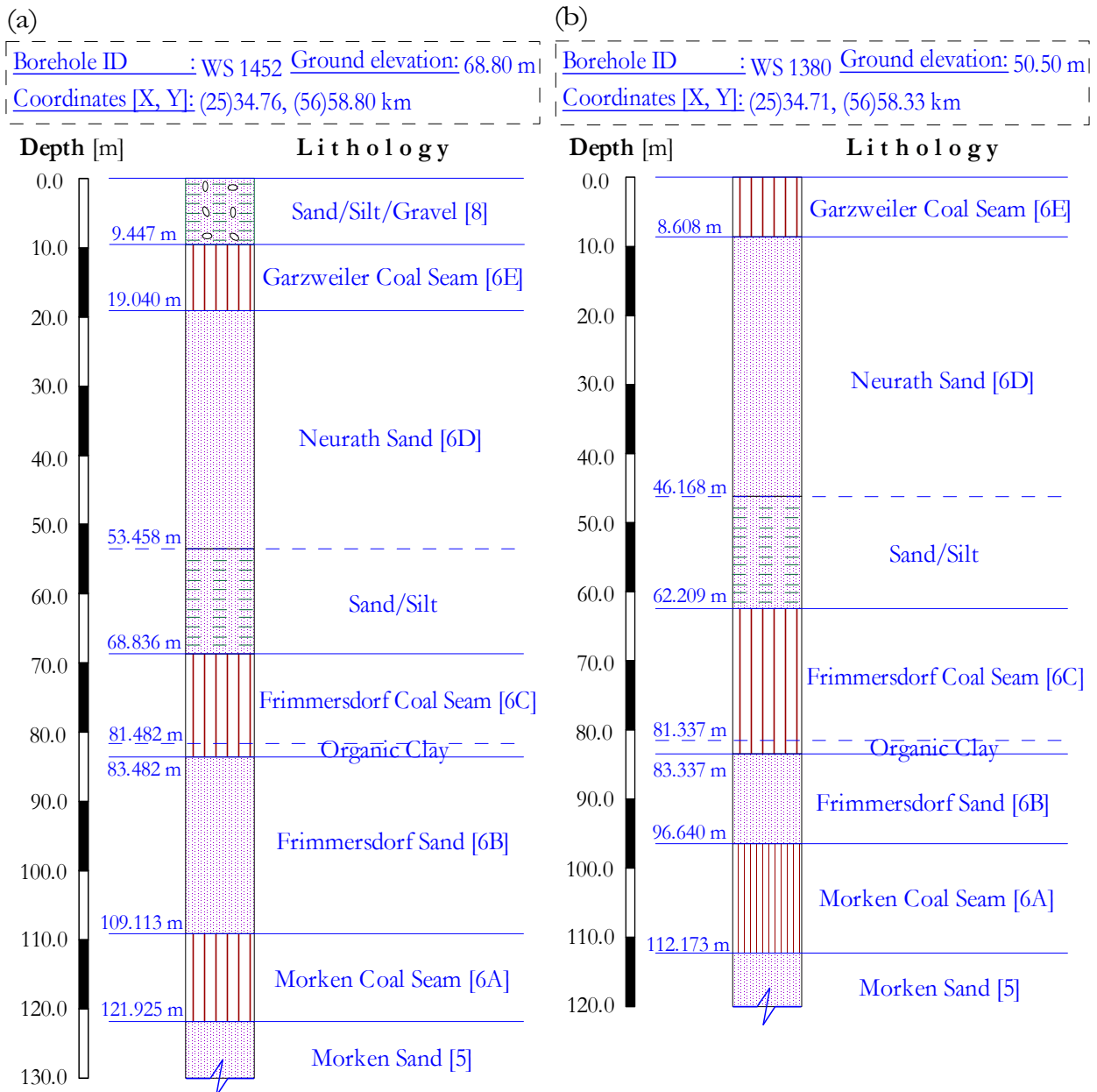


Figure 1.4: Borehole-geology at the survey areas: (a) 'Sand-covered Area' and (b) 'Coal-covered Area'. The stratigraphic extent is from the Early/Middle Miocene Ville Formation (horizons 5, 6A, 6B, 6C, 6D and 6E) to the Early Pliocene Hauptkies Series (horizon 8). Coordinates are given by the German national (Gauss–Krüger) coordinate system.

Preliminary notes

Throughout this dissertation, the measured quantities are expressed in *Systeme Internationale* (SI) units. Matrices are denoted by boldfaced capitals and vectors by boldfaced lowercases. Scalars are represented by italic capitals or lowercases as in elementary algebra. The notation \mathbf{A}^T signifies the transpose of \mathbf{A} .

CHAPTER 2

INVERSION OF ELECTROMAGNETIC DATA

In applied electromagnetics, the data as a result of the earth are measured. This is what we might call a forward problem: a model is given and the data are calculated. The forward (or direct) problem is always uniquely solvable. It is often the other way around: data have been measured and we wish to derive a plausible earth model that is consistent with the data, what may be described as inverse problem. *Inverse Theory* is concerned with the problem of making physical interfaces (i.e. layer boundaries) from the measured data. Since nearly all field data are subjected to some uncertainty, these interfaces are statistically dependent, and therefore no inverse problem in electromagnetics is uniquely solvable. Due to such an invariable non-linearity between the measured data and desired earth model parameters, we usually use an iterative procedure in which the non-linear inverse problem is replaced at each iteration by its linearized approximation to be solved. At the k^{th} iteration, we are interested in minimizing an objective function. Convergence then occurs hopefully to the solution of the non-linear problem. To gain a physically reasonable model, it is therefore necessary to carefully inspect the inversion statistics. The inversion statistics and its sensitivity (or resolution) analysis are just as important as the inversion itself [Strack, 1992]. The purpose of this chapter is to give an introduction to the inversion of EM data. Special attention will be given to the 1D, 2D and 3D RMT/TEM inversion and modeling schemes which have been used in the present work.

2.1 General Statement

Assume there are N measured data values (e.g. apparent resistivities and impedance phases at i^{th} frequencies for RMT data or voltages at i^{th} sampling times for TEM data), which are sorted into the data vector

$$\mathbf{d}=(d_1, d_2, d_3, \dots, d_N)^T, \quad \mathbf{d} \in E^N \quad (N\text{-dimensional Euclidean space}).$$

Each of the data points has a corresponding relative standard deviation (or error) σ_{si} , $i=1, 2, 3, \dots, N$. The desired earth model is determined by M free parameters, which we write as the vector

$$\mathbf{m}=(m_1, m_2, m_3, \dots, m_M)^T, \quad \mathbf{m} \in E^M \quad (M\text{-dimensional Euclidean space}).$$

In practical non-linear problems, the data and the model parameter vectors are related via a non-linear response function \mathbf{f} , which tells us how to calculate the synthetic data from the given model. This inter-relationship is expressed as

$$\mathbf{d}=\mathbf{f}(\mathbf{m})+\mathbf{e} \quad (2.1)$$

so that

$$\Phi(\mathbf{m})=\mathbf{e}^T \mathbf{e}=(\mathbf{d}-\mathbf{f}(\mathbf{m}))^T(\mathbf{d}-\mathbf{f}(\mathbf{m})), \quad (2.2)$$

where \mathbf{e} is the $N \times 1$ column vector of residuals [Lines and Treitel, 1984]. The overall goal of the inversion is then to minimize the deviation between the measured and calculated data $\Phi(\mathbf{m})$, what may be described as the *objective function*.

To derive an iterative inversion scheme, the response function \mathbf{f} is linearized about a starting model (initial guess) \mathbf{m}_0 by expanding it into a *Taylor's series* approximation and ignoring the higher terms as

$$\mathbf{f}(\mathbf{m}) \approx \mathbf{f}(\mathbf{m}_0) + \mathbf{J} \Delta \mathbf{m} \quad \text{with} \quad \Delta \mathbf{m} = \mathbf{m}_0 - \mathbf{m}, \quad (2.3)$$

where $\Delta \mathbf{m}$ is the model update (or perturbation) vector and \mathbf{J} is the *Jacobian matrix*.

The $N \times M$ Jacobian matrix \mathbf{J} is a by-product of linearizing a non-linear problem. Its elements are the partial derivatives of the calculated data with respect to the model parameters (i.e. layer resistivities and thicknesses)

$$J_{ij} = \left. \frac{\partial f_i(\mathbf{m})}{\partial m_j} \right|_{\mathbf{m} = \mathbf{m}_0}, \quad i = 1, 2, 3, \dots, N; j = 1, 2, 3, \dots, M.$$

Because, each column indicates the operating RMT frequencies or TEM time windows in which an individual parameter can be predominantly resolved, this matrix is called *parameter sensitivity matrix*. The full space Jacobian can be written as

$$\mathbf{J} = \begin{bmatrix} \frac{\partial f_1}{\partial m_1} & \frac{\partial f_1}{\partial m_2} & \cdot & \cdot & \cdot & \frac{\partial f_1}{\partial m_M} \\ \frac{\partial f_2}{\partial m_1} & \frac{\partial f_2}{\partial m_2} & \cdot & \cdot & \cdot & \frac{\partial f_2}{\partial m_M} \\ \vdots & \vdots & & & & \vdots \\ \vdots & \vdots & & & & \vdots \\ \vdots & \vdots & & & & \vdots \\ \frac{\partial f_N}{\partial m_1} & \frac{\partial f_N}{\partial m_2} & \cdot & \cdot & \cdot & \frac{\partial f_N}{\partial m_M} \end{bmatrix}_{N \times M} \quad (2.4)$$

The calculation of the Jacobian at each iteration is usually the most time-consuming part in the inversion. Statistically, sensitivity values show whether the layer parameters are seen individually in the measured data at all or, if not, they qualitatively display which a parameter correlation is resolved by the data instead. Therefore, a model parameter is only well-resolved by the measurements if the data points depend strongly on this parameter, i.e. if its sensitivity has large entries in the corresponding column. On the other hand, the normalized Jacobian values or *relative sensitivities* give an idea of each data point's sensitivity to a change of an individual parameter in the solution [Jupp and Vozoff, 1975; Lines and Treitel, 1984].

If we define the vector $\mathbf{y} = \mathbf{d} - \mathbf{f}(\mathbf{m}_0)$ as the discrepancy vector, then the Equation (2.2) can be written in the form

$$\Phi(\mathbf{m}) = \mathbf{e}^T \mathbf{e} = (\mathbf{y} - \mathbf{J} \Delta \mathbf{m})^T (\mathbf{y} - \mathbf{J} \Delta \mathbf{m}), \quad (2.5)$$

which has a solution for the model update as

$$\Delta \mathbf{m} = (\mathbf{J}^T \mathbf{J})^{-1} \mathbf{J}^T \mathbf{y}. \quad (2.6)$$

This is the classical 'Gauss–Newton' solution, which can be applied successively to improve the initial model \mathbf{m}_0 until an optimal model update $\Delta \mathbf{m}$ is obtained. Generally, to calculate an appropriate least-squares model, we should refine the model \mathbf{m} at k^{th} iteration as

$$\mathbf{m}_{k+1} = \mathbf{m}_k + (\mathbf{J}^T \mathbf{J})^{-1} \mathbf{J}^T \mathbf{y}. \quad (2.7)$$

The process iterates until a given convergence criterion or a maximum number of iterations is reached.

To determine how well the model fits the measured data, the usual weighted least-squares criterion (i.e. χ^2 misfit) [Jackson, 1972] is used

$$\chi^2 = \sum_{i=1}^N \left[\frac{d_i - f_i(\mathbf{m})}{\sigma_{si}} \right]^2. \quad (2.8)$$

In the present work, all inversion schemes attempt at minimizing the familiar root mean-square (RMS) defined by

$$\text{RMS} = \sqrt{\frac{\chi^2}{N}}. \quad (2.9)$$

2.2 Inversion as Optimization

An unconstrained least-squares inversion like 'Gauss–Newton' approach (Equation (2.7)) has a difficulty when the EM inverse problem is ill-conditioned, i.e. the ratio between the largest and smallest eigenvalue in the matrix $\mathbf{J}^T \mathbf{J}$ becomes too large. In other words, when the matrix $\mathbf{J}^T \mathbf{J}$ is inherently singular or nearly singular (i.e. $\det \mathbf{J}^T \mathbf{J} \ll 1$). In this case, the 'naive' least-squares solution is completely dominated by contributions from data errors and rounding (perturbation) errors [Tikhonov and Arsenin, 1977], and therefore the solution becomes non-unique and even unstable. That means, one can find several very different geoelectric models fitting the measured data with approximately the same accuracy, but they are statistically unreliable.

However, it is common to pose the problem as a *non-linear optimization* problem in which the penalized objective function $\Phi(\mathbf{m})$ comprises a residual norm (i.e. a measure of data misfit) $\Phi_d(\mathbf{m})$ and a regularized solution norm (i.e. a measure of model character) $\Phi_m(\mathbf{m})$. For instance, by requiring the solution to minimize certain functionals in addition to the standard least-squares data fitting. This approach is known as the classical 'Tikhonov's regularization' [Tikhonov and Arsenin, 1977]

$$\Phi(\mathbf{m}) = \Phi_d(\mathbf{m}) + \tau \Phi_m(\mathbf{m}). \quad (2.10)$$

Practically, *regularization* is necessary when computing a stable solution to an EM inverse problem. By adding regularization we are able to damp the error contributions and keep the regularized solution of reasonable size. This philosophy underlies the most regularization methods. However, all regularization methods for computing stable solutions to inverse problems involve a trade-off τ between the two terms of the objective function. What distinguishes the various regularization methods is how they measure these quantities, and how decide on the optimal trade-off between the two terms.

2.3 Marquardt–Levenberg Inversion Scheme

With this optimization algorithm the least-squares solution of the 1D EM inverse problem is regularized to minimize the model update [Jupp and Vozoff, 1975; Lines and Treitel, 1984]. It is also referred to as *ridge regression* optimization [Inman, 1975]. The scheme is a standard implementation of the 1D layered-earth inversion. It tries to solve an over-determined EM inverse problem (i.e. $M < N$), and hence requires a starting model which has the desired (not more) number of layers. It modifies the layer resistivities and thicknesses in the starting model iteratively to best fit the data. Furthermore, the scheme is more adequate to incorporate a-priori information.

Here the objective function can be written as

$$\begin{aligned}\Phi(\mathbf{m}) &= \|\mathbf{e}\|^2 + \varepsilon^2 (\|\Delta\mathbf{m}\|^2 - \Delta m_0^2) \\ &= \mathbf{e}^T \mathbf{e} + \varepsilon^2 (\Delta\mathbf{m}^T \Delta\mathbf{m} - \Delta m_0^2),\end{aligned}\quad (2.11)$$

where $\|\cdot\|$ denotes the usual L_2 (Euclidean) norm, Δm_0 is a finite quantity, and ε is the Marquardt–Levenberg damping factor [Marquardt, 1963; Levenberg, 1944], i.e. a varying very small positive number allowed to numerically damp the model update at each iteration.

The minimization of the objective function leads to so-called damped least-squares solution

$$\Delta\mathbf{m} = (\mathbf{J}^T \mathbf{J} + \varepsilon^2 \mathbf{I})^{-1} \mathbf{J}^T \mathbf{y} \quad (2.12)$$

or generally

$$\mathbf{m}_{k+1} = \mathbf{m}_k + (\mathbf{J}^T \mathbf{J} + \varepsilon^2 \mathbf{I})^{-1} \mathbf{J}^T \mathbf{y}, \quad (2.13)$$

where \mathbf{I} is the $M \times M$ identity matrix.

Incorporating the data weighting into the minimization problem (2.13) [Hördt *et al.*, 1992b] changes the solution to

$$\Delta\mathbf{m} = (\mathbf{J}^T \mathbf{W}^2 \mathbf{J} + \varepsilon^2 \mathbf{I})^{-1} \mathbf{J}^T \mathbf{W}^2 \mathbf{y}, \quad (2.14)$$

where \mathbf{W} is a $N \times N$ weighting matrix, its diagonal elements are the reciprocal values of σ_{si} .

There are several ways to evaluate the performance of the Marquardt–Levenberg inversion and reliability of results. The most favorable statistical approaches are either the singular-value decomposition (SVD) analysis or the resolution matrix analysis. Typically, these inversion statistics are only applicable for the best-fitted model, where the linearity assumption is valid [Lines and Treitel, 1984].

Singular-value decomposition

A way of obtaining an evaluation of the parameter resolution is the additional use of the so-called singular-value decomposition (SVD) [Jupp and Vozoff, 1975; Jackson, 1972]. The weighted Jacobian $\mathbf{J}_w = \mathbf{W}\mathbf{J}$ is substituted by the product of two orthogonal matrices \mathbf{V} and \mathbf{U} , and one $M \times M$ matrix \mathbf{S} , its diagonal elements contain the positive roots of the eigenvalues of \mathbf{J}_w , S_i .

$$\mathbf{J}_w = \mathbf{W}\mathbf{J} = \mathbf{U}\mathbf{S}\mathbf{V}^T, \quad (2.15)$$

where \mathbf{U} is a $N \times M$ matrix which contains the data space eigenvectors of $\mathbf{J}_w^T \mathbf{J}_w$ in its columns, \mathbf{V} is a $M \times M$ matrix which contains the parameter space square-roots of the eigenvalues of $\mathbf{J}_w^T \mathbf{J}_w$ in its columns (i.e. singular values of \mathbf{J}_w). All matrices satisfy $\mathbf{U}^T \mathbf{U} = \mathbf{V}^T \mathbf{V} = \mathbf{V}\mathbf{V}^T = \mathbf{I}$,

where \mathbf{I} is the $N \times N$ identity matrix. Applying this matrix decomposition to the Equation (2.14), we obtain

$$\Delta \mathbf{m} = \mathbf{V} \text{diag}(1/S_i) \text{diag}(S_i^2/(S_i^2 + \varepsilon^2)) \mathbf{U}^T \mathbf{W} \mathbf{y}. \quad (2.16)$$

The $S_i^2/(S_i^2 + \varepsilon^2)$ are the by-products of the SVD analysis, which are called the damping factors of the inverted layer parameters. In the present work, an exponent of 4 was used instead of 2. In this case, the damping factors act more like thresholds at each iteration. They are generally measures of 'importances' of the corresponding layer parameters, and vary between 0 and 1 to represent the minimal and maximal parameter resolution respectively.

Resolution matrix

For simplicity, we rewrite the solved inverse problem (2.14) in the general form of

$$\mathbf{m}_{\text{Est}} = \mathbf{G}^{-g} \mathbf{d}, \quad (2.17)$$

where \mathbf{G}^{-g} denotes the generalized inverse, which we can use to examine the resolution of the estimated model \mathbf{m}_{Est} , and therefore

$$\mathbf{m}_{\text{Est}} = \mathbf{G}^{-g} \mathbf{G} \mathbf{m} = \mathbf{R} \mathbf{m}, \quad (2.18)$$

where $\mathbf{R} = \mathbf{G}^{-g} \mathbf{G}$ is the parameter resolution matrix. It is a matrix which, when multiplied onto the model vector \mathbf{m} , determines the linear combination of the layer parameters that could be resolved. Its diagonal elements are generally called 'importances' of the corresponding inverted layer parameters. If the resolution matrix is the identity matrix (1's along the main diagonal and 0's elsewhere), then each model parameter is uniquely resolved. In practice, we just desire \mathbf{R} to be diagonally dominated.

Joint-inversion

When inverting two (or more) independent EM data sets simultaneously at the same sounding center to obtain one realistic model, different resolution properties of these data sets are normally combined. Theoretically, each of them can compensate for the weaknesses of the other, and therefore the overall benefit would be a reduction of the interpretation ambiguity [Vozoff and Jupp, 1975; Raiche et al., 1985]. In the 1D layered-earth inversion, the data vector has the length of both data sets, while the model parameter vector remains of the same length as for ordinary individual inversion.

2.4 Occam's Inversion Scheme

With this optimization algorithm the least-squares solution of the EM inverse problem is regularized to minimize the change of model update or roughness (converse of smoothness) [Constable et al., 1987]. The philosophy of the Occam's inversion scheme is to find the smoothest resistivity model which matches the measured data to some required level (i.e. data misfit tolerance). The interpreter determines how well to fit the data, and the inversion determines how much structure the model requires. The scheme is a standard implementation of the 1D smoothed-earth inversion. It tries to solve an under-determined EM inverse problem (i.e. $N < M$), and hence requires a starting model which has much more number of layers. Indeed, the computational expense depends linearly on the number of layers. The layer thicknesses are fixed, while only resistivities are free parameters in the inversion. Layer resistivities are then adjusted iteratively until the model response is as close as possible to the measured data, given constraints which keep the resistivity model smooth. A smoothed-earth

inversion, such as Occam's inversion, is an important step in the 1D interpretation strategy, as it can formulate a good starting model for the further full non-linear layered-earth inversion.

The model roughness $\|\mathbf{Dm}\|^2$ is given as the integrated square of the first (or second) derivative of the logarithm of resistivity m with respect to the depth z

$$\|\mathbf{Dm}\|^2 = \int (\partial m / \partial z)^2 \partial z. \quad (2.19)$$

In discrete representation the roughness can be given in terms of a simple matrix operations, where its penalty matrix is

$$\mathbf{D} = \begin{bmatrix} 0 & \dots & \dots & \dots & \dots & \dots & \dots & \dots & \dots & \dots & 0 \\ -1 & & 1 & & 0 & \dots & \dots & \dots & \dots & \dots & 0 \\ 0 & & -1 & & 1 & & 0 & \dots & \dots & \dots & 0 \\ \dots & \dots & \dots & \dots & \dots & \dots & \dots & \dots & \dots & \dots & \dots \\ 0 & \dots & \dots & \dots & \dots & \dots & 0 & -1 & & 1 & \dots \end{bmatrix}_{M \times M}.$$

Here the objective function can be written as

$$\begin{aligned} \Phi(\mathbf{m}) &= \|\mathbf{Dm}\|^2 + \mu^{-1}(\chi(\mathbf{m})^2 - \chi^*(\mathbf{m})^2) \\ &= \|\mathbf{Dm}\|^2 + \mu^{-1}(\|\mathbf{Wd} - \mathbf{Wf}(\mathbf{m})\|^2 - \chi^*(\mathbf{m})^2), \end{aligned} \quad (2.20)$$

where μ^{-1} is the 'Lagrange multiplier' which controls both the model roughness and data misfit. The μ^{-1} is usually chosen so that $\chi(\mathbf{m}) = \chi^*(\mathbf{m})$, where $\chi^*(\mathbf{m})$ is the desired data misfit (or tolerance).

Following *Constable et al.* [1987], the objective function is minimized by differentiation with respect to \mathbf{m} and rearranged to yield an expression for the model

$$\mathbf{m} = [\mu \mathbf{D}^T \mathbf{D} + (\mathbf{WJ})^T \mathbf{WJ}]^{-1} (\mathbf{WJ})^T \mathbf{Wd}. \quad (2.21)$$

2.5 Mackie's Inversion Scheme

Unlike the case for TEM methods, multi-dimensional interpretation of RMT data is almost straight forward. In general, 2D and 3D forward modeling/inversion are performed numerically using the integral, differential or hybrid forms of the diffusive Maxwell's differential-equations. Of these, the finite-difference (FD) and finite-element (FE) network solutions are the most widely used for modeling arbitrarily complex geometries in MT methods. However, the existing 2D modeling/inversion schemes are yet to be rigorously tested on the real data [*deGroot-Hedlin and Constable*, 1990; *Smith and Booker*, 1991; *Rodi and Mackie*, 2001; *Mehanee and Zhdanov*, 2002], whilst the 3D modeling/inversion schemes are yet to be developed and perfected. The most flexible approach is using the Mackie's inversion scheme which is based on either Gauss-Newton (GN) or non-linear conjugate gradients (NLCG) algorithms to solve the 2D RMT inverse problem using Tikhonov's regularization. The decoupled Maxwell's equations in the frequency-domain for the EM fields excited by a plane-wave source over an arbitrary complex 2D resistivity and topographic structures (see Section 3.1.1) are solved numerically using the finite-difference algorithm. The scheme was introduced and efficiently coded by *Mackie et al.* [1997], and applied to real RMT data for the first time by *Recher* [1998] and *Ziebell* [1998] to image the resistivity structures of some industrial waste sites in Germany.

With this optimization algorithm the least-squares solution of the 2D RMT inverse problem is regularized to minimize the change of model update or roughness (converse of smoothness), acting in the horizontal and vertical planes [Rodi and Mackie, 2001]. Initially, the subsurface earth should be parametrized (or broken down) into rectangular blocks of uniform resistivity, which is like a 'stick-of-bricks', by means of discretized rectangular grid elements. This is generally called 2D finite-difference *earth-mesh*. Mackie's inversion scheme utilizes the calculated apparent resistivities and impedance phases from the forward modeling to modify the mesh resistivities iteratively to best fit the data, given constraints which keep the resistivity model smooth.

Mackie's objective function can be written as

$$\begin{aligned}\Phi(\mathbf{m}) &= \|(\mathbf{d} - \mathbf{f}(\mathbf{m})) / \sigma_s\|^2 + \tau \| \mathbf{L}(\mathbf{m} - \mathbf{m}_0) \|^2 \\ &= (\mathbf{d} - \mathbf{f}(\mathbf{m}))^T \mathbf{V}^{-1} (\mathbf{d} - \mathbf{f}(\mathbf{m})) + \tau (\mathbf{m} - \mathbf{m}_0)^T \mathbf{L}^T \mathbf{L} (\mathbf{m} - \mathbf{m}_0),\end{aligned}\quad (2.22)$$

where \mathbf{V} is the error covariance matrix, τ is the regularization parameter and \mathbf{L} is a linear operator (or *Laplacian*) which acts on the difference between the model vector \mathbf{m} and a start (or an optionally given a-priori) model vector \mathbf{m}_0 and yields

$$\| \mathbf{L}(\mathbf{m} - \mathbf{m}_0) \|^2 = \int (\nabla^2(m(x) - m_0(x)))^2 \tilde{\alpha}x.$$

2.5.1 Gauss–Newton Algorithm

The classical Gauss–Newton (GN) method generates a model sequence \mathbf{m}_0 (given), \mathbf{m}_1 , \mathbf{m}_2 , ..., \mathbf{m}_j , \mathbf{m}_{j+1} by a recursive minimizing of the objective function. It solves the following equation

$$\begin{aligned}(2\mathbf{J}(\mathbf{m}_j)^T \mathbf{V}^{-1} \mathbf{J}(\mathbf{m}_j) + 2\tau \mathbf{L}^T \mathbf{L})(\mathbf{m}_{j+1} - \mathbf{m}_j) &= -2\mathbf{J}(\mathbf{m}_j)^T \mathbf{V}^{-1} (\mathbf{d} - \mathbf{f}(\mathbf{m}_j)) + 2\tau \mathbf{L}^T \mathbf{L} \mathbf{m}_j \\ \mathbf{H}(\mathbf{m}_j)(\mathbf{m}_{j+1} - \mathbf{m}_j) &= -\mathbf{g}(\mathbf{m}_j),\end{aligned}\quad (2.23)$$

where $\mathbf{g}(\mathbf{m}_j)$ and $\mathbf{H}(\mathbf{m}_j)$ are the gradient and approximated Hessian matrix of the objective function respectively, after \mathbf{f} is well-linearized about a start model.

Rodi and Mackie [2001] modified Equation (2.23), using the simple version of Marquardt–Levenberg scheme [Marquardt, 1963; Levenberg, 1944] as

$$(2\mathbf{J}(\mathbf{m}_j)^T \mathbf{V}^{-1} \mathbf{J}(\mathbf{m}_j) + 2\tau \mathbf{L}^T \mathbf{L} + \varepsilon \mathbf{I})(\mathbf{m}_{j+1} - \mathbf{m}_j) = -\mathbf{g}(\mathbf{m}_j),\quad (2.24)$$

where \mathbf{I} is the $M \times M$ identity matrix and ε is the usual Marquardt–Levenberg damping factor. Finally, the algorithm solves the linear system in Equation (2.24) by inverting the damped Hessian matrix, $\mathbf{H}(\mathbf{m}_j) + \varepsilon \mathbf{I}$, as follows

$$\mathbf{m}_{j+1} = \mathbf{m}_j - 1/2(\mathbf{J}(\mathbf{m}_j)^T \mathbf{V}^{-1} \mathbf{J}(\mathbf{m}_j) + \tau \mathbf{L}^T \mathbf{L} + \varepsilon \mathbf{I})^{-1} \mathbf{g}(\mathbf{m}_j).\quad (2.25)$$

We can make the abbreviations $\mathbf{g}_j \equiv \mathbf{g}(\mathbf{m}_j)$ and $\mathbf{H}_j \equiv \mathbf{H}(\mathbf{m}_j)$ for further discussion.

2.5.2 Non-linear Conjugate Gradients Algorithm

The non-linear conjugate gradients (NLCG) method [Fletcher and Reeves, 1964; Polak, 1971; Rodi and Mackie, 2001] generates a model sequence \mathbf{m}_0 (given), \mathbf{m}_1 , $\mathbf{m}_2, \dots, \mathbf{m}_j$, $\mathbf{m}_{j+1} = \mathbf{m}_j + \alpha_{j+1} \mathbf{P}_{j+1}$ by a direct sequence of univariate minimizing, or line searches, of the objective function along computed search directions \mathbf{P}_{j+1} in the model space. It solves the

linear system given in Equation (2.22) incompletely by halting the conjugate gradients (CG) iteration prematurely after a prescribed number of steps. For this, computing the step size α_{j+1} involves an iterative line minimization procedure. The line minimization automatically defaults to a one-step computation of α_{k+1} , when \mathbf{f} is well-linearized about a start model, as

$$\alpha_{j+1,k+1} = \alpha_{j+1,k} - \frac{\mathbf{g}_{j,k} \mathbf{P}_{j+1}^T}{\mathbf{P}_{j+1}^T \mathbf{H}_{j,k} \mathbf{P}_{j+1}}, \quad k = 0, 1, 2, \dots \quad (2.26)$$

Like the CG [Mackie and Madden, 1993], the NLCG computes the search directions as

$$\mathbf{P}_{j+1} = \mathbf{C}_j \mathbf{g}_j + \beta_j \mathbf{P}_j, \quad (2.27)$$

where

$$\mathbf{C}_j = (\gamma_j \mathbf{I} + \tau \mathbf{L}^T \mathbf{L})^{-1}$$

and

$$\beta_j = \frac{\mathbf{g}_j^T \mathbf{C}_j (\mathbf{g}_j - \mathbf{g}_{j-1})}{\mathbf{g}_{j-1}^T \mathbf{C}_{j-1} \mathbf{g}_{j-1}}.$$

The $M \times M$ positive matrix \mathbf{C}_j is known as a preconditioner, which acts in some sense like the inverse of the approximated Hessian matrix and has a big impact on efficiency in NLCG algorithm. Two competing considerations in its choice are the computational cost when applied and its effectiveness in 'steering' the gradient vector into a more productive search direction. The amount of computation needed to solve the above preconditioned system is less than one forward function evaluation, and thus adds little overhead to the NLCG algorithm. The parameter β_j refers back to the Polak–Ribiere technique [Polak, 1971], while the specified scalar γ_j is proportional to $\|\mathbf{V}^{-1/2} \mathbf{J}\|$. The first term of Equation (2.27) is the preconditioned 'steepest descent' direction that minimizes the directional derivative of the objective function evaluated at \mathbf{m}_{j+1} . Whereas, the second term modifies the search direction so that it is conjugate to previous search directions. However, if the line search is converged, the new search direction \mathbf{P}_{j+1} is taken as the steepest descent direction, breaking down the conjugacy with the previous search iterations.

In Mackie's inversion scheme a clever method is applied, where both the GN and NLCG algorithms compute the elements of Jacobian (or its transpose) efficiently based on the EM reciprocity theorem. This decreases the number of forward solutions required [Farquharson and Oldenburg, 1996; McGillivray and Oldenburg, 1990]. The GN algorithm entails the generation of a full sensitivity matrix and the complete solution of linearized inverse problem at each iteration. This involves computing an extra forward problem for each frequency, each sounding and each polarization mode, and therefore the required CPU time is actually dominated by the storage of the Jacobian ($N \times M$ real numbers) and Hessian (M^2 real numbers) matrices. The NLCG algorithm, in contrast, employs the Jacobian (or its transpose) only in the computation of specific quantities and vectors [Rodi and Mackie, 2001; Mackie and Madden, 1993]. This involves only computing two extra forward problems for each frequency. Therefore, the storage of the whole, often very large Jacobian matrix can even be completely avoided. As a result, the algorithm NLCG is always found more superior to the conventional GN algorithm with regard to the computational expense, where it scales much more favorably with problem size in both CPU and memory usage [Rodi and Mackie, 2001; Recher 2002]. This is realized in newer versions of Mackie's inversion code, but since the Jacobian matrix contains valuable information, an older version based on GN algorithm was used in the present work too. Figure 2.1 shows how the NLCG algorithm reduces the objective function at

a faster rate, versus CPU time, than GN algorithm which mostly duplicates (or triplicates) CPU time throughout all minimization stages. As a rough rule for both algorithms, the computational expense depends linearly on the number and size of horizontal and vertical grid elements.

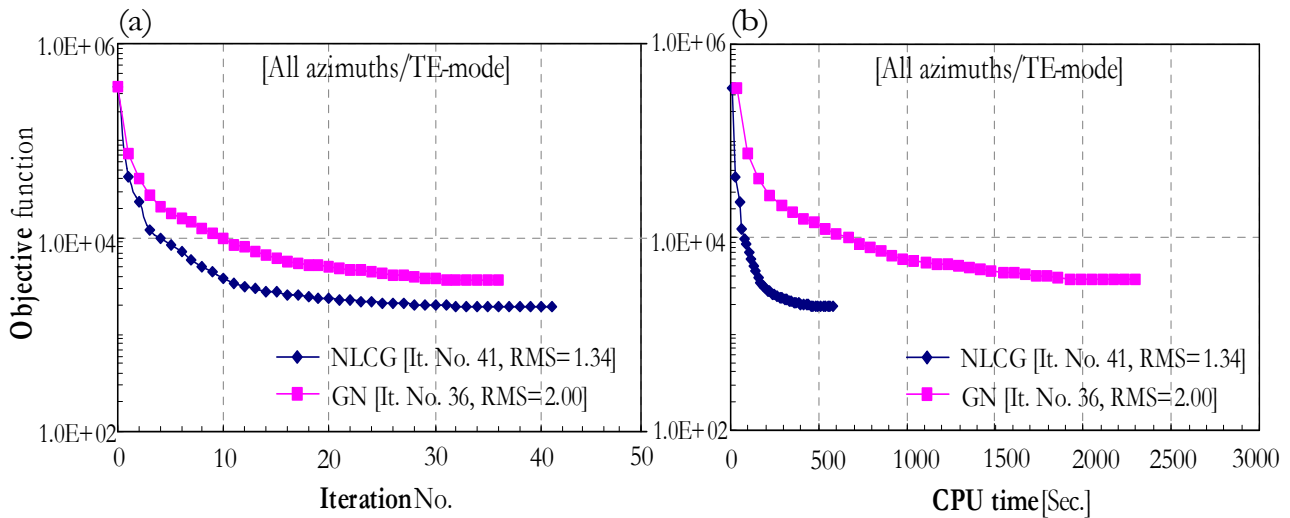


Figure 2.1: The objective function versus (a) iteration number and (b) CPU time, resulting from the application of NLCG and GN algorithms in 2D inversion of RMT data along profile I at the 'Coal-covered Area.' Here we can see the computational advantages of the NLCG over the conventional GN algorithms in accelerating the solution convergence. All computations were performed on a Pentium III (800 MHz) PC.

2.6 SLDM Forward Modeling Scheme

The standard interpretation of TEM data is still based on the conventional 1D inversion or forward modeling schemes. Although they have proved feasible in many practical cases, significant ambiguity may occur when the geoelectric model is essentially multi-dimensional, i.e. not an uniform horizontally layered-earth, or when transient-decay data are so strongly distorted by highly-conductive surficial anomalies. In order to interpret TEM data in a multi-dimensional fashion, one must have an inversion or forward modeling scheme on hand. Unfortunately at present, multi-dimensional inversion tools have not been routinely available for TEM soundings, mainly due to the more difficult simulation of artificial EM sources. Alternatively, the most flexible approach is using 3D trial-and-error forward calculations based on the spectral Lanczos decomposition method (SLDM). It solves the diffusive Maxwell's differential-equations using finite-difference algorithm with the help of 'Krylov subspace' technique. This provides for a fast implicit 3D numerical solver of the EM fields in arbitrarily complex geometries and implements mainly the conjugate-gradients method [Madden and Mackie, 1989; Druskin and Knizhnerman, 1994], which is very efficient for the solution of large linear systems with a sparse matrix. The solution of the differential-equation system is written as the product of functions of its stiffness matrix and the vector describing the integral initial and boundary conditions specified at the grid boundaries. The scheme was introduced and efficiently coded by Druskin and Knizhnerman [1988], and applied to real data for the first time by Hördt *et al.* [1992a] to simulate the influence of the surficial highly-conductive inhomogeneities on the LOTEM field transients in Germany. Recently, SLDM scheme has been successfully applied to simulate also the influence of the mountainous terrain on the LOTEM field transients [Hördt and Müller, 2000; Commer, 2003].

Initially, a staggered grid should be designed. This grid sections the model workspace into cells (or rectangular blocks), each of specified dimensions and uniform resistivity. This is collectively called 3D finite-difference *earth-mesh*. Yee [1966] introduced an efficient numerical convention to solve EM differential-equations on the FD grid. The individual electric and magnetic field components in 3D space are defined along the block edges and across block faces respectively. The total fields are then calculated successively from these components at each cell using the 'leap-frog' implementation. The SLDM scheme allows the displacement of electric and/or magnetic dipole elements as radiators and sensors at arbitrary locations and directions within the grid. Moreover, the model parameterization does not necessarily conform to the FD grid discretization. This feature is practically realized by a 'material averaging theorem' to inversely interpolate any resistivity-distribution within the model workspace [Moskow *et al.*, 1999], and hence allows the horizontal and/or vertical resistivity-contrasts to be changed and moved without having to modify the FD grid.

Here a brief summary of the SLDM scheme based on *Druskin and Knizhnerman* [1988 and 1994] and *Hördt et al.* [1992a].

We wish to solve Maxwell's equations in the time-domain [Ward and Hohmann, 1988] as

$$\nabla \times \mathbf{e} = -\mu_0 (\partial \mathbf{h} / \partial t) \quad (2.28)$$

and

$$\nabla \times \mathbf{h} = \sigma \mathbf{e} + \mathbf{j}, \quad (2.29)$$

where \mathbf{e} [V/m] and \mathbf{h} [A/m] are the electric and magnetic field vectors respectively, μ_0 is the magnetic permeability of free space [$=4\pi \times 10^{-7}$ W/Am], σ is the electric conductivity [S/m] and \mathbf{j} [A/m²] is the electric current density vector. Equation (2.28) is the mathematical statement of *Faraday's* law, while Equation (2.29) is the mathematical statement of *Ampere's* law. Displacement currents are assumed to be neglected. The conductivity is assumed to be zero for $z < 0$ and $z > Z$, where z is positive downward Z is a given depth. This means that the conductive medium consists of a layer of finite thickness Z . At the surface and at the layer boundaries, the integral boundary conditions [Tabarovski, 1982] are directly employed.

By applying the curl operator ∇ to Equation (2.28) and substituting (2.29) into (2.28), we obtain

$$\mathbf{1} / \mu_0 \nabla \times (\nabla \times \mathbf{e}) + \sigma (\partial \mathbf{e} / \partial t) = -(\partial \mathbf{j} / \partial t). \quad (2.30)$$

For TEM methods, the source current is switched at $t=0$, which means that we can express the function \mathbf{j} as

$$\mathbf{j} = -\boldsymbol{\psi}(x, y, z) \eta(t), \quad (2.31)$$

where $\eta(t)$ is the 'Heaviside' function ($\eta(t < 0) = 0$, $\eta(t > 0) = 1$) and $\boldsymbol{\psi}$ is the external source function. We obtain from Equations (2.30) and (2.31)

$$\mathbf{1} / \mu_0 \nabla \times (\nabla \times \mathbf{e}) + \sigma (\partial \mathbf{e} / \partial t) = 0; \quad t > 0, \quad \mathbf{e} |_{t=0} = \boldsymbol{\psi}. \quad (2.32)$$

The conductive medium is discretized spatially on a staggered Yee's grid, and the spatial differential operators in Equation (2.32) are approximated by 3D finite-differences. The discretization leads to the following set of differential equations

$$\mathbf{B} \underline{\mathbf{e}} + \sigma (\partial \underline{\mathbf{e}} / \partial t) = 0; \quad t > 0, \quad \underline{\mathbf{e}} |_{t=0} = \boldsymbol{\psi}, \quad (2.33)$$

where $\mathbf{B} = \mu_0^{-1} \nabla \times \nabla \times$ is a positive symmetrical $n \times n$ matrix operator and the ' $\underline{\quad}$ ' denotes the spatial grid discretization. The element $n = n_x(n_y - 1)n_z + (n_x - 1)n_y n_z + (n_x - 1)(n_y - 1)n_z$, where n_x ,

n_y , and n_z are the number of grid nodes in the x -, y -, and z -directions respectively. In practice, this can become up to $100 \times 100 \times 80$. For simplicity, we transform the differential equation system (2.33) to one of normalized form with conservation of symmetry and non-negativeness of the matrix

$$\mathbf{A}\mathbf{u} + (\partial\mathbf{u}/\partial t) = 0; \quad t > 0, \quad \mathbf{u}|_{t=0} = \Psi, \quad (2.34)$$

where

$$\mathbf{u} = \sqrt{\underline{\sigma}} \underline{\mathbf{e}}, \quad \Psi = \sqrt{\underline{\sigma}} \psi \quad \text{and} \quad \mathbf{A} = \sqrt{\frac{1}{\underline{\sigma}}} \mathbf{B} \sqrt{\frac{1}{\underline{\sigma}}}.$$

The elements n and $t\|\mathbf{A}\|$ can come up to 10^5 and 10^{10} respectively. In practice, solving Equation (2.34) by conventional time-stepping algorithms might be extremely time-consuming for large scale 3D problems. We apply the spectral Lanczos decomposition method (SLDM) to solve Equation (2.34). This system of equations can be solved by an explicit difference scheme as

$$\mathbf{A}\mathbf{u}_k + (\mathbf{u}_{k+1} - \mathbf{u}_k)/\tau_s = 0, \quad k = 1, 2, 3, \dots, m-1, \quad \mathbf{u}_0 = \Psi, \quad (2.35)$$

where m is the number of time steps τ_s .

A solution would be presented by the matrix polynomial

$$\mathbf{u}_k = (\mathbf{I} - \tau_s \mathbf{A})^k \Psi, \quad (2.36)$$

where \mathbf{I} is the $n \times n$ identity matrix.

The approximate solution can be considered as an element of the so-called Krylov subspace [Parlett, 1980].

$$\mathbf{K}^m = \text{span}(\Psi, \mathbf{A}^1\Psi, \mathbf{A}^2\Psi, \mathbf{A}^3\Psi, \dots, \mathbf{A}^{m-1}\Psi). \quad (2.37)$$

The main arithmetical expenditures are connected with multiplications of the matrix with vectors and are proportional to m . The SLDM allows the construction of an optimal solution in the sense of an accurate result as an element of the Krylov subspace without essential additional expenditures. An orthonormal basis of the Krylov subspace consisting of m vectors \mathbf{q} can be obtained as the result of the 'Gram-Schmidt' orthogonalization, carrying out the three-term Lanczos recurrence

$$\mathbf{A}\mathbf{q}_i = \beta_{i-1}\mathbf{q}_{i-1} + \alpha_i\mathbf{q}_i + \beta_i\mathbf{q}_{i+1}, \quad i = 1, 2, 3, \dots, m-1 \quad (2.38)$$

with

$$\beta_0\mathbf{q}_0 = 0, \quad \mathbf{q}_1 = \Psi / \|\Psi\|, \quad \alpha_i = \mathbf{q}_i^T \mathbf{A} \mathbf{q}_i \quad \text{and} \quad \beta_i = \|\mathbf{A}\mathbf{q}_i - \alpha_i\mathbf{q}_i - \beta_{i-1}\mathbf{q}_{i-1}\|.$$

If we denote

$$\mathbf{T}_m = \begin{bmatrix} \alpha_1 & \beta_1 & & & 0 \\ \beta_1 & \alpha_2 & \beta_2 & & \\ & & \ddots & \ddots & \\ & & & \beta_{m-2} & \alpha_{m-1} & \beta_{m-1} \\ 0 & & & & \beta_{m-1} & \alpha_m \end{bmatrix}$$

and

$$\mathbf{Q} = (q_1, q_2, q_3, \dots, q_m),$$

the Lanczos process can be summarized by

$$\mathbf{A}\mathbf{Q}=\mathbf{Q}\mathbf{T}. \quad (2.39)$$

We let $(\lambda_i$ and $\mathbf{s}_i)$ be the pairs of eigenvalues and normalized eigenvectors of the symmetrical tridiagonal matrix \mathbf{T} respectively. Furthermore, we define $\mathbf{e}_1=(1, 0, \dots, 0)^T$ and \mathbf{s}_{1i} is the first component of the vector \mathbf{s}_i . Finally, the essence of the SLDM is to define

$$\mathbf{u}_m \approx \|\Psi\| \mathbf{Q} \sum_{i=1}^m \mathbf{s}_{1i} f(\lambda_i) \mathbf{s}_i \approx \|\Psi\| \mathbf{Q} f(\mathbf{T}) \mathbf{e}_1 \quad (2.40)$$

such that \mathbf{u}_m is the approximate solution for \mathbf{u} in the Krylov subspace \mathbf{K}^m . It may be called a spectral decomposition of \mathbf{u} , because it is decomposed into a linear combination of subspace basis vectors. Here the \mathbf{u}_m becomes a good approximation for \mathbf{u} when m is considerably smaller than the corresponding number of time steps for conventional difference methods solving Equation (2.40).

The SLDM scheme is practically unlimited in terms of 3D model complexity and allows the closest approximation of the real geology, but it can become very CPU time intensive for complicated models encountered in real TEM situations.

Model parameterization

Parameterization of the earth model in terms of electrical resistivity has special significance in EM inversion. The simplest parameterization is the 1D earth model wherein the resistivity is assumed to vary only with depth. More realistic models are 2D or 3D earth models where the resistivity also varies in either one or two horizontal directions respectively. An important constraint on model parameters (layer thicknesses and resistivities) is that they must be positive quantities. To enforce this on the inverse solution, a logarithmic parameterization is preferably used. Moreover, the resistivity of naturally occurring rocks and minerals and ores shows a great variation over several orders of magnitude (see Section 5.1). This makes it more nature to invert the logarithms of layer resistivities rather than the resistivities themselves.

CHAPTER 3

RADIOMAGNETOTELLURIC RESISTIVITY MODELS

The conventional azimuthal DC resistivity methods, using either symmetrical or asymmetrical electrode configurations that rotate in steps up to 30° , are often applied to study the electrical anisotropy and earth model dimensionality [e.g. *Watson and Barker*, 1999]. Alternatively, *Bosch and Müller* [2002] and *Linde and Pedersen* [2004] have used the azimuthal radiomagnetotelluric (RMT) methods, as their data can be acquired in the field more faster than DC resistivity methods, to study the large-scale electrical anisotropy in some limestone aquifers and its hydrogeological impacts. This chapter explains the conceptual background of RMT methods and gives detailed description on how to acquire azimuthal RMT data sets in the field and to interpret them reliably in terms of 1D and 2D resistivity models. Furthermore, the effect of nearby-topography on the RMT data will be qualitatively assessed.

3.1 Radiomagnetotelluric Methods

3.1.1 Conceptual Background

Radiomagnetotelluric (RMT) methods utilize EM radiation generated by remote powerful radio-transmitters which are distributed all around the world for the purpose of military communication and civilian broadcasting. These radio-transmitters operate at the frequency range from 10 to around 300 kHz and emit continuously either superimposed frequency-modulated EM wave or occasionally chopped unmodulated 'Morse code' [*Turberg et al.*, 1994; *Turberg and Barker*, 1996]. A radiated EM wave consists of coupled alternating vertical electrical and concentric horizontal magnetic fields, perpendicular to each other and to the direction of propagation, and travels efficiently over long distances close to the ground surface. When the sounding center is located at least seven skin-depths (few hundreds of meters) away from a radio-transmitter, the primary EM waves are essentially planar and horizontal [*McNeill and Labson*, 1991; *Schröder*, 1994]. Because the ground surface is not a perfect conductor, some EM energy is lost into space or penetrates the ground. Induced currents in the ground by RMT magnetic field produce an opposite secondary magnetic field with the same frequency as the primary, but generally with a different amplitude and phase depending on the ground resistivity and excitation frequency of the primary field. The secondary magnetic field has both horizontal and vertical components. Any vertical secondary magnetic field component is by definition anomalous, causing a tilted or elliptically polarized resultant field, if recorded. Because the RMT electric field near the ground surface is titled, not vertical, it has also a horizontal component.

If the penetrated wave is polarized in the xy -plane, traveling downward in the z -direction. Locally, the horizontal resultant electric field component E_x [V/m] is measured by the voltage drop between a pair of potential electrodes planted into the ground, while the horizontal resultant magnetic field component H_y [A/m] is sensed by a small vertical induction at the mid-point coil between electrodes. Analogous to MT methods, data analysis usually commences with calculation of the complex surface impedance Z_{xy} [Ω] in the vicinity of the RMT sounding [Wait, 1954]. It is the frequency-domain ratio of the measured orthogonal horizontal electric and magnetic field components, at angular-frequency $\omega=2\pi f$ [Hz], for the selected operating frequency f ,

$$Z_{xy} = \frac{E_x}{H_y}. \quad (3.1)$$

In field situations, the orthogonal electric and magnetic field components are measured in both horizontal directions (x, y) and related to each other by the following expression

$$\begin{bmatrix} E_x \\ E_y \end{bmatrix} = \mathbf{Z} \begin{bmatrix} H_x \\ H_y \end{bmatrix}, \quad (3.2)$$

allowing the definition of the complete-element impedance tensor (or MT transfer function) as

$$\mathbf{Z} = \begin{bmatrix} Z_{xx} & Z_{xy} \\ Z_{yx} & Z_{yy} \end{bmatrix}. \quad (3.3)$$

For an ideal ground resistivity structure (i.e. an uniform horizontally layered-earth) the diagonal elements are zero, i.e. $|Z_{xx}|=|Z_{yy}|=0$, and the off-diagonal elements differ in sign, i.e. $Z_{xy}=-Z_{yx}$. For a 2D resistivity structure in which the resistivity is invariant in one horizontal plane, the diagonal elements will be zero and off-diagonal elements are completely different, i.e. $|Z_{xx}|=|Z_{yy}|=0$ and $|Z_{xy}| \neq |Z_{yx}|$, if the EM fields are defined in a coordinate system orthogonal to a known geological-strike of the structure. The structure strikes towards the radio-transmitter is well-coupled, as the magnetic field is perpendicular to it and current can flow freely. If the two electrodes are maintained parallel to the strike along the survey profile, the measured electric field is defined as E -polarization or transverse electric (TE) mode. For which the scalar diffusion equation in H_x becomes

$$\frac{\partial^2 E_x}{\partial y^2} + \frac{\partial^2 E_x}{\partial z^2} = i\omega\mu_0\sigma E_x. \quad (3.4)$$

Here the boundary condition on the tangential component of the electric field does not impose free charge accumulation at the strike interface. Therefore, the electric field continuously varies across this interface.

On the other hand, the structure strikes perpendicular to the radio-transmitter is minimally-coupled, as the magnetic field is parallel to it and current flow would be restricted. If the two electrodes are maintained normal to the strike, the measured electric field is defined as H -polarization or transverse magnetic (TM) mode. For which the scalar diffusion equation in E_x becomes

$$\frac{\partial^2 H_x}{\partial y^2} + \frac{\partial^2 H_x}{\partial z^2} = i\omega\mu_0\sigma H_x. \quad (3.5)$$

Here the boundary condition on the normal component of the electric field imposes free charge accumulation at the strike interface. This gives rise to discontinuity in the electric field close to that interface.

For a general 3D resistivity structure in which the resistivity is variant in both the vertical and horizontal planes, there are no strict rules that impedance tensors must obey. Nevertheless, it is common that the off-diagonal elements are all nonzero, completely different and may lie in the first and third quadrant in the complex plane. One very useful measure of the dimensionality is *skewness* (the absolute ratio of the summation of diagonal elements to the subtraction of off-diagonal elements) [Swift, 1971], which is rotationally invariant and equal to zero only for the 1D and 2D resistivity structures. However, instead of a time-consuming 3D analysis of the impedance data, different average or determinant responses are commonly used to represent the impedance response for 3D data and to provide a response that can be interpreted using 1D methods [e.g. Li and Pedersen, 1991].

The magnitude of the surface impedance is commonly expressed in terms of the apparent resistivity $\rho_{a,xy}$ [Ωm] and impedance phase ϕ_{xy} [$^\circ$], the phase lag in time of the measured electric field relative to magnetic field at the operating frequency, using the well-known Cagniard formulas of MT [Tikhonov, 1950; Cagniard, 1953]

$$\rho_{a,xy} = \frac{1}{\omega\mu_0} \left| Z_{xy} \right|^2 \quad (3.6)$$

and

$$\phi_{xy} = \tan^{-1} \left| \frac{\text{Im}[Z_{xy}]}{\text{Re}[Z_{xy}]} \right|, \quad (3.7)$$

where $\text{Re}(Z_{xy})$ and $\text{Im}(Z_{xy})$ are the in-phase and quadrature components of the surface impedance respectively.

Over a homogeneous half-space, the apparent resistivity gives the true resistivity of the half-space at all frequency range, while the impedance phase is 45° . Over an uniform horizontally layered-earth, the apparent resistivity is a weighted-average resistivity over the depth-of-investigation of the signal, while the phase is greater than 45° if the resistivity decreases with depth and less than 45° if the resistivity increases. Sharp lateral resistivity variations distort this simple picture. For 1D and 2D resistivity structures, and for most 3D structures, the measured impedance phase values fall between 0° and 90° . For a well-defined 2D resistivity structure, the TE-mode phase will be different from TM-mode phase, whereas for data measured in an arbitrary coordinates over a 2D structure, the phase of the off-diagonal impedance elements will be weighted-average of both TE- and TM-mode phases.

Much more analytical and statistical analyses for MT methods can be found elsewhere [e.g. Junge, 1988; Li and Pedersen, 1991; Bastani and Pedersen, 2001].

3.1.2 Depth-of-investigation

Theoretically, the maximum penetration depth at which an EM plane-wave has been attenuated to $1/e$ (or 37%) in a fairly conductive homogeneous half-space and results in magnetic and electric field components that are detectable by an RMT equipment at a particular operating frequency, is known as *skin-depth* [m]

$$\delta_{RMT} = \sqrt{\frac{2\rho_{a,xy}}{\omega\mu_0}} \approx 503.3 \sqrt{\frac{\rho_{a,xy}}{f}}. \quad (3.8)$$

For an uniform horizontally layered-earth, the effective depth-of-investigation may be several skin-depths, whereas in geologically complex structure or at noisy survey areas, it may be much less than one skin-depth. Thus, a reasonable estimate for the effective depth-of-investigation is approximately equal to 1.5 skin-depths [Spies, 1989]

$$d_{RMT} \approx 1.5\delta_{RMT} \approx 755 \sqrt{\frac{\rho_{a,xy}}{f}}. \quad (3.9)$$

Unlike TEM soundings, the effective depth-of-investigation is practically not limited by the configuration size and geometry. It depends only upon the operating frequency, ground resistivity and the overall signal-to-noise ratio (SNR), and hence the sensitivity and accuracy of the instrumentation.

The highest operating frequency determines the minimum depth-of-investigation at which near-surface resistivity variations can be reasonably resolved. In some field situations, highly-conductive near-surface masses usually dominate the measurements and effectively short the current flow circuit, leaving very little to penetrate to deeper structures. In addition to that blanking effect, they themselves cause highly irregular anomalies. This is only half of the story since induced signals returning from the ground lose some of their EM energy to be detectable at the ground surface. This effect is widely known under the name of *screening*. In other situations, when the near-surface layers become extremely resistive and too thick, they also act as screening block, blanking the deep resistivity structures [Strack, 1992].

3.1.3 Scalar CHYN RMT Equipment

The present RMT data were collected using a prototype equipment developed by the Center of Hydrogeology Neuchâtel (CHYN) at the University of Neuchâtel, Switzerland. The CHYN RMT data can only be acquired in a scalar mode over a frequency range between 12 and 260 kHz. That means, the off-diagonal elements of the impedance tensor are assumed to be independent of each other and measured separately, while the diagonal elements are assumed to be zero as they should be in ideal 2D case, and hence are not measured. The measuring procedure for the CHYN RMT survey is rather simple, carried out as follows: the RMT receiver (a small hand-held device) is tuned to a particular frequency of the selected radio-transmitter. The azimuth (or bearing) of the radio-transmitter is obtained by rotating a small vertical induction coil, of about 40 cm diameter, around a vertical axis until the null position (i.e. minimum audibility) is found. Along the survey profile and perpendicular to that azimuth, the horizontal resultant electric field component is measured by the voltage drop between a pair of potential Al-electrodes planted into the ground. The horizontal resultant magnetic field component is sensed by the induction coil at the mid-point between electrodes at each sounding (Figure 3.1). The SNR of the equipment is inversely proportional to the potential-

electrode spacing, but an electrode spacing of about 5 m was ascertained as sufficient compromise between measuring accuracy and signal audibility [Turberg *et al.*, 1994; Bosch and Gurk, 2000]. Furthermore, the smaller size and fewer turns of the induction coil reduce the self-capacitance and permit resonant tuning to the frequency selected in the receiver bandpass section. The RMT receiver directly delivers both the apparent resistivity and impedance phase values. Figure 3.2 shows a photograph of the CHYN RMT equipment and other connections in the field.

The accuracy of measurements depends not only of the ground earth, but also of strength, remoteness and departure from the true azimuth of the radio-transmitter, and the background noise. It is on an average of $\pm 3 \Omega\text{m}$ for the apparent resistivity and $\pm 0.5^\circ$ for the impedance phase. Identifying the sources of error is crucial in the scalar RMT equipment because it has no real-time series. A procedure to get rough error estimates is repeating the measurements at certain soundings few times for each operating frequency to validate the data, and ranking the signal audibility of radio-transmitters (Table 3.1). These error estimates assess the background noise and can be representative throughout the rest of other soundings.

As explained above, in RMT work the profile direction is almost irrelevant, the critical parameter being the relationship between the geological-strike of a resistivity structure and the radio-transmitter azimuth. Since the geological-strike direction was often unknown at the present survey areas, the measurements were made at three different pairs of roughly orthogonal azimuths, namely at 0° – 80° , 30° – 120° and 60° – 150° N, revealing 19 radio-frequencies (Table 3.1 and Figure 3.1).

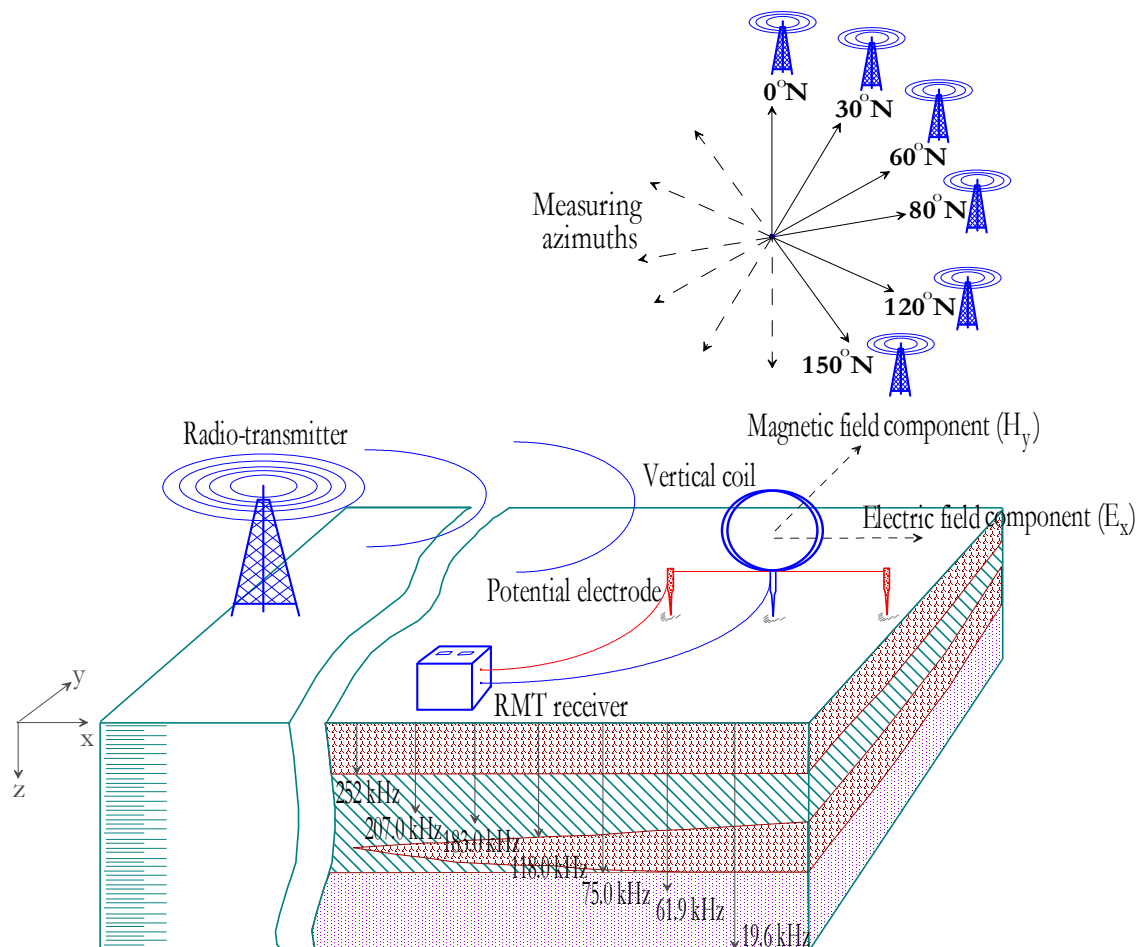


Figure 3.1: Field setup of the CHYN RMT equipment, at each measuring azimuth, over a non-homogeneous ground.

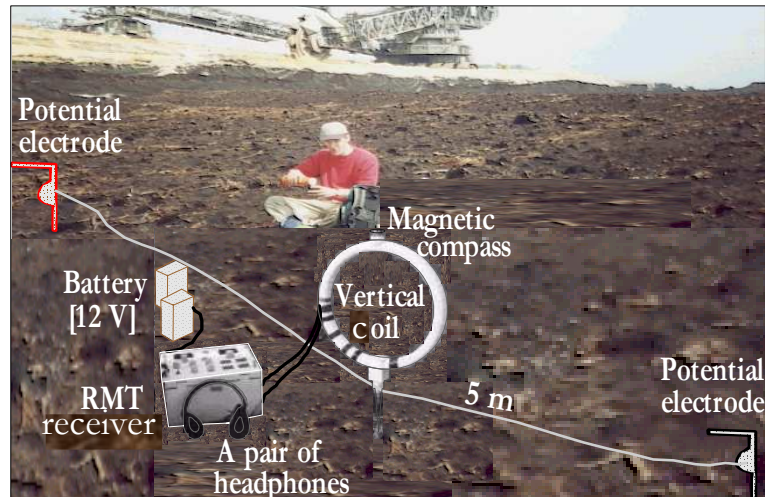


Figure 3.2: Photograph showing the CHYN RMT equipment and other connections in the field.

3.1.4 Radio-transmitters

Although the natural EM fields have a very broad frequency spectrum with considerable energy in parts of the RMT frequency band, defined here from 12 to 260 kHz, no serious attempts have been made to date to use it for geophysical use. This is contrasted with the natural frequency band between 0.001 Hz and up to 10 kHz which has been exploited by the plane wave FDEM methods, including MT and AMT (see Section 1.2.1). On the other hand, while the vast majority of the military communication or long-wave (LW) broadcasting now takes place over the practical RMT frequency range, providing the possibility of performing reliable measurements, the distribution of their transmitters still deviate considerably from region to other worldwide. Moreover, some of them operate interchangeably at more than one frequency and others sometimes temporary discommunicate. Only in Europe, parts of Asia and North Africa, the LW band (below 500 kHz) is used for broadcasting, whereas in America and Australia LW band broadcast is not in wide use.

At the opencast mine 'Garzweiler I', as an example from Central Europe, between April and May 2002, a total of 32 remote radio-transmitters, covering almost the entire RMT frequency band, could be detected. These transmitters provide weakly to strongly audible radio-signals and show a highly irregular azimuthal distribution, with a concentration in the frequency bands between 14 to 24 kHz (traditional VLF transmitters), 53 to 81 kHz and 111 to 262 kHz, exhibiting two frequency gaps in-between. Table 3.1 shows the azimuths at which the best radio-signals were received at the opencast mine 'Garzweiler I', and the expected geographic locations from which they were initially emitted, based on the measuring azimuths.

The same observation was also noted by *Bastani and Pedersen* [2001] from their RMT monitoring, where a total of 36 radio-signals could be detected in Sweden and the Netherlands in November 1998, covering the frequency range between 14 and 250 kHz. Interestingly, they showed that below 14 kHz there are no strong radio-signals except some net-harmonics, which may or may not be considered to be far-field sources. This gave rise to utilize a controlled-source to fill in the gaps inherent in the usual RMT frequency spectrum, and was realized in the newly developed tensor impedance meter *EnviroMT* [Bastani, 2001]. This equipment operates at the frequency range between 1 and up to 500 kHz.

Operating frequency [kHz]	Measured / approximated azimuth [°N]	Radiated power [kW]	Call sign / Name	Geographic location [remarks]	Coordinates (Lat., Long.) [°N/S, °E/W]	Audition
21.7	192 / 0	200	HWU	Le Blanc, France [Navy]	46° 37' N, 01° 50' E	(+–)
75	178 / 0	20	HBG	Prangins, Switzerland	46° 24' N, 06° 15' W	(++)
183	172 / 0	2000	Europe 1	Felsberg, Germany	49° 17' N, 06° 45' W	(+)
216	185 / 0	1200–1400	RMC	Roumoules, France	43° 80' N, 06° 13' E	(++)
234	186 / 0	2000	RTL	Beidweiler, Luxembourg	49° 43' N, 06° 18' E	(+)
23.4	24 / 30	300	DHO	Ramsloh, Germany	53° 05' N, 07° 36' E	(+)
162	35 / 30	2000	FRI	Allouis, France	47° 10' N, 02° 12' W	(+)
243	32 / 30	300	DR P1	Kalundborg, Denmark	55° 42' N, 11° 06' E	(+–)
65.8	65 / 60	–	FUE	Brest, France [Navy]	48° 24' N, 04° 20' W	(+–)
177	63 / 60	500	DLR	Zehlendorf, Berlin, Germany	52° 32' N, 13° 25' E	(++)
19.6	89 / 80	500	GBZ	Anthorn, UK	55° 00' N, 03° 30' W	(+)
225	78 / 80	600–1000	PR 1	Warsaw, Poland	52° 18' N, 21° 00' E	(+–)
24	109 / 120	1000	NAA	Cutler, Maine, USA	44° 38' N, 67° 17' W	(+)
61.9	114 / 120	–	GIZ	Criggon, UK	52° 43' N, 03° 30' W	(+–)
118.7	115 / 120	40	GYE	London, UK	51° 50' N, 00° 17' W	(+)
153	124 / 120	250–500	DLF	Cologne (Donebach) Germany	50° 56' N, 06° 56' E	(++)
207	122 / 120	500	DLF	Cologne (Aholming) Germany	50° 56' N, 06° 56' E	(+)
252	128 / 120	500	RTE 1 [Atlantic 252]	Dublin, Ireland	53° 20' N, 06° 18' W	(+)
198	141 / 150	500	BBC R4	Droitwich, UK	52° 16' N, 02° 09' W	(+)

(++): very strongly audible, (+): strongly audible, (+–): moderately audible, (–): weakly audible, (––): very weakly audible.

Table 3.1: The possible geographic locations of the best-detectable radio-transmitters at the opencast mine 'Garzweiler I' based on their unique azimuths. Note that the geographic locations have been cross-checked for the 180° ambiguity, with a maximum departure of $\pm 10^\circ$ from the true azimuth of the radio-transmitter. (Radio-transmitter information compiled from different sources [McNeill and Labson, 1991; Siebel, 1991; Knödel et al., 1997; Klawitter, 1998; Pedersen et al., 2003].)

3.2 Data Interpretation

3.2.1 Data Viewing

Coal-covered Area

The locations of all RMT sounding centers at the survey areas are accurately marked in Figure 1.3. At the 'Coal-covered Area', the collected data along all profiles are rather similar. Plotting both apparent resistivity and impedance phase versus measuring distance (Figure 3.3a) shows a slight increase of apparent resistivity and decrease of phase values along the profiles from SW to NE. No remarkable local resistivity anomaly is encountered. Taking into account all operating frequencies from different measuring azimuths, apparent resistivity curves show a

descending behavior with increasing frequency, whereas phase curves show a change from about 25° to 50° with increasing frequency (Figure 3.3b). This can roughly be explained by an upper conductor overlying a fairly resistive half-space, corresponding to the Garzweiler Coal and Neurath Sand/Silt respectively. The small parallel differences between curves can be attributed to a gradual small thickness change of the Garzweiler Coal along the profiles from SW to NE. Along profile III, about 33% of apparent resistivity and/or impedance phase data is scattered and deviates a little from this simple picture, particularly for the soundings close to the very steep cliff located on the southern side. Plotting both apparent resistivity and impedance phase versus measuring azimuth for each RMT frequency band (Figure 3.3c) shows that their changes throughout different measuring azimuths are quite small. This may assume that the data has almost 1D character, i.e. the two orthogonal horizontal electric and magnetic field components at each measuring azimuth are laterally-invariant. Because the surface impedance is almost independent of the measuring azimuth, all transmitting frequencies can be used safely in both the 1D and 2D inversions to obtain highly-resolved resistivity models.

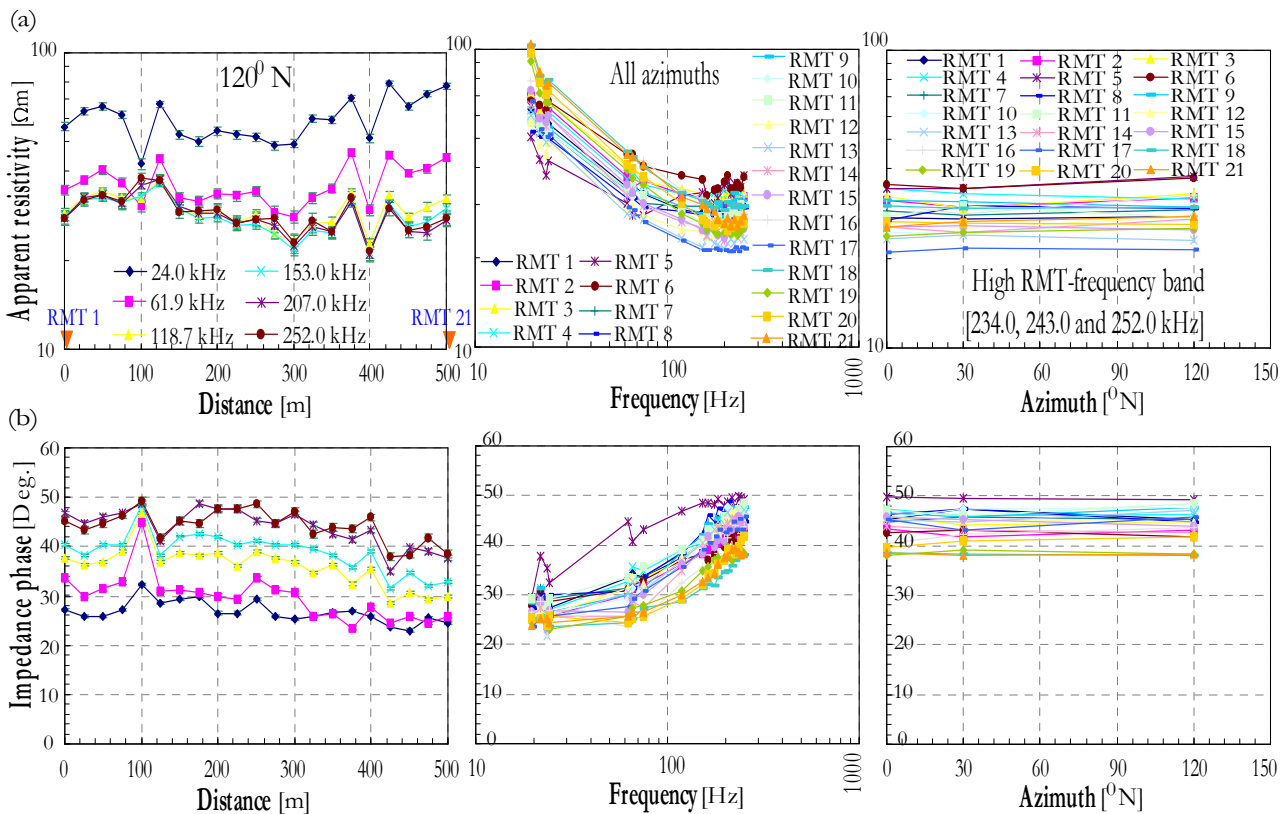


Figure 3.3: (a) Apparent resistivity and (b) impedance phase plotted as a function of measuring (left) distance, (middle) frequency and (right) azimuth along profile I at the 'Coal-covered Area.' On the left side, the error bars describe the standard deviations derived from the repeated measurements.

Sand-covered Area

The collected data indicated a rather complicated geoelectrical model. Plotting both apparent resistivity and impedance phase versus measuring distance (Figure 3.4a) does not show a clear direct correlation between the two parameters. For profile I, two anomalous apparent resistivity highs, associated with impedance phases greater than 45° for higher and intermediate RMT frequencies, are encountered roughly at soundings RMT 3 to 7 and RMT 16 to 18. Taking into account all operating frequencies from different measuring azimuths, neither apparent resistivity nor phase curves show a particular behavior or trend with

increasing frequency (Figure 3.4b), the most inconsistent frequency data come from measuring azimuths perpendicular to the large hillock located on the northern side, i.e. 0° and 150° N. The effect of this large hillock manifests itself as an azimuth-dependence for both apparent resistivity and impedance phase (Figure 3.4c), particularly at the lower RMT-frequencies. Here the surface impedance may be dependent on measuring azimuth. Sharing all transmitting frequencies safely in either 1D or 2D inversion seems to be difficult, or even misleading.

Frequency data from individual azimuths which are parallel and subparallel to the hillock, i.e. 80° , 30° , 60° and 120° N, show very smooth curves and approximately similar trends with increasing frequency (Figure 3.5). For most sounding curves, the higher and lower RMT frequency phases exhibit values below 45° , whereas the intermediate frequency phases show transitional values close to 45° . On the other hand, the apparent resistivities start constant or with a slight decrease at lower frequencies, then increase gradually with increasing frequency and finally decrease a little at higher frequencies. This may be explained by a model consists of an intermediate conductor sandwiched between a relatively thick upper resistor and lower resistive half-space. Highly-conductive surficial anomalies within the upper resistor could be the reason for high frequency undulations on most apparent resistivity and impedance phase curves. This resistivity behavior can be sketched out as the Garzweiler Coal between Surface Sand and lower Neurath Sand/Silt, i.e. *undisturbed model*. The Surface Sand could be *disturbed* by separate surficial clay masses, and therefore apparent resistivity or phase curves may be undulated at higher frequencies. This behavior may be shown in the data at measuring azimuths 30° and 120° N, but not developed well in the data at azimuths 60° and 80° N due to the lack of frequencies.

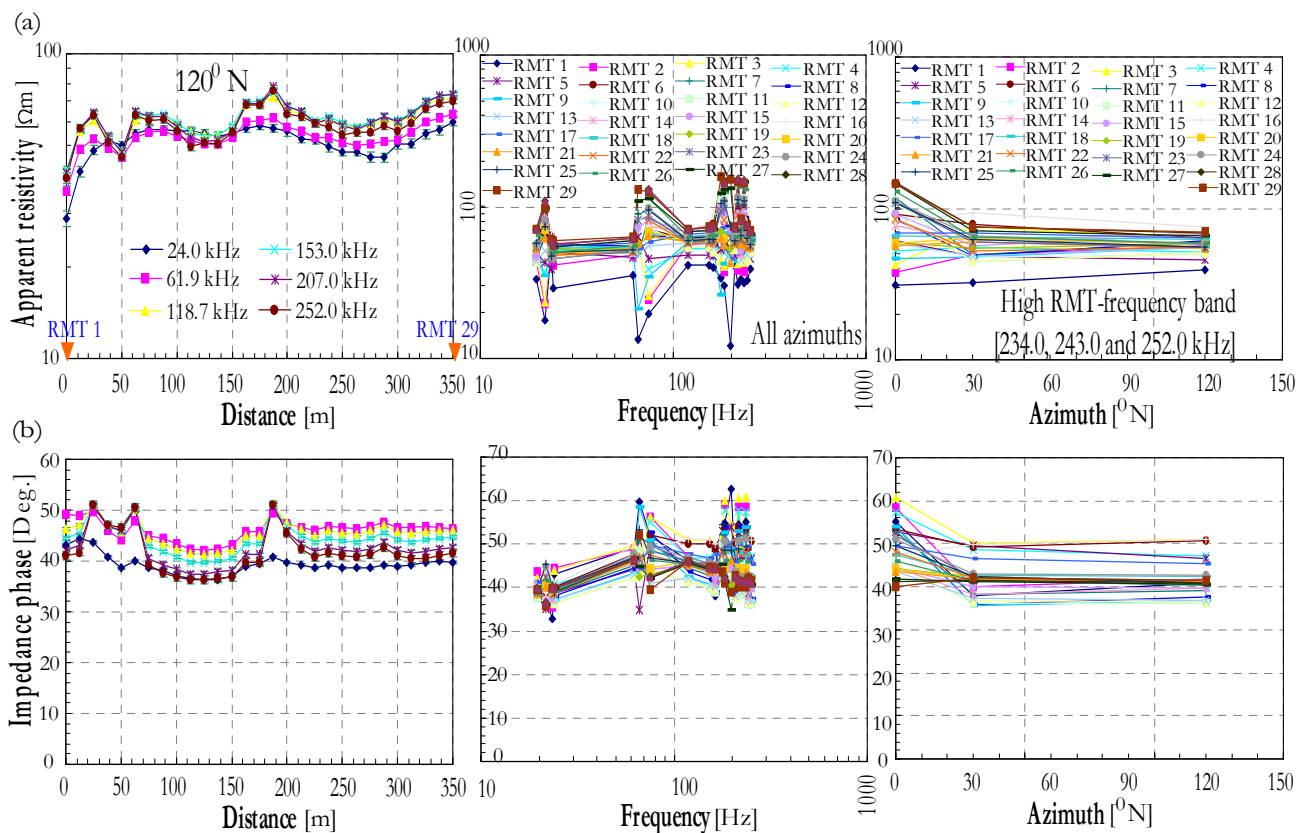


Figure 3.4: (a) Apparent resistivity and (b) impedance phase plotted as a function of measuring (left) distance, (middle) frequency and (right) azimuth along profile I at the 'Sand-covered Area.' On the left side, the error bars describe the standard deviations derived from the repeated measurements.

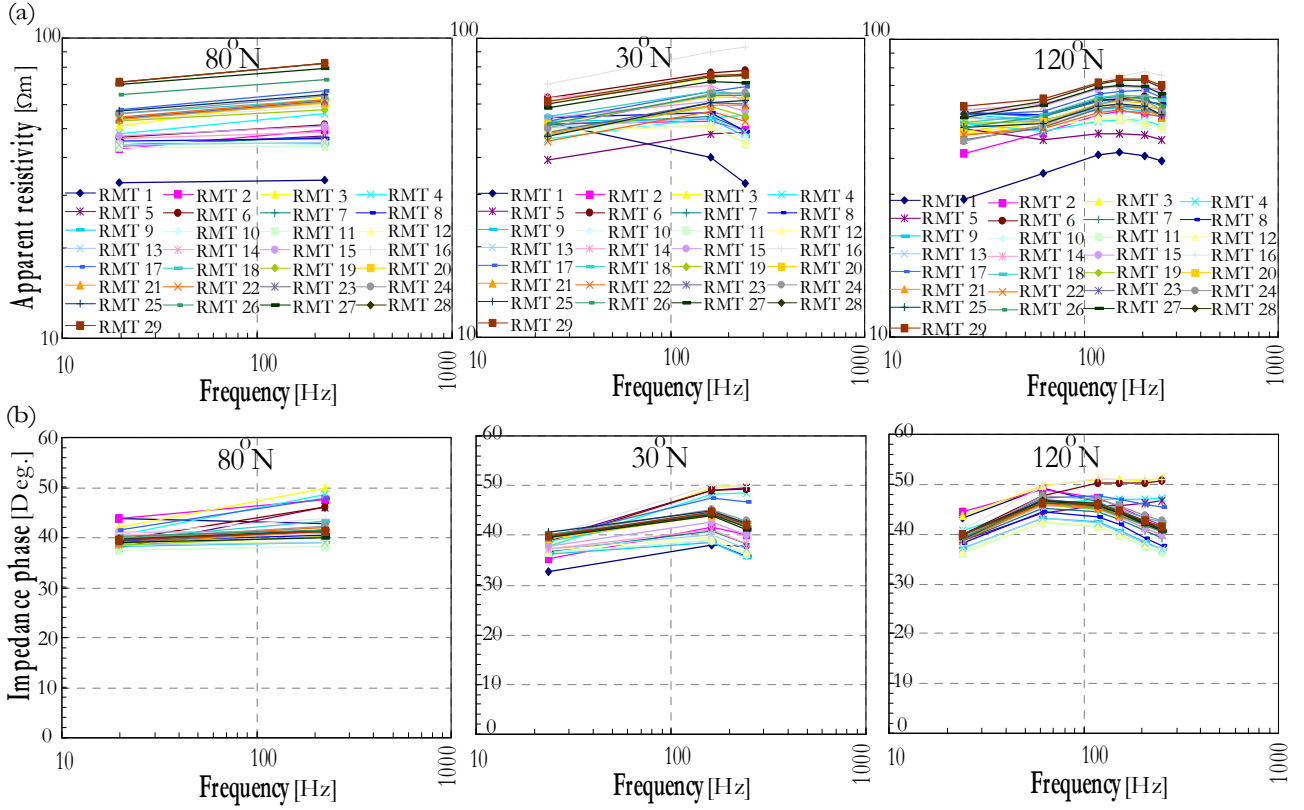


Figure 3.5: (a) Apparent resistivity and (b) impedance phase plotted as a function of operating frequency for measuring azimuths (left) 80° , (middle) 30° and (right) 120° N along profile I at the 'Sand-covered Area.'

Apparent resistivity and impedance phase data along profile II (not shown here) also showed the two model behaviors interchangeably. The disturbed model with surficial clay masses may influence the curves at soundings RMT 30 and 31. Generally, the lateral variations encountered in both apparent resistivity and impedance phase values may indicate that 1D inversion results at the 'Sand-covered Area' will be inconsistent along the profiles.

3.2.2 Data Transformation

Theoretically, measured RMT data can be interpreted according to the $\rho^*(z^*)$ transformation [Schmucker, 1987] to show first estimates of the ground resistivity-distribution. This can be achieved by using a substitute resistivity ρ^* to a frequency-dependent depth z^* of phases ϕ ranging between 0° and 45° or between 45° and 90° :

$$\rho_{xy}^* = \frac{\rho_{a,xy}}{2\sin^2\phi_{xy}} \quad [0^\circ \leq \phi_{xy} < 45^\circ] \quad (3.10)$$

$$\rho_{xy}^* = 2\rho_{a,xy}\cos^2\phi_{xy} \quad [45^\circ < \phi_{xy} < 90^\circ] \quad (3.11)$$

$$z_{xy}^* = \text{Re}[C_{xy}] = \frac{1}{\mu_o\omega} |\text{Im}[Z_{xy}]| = \sqrt{\frac{\rho_{a,xy}}{\omega\mu_o}} \sin\phi_{xy} \quad (3.12)$$

where $C_{xy} = Z_{xy}/i\omega\mu_o$ [m] is the inductive-scale length (i.e. the vertical center-of-mass of the in-phase induced current pattern in a 1D earth model which relates both the orthogonal horizontal electric and magnetic field components) [Schmucker, 1970].

Coal-covered Area

The stitched $\rho^*(z^*)$ depth-sections along all profiles (Figure 3.6a) shows approximately a monotonic increase of ρ^* values downwards with decreasing frequency, indicating an upper conductor overlying a fairly resistive half-space. This is interpreted as Garzweiler Coal, which is known to be at that approximate depth, overlying Neurath Sand/Silt. The Garzweiler Coal shows a gradual thickness decrease from SW to NE, while its ρ^* is ranged between 15 to around 55 Ωm . The Neurath Sand/Silt has ρ^* values between 100 and 300 Ωm . The ρ^* values are scattered at the lowest frequencies. Here all frequency data from different measuring azimuths could be consistently used for each sounding data. Along profile III, about 33% of the ρ^* data is scattered and has to be skipped from the transformation to follow the predominant $\rho^*(z^*)$ model.

Sand-covered Area

Only frequency data at measuring azimuth 120° N could be used to derive reasonable $\rho^*(z^*)$ depth-sections. The sections derived at measuring azimuths 30°, 60° and 80° N are greatly broadened due to the lack number of frequencies. The $\rho^*(z^*)$ depth-sections along profiles I and II, at the measuring azimuth 120° N (Figure 3.6b), broadly exhibit a discontinuous conductor embedded in a fairly resistive background. This is corresponding to the Garzweiler Coal, with ρ^* values ranged from 20 to 55 Ωm , between the Surface Sand and lower Neurath Sand/Silt, where ρ^* values do not exceed 100 Ωm . Here Garzweiler Coal is slightly shallow, and obviously more broadened on the western side, and thus closer to the surface. Its lower boundary is almost not well-determined. Along profile II, the Garzweiler Coal is essentially shallower and more conductive, and hence not distinguished from the highly-conductive surficial anomalies or clay masses.

In the sense of $\rho^*(z^*)$ transformation, the maximum depth-of-investigation is about 12 m at the survey areas. Since the definition of z^* relies on a 1D assumption, the $\rho^*(z^*)$ depth-section should be more regarded as a qualitative image than used as a direct measure of the depth-of-investigation. Ziebell [1998] carried out extensive numerical calculations on the resolution of 2D inversion of different resistivity models over the practical RMT frequency range. He derived rules to estimate a reliable depth-of-investigation for the 2D RMT interpretation, below which no information can be gained, and found that $2z^*$ is a reasonable approximation in many cases. Here a depth of about $2z^*$ to $2.5z^*$ was found to be quite satisfactory for further 1D and 2D interpretations respectively (see Section 3.2.6).

3.2.3 One-dimensional Inversion of Synthetic Data

In order to predict RMT responses at the survey areas and to determine how sensitive a real RMT survey would be for the target coal seams in some suggested earth models, forward calculations were performed over the real RMT frequency range that was observed at the opencast mine 'Garzweiler I.' For each survey area, a detailed geoelectric model was first constructed based on layer thicknesses derived from the available stratigraphic-control boreholes (Figure 1.4) and average layer resistivities derived from the laboratory electrical measurements on rock samples (Table 5.2). The general model fashion comprises a layer-cake sequence, from top to bottom, of the conductive Garzweiler and Frimmersdorf Coals embedded in sufficiently resistive Surface, Neurath and Frimmersdorf Sands. The lowermost of the Neurath Sand between Garzweiler and Frimmersdorf Coals is less resistive, i.e. sand/silt, and Frimmersdorf Coal overlies a two-meter highly-conductive organic clay layer.

Next, for the 'Sand-covered Area' model, a highly-conductive surficial clay layer was embedded within the Surface Sand and gradually replaced its thickness, from 0.0 to around 9.45 m, simulating the absence of clay to the complete sand-replacement by clay.

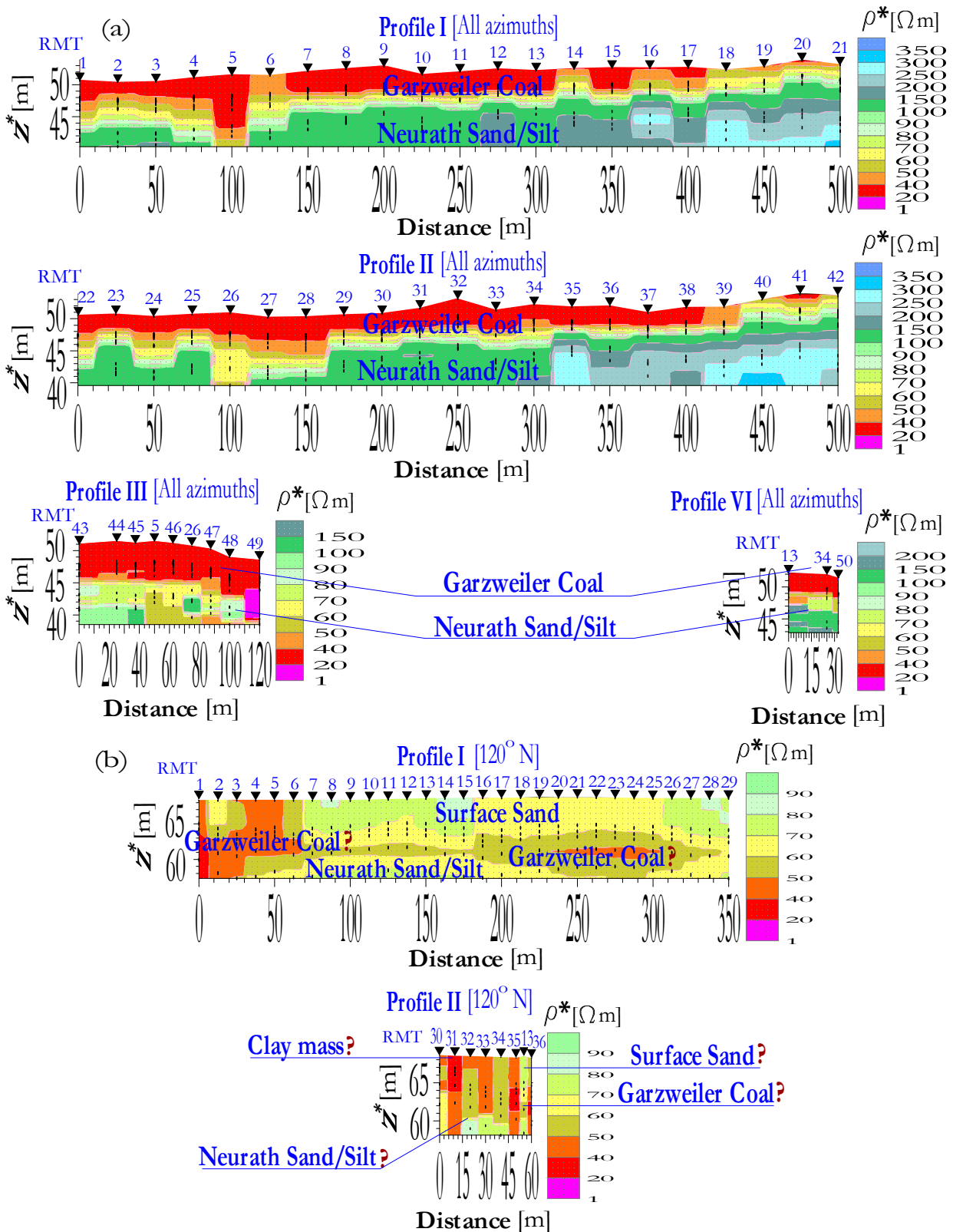


Figure 3.6: Stitched $\rho^*(z^*)$ depth-sections at the survey areas: (a) 'Coal-covered Area' and (b) 'Sand-covered Area.'

Starting from these models, three synthetic data sets were created by 1D forward calculations, and then inverted in terms of 1D smoothed-earth resistivity images [Constable, 1987]. 4% Gaussian noise, which can be tolerated with the scalar CHYN RMT equipment, was added to the resulting synthetic data in order to artificially allow a realistic resolution assessment. The starting models chosen for all Occam's inversion runs were always average-apparent-resistivity homogeneous half-spaces, in which the number of layers is equal to the number of operating frequencies. Their thicknesses increase successively in the logarithmic-domain and were kept fixed during the inversion runs. In this model study, synthetic apparent resistivities and impedance phases satisfy all data acquisition parameters and specifications for the scalar CHYN RMT equipment.

Coal-covered Area

Because any simulated (or real) RMT data are skin-depth limited, the recovered models here are rather simple. Figure 3.7 shows the smoothed-earth model and the responded apparent resistivities and impedance phases for the 'Coal-covered Area' synthetic data. The final inversion results fit the data within 0.91 RMS. We can see obviously that the only first two blocked-layers, i.e. Garzweiler Coal and Neurath Sand/Silt, are needed to explain the data. The average resistivity of the Garzweiler Coal is recovered fairly well by the inversion, while the average resistivity of the Neurath Sand/Silt is significantly overestimated. The lower boundary of Garzweiler Coal is well-determined.

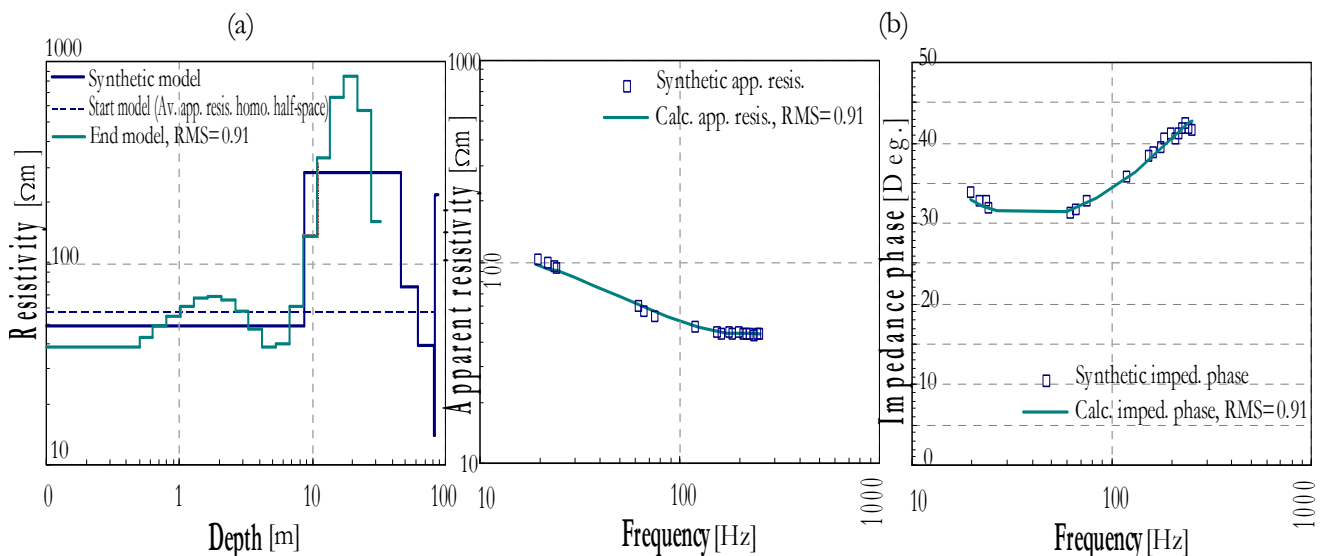


Figure 3.7: (a) 1D RMT smoothed-earth models and (b) the corresponding apparent resistivity and impedance phase curves of 'Coal-covered Area' synthetic data.

Sand-covered Area

The apparent resistivities and impedance phases of the final smoothed-earth model fit the synthetic data better than 1.11 RMS (Figure 3.8, upper). The data are quite sensitive not only to the Garzweiler Coal and Neurath Sand/Silt but also to the Surface Sand. The recovered Surface Sand has an essentially overestimated resistivity, while its thickness is well-determined. The Garzweiler Coal is almost the same as in the synthetic model. The Neurath Sand/Silt resistivity is recovered fairly well. The lower boundary of both the Neurath Sand/Silt and Frimmersdorf Coal/Clay or Sand is not recovered at all.

The presence of a highly-conductive surficial clay layer within the clean Surface Sand, with a thickness of at least 3 m, changes the whole smoothed-earth model, but more drastically at the deeper depths, where there is no resemblance with the synthetic model (Figure 3.8, lower). Here the general fashion of the recovered model appears as a downward low-over-high resistivity-gradient. The responded apparent resistivities and impedance phases, corresponding to different clay thicknesses, at the whole frequency range were all well-separated from each other, and significantly different from that of the undisturbed model. This may indicate that the surficial clay layer can therefore be detected and uniquely resolved if a real RMT survey is conducted. Whereas, the underlying succession of the Surface Sand, Garzweiler Coal and Neurath Sand/Silt appear as a moderately-conductive blocked-layer with increasing clay thickness, and can not be resolved as individual units, but only as a whole. This also indicates that the negative contribution of the surficial clay layer is significant at the whole frequency range, and hence screens the underlying conductive coal seam(s) from being sounded. It is worth mentioning that the minimum detectable clay thickness is within close proximity to the practical minimum skin-depths of the scalar CHYN RMT equipment frequency range. Note that the data fit RMS decreases from 1.11 to 0.89 with increasing clay thickness. Here the model situation dictates that the resolution of RMT survey is poor for thin resistive layers.

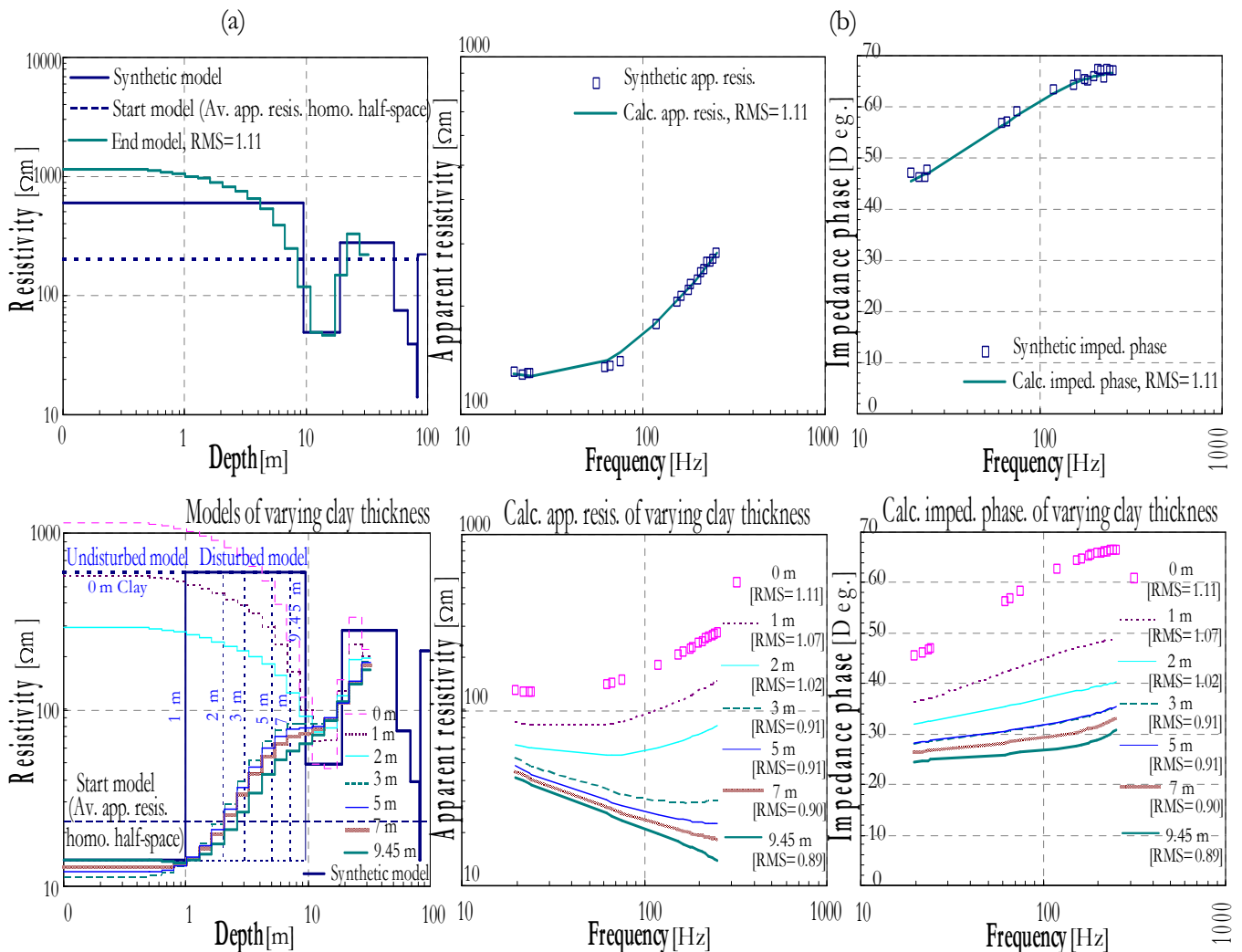


Figure 3.8: (a) 1D RMT smoothed-earth models and (b) the corresponding apparent resistivity and impedance phase curves of the 'Sand-covered Area' synthetic data: (upper) undisturbed model and (lower) disturbed model with a surficial clay layer of varying thickness.

3.2.4 One-dimensional Inversion of Field Data

The 1D inversion of the RMT data at each survey area was carried out using a standard scheme of successive techniques. No a-priori information was initially introduced. The data were first inverted in terms of 1D smoothed-earth models using average-apparent-resistivity homogeneous half-spaces as starting models, in which the number of layers is equal to the number of operating frequencies. Their thicknesses were increased successively in the logarithmic-domain, set to the average effective depth-of-investigation and kept fixed during the inversion. To drive a reasonable start model for further 1D full non-linear, layered-earth inversion [Inman, 1975], Occam's inversion results were then blocked (or combined) such that a minimum structure is obtained. This least number of vertical layers is still well-adapted to the intrinsic resolution capabilities of RMT data and preservative to the general trend of the borehole-geology. Applying the standard sensitivity (or resolution) analysis [Inman, 1975], typically for the best-fitted layered-earth model at each control sounding was very important, as it showed quantitatively how much confidence can be placed in that model.

Beginning from a control RMT sounding and using a kind of recursive starting modeling, which means that the output layered-inversion results of the previous sounding is used as starting model for the present sounding, the inverted section could be driven consistently and reasonably well with a resolution depth of approximately 30 m. This multi-sequential inversion is usually applicable where changes between soundings are gradational, but can grossly oversimplify the interpretation if these changes are abrupt [Hördt *et al.*, 1992b]. The individual inversion results from successive soundings, along each profile, were then assembled to create 2D pseudo-sections. These stitched sections were usually successful in determining any lateral resistivity variations present in the survey area. The final inversion statistics for the inverted layer parameters were used to cross-check their resolution in detail at each sounding. During all phases of the 1D inversion, one must make sure that the direct correlation to the borehole-geology was still reasonably maintained. However, the highly-conductive surficial anomalies at the 'Sand-covered Area', due to the presence of separate clay masses (or lenses) within the Surface Sand, broke down such interpretation scheme. In this case, to greatly improve the resistivity resolution for these surficial masses and for the underlying conductive coal seams, 2D inversion [Rodi and Mackie, 2001] was additionally carried out.

Coal-covered Area

The smoothed-earth model obtained from Occam's inversion of measured data at the sounding RMT 32, close to the borehole 'WS1380', is shown in Figure 3.9a (upper). It clearly exhibits an upper conductor overlying a resistive half-space, corresponding to the Garzweiler Coal and Neurath Sand/Silt respectively, which are known to be at these approximate depths. The deepest Frimmersdorf Coal/Clay and Morken Coal within their sand background are beyond the depth-of-investigation of the present measurements and need not be considered. The final inversion results fit the data within 1.50 RMS.

Although the inversions were all carried out independently, Occam's results vary very little throughout each profile, with final data misfits ranged between 0.79 and 2.00 RMS (Figure 3.10). No remarkable local resistivity anomaly is encountered. This indicates that the 1D interpretation is very consistent and validated throughout the area, and means that the general geoelectric model is essentially of 1D character. The conductive Garzweiler Coal is

considered as a marker layer within this simple vertical succession. It shows a gradual thickness decrease from SW to NE, while its resistivity is ranged from 15 to around 50 Ωm . The resistivity change from the Garzweiler Coal to Neurath Sand/Silt at about 11 to 5.5 m depth is more abrupt. The Neurath Sand/Silt resistivity increases laterally towards the NE from 300 to 650 Ωm .

The layered-earth inversion results at the sounding RMT 32 showed that the least number of layers, which best represents the RMT data, is two blocked-layers with a final data misfit of 1.30 RMS (Figure 3.9a, lower), while the correlation with the borehole-geology is still satisfied, if not perfect. It is obvious that the inversion closely maintained the starting model, which was derived from the Occam's blocked-layers. The estimated error bounds of the inverted model parameters are sufficiently small, and do not greatly increase with depth, indicating that the RMT signal is still able to accurately resolve the lower boundary of the Garzweiler Coal with decreasing frequency.

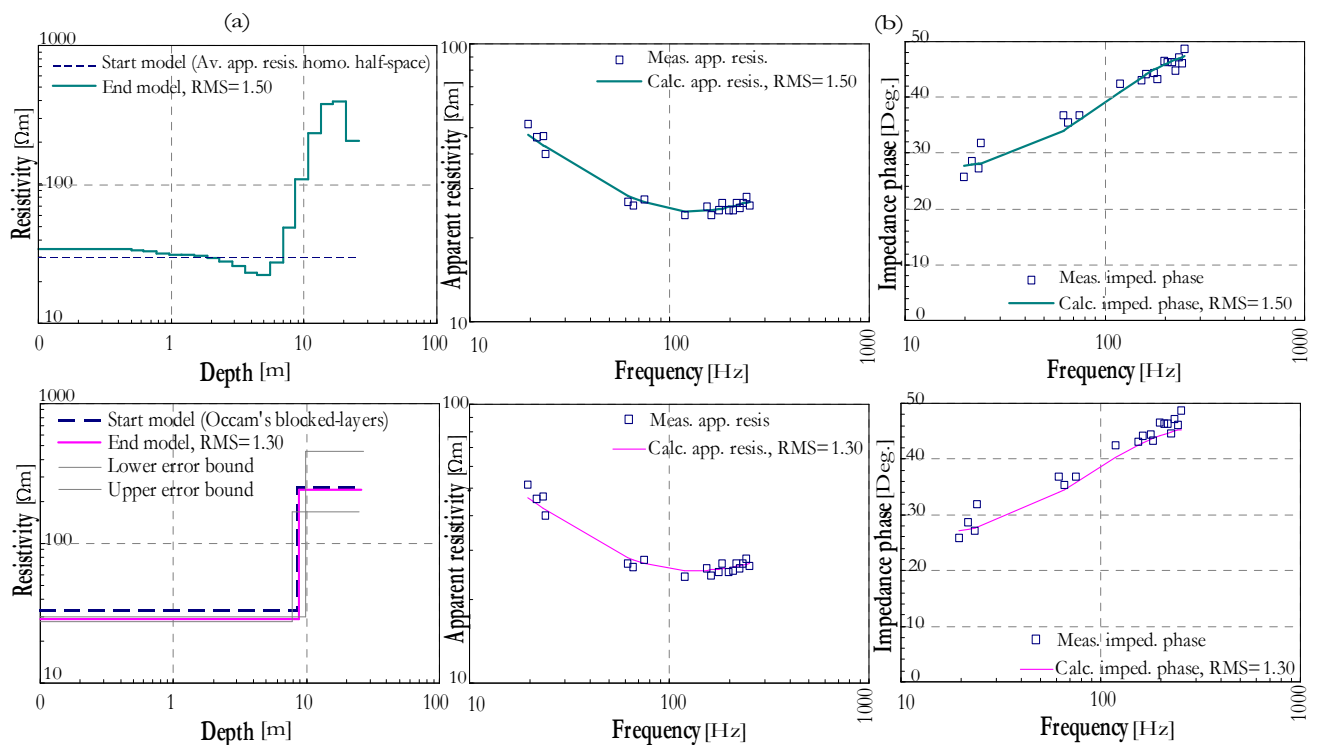


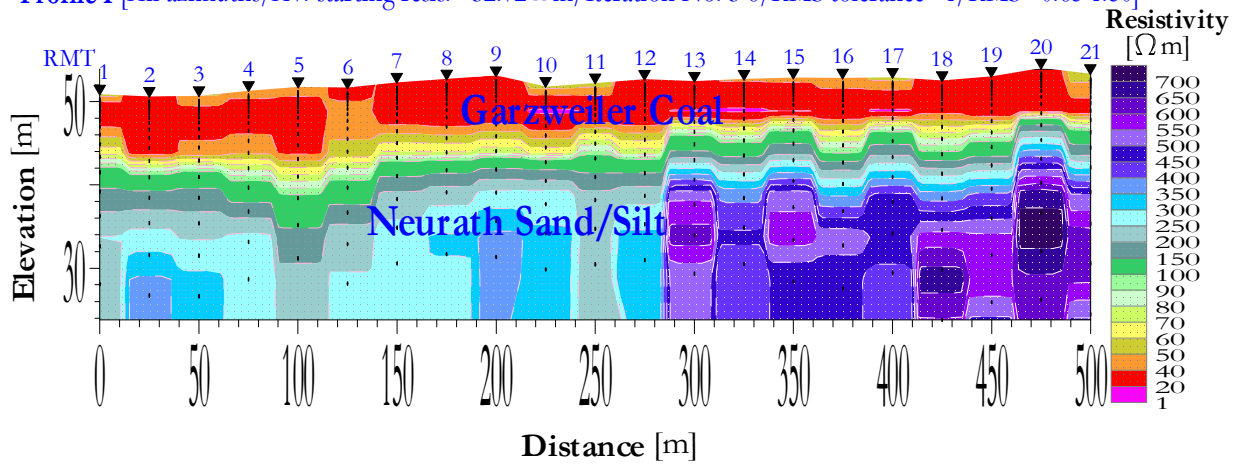
Figure 3.9: (a) 1D RMT (upper) smoothed- and (lower) layered-earth inverted models and (b) the corresponding apparent resistivity and impedance phase curves of the sounding RMT 32 at the 'Coal-covered Area.'

The final 1D RMT layered-earth sections at the 'Coal-covered Area' seem to be readily very consistent and geologically reasonable (Figure 3.11). The Garzweiler Coal is normally responded as resistivity lows with an averaged value of about 31 Ωm . Whereas, the resistive Neurath Sand/Silt exhibits an average resistivity of about 263 Ωm . Note that inverting with models having more than two layers resulted in a comparable data fit, while the resulting models were justified neither by statistical analysis nor by correlation with the borehole-geology. Along profile III, about 33% of the apparent resistivity and/or impedance phase data is scattered and has to be masked¹ in

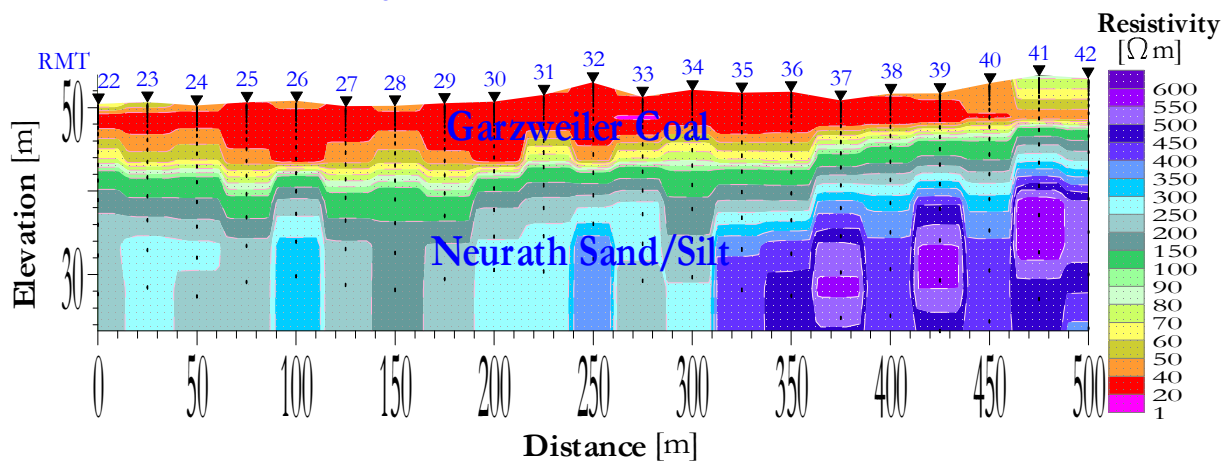
¹Data masking is keeping unwanted data points as part of the whole data set, while excluding them from forward modeling and inversion, and hence from the RMS misfit calculations.

the inversion, particularly for the soundings close to the very steep cliff located on the southern side, to accurately follow the predominant resistivity model.

Profile I [All azimuths/Av. starting resist. = $32.72 \Omega \text{ m}$ /Iteration No. 3-8/RMS tolerance = $1/\text{RMS} = 0.85\text{-}1.50$]



Profile II [All azimuths/Av. starting resist. = $32.72 \Omega \text{ m}$ /Iteration No. 3-8/RMS tolerance = $1/\text{RMS} = 0.79\text{-}1.70$]



Profile III [All azimuths/Av. starting resist. = $32.72 \Omega \text{ m}$
/Iteration No. 3-8/RMS tolerance = $1/\text{RMS} = 1.21\text{-}1.52$]

Profile IV [All azimuths/Av. starting resist. = $32.72 \Omega \text{ m}$
/Iteration No. 3-8/RMS tolerance = $1/\text{RMS} = 1.22\text{-}2.00$]

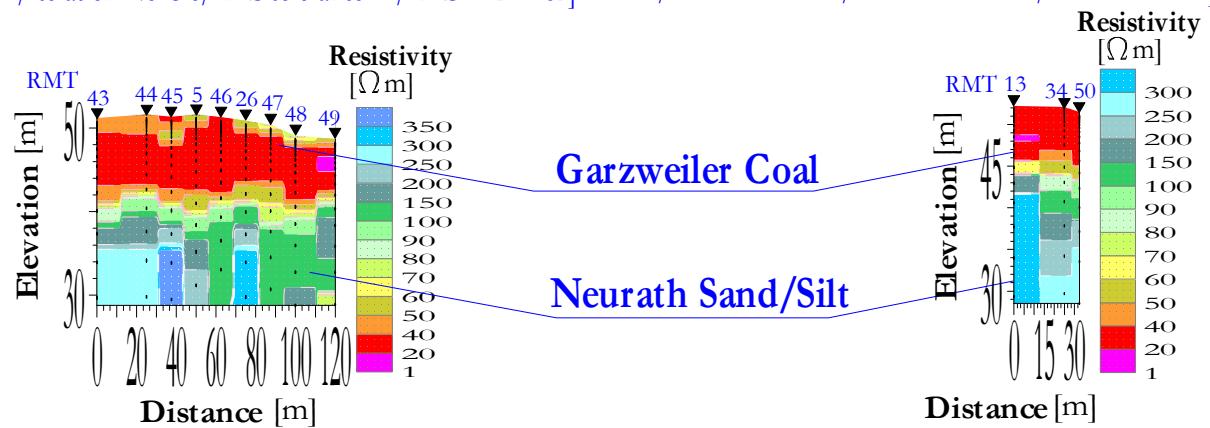


Figure 3.10: Stitched 1D RMT smoothed-earth inverted sections below profiles I, II, III and IV at the 'Coal-covered Area.' Warm colors indicate resistivity lows, while cold colors indicate resistivity highs.

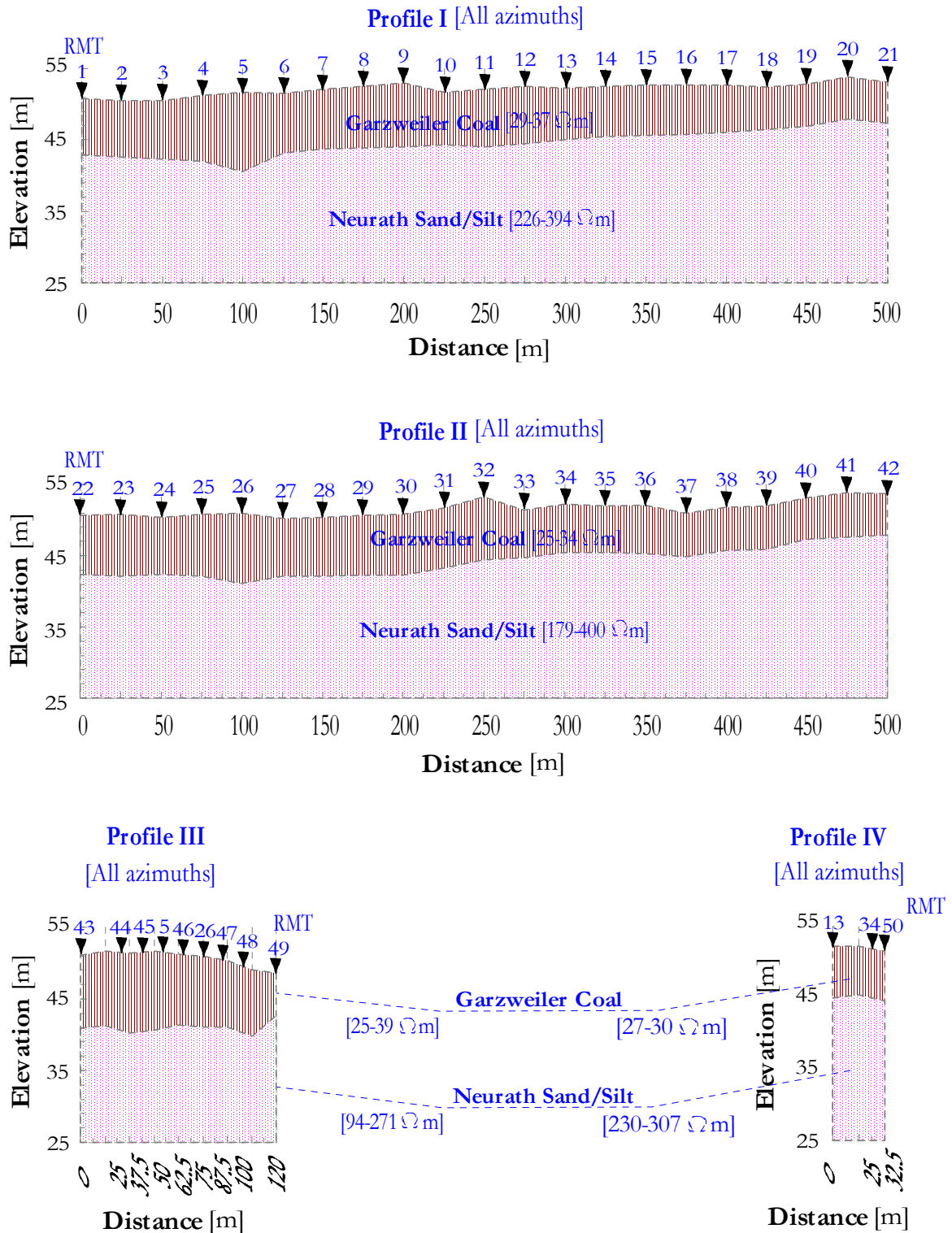


Figure 3.11: Stitched 1D RMT layered-earth inverted sections below profiles I, II, III and IV at the 'Coal-covered Area.'

Upon inspecting the diagonal elements of resolution matrix, or importances, for the inverted layer parameters at all soundings, it becomes clear that none of them are poorly resolved (Figure 3.12). The derived importances for Garzweiler Coal and Neurath Sand/Silt resistivities and the Garzweiler Coal thickness range between 1.00 and 0.58, indicating that they are very well- to moderately-resolved. Furthermore, the data misfits are ranged between 0.78 and 3.20 RMS respectively.

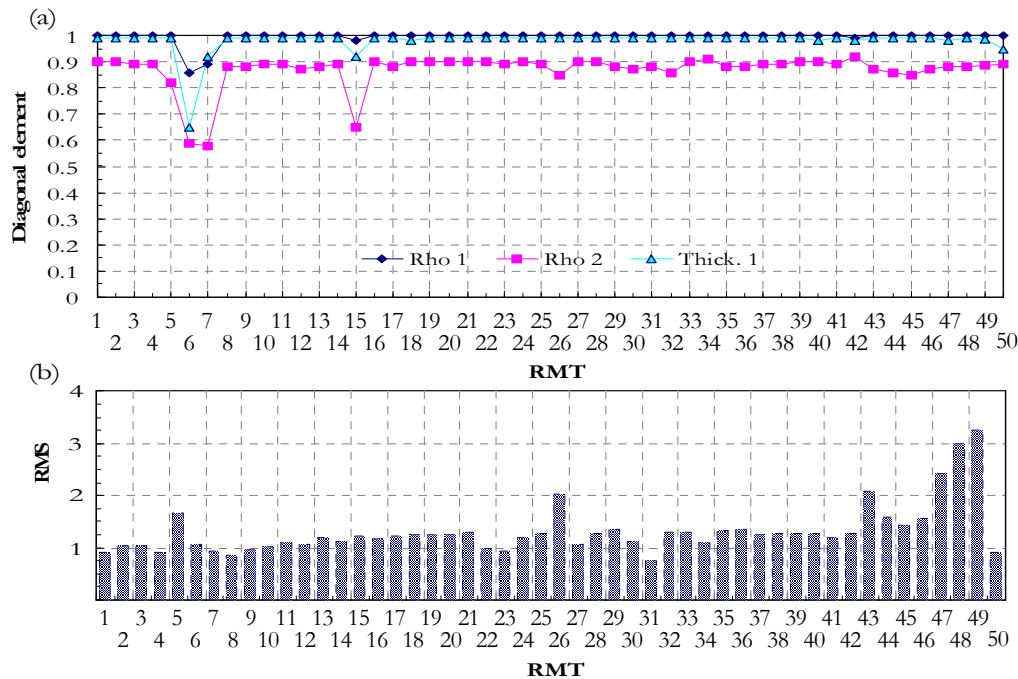


Figure 3.12: (a) The diagonal elements of resolution matrix for the inverted layer parameters, and (b) a histogram of the RMS misfit values of all soundings at the 'Coal-covered Area.'

Sand-covered Area

Again, only frequency data at the measuring azimuth 120° N could be used to derive reasonable smoothed-earth models. Models derived at measuring azimuths 30° , 60° and 80° N are all greatly broadened due to the lack number of frequencies. The smoothed-earth model for obtained from Occam's inversion of measured data at soundings RMT 1 and 5, close to the borehole 'WS 1452', is shown in Figure 3.13. Here the inversion results would be completely different at each sounding. Sounding RMT 5 broadly exhibits an upper semi-conductor overlying a fairly resistive half-space, interpreted as a blocked-layer of surficial clay, thinned Surface Sand and Garzweiler Coal followed by Neurath Sand/Silt. The Garzweiler Coal is more shallower than approximate depths known for it, and thus closer to the surface. The final inversion results fit the data within 1.03 RMS. Interesting is the appearance of an anomalously highly-conductive surficial layer at the sounding RMT 1 that is always necessary to obtain a reasonable data misfit of about 1.22 RMS. This surficial layer is interpreted as a separate clay mass within the clean Surface Sand. The lower boundary of the Garzweiler Coal is not readily resolved, but it appears normally conductive.

Collectively, the Occam's inversion results are not quite consistent along profile I (Figure 3.14). The results at soundings RMT 3 to 8 and RMT 16 to 29 belong to the consistent part of the profile which still has almost 1D character. They correlate satisfactory with the known borehole-geology, except that the uppermost part of the Surface Sand becomes more clayey. Their final data misfits ranged between 0.76 and 1.42 RMS. Whereas, the results at soundings RMT 1 to 2 and RMT 9 to 15 neither agree with neighboring-sounding results nor correlate with the known borehole-geology. Their final data fits worsen a little, ranged from 0.78 to 1.90 RMS. Along the consistent part, the Surface Sand has about 75 to 200 Ωm resistivity, while its uppermost part has about 40 Ωm average resistivity. As stated above, the Garzweiler Coal is slightly shallower than approximate depths known for it, and thus closer to the surface, practically on the western side. Its lower boundary is not well-resolved, while its resistivity is normally averaged as 40 Ωm . The earth model along the inconsistent part suffers from a slight bias to deeper depths, probably due to the presence of the highly-conductive surficial clay masses, which have about 3 to 20 Ωm resistivity. The Surface Sand resistivity is not greater

than 150 Ωm . Generally, the resistivity change from the sand to coal is smooth. Inversion results along the profile II show the same model characters. The soundings from RMT 32 to 36 represent the consistent earth model with final data misfits ranged between 0.95 and 1.45 RMS, while soundings RMT 30 and 31 represent clearly the inconsistent model with final data misfits ranged between 1.00 and 1.90 RMS.

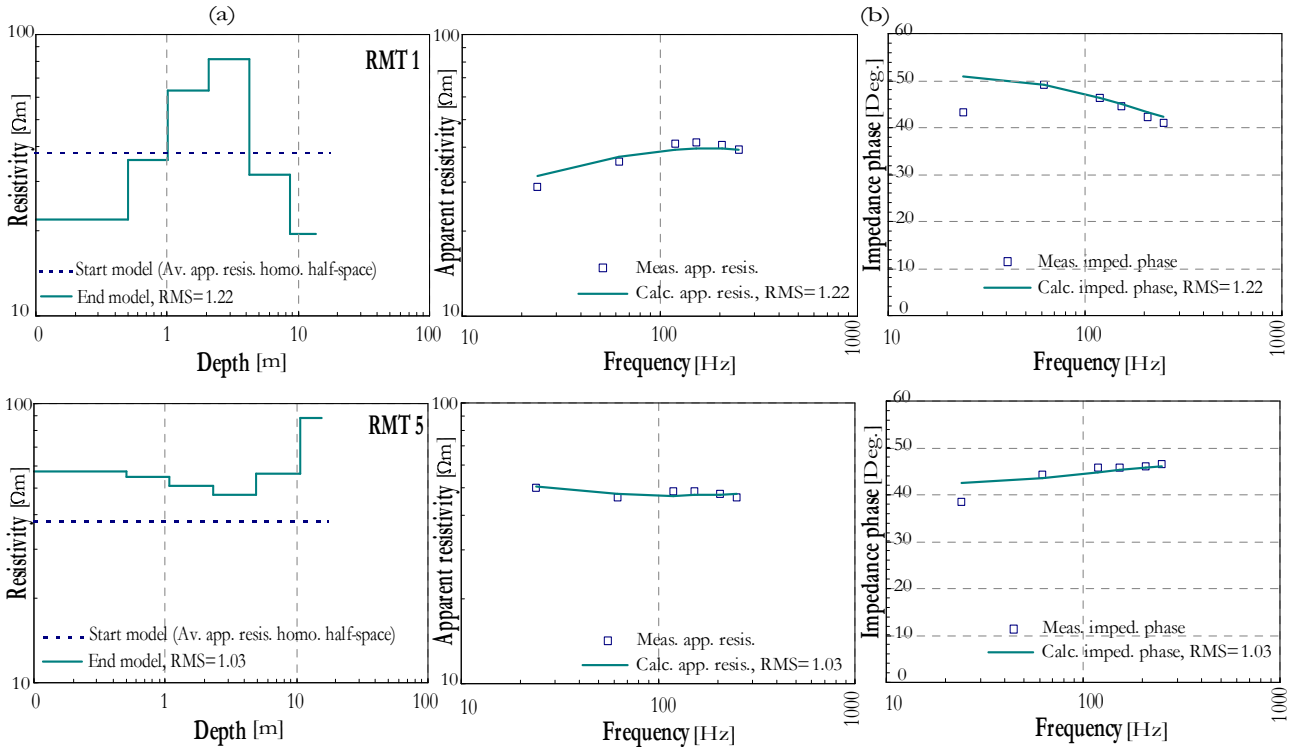


Figure 3.13: (a) 1D RMT smoothed-earth inverted models and (b) the corresponding apparent resistivity and impedance phase curves at the measuring azimuth 120° N of the soundings (upper) RMT 1 and (lower) RMT 5 at the 'Sand-covered Area.'

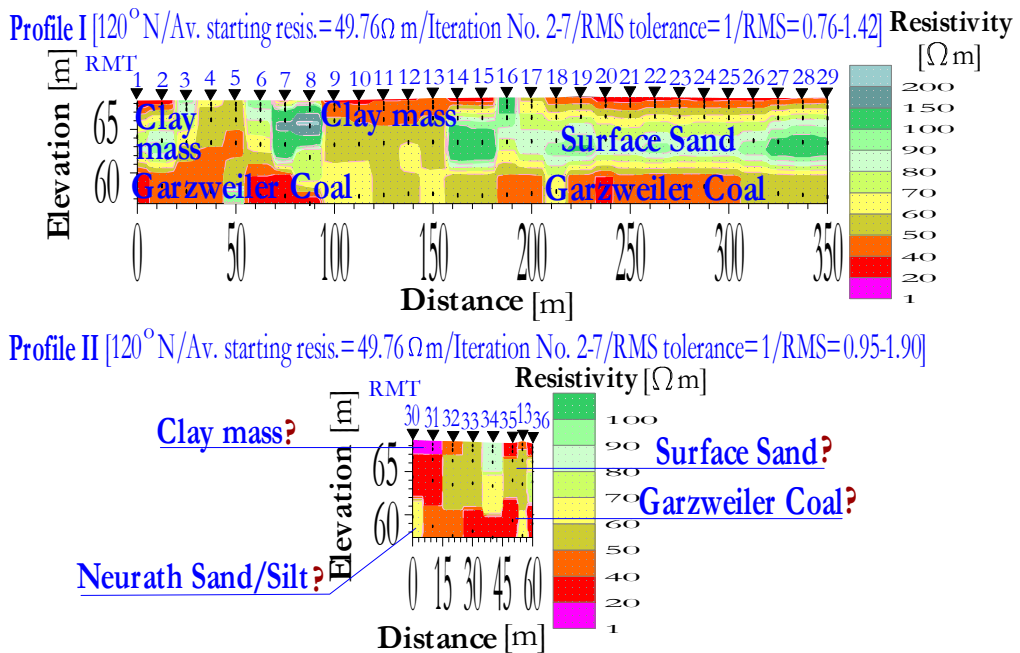


Figure 3.14: 1D RMT smoothed-earth inverted sections below profiles I and II at the 'Sand-covered Area.' Warm colors indicate resistivity lows, while cold colors indicate resistivity highs.

Taking into account a surficial clay layer of about 3 m depth at all soundings, the starting model thicknesses for further 1D layered-earth inversion at measuring azimuths 80° , 30° and 120° N were adjusted from the available borehole 'WS 1452.' At a considerable number of soundings, a homogeneous half-space was used as a starting model instead. A discussion about the criteria used to choose the most appropriate measuring azimuths, which are not distorted by nearby-topography, for all inversion schemes will be given later in Section 3.2.6. The inversion results at soundings RMT 1 and 5 at the measuring azimuth 120° N show that the least number of layers which best represents the RMT data is two and four blocked-layers, with final data misfits of 0.94 and 1.36 RMS respectively (Figure 3.15). Here the inversion could not maintain the starting model. The estimated error bounds of the inverted model parameters are satisfactory and do not greatly increase with depth, indicating that the RMT signal is still able, at the best, to accurately resolve the lower boundary of the Garzweiler Coal with decreasing frequency.

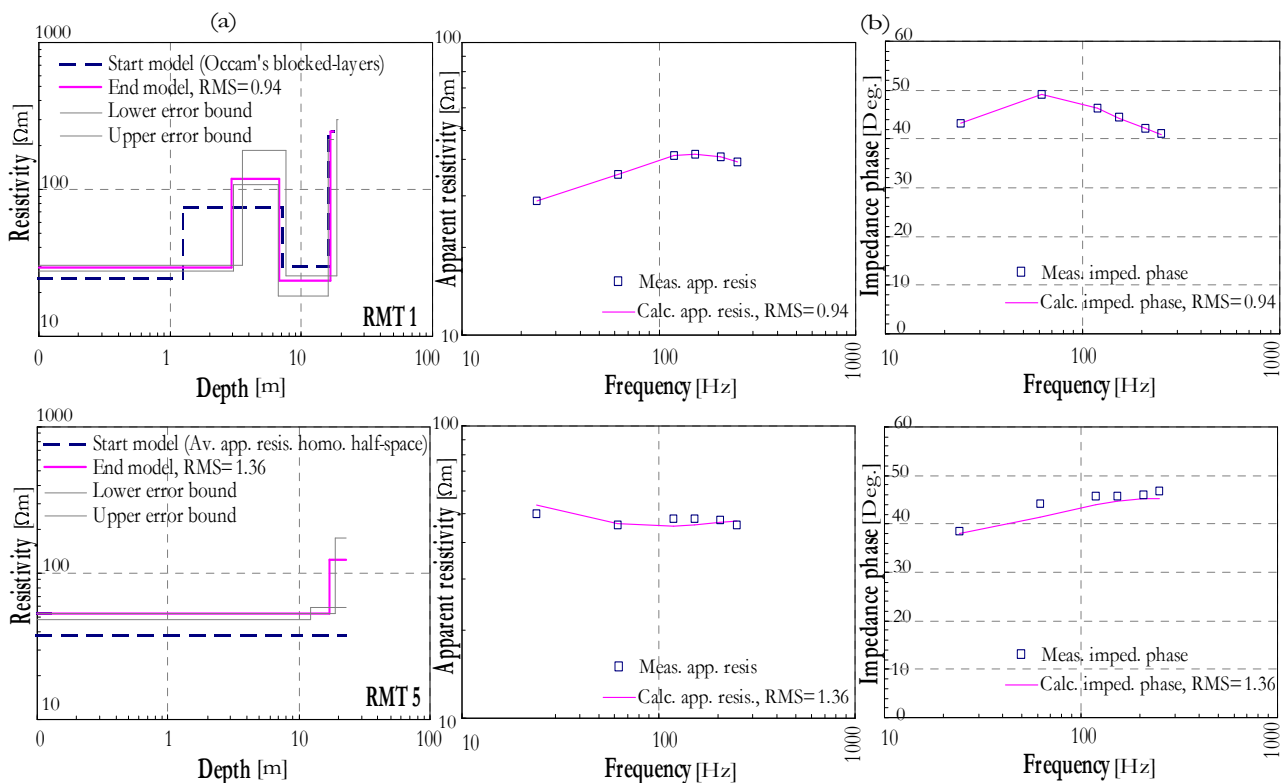


Figure 3.15: (a) 1D RMT layered-earth inverted models and (a) the corresponding apparent resistivity and impedance phase curves, at the measuring azimuth 120° N, of soundings (upper) RMT 1 and (lower) RMT 5 at the 'Sand-covered Area.'

The final 1D RMT layered-earth sections at the 'Sand-covered Area' (Figure 3.16) seem to be sufficiently consistent and geologically reasonable, particularly at measuring azimuths 30° and 120° N. The whole RMT frequency range is almost well-representative at these azimuths by three and six frequencies respectively. Here the surficial clay masses and underlying Garzweiler Coal are almost uniquely determined as individual units. The thicknesses of the highly-conductive surficial masses are close to 3 m, while their resistivity is averaged as $30 \Omega\text{m}$. The Garzweiler Coal is normally responded as resistivity lows with an averaged value of about $45 \Omega\text{m}$. Along profile I at the measuring azimuth 30° N, it is generally more broadened

or disappeared westwards, and suffers from a slight bias to deeper depths at the middle part of the profile. The Surface Sand exhibits average resistivity of about 125 Ωm , while Neurath Sand/Silt shows a resistivity range between 135 and 309 Ωm .

Nevertheless, at a considerable number of soundings, the 1D inversion can not distinguish among the surficial clay masses, Surface Sand and Garzweiler Coal, where they appear as a moderately-conductive blocked-layer with a total thickness equals the sum of their individual thicknesses. Models at the measuring azimuth 80° N show also that this shallower succession can not be resolved as individual units, but only as a whole. For this azimuth, the total thickness of the blocked-layer is slightly broadened, or even undetermined along profile II. Note that all attempts to invert the data in terms of models having more (or less) than the layers given in the resultant models, at measuring azimuths 80°, 30° and 120° N, were statistically unreliable and not justified by correlation with the borehole-geology.

Most of the data misfits fluctuate around 1.0 RMS, but generally do not exceed 2.30 RMS, for all soundings at the measuring azimuths 80°, 30° and 120° N (Figure 3.17). Only along profile II at the measuring azimuth 80° N, they reach as high as 3.85 RMS. Inspecting the diagonal elements of resolution matrix for the inverted layer parameters at measuring azimuths for all soundings shows that the resistivities of the conductive surficial clay masses and the Garzweiler Coal are well-resolved. Their importances are close to 1.0 and 0.75 respectively. Whereas, the resistivities of the fairly resistive Surface Sand and Neurath Sand/Silt are ranked between moderately- to well-resolved, as their importances ranged between 0.98 and 0.5. The derived values for almost all thicknesses are varied between 0.42 and 0.98, indicating that they are moderately- to well-resolved.

In the light of the above 1D inversion results at the 'Sand-covered Area' and the corresponding statistical analyses, where the inverted layer thicknesses do not exhibit regularly high importances as usual, one would not fully trust the output from 1D interpretation. The RMT data could suffer from 2D (or even 3D) effects for the soundings close to the edges of surficial clay masses within the earth model.

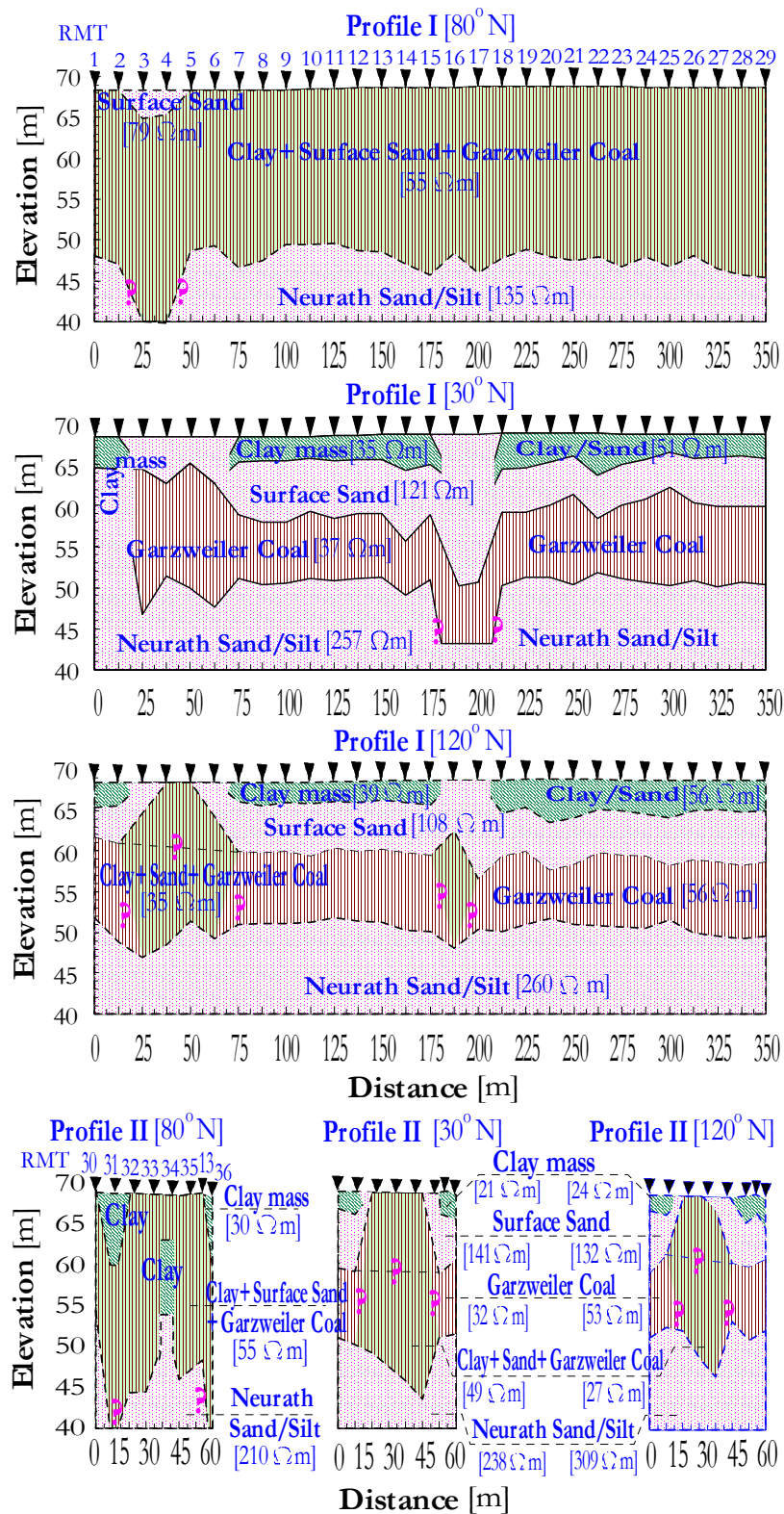


Figure 3.16: Stitched 1D RMT layered-earth inverted sections below profiles I and II at the 'Sand-covered Area.'

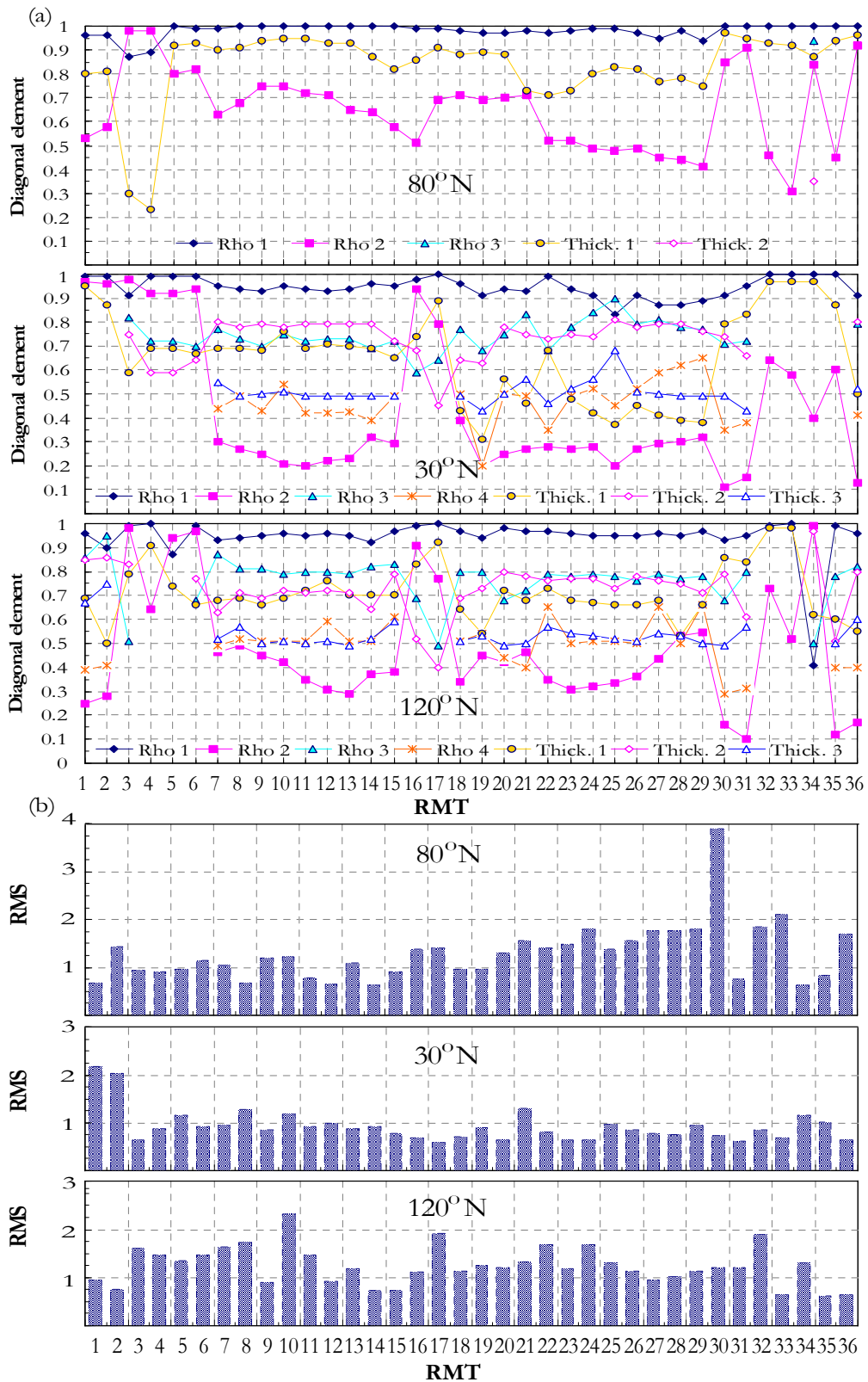


Figure 3.17: (a) The diagonal elements of resolution matrix for the inverted layer parameters and (b) a histogram of the RMS misfit values of all soundings, for the measuring azimuths 80°, 30° and 120° N, at the 'Sand-covered Area.' Here the inverted layer parameters are not comparable throughout all sounding models.

3.2.5 Two-dimensional Inversion of Field Data

3.2.5.1 Mesh Design and Verification

Using the Mackie's inversion scheme, the accuracy of final results depends mainly on the 2D finite-difference gridding (or meshing) that has an accuracy consistent with the forward solution. Carelessly designed grids can give independent users quite different results. Certain guidelines (or rules-of-thumb) already exist, relating in principle to the physics of EM diffusion, and can be considered in designing a sensible 2D earth-mesh [Wannamaker *et al.*, 1987a and 1987b; Chen and Fung, 1989; deGroot-Hedlin and Constable, 1990], but no simple formulas can be applied across different inversion problems. During the course of discretizing the 2D earth-mesh, four meshing parameters should be well-adjusted to aid in the design: the skin-depth limit (the nominal maximum size which may exist for each block before it splits), size-delta limit (the maximum size factor which may exist between two neighbor blocks), the optimal number of horizontal and vertical grid nodes (or elements) within the earth-mesh, and setting up the topography. The most important empirical guidelines which can reasonably control such meshing parameters are:

- (1) The inner-grid nodes should be small throughout sounding locations, along the profile, to properly represent the gradients of the horizontal and vertical magnetic fields. While, the outer-grid nodes should be far enough from the sounding locations, almost logarithmically increased. This is because the magnetic fields are smoothly varying, away from any expected resistivity contrasts. However, horizontal and vertical element dimensions should not change from one element to the next by more than a factor of about 3 to 5. Furthermore, the maximum vertical element dimensions should still ideally be held to 1 to 2 skin-depths.
- (2) Near any expected resistivity-contrast, where the EM fields change rapidly within the earth-mesh, element dimensions should be finer, approximately 1/4 a skin-depth, to ensure that the EM fields are computed correctly. Whereas, away from such resistivity-contrast within relatively homogeneous regions, element dimensions should be coarser, approximately 2 to 3 skin-depths.
- (3) The vertical and horizontal mesh boundaries should ideally be extended from 8 to 10 skin-depths away from any expected 2D resistivity structure or topographic edges within the earth-mesh.
- (4) Excessively finer grid nodes than usually needed, are necessary close to the air-ground interface to maintain accuracy in the forward calculations when the sampled topography is set up within the earth-mesh. Requirements may be more stringent for very rugged topography.
- (5) Model parameterization should be conformed to the grid discretization.

The 2D forward response for a well-designed earth-mesh, based collectively on these guidelines, was verified throughout the inversion itself, using an average-apparent-resistivity homogeneous half-space as starting model. Along each profile at the survey areas, the calculated apparent resistivity and impedance phase curves over the used frequency range, at 'iteration No. 0', have been converged to common values of the starting half-space resistivity and 45° respectively (see Figures 3.24 and 3.25). For all inversion modes, this behavior has been validated. This implies that the 2D solutions excellently satisfy the finite-difference analog of the governing differential-equations as well as all boundary and initial conditions. The final earth-mesh (Figure 3.18) that has been used in the present 2D inversion contains 37(X)×45(Z) grid nodes. The minimum and maximum grid-element sizes are about 5(X)×0.1(Z) m² (not shown here) and 0.05(X)×30(Z) km² respectively. Along each profile at the survey areas, the core design differs whilst the rest design remains fixed. This finely-discretized earth-mesh allowed real topography to be accurately set up.

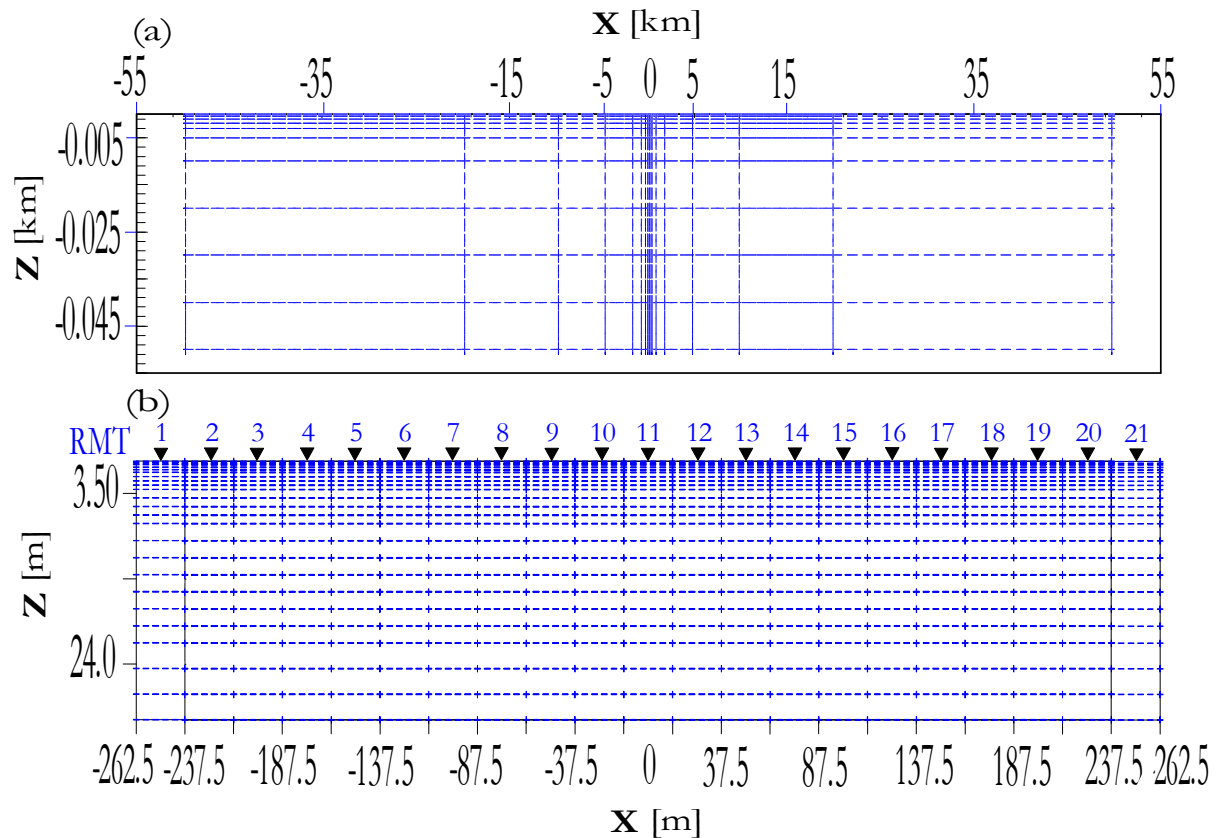


Figure 3.18: Final grid (earth-mesh) used for 2D inversion below profile I at the 'Coal-covered Area': (a) main and (b) core designs. Along each profile at the survey areas, the core design differs whilst the rest design remains fixed.

3.2.5.2 The Regularization Parameter

Following any regularization method that concerns the idea of the minimum-structure (or smoothed) model [*de Groot-Hedlin and Constable, 1990*], we are seeking a model that represents a compromise between the residual norm (i.e. χ^2 data misfit) Φ_d and the regularized solution norm (i.e. model roughness) Φ_m of the objective function. Therefore, if too much regularization is imposed on the regularized solution, then it will not fit the given data properly and the data misfit becomes large. On the other hand, if too little regularization is imposed then the fit will be good but the solution will be dominated by the contributions from the data errors, and hence the model roughness will be too large. Having realized the important roles played by the norms of the regularized solution and residual, it is quite natural to plot these two quantities versus each other on double-logarithmic axes, i.e. as a curve parametrized by the regularization (or trade-off) parameter τ . This is usually referred as to 'L-curve' [*Hansen, 1992*].

Practically, to find an appropriate choice for τ , the inversion is usually started several times with increasing τ stepwise throughout a wide range. In this case, if the χ^2 misfit is plotted against the model roughness for that wide range of τ , the resulting curve tends to have a characteristic 'L-shape' (Figure 3.19). The corner (i.e. the point of maximum curvature) of this L-curve corresponds to a roughly equal balance of the two quantities [*Hansen, 1999*]. Moving along the L-curve, away from the corner is associated with a progressively smaller decrease in the data misfit for large increases in the model roughness or with a progressively smaller decrease in the model roughness for large increases in the data misfit. In the majority of the 2D smoothed-earth sections inverted at the survey areas, the L-curves do not always have a

distinct corner at earlier iterations, whereas at later iterations they are developed well and, in this case, the L-curve criterion proves effective in determining the optimal τ . Figure 3.20 shows 2D RMT smoothed-earth inverted sections at different τ thresholds below profile I at the 'Coal-covered Area.' Here the data fit degrades significantly with increasing τ , while smaller τ results in rougher models. This clearly shows that the inversion results depend significantly on the value of the τ , an inappropriate choice for τ may create unwanted artificial features (artifacts) or even overinterpreted resistivity images. Occasionally, when τ is chosen too small, the solution shows oscillatory behavior and even may become unstable, causing the data misfit to oscillate or even diverge, which means that no reliable model can be found [Schwalenberg *et al.*, 2002].

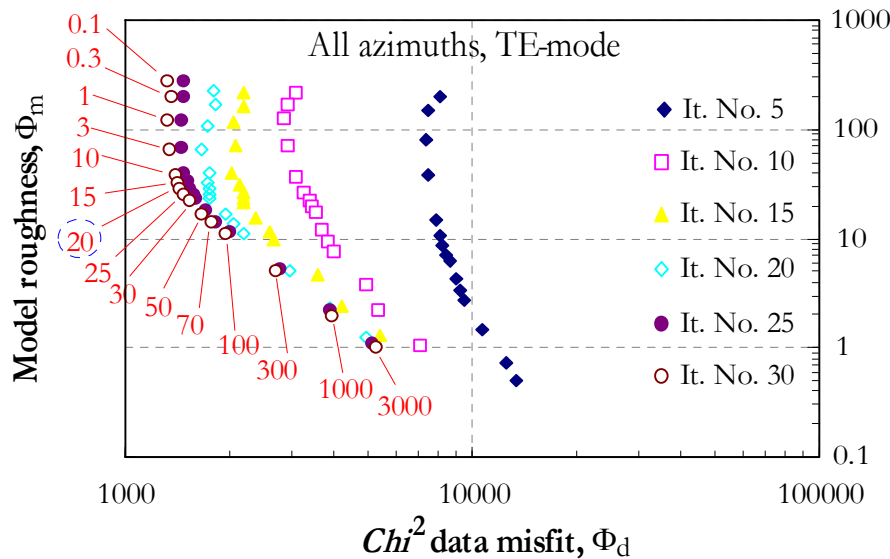


Figure 3.19: The L-curves, at different iteration and τ thresholds for several inversion runs, and the optimal τ for the 2D smoothed-earth inverted section below profile I at the 'Coal-covered Area.' The curves change, both in location and shape, as the iterations in the inversion proceed. Inverting using the optimal $\tau=20$ represents appropriate smoothing, while inverting using $\tau < 20$ and $\tau > 20$ represents under-smoothing and over-smoothing respectively.

3.2.5.3 2D Sensitivity

Because the Jacobian or sensitivity matrix in the Mackie's inversion scheme contains as many rows as data and as many columns as model parameters. That means, for joint-inversion mode, in one column you will find the partial derivatives of each datum ($\log \rho_{aTE}$, $\log \rho_{aTM}$, ϕ_{aTE} , ϕ_{aTM}) to one specific model parameter as the number of soundings by the number of frequencies. Hence, an urgent problem arises from the dimensions of the sensitivity matrix, where the visualization of the whole matrix elements is quite difficult. For instance, in each inverted section considered in Figure 3.20, which represents only the core of a giant earth-mesh, the sensitivity matrix contains 798 rows [N -data= No. of measured parameters (2) \times No. of modes (1) \times No. of soundings (21) \times No. of frequencies (19)] and 504 columns [M -model parameter= No. of horizontal grid elements (21) \times No. of vertical grid elements (24)]. Furthermore, the larger grid elements will excessively bias the presentation, particularly for the deeper elements. Schwalenberg *et al.* [2002] solved this problem by calculating columnwise sums from the sensitivity matrix and assign them to the particular grid elements, and normalizing these total sensitivities from the respective standard deviation σ_{si} of each measured parameter, either apparent resistivity or impedance phase. This made the sensitivities for authors numerically comparable and dimensionless. Consequently, they took the absolute values of the sensitivities, because the term *sensitive* (or *resolved*) is usually understood in a positive sense.

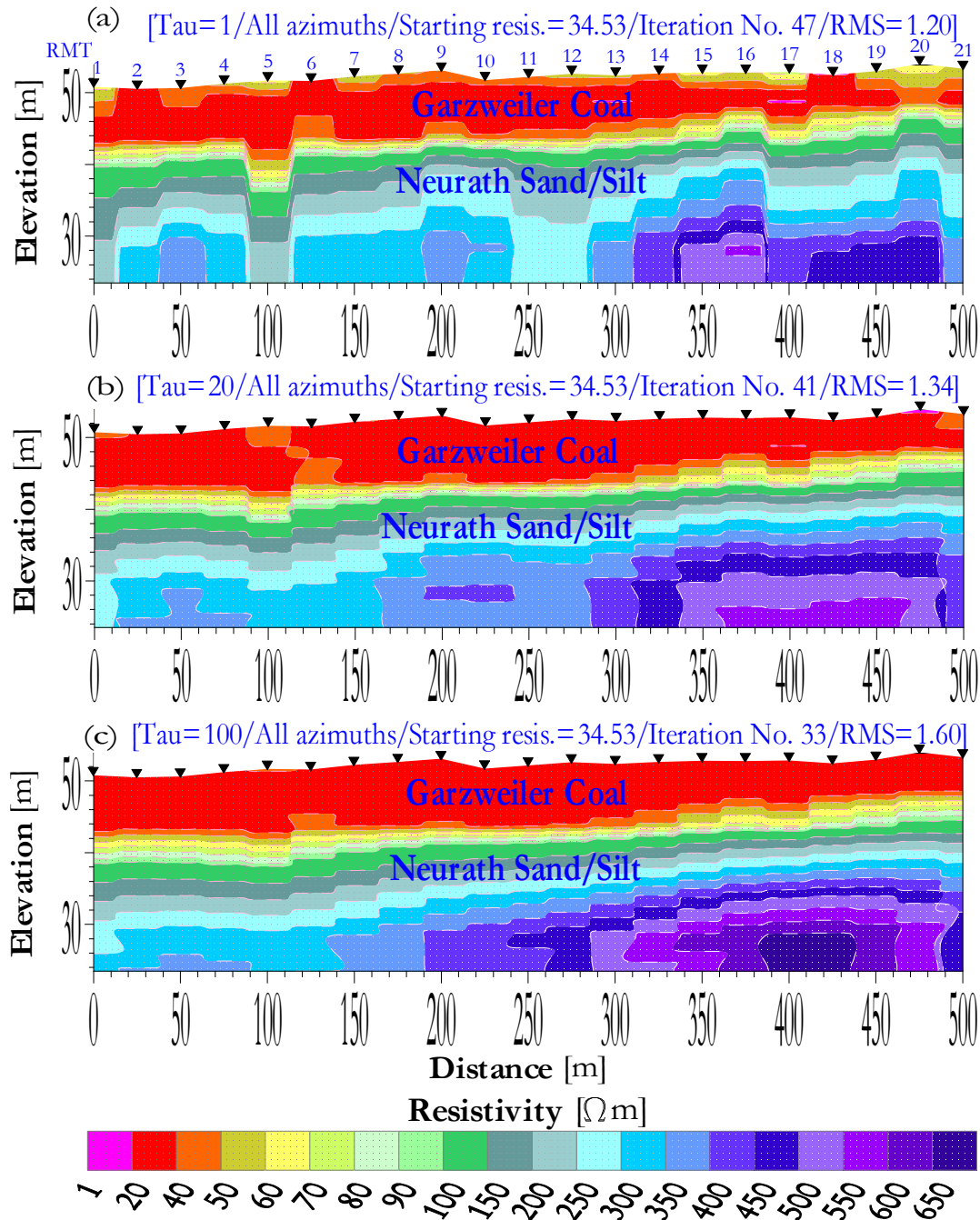


Figure 3.20: 2D RMT smoothed-earth inverted sections, at different τ thresholds, below profile I at the 'Coal-covered Area.' With increasing τ the resistivity model becomes smoother, while the data fit worsens. Inverting using the optimal (b) $\tau=20$ represents appropriate smoothing, while inverting using (a) $\tau=1$ and (c) $\tau=100$ represents under-smoothing and over-smoothing respectively.

These normalized total sensitivities were later divided by the size Δ_j of the respective assigned grid element. Altogether the resulting normalized total sensitivities can be denoted by

$$J_{ij} = \frac{1}{\Delta_j} \sum_{i=1}^N \left\| \frac{1}{\sigma_{si}} \frac{\partial f_i(\mathbf{m})}{\partial m_j} \right\|. \quad (3.13)$$

Finally, the respective values calculated from Equation (3.13) were normalized by maximum sensitivity so that the maximum value is 1. They can be assembled vertically, along the same profile, to represent a relative sensitivity section which can be used further as a quantitative interpretation aid. In the present sensitivity calculations we follow closely the strategy done by *Schwalenberg et al.* [2002].

3.2.5.4 Inversion Results

Coal-covered Area

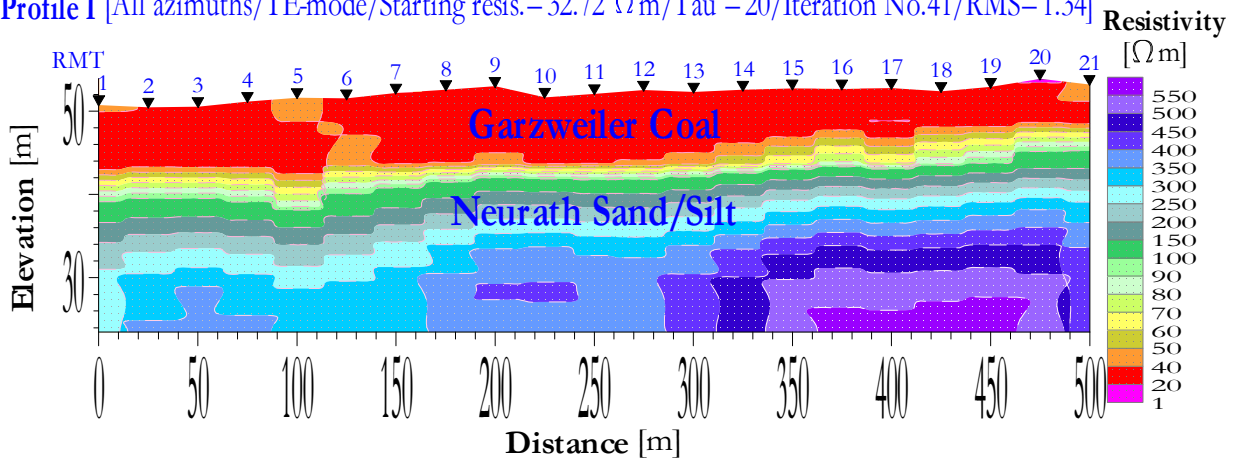
The 2D RMT inversions and corresponding sensitivity calculations were performed, using all frequency data from different measuring azimuths, in the TE-mode. Again, a discussion about the criteria used to choose the most appropriate measuring azimuths, which are not distorted by nearby-topography, for all inversion schemes will be given later in Section 3.2.6. Because the topographic relief was finely sampled, by means of a theodolite and differential GPS readings, it is nicely discretized onto the earth-mesh by setting up the relief to the nearest grid nodes. Each RMT sounding is appeared at a reasonably correct elevation along each profile. Grid elements in air are assigned a sufficiently high resistivity of about $10^6 \Omega\text{m}$. The starting mesh resistivities are initialized to an average-apparent-resistivity homogeneous half-space. No a-priori information was introduced. Because the data errors are used for weighting and in practice it may well happen that they are unrealistically small, an error floor of about 4% can be imposed to avoid unrealistic weightings.

The obtained 2D smoothed-earth sections clearly exhibit an upper conductor overlying a resistive half-space, corresponding to the Garzweiler Coal and Neurath Sand/Silt respectively, which are known to be at these approximate depths (Figure 3.21). The Garzweiler Coal is considered as a marker layer within this simple vertical succession. It shows a gradual thickness decrease from SW to NE, while its resistivity is averaged around $30 \Omega\text{m}$. The resistivity change from the Garzweiler Coal to Neurath Sand/Silt at about 11 to 5.5 m depth is slightly smooth, where the Neurath Sand/Silt resistivity increases laterally towards the NE from 300 to $600 \Omega\text{m}$. No remarkable local resistivity anomaly is encountered. The calculated and measured responses for three representative operating frequencies, at all soundings, are shown in Figure 3.24. The overall data misfits of the obtained models are quite satisfactory, ranged between 1.29 to 1.73 RMS.

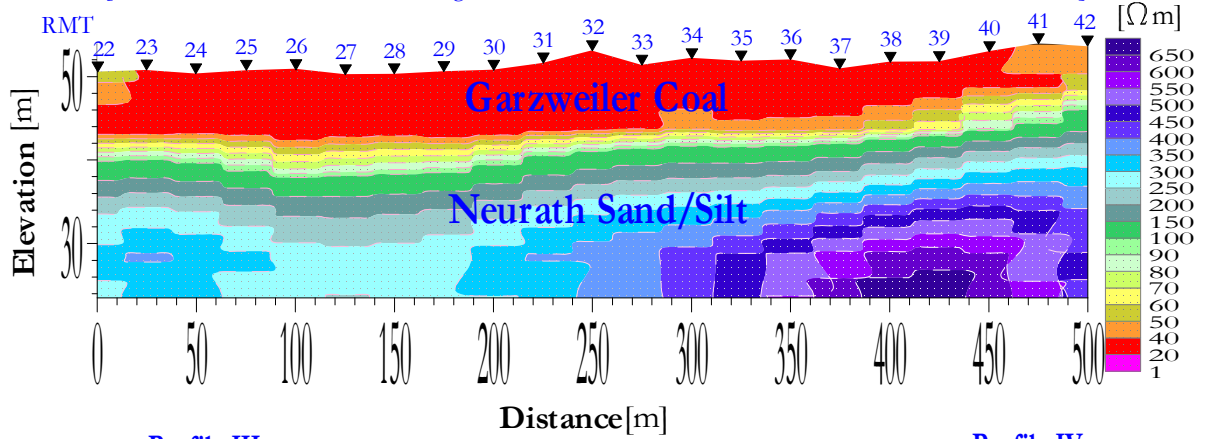
The sensitivity uniformly expands downwards with increasing depth, displaying the integrated induction space of the whole data base (Figure 3.22). The Garzweiler Coal is always associated with higher sensitivities. Laterally, they decrease more rapidly from SW to NE, wherein the Garzweiler Coal thickness gradually decreases.

Comparison between 1D and 2D inversion results showed that both 1D smoothed and layered models represent the Garzweiler Coal–Neurath Sand/Silt boundary very clearly and accurately where the borehole-geology and models are matched well (Figure 3.26a). Whereas, the 2D smoothed model shows a less distinct boundary. Here one of the best uses of 2D inversion scheme was to confirm that 1D character is reasonably valid. The simplicity of 1D inversion scheme can provide sometimes an interpretation with better resolution, or even with more detail, than a complex 2D scheme.

Profile I [All azimuths/TE-mode/Starting resist. = 32.72 Ω m/ τ = 20/Iteration No. 41/RMS = 1.34]

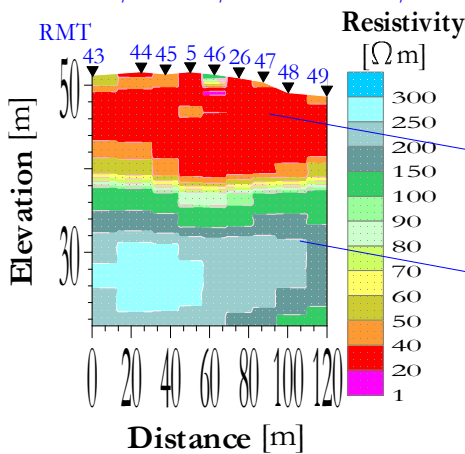


Profile II [All azimuths/TE-mode/Starting resist. = 32.72 Ω m/ τ = 30/Iteration No. 40/RMS = 1.29]



Profile III

[All azimuths/TE-mode/Starting resist. = 32.72 Ω m/ τ = 20/Iteration No. 32/RMS = 1.73]



Profile IV

[All azimuths/TE-mode/Starting resist. = 32.72 Ω m/ τ = 20/Iteration No. 39/RMS = 1.63]

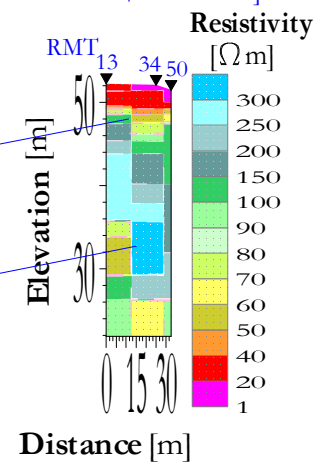


Figure 3.21: 2D RMT smoothed-earth inverted sections below profiles I, II, III and IV at the 'Coal-covered Area.' Warm colors indicate resistivity lows, while cold colors indicate resistivity highs.

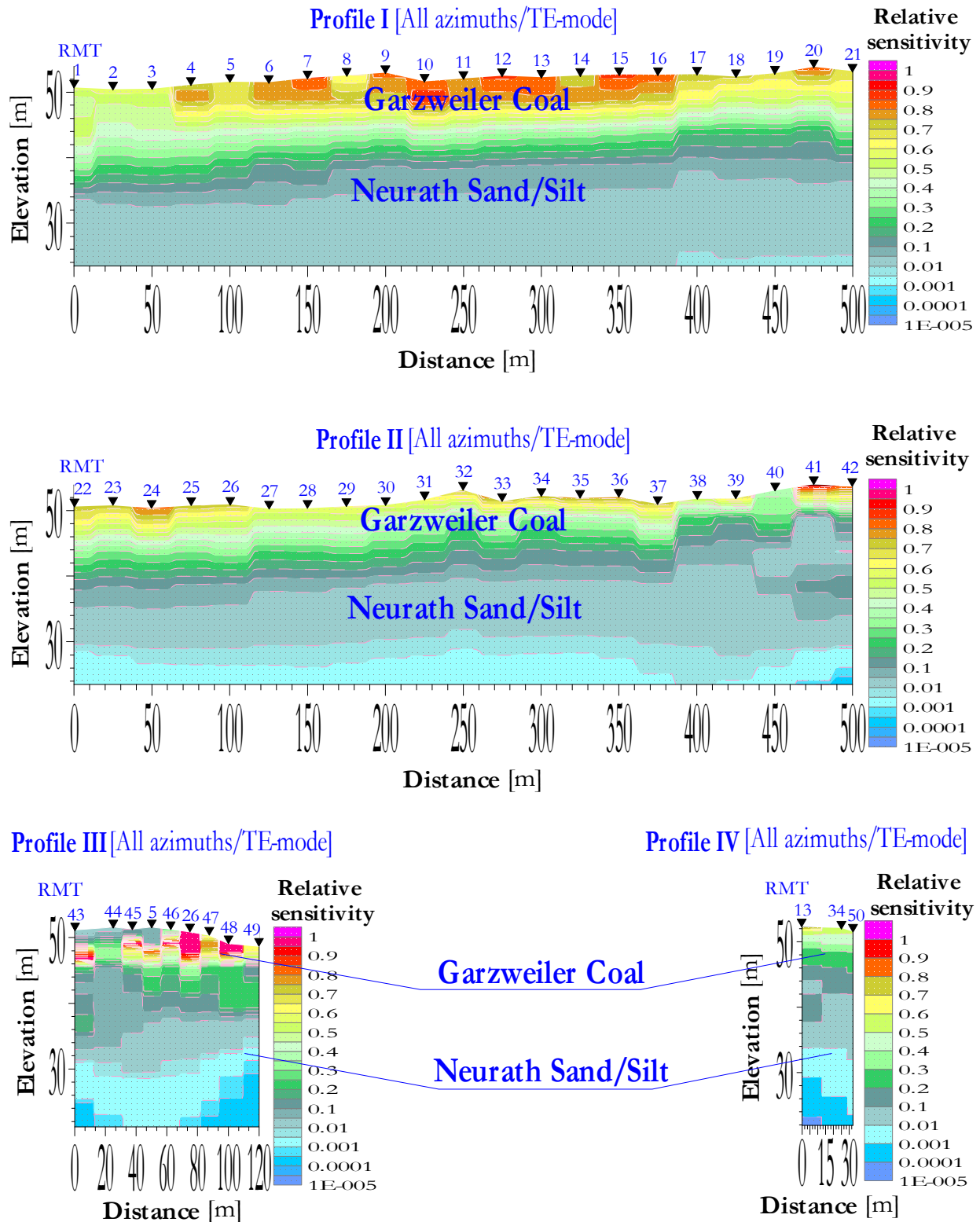


Figure 3.22: Relative sensitivity sections derived from the 2D RMT inversions below profiles I, II, III and IV at the 'Coal-covered Area.' Warm colors indicate high sensitivity fractions, while cold colors indicate low sensitivity fractions.

Sand-covered Area

The 2D RMT inversions and corresponding sensitivity calculations were performed using the frequency data at measuring azimuths 30° and 120° N in the joint-inversion of both TE- and TM-modes respectively. The topography along each profile was discretized onto the earth-mesh with the same specifications described before. The starting mesh resistivities are initialized to an average-apparent-resistivity homogeneous half-space. No a-priori information was introduced. An error floor of about 4% can be imposed to avoid unrealistic weightings.

The obtained 2D smoothed-earth sections seem to be more consistent and geologically reasonable than the 1D earth sections (Figure 3.23a). An intermediate conductor embedded mainly in a fairly resistive background can be clearly seen from these sections. This is interpreted as Garzweiler Coal with an average resistivity of about 30 Ωm between Surface Sand and the lower Neurath Sand/Silt with a resistivity range between 70 and 250 Ωm . Two conductive surficial anomalies of about 35 Ωm average resistivity and 3 m thickness are roughly located at soundings RMT 1 to 2 and RMT 7 to 15 along profile I. An additional, but more conductive, surficial anomaly of about 15 Ωm average resistivity and about 3 m thickness is also roughly located at the soundings RMT 30 to 32 along profile II. These surficial anomalies are interpreted as separate clay masses (or lenses) within the clean Surface Sand. Taking into account the in-loop Nano/ZeroTEM transmitter-loop size, these separate surficial clay masses, which are already confirmed from the resultant 1D/3D TEM resistivity models (see Sections 4.2.3 and 4.2.5), are located close to the above-described RMT soundings. The calculated and measured responses for two representative operating frequencies in each mode, at all soundings, are shown in Figure 3.25. The overall data misfits of the obtained models are also quite satisfactory and do not exceed 1.33 RMS.

The sensitivities are rather low and discontinuously expand downwards with increasing depth (Figure 3.23b). The surficial clay masses are almost associated with higher sensitivities. Following the clay masses, the sensitivity generally decreases more rapidly with depth than elsewhere. The lower boundary of Garzweiler Coal seems to be moderately-resolved.

Comparison between 1D and 2D inversion results shows that both 1D smoothed and layered inversion can roughly resolve the separate surficial clay masses, but they can not yield clear or accurate coal–sand boundaries. At some considerable number of soundings, 1D models exhibit a blocked-layer of surficial clay mass, thinned Surface Sand and Garzweiler Coal followed by Neurath Sand/Silt. The 1D models do not agree very well with the borehole-geology (Figure 3.26b). Here the 1D interpretation has almost reached its limits to explain the validity of the 1D assumption at the 'Sand-covered Area.' The 2D inversions, in stead, position the surficial clay masses and Garzweiler Coal reasonably well within their sand background, yet the feeling of more confidence in the interpretation has been left.

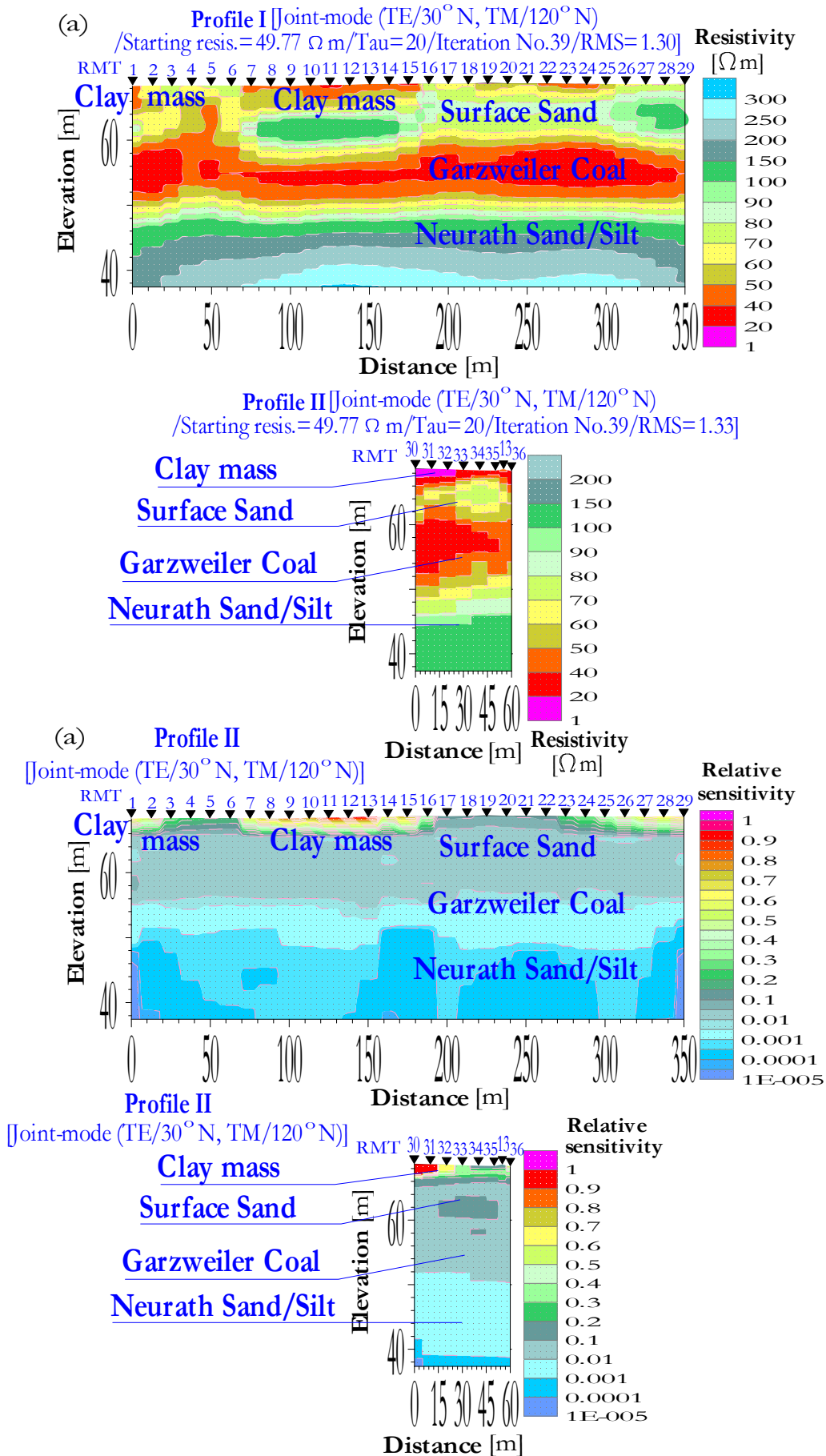


Figure 3.23: 2D RMT (a) smoothed-earth and (b) relative sensitivity sections inverted sections below profiles I and II at the 'Sand-covered Area.'

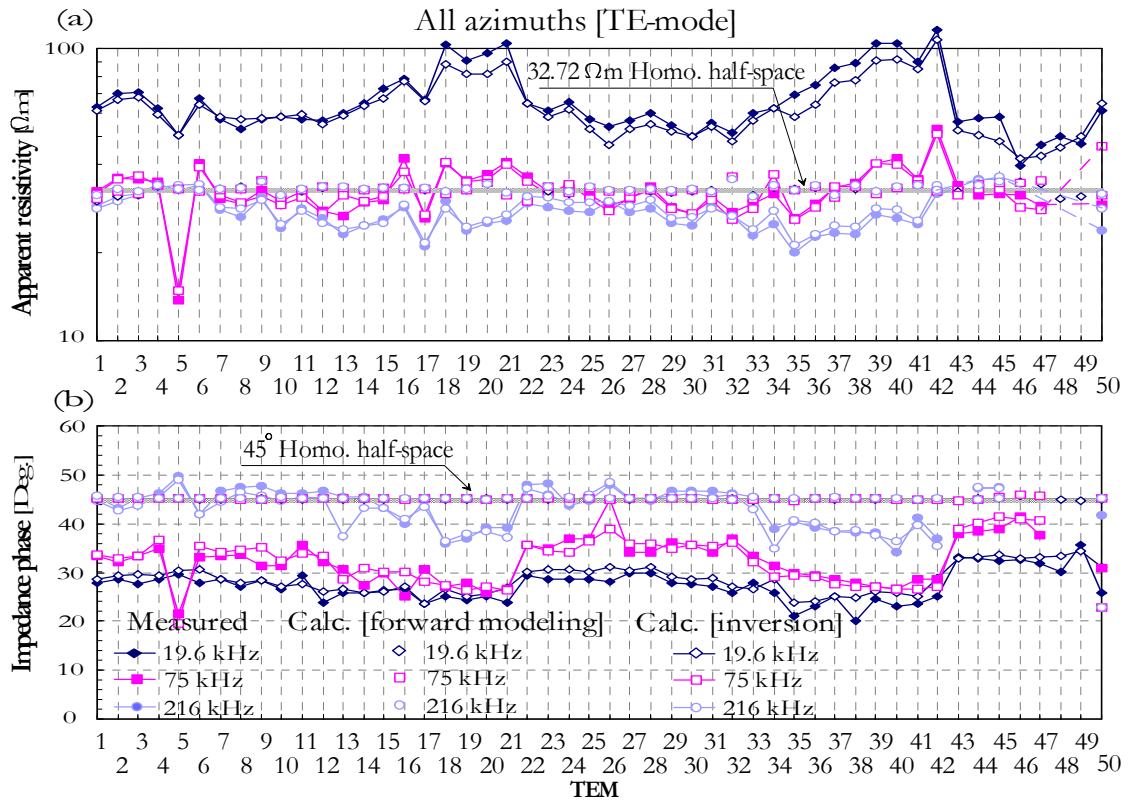


Figure 3.24: The calculated 2D and measured (a) apparent resistivity and (b) impedance phase for operating frequencies 19.6, 75 and 216 kHz at the 'Coal-covered Area.' The corresponding forward modeling responses, at 'iteration No. 0', converged to both starting half-space resistivity and 45° impedance phase.

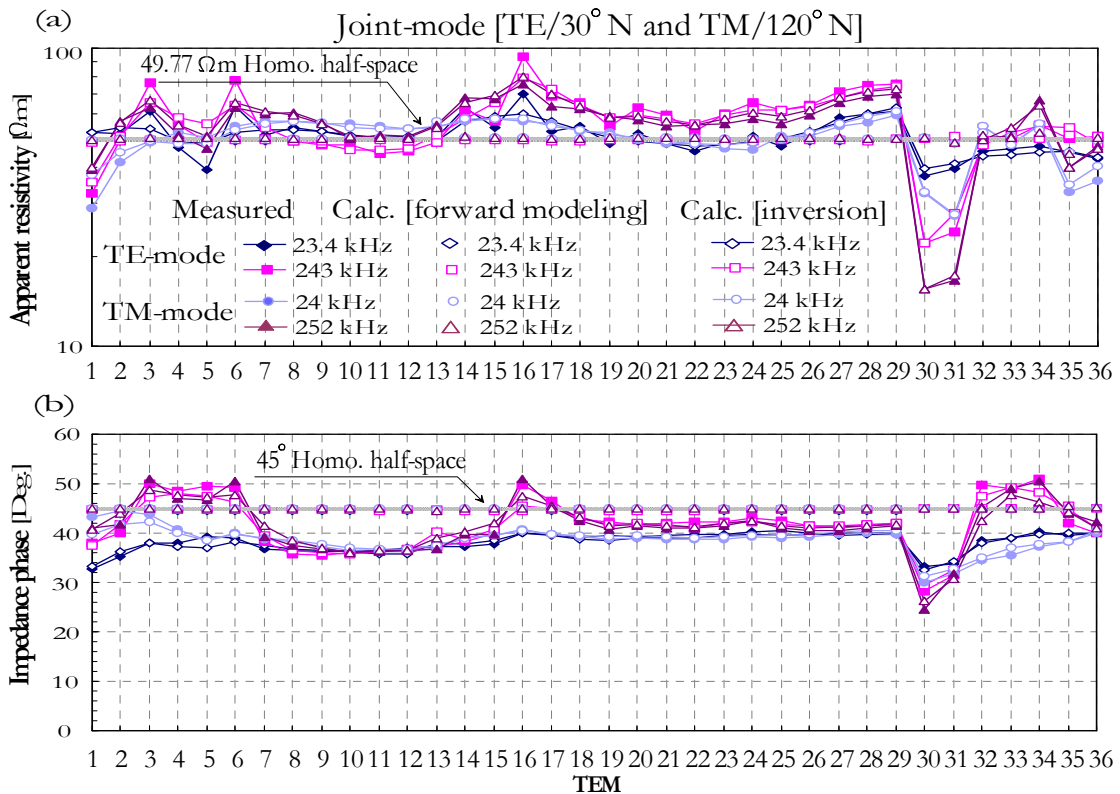


Figure 3.25: The calculated 2D and measured (a) apparent resistivity and (b) impedance phase for operating frequencies 23.4, 24, 243 and 252 kHz at the 'Sand-covered Area.' The corresponding forward modeling responses, at 'iteration No. 0', converged to both starting half-space resistivity and 45° impedance phase.

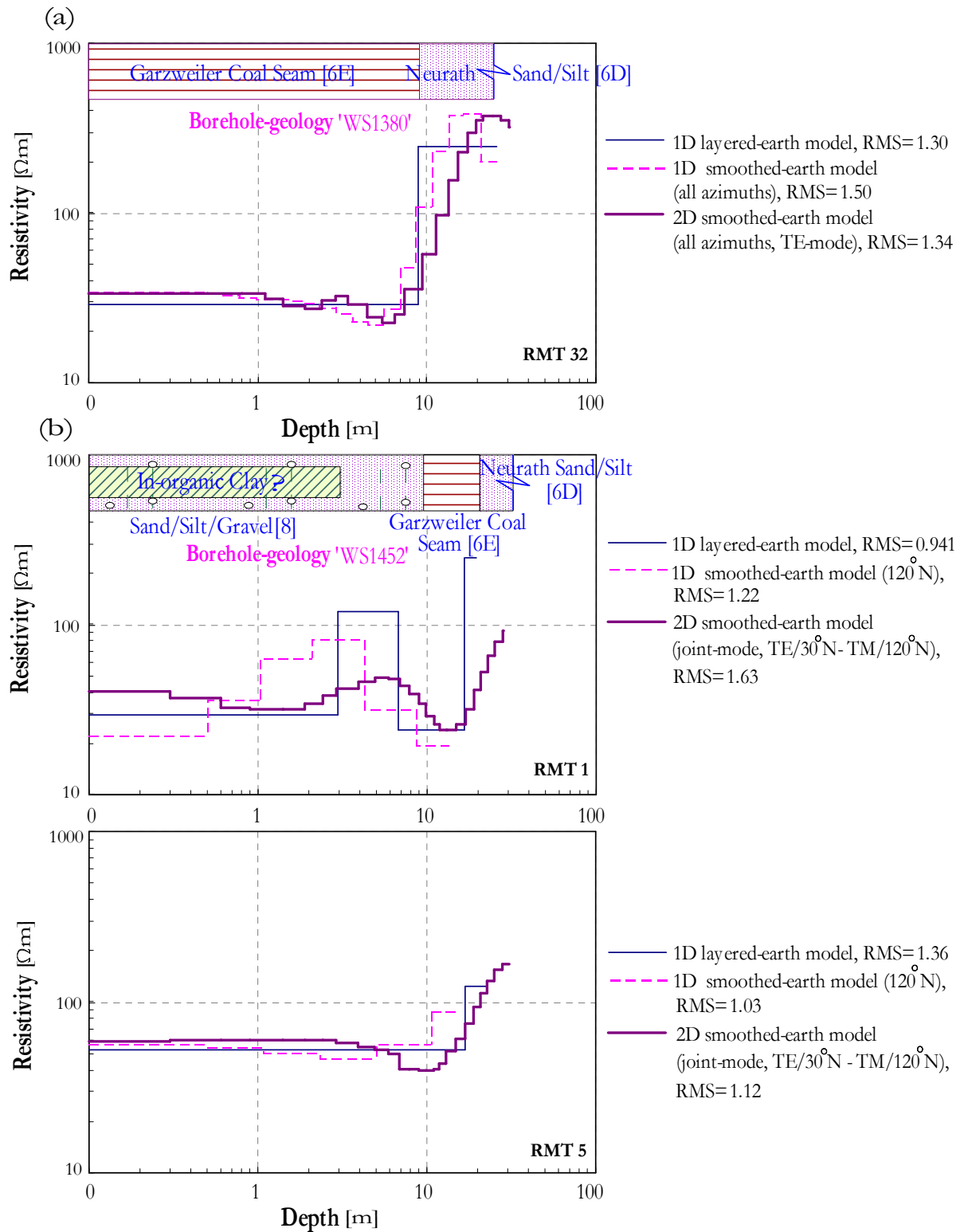


Figure 3.26: Comparison of different resistivity models derived from 1D and 2D RMT inversions with the borehole-geology at the soundings (a) RMT 32, the 'Coal-covered Area' and (b) RMT 1/5, the 'Sand-covered Area.'

3.2.6 Nearby-topography Effect

Practically, the EM response from the nearby-topography is a function of orientation of the topographic-strike with respect to the direction of plane-wave propagation, and of the effective depth-of-investigation of the RMT survey [McNeill and Labson, 1991]. There is no simple quantitative way to assess (or to correct for) topography without knowledge of the terrain resistivity, and without conducting enough reference soundings covering the topographic features that are needed to be assessed. Fischer [1989] carried out extensive numerical calculations of steeply embanked valley-like models (about 1000 m deep) and nicely simulated the nearby-topography effect on the VLF-R apparent resistivity and impedance phase data in both TE- and TM-topographic-modes. At a low resistivity-contrast between the valley floor and the surrounding topography, very strong effect in the TM-topographic-mode would be recovered, while the TE-topographic-mode exhibits a less pronounced effect.

In this section, we will present systematic experiments including 2D RMT inversion runs and corresponding sensitivity calculations, at each measuring azimuth, on the data only along profile I at each survey area, reference to an approximate inversion mode, either TE- or TM-mode. The topography along profile I was discretized onto the earth-mesh with the same specifications described before. During all inversion runs, the starting mesh resistivities were always initialized to an average-apparent-resistivity homogeneous half-space. No a-priori information was introduced. An error floor of about 4% is imposed to avoid unrealistic weightings. These experiments were mainly performed in order to cross-check the effect of nearby-topography on the azimuthal RMT data at the survey areas. They can also derive reasonable estimates of the maximum depth-of-investigation for the RMT soundings, below which the model parameters are less resolved by the data, and thus should not form part of an interpretation. Furthermore, the calculated sensitivities may indicate whether increasing the number of operating frequencies at each sounding increases the resistivity resolution or not.

Let us now simplify the nearby-topography at the survey areas by considering the southern very steep cliff (and the northern small hillock) at the 'Coal-covered Area', and the northern large hillock at the 'Sand-covered Area' as 2D resistivity structures with a general topographic-strike directed at 85° N. Here the EM fields can be roughly defined in a coordinate system orthogonal to that strike. If the 2D topographic-structure roughly strikes towards radio-transmitters at measuring azimuths 80° , 30° , 60° and 120° N, it may be fairly well coupled. This represents the nominal TE-topographic-mode, as the magnetic field is approximately perpendicular to the strike and current can flow freely. Note that both the apparent resistivity and phase data from these parallel and subparallel azimuths showed already similar smooth frequency trends and fairly similar 1D resistivity models. Therefore, they can be tested individually in the nominal TE-topographic-mode during the inversion. On the other hand, if the topographic-structure strikes perpendicular to radio-transmitters at measuring azimuths 0° and 150° N, it may be minimally-coupled. This represents the nominal TM-topographic-mode, as the magnetic field is parallel to the strike and current flow would be restricted. Note that both the apparent resistivity and phase data from these perpendicular azimuths showed different (and irregular) frequency trends. Similarly, they can also be tested individually in the nominal TM-topographic-mode during the inversion.

Coal-covered Area

The obtained resistivity models for different measuring azimuths are almost very similar, if not structurally identical. This means that every two orthogonal horizontal electric and magnetic field components are laterally invariant, and therefore the data have almost 1D character. It also indicates that the nearby-topography has insignificant effect on the RMT data, and that the distances between the nearby-topography and main parallel profiles were chosen adequately enough to avoid its effect. In all cases, resistivity models display clearly the Garzweiler Coal overlying the resistive Neurath Sand/Silt.

The coal–sand boundary is more sharp and clear as the number of operating frequencies increases at each measuring azimuth (e.g. 120° N model with 24, 61.9, 118.7, 153, 207, 252 kHz). Models having small number of frequencies show a broadened coal–sand boundary (e.g. 150° N model with only 198 kHz). Because the surface impedance is independent of the measuring azimuth, all frequency data can be used safely at each sounding, in both 1D and 2D inversions, to produce highly-resolved resistivity models. Interestingly, the results illustrate that even when very few frequencies are used in the Mackie's inversion scheme, they help in deciphering an approximate, but not a highly-resolved, resistivity model. Note that the single-frequency data, as an example, should be doubled in the Mackei's inversion codes, otherwise will be not workable.

The sensitivity uniformly expands downwards with increasing depth, displaying the integrated induction space of the whole data base. The Garzweiler Coal is always associated with higher sensitivities. These changes are equally distinct in both TE- and TM-modes. Laterally, they decrease more rapidly from east to west, wherein the Garzweiler Coal thickness gradually decreases. The most remarkable feature of all sensitivity sections is the sensitivity decreases less rapidly with increasing number of operating frequencies. In other words, the shallow to sufficiently-deep structure details become more resolved with increasing the number of operating frequencies. Although the choice of the sensitivity limit is still an open question requiring further 2D RMT modeling of synthetic data [Schwalenberg *et al.*, 2002], the 10^{-4} isoline may represents, at least, the moderately resolved model parameters and may coincide with the maximum depth-of-investigation. Following this, a depth of about 30 m ($\approx 2.5z^*$) is found to be quite satisfactory.

Sand-covered Area

The most dramatic nearby-topography effect is occurred mainly at measuring azimuths 0° and 150° N, where the entire current flow should round from the hillock to the ground of the area or vice versa. The magnetic field remains uniform along the hillock. The high current concentration close to the ground leads to high electric fields, and hence to relatively higher apparent resistivities. The impedance phases are frequently close to or grater than 45°, as if there is discontinuous deep conductor. This is may be evident from both the raw data and derived resistivity models at measuring azimuths 0° and 150° N, where the resistivity highs are predominant. Here the conductive anomalies due to the surficial clay masses and Garzweiler Coal are discontinuous, or even rided somewhere on the regional topographic anomalies. That means, every two orthogonal horizontal electric and magnetic field components are not necessarily laterally-invariant, and hence the 2D inversion response for these measuring

azimuths are dependent on their orientation with respect to the hillock. On the other hand, the derived models for azimuths parallel (80° N) and subparallel (30° , 60° and 120° N) to the hillock show all reliable resistivity anomalies which are not significantly affected by the nearby-topography. Both the highly-conductive surficial clay masses and Garzweiler Coal can be easily recognized from the resistive Surface Sand and the lower Neurath Sand/Silt.

Generally, the clay–sand–coal boundaries are more sharp and clear as the number of operating frequencies increases at each measuring azimuth. Models having small number of frequencies show little broadened layer boundaries. Here the surface impedance is dependent on the measuring azimuth, and of course using all frequency data at each sounding, in either 1D or 2D inversion, would be impossible. Adopting this view, the joint-inversion of both TE-mode and TM-mode data, for measuring azimuths 30° and 120° N respectively, was finally chosen and found to give much better resolution of resistivity models than individual mode data on their own.

The sensitivities at the 'Sand-covered-Area' are rather low. They discontinuously expand downwards with increasing depth. The surficial clay masses are almost associated with higher sensitivities. Following the clay masses, the sensitivity generally decreases more rapidly with depth than elsewhere. The lower boundary of Garzweiler Coal seems to be moderately resolved. Apart from the model validity for further interpretation, throughout all sensitivity sections the sensitivity decreases less rapidly with increasing number of operating frequencies. This may reflect again the relationship between the model resolution and the number of operating frequencies. Yet unclear are the calculated sensitivities affected by the nearby-topography effect or not. Here the maximum depth-of-investigation worsens a little to be averaged around 24 m ($\approx 2z^*$).

Lastly, the above 2D RMT inversion experiments assume that the results are sufficiently accurate for a qualitative assessment of the nearby-topography effect on the RMT data, which is one of the present intentions.

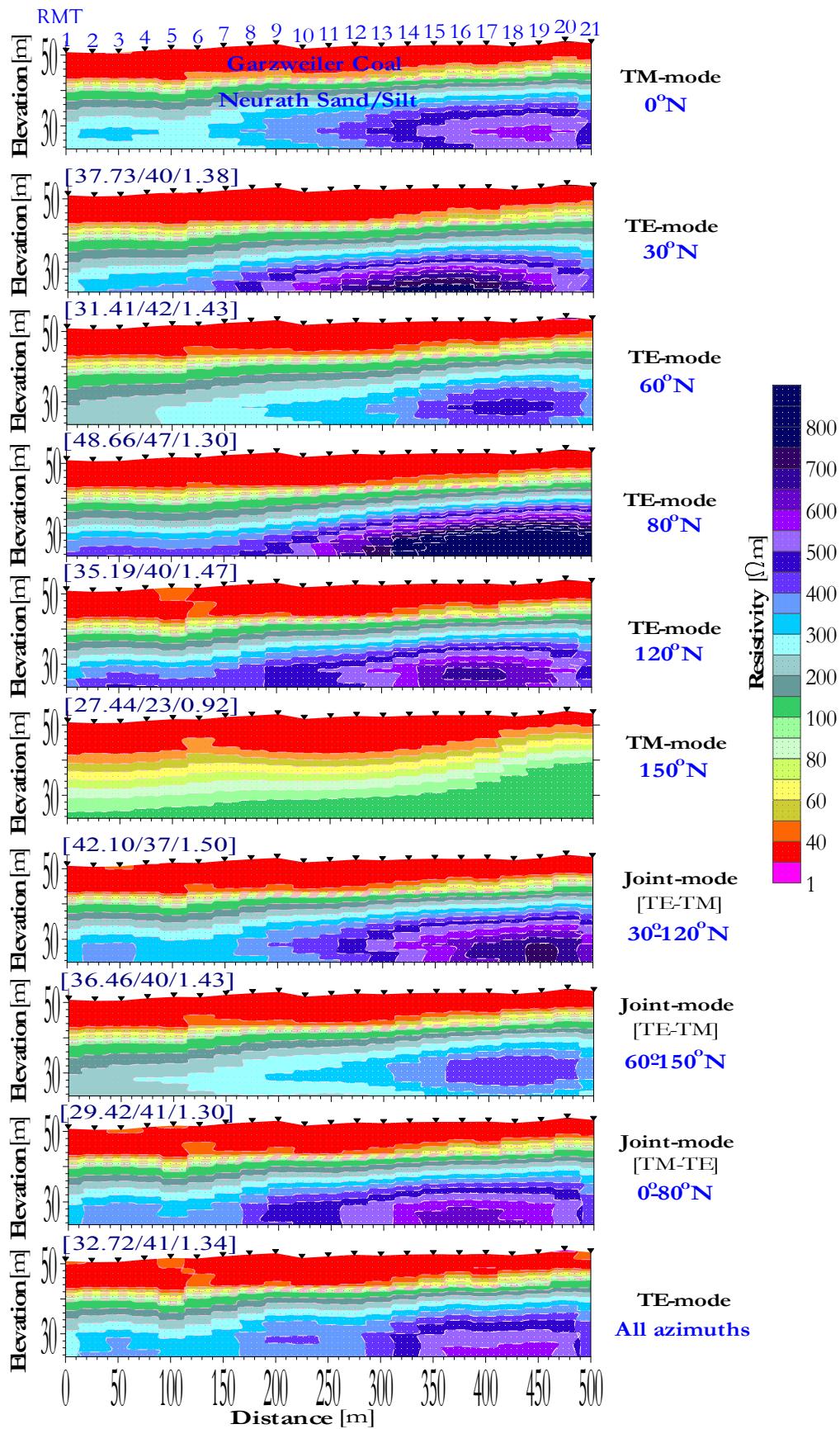


Figure 3.27: 2D RMT smoothed-earth inverted sections, at each measuring azimuth, below profile 1 at the 'Coal-covered Area.' Here the resistivity model is well-defined when inversion is performed using (lowermost) all the 19 frequency data. The values given above each section are the start modeling resistivity, number of iterations and overall RMT misfit respectively.

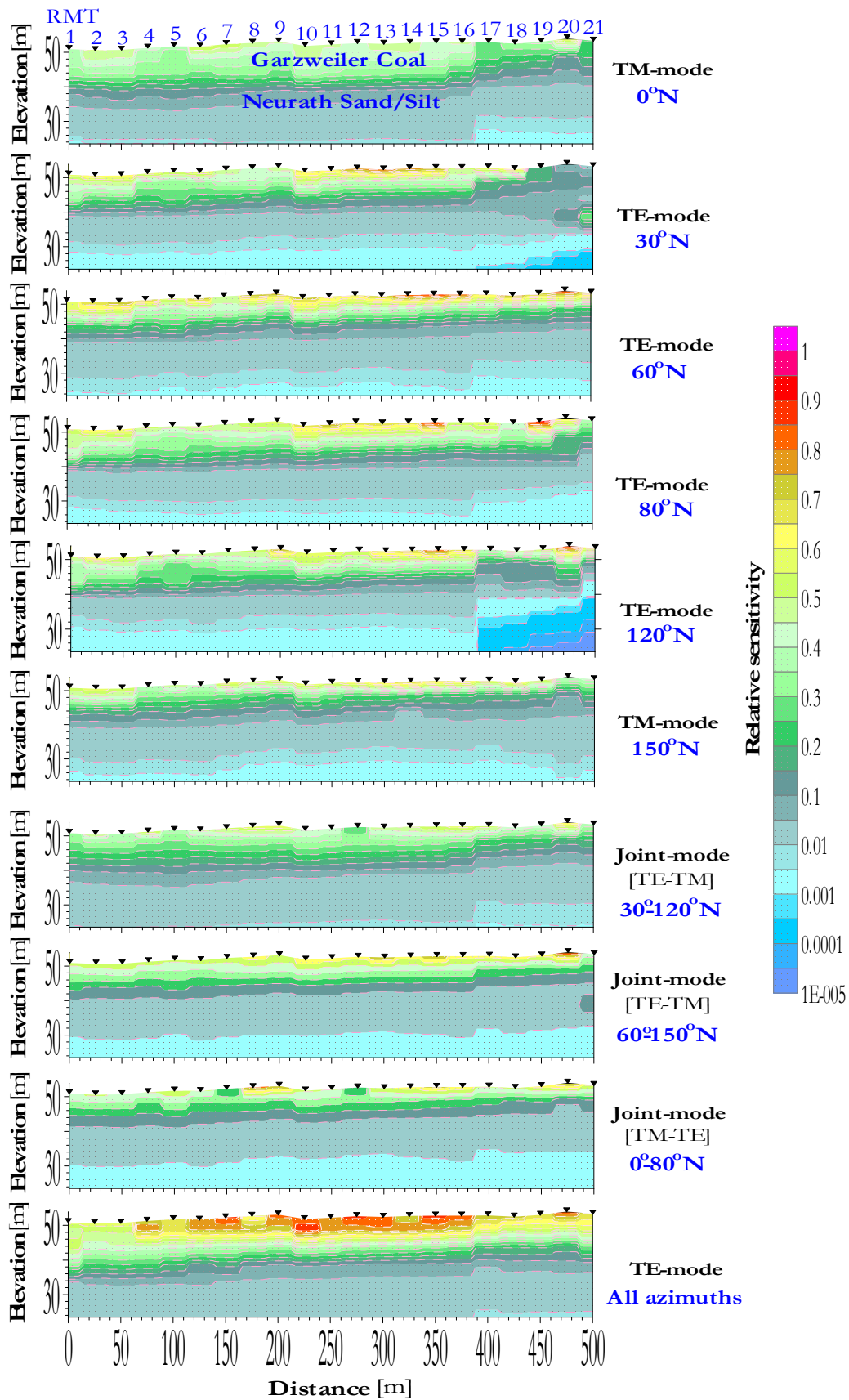


Figure 3.28: Relative sensitivity sections derived from the 2D RMT inversions, at each measuring azimuth, below profile I at the 'Coal-covered Area.' Here the resistivity model is best-resolved when inversion is performed using (lowermost) all the 19 frequency data.

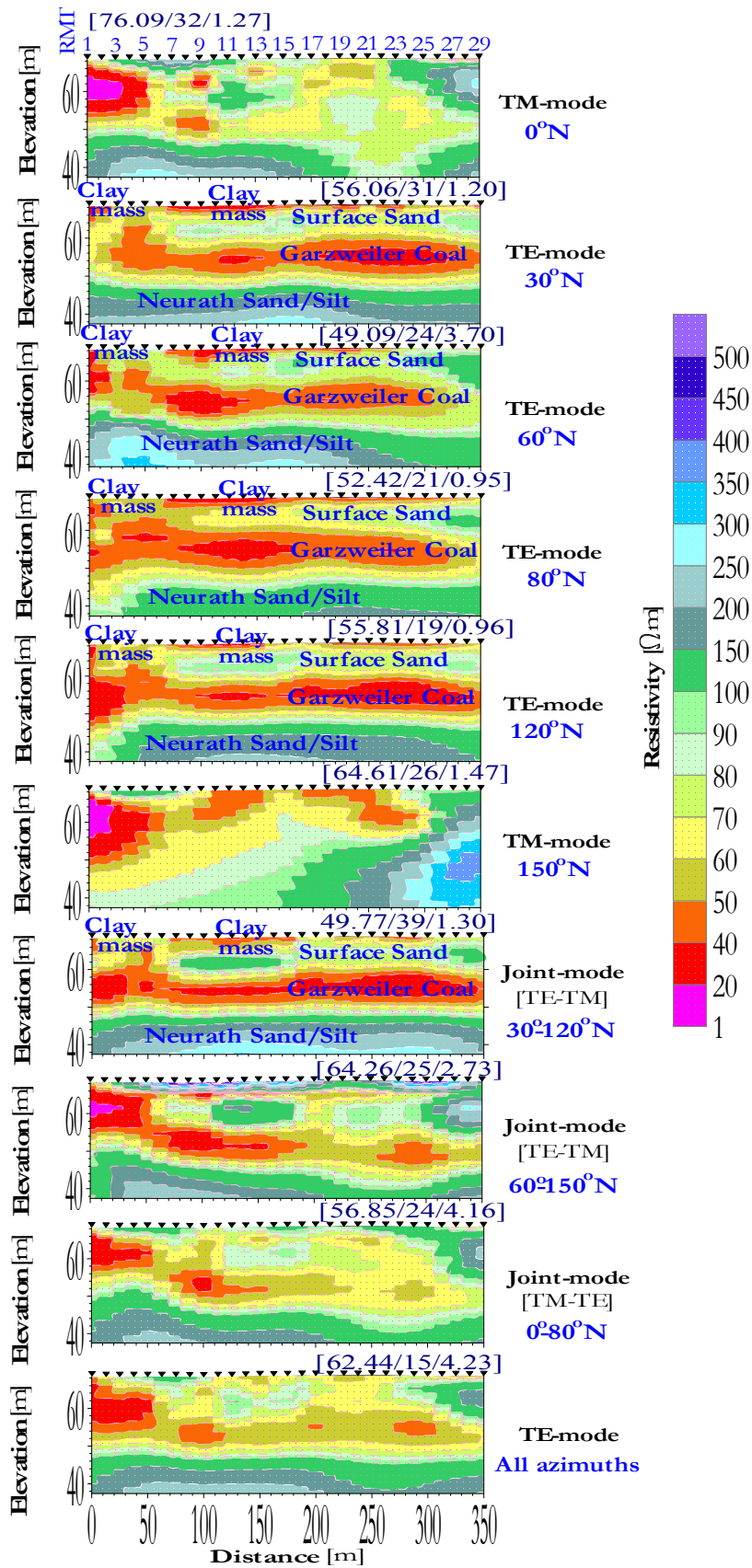


Figure 3.29: 2D RMT smoothed-earth inverted sections, at each measuring azimuth, below profile 1 at the 'Sand-covered Area.' Here the resistivity model is well-defined when inversion is performed using the frequency data at parallel and subparallel azimuths to the large hillock. The values given above each section are the start modeling resistivity, number of iterations and overall RMT misfit respectively.

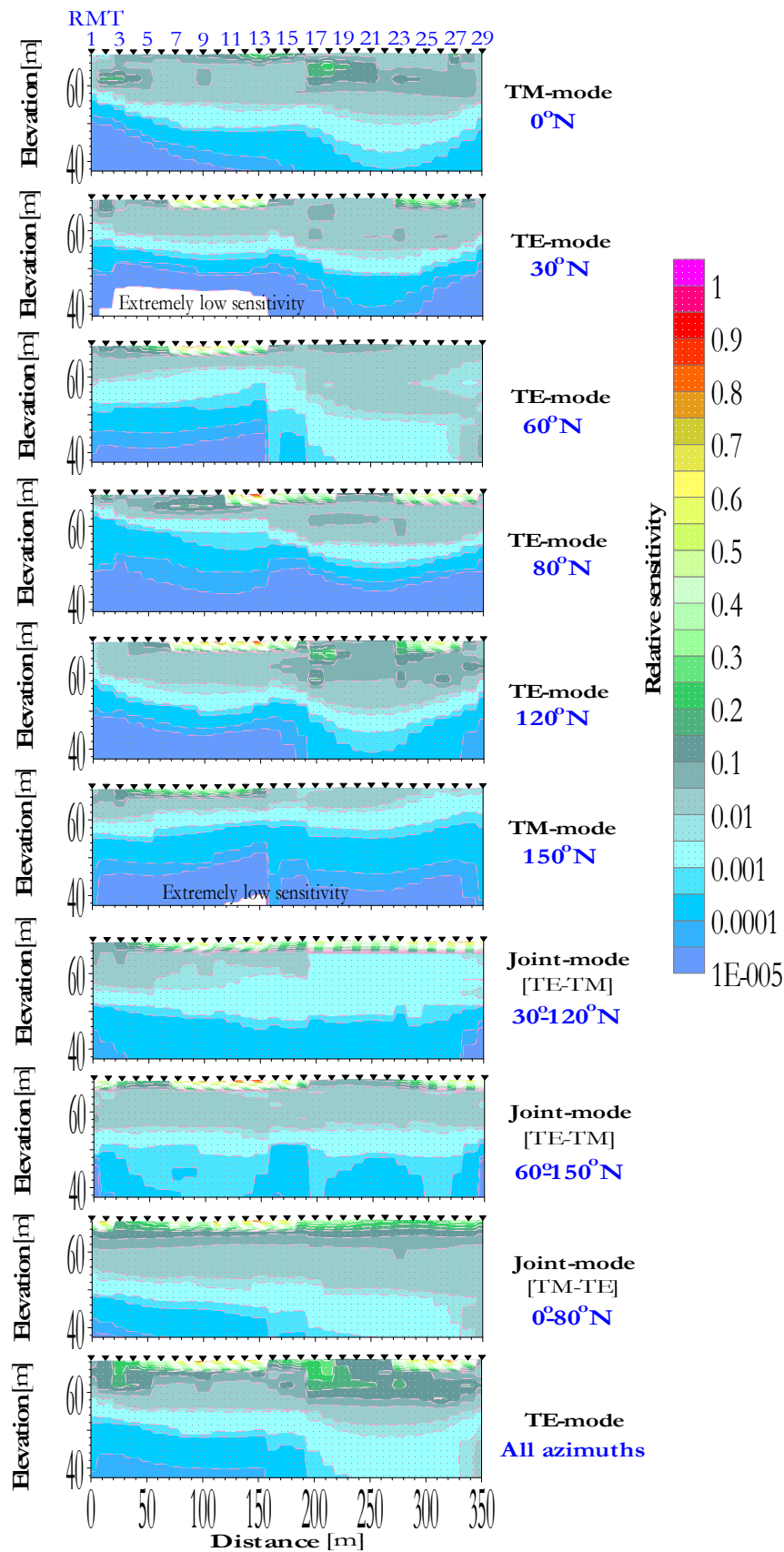


Figure 3.30: Relative sensitivity sections derived from the 2D RMT inversions, at each measuring azimuth, below profile I at the 'Sand-covered Area.' Here the resistivity model is best-resolved when inversion is performed using the frequency data at parallel and subparallel azimuths to the large hillock.

CHAPTER 4

TRANSIENT ELECTROMAGNETIC RESISTIVITY MODELS

Ground-based transient EM (TEM) methods can be used in a number of different transmitter-receiver configurations [Nabighian and Macnae, 1991] for routine environmental, hydrogeological and mineral investigations. Among these different loop-loop configurations, the in-loop or central-loop configuration has become more popular and is presently in wide use. This chapter explains the conceptual background of TEM methods and gives detailed description on how to acquire segmented in-loop Nano/ZeroTEM data sets in the field and to interpret them reliably in terms of 1D and 3D resistivity models at the survey areas. Furthermore, the effect of nearby-topography on the TEM data will be qualitatively assessed. A correlation of the final 1D/2D RMT and 1D/3D TEM earth models with laboratory-based resistivity models, and some useful geological implications derived from such models are give

4.1 Transient Electromagnetic Methods

4.1.1 Conceptual Background

Transient EM (TEM) methods utilize EM energy introduced into the ground as transient pulses, instead of continuous waves, by a large transmitter-loop carrying steady current and primary magnetic field. Satisfying *Faraday's* law, immediately after the current and primary field are suddenly turned-off, an associated secondary magnetic field resulting from an induced current pattern in the ground is sensed by a centrally-placed small receiver-loop and decays with time as the current gradually dissipates. The configuration forms the basis of the *in-loop* TEM sounding and can be schematically demonstrated in Figure 4.1. The spreading out of induction currents is much like the downward movement of a system of *smoke rings* [Nabighian, 1979; Oristaglio and Hohmann, 1984; West and Macnae et al., 1991], which have a consequential amplitude decay with increasing time. These current rings are snapshots in time through a vertical section in the ground and can move outwards once they reach a layer interface with a sufficient resistivity-contrast.

Initially, the induced currents are concentrated close to the ground surface, just below the transmitter-loop, and dissipated through ohmic losses. This is known as the *early-time stage*, where the secondary magnetic field is time-invariant and weakly-dependent on the near-surface resistivity. Effectively, this is the start of downward diffusion of the current system towards the ground interior, approaching the *intermediate-time stage*. As time passes and the locus of maximum current amplitude diffuses downwards, the secondary field becomes time-variant and proportional to $t^{-5/2}$ and to $\rho^{-3/2}$, where t is the decay time after current turn-off [sec.] and ρ is the deep-ground resistivity [Ωm]. This is known as the *late-time stage*. Generally, the magnetic field decays rapidly when the currents diffuse in a resistive ground, and more slowly when they flow in a conductive ground. The recorded signal is either a decay of the vertical secondary magnetic field component (step response) or its time-derivative (impulse response or voltage), and generally called a *transient*. Magnetic field measurements are usually superior only in penetrating conductive ground, while voltage measurements are suitable for both conductive and fairly resistive grounds. Only the latter will be considered here.

Now consider a fairly conductive homogeneous half-space or an uniform horizontally-layered earth with geometry applicable to many opencast mining problems. According to *Ward and Hohmann* [1988], the in-loop voltage response is given by

$$\frac{\partial h_z}{\partial t} = \frac{-I\rho}{\mu_o a^3} \left[3\text{erf}(\theta a) - \frac{2\theta a}{\sqrt{\pi}} (3 + 2\theta^2 a^2) e^{-\theta^2 a^2} \right], \quad (4.1)$$

where I is the transmitter current [A], $\theta = (\mu_o / \rho 4t)^{1/2}$, a is the transmitter-loop radius [m] and $\text{erf}(\theta a)$ is the error function

$$\text{erf}(\theta a) = \frac{2}{\sqrt{\pi}} \int_0^{\theta a} e^{-t^2} dt. \quad (4.2)$$

At later times, the mathematics simplifies the definition considerably and the relevant asymptotic formula can be given as

$$\frac{\partial h_z}{\partial t} \approx \frac{-I\mu_o^{3/2} a^2}{20\pi^{1/2} \rho^{3/2} t^{5/2}}. \quad (4.3)$$

Commonly, in-loop TEM data are presented in the form of bilogarithmic plot of transient-decay response versus time (Figure 4.3, upper). Although the rate and spatial characteristics of this decay are dependent on the ground resistivity-distribution [*Nabighian*, 1979], they are not directly representative of the resistivity structure at the sounding location. To make the curve more representative, the transient-decay response should be transformed into apparent resistivity (see Section 4.1.5).

4.1.2 Depth-of-investigation

Analogous to RMT methods, defining a depth-of-investigation is crucial for TEM methods. Theoretically, the maximum penetration depth at which the induced currents still strongly diffuse, and therefore the response due to a buried homogeneous half-space r can be detected by a TEM system at a particular sampling time, is known as *diffusion-depth* [m] [*Spies*, 1989]

$$\delta_{TEM} = \sqrt{\frac{2t\rho_a}{\mu_0}}. \quad (4.4)$$

The similarity between the RMT skin-depth and the TEM diffusion-depth is remarkable: the skin-depth is proportional to $(1/f)^{1/2}$, whereas the diffusion-depth is proportional to $t^{1/2}$. So, it is to TEM methods what the skin-depth is to RMT methods. Furthermore, it is apparently independent of the configuration size and geometry. In practice, the effective depth-of-investigation is dependent not only on the average ground resistivity and sampling time, but also on the transmitter-dipole moment (the effective area times output-current) M and the overall SNR, and hence the sensitivity and accuracy of the instrumentation. For conventional near-zone in-loop TEM soundings, in which the transmitter-loop size is less than the expected depth-of-investigation, it can be given as

$$d_{TEM} \approx 0.55 \left[\frac{M\rho_a}{\eta_v} \right]^{1/5}, \quad (4.5)$$

where η_v the background noise level [typically 0.1 nV/Am²]. That means, it is more difficult to sound more deeply unless the transmitter-dipole moment is effectively large and the signal is sufficiently strong with respect to the background noise. Generally, the earliest sampling time determines the minimum depth-of-investigation at which near-surface resistivity variations can be reasonably resolved.

4.1.3 Zonge Nano/ZeroTEM System

The present TEM data were collected using the commercially available Nano/ZeroTEM system (Zonge Engineering and Research Organization Inc., USA). It is a single-site acquisition system that offers a high-resolution imaging of the shallow and sufficiently-deep resistivity structures. When the standard *in-loop* configuration is used (Figure 4.1), a single-turn 50 x 50 m² transmitter-loop is laid out on the ground and connected to the battery-powered 'NT/ZT-20' transmitter. Tall wooden sticks are usually pushed into the ground at the corners of the transmitter-loop to provide sighting targets. A single-turn 20 x 20 m² receiver-loop is located at the center of the transmitter-loop, by sighting on the corner sticks with the right-angle prism, and connected to the 'GDP-32^{II}' receiver as pictured in Figure 4.2. The instrumental resolution is limited around 0.05 μ V. Data acquisition parameters and specifications of the Nano/ZeroTEM system are given in Table 4.1.

The transmitter passes a commutated DC current (up to 9 A) of sufficiently precise square waveform with a pulse train of alternating polarity (positive and negative going pulses) through the transmitter-loop. Between pulses is an off-time, during which the received signal is measured. The off-time always equals the on-time, its duration is determined by the selected bandwidth. The use of bipolar current-waveforms is widely preferable because the averaging of the transients of opposite polarity is essential to avoid ground polarization effects. Although it is difficult to visualize exactly the shape of the transmitted-current waveform [Spies and Frischknecht, 1991], after setting up the equipment, this can be checked using a suitable digital oscilloscope and waveform processor.

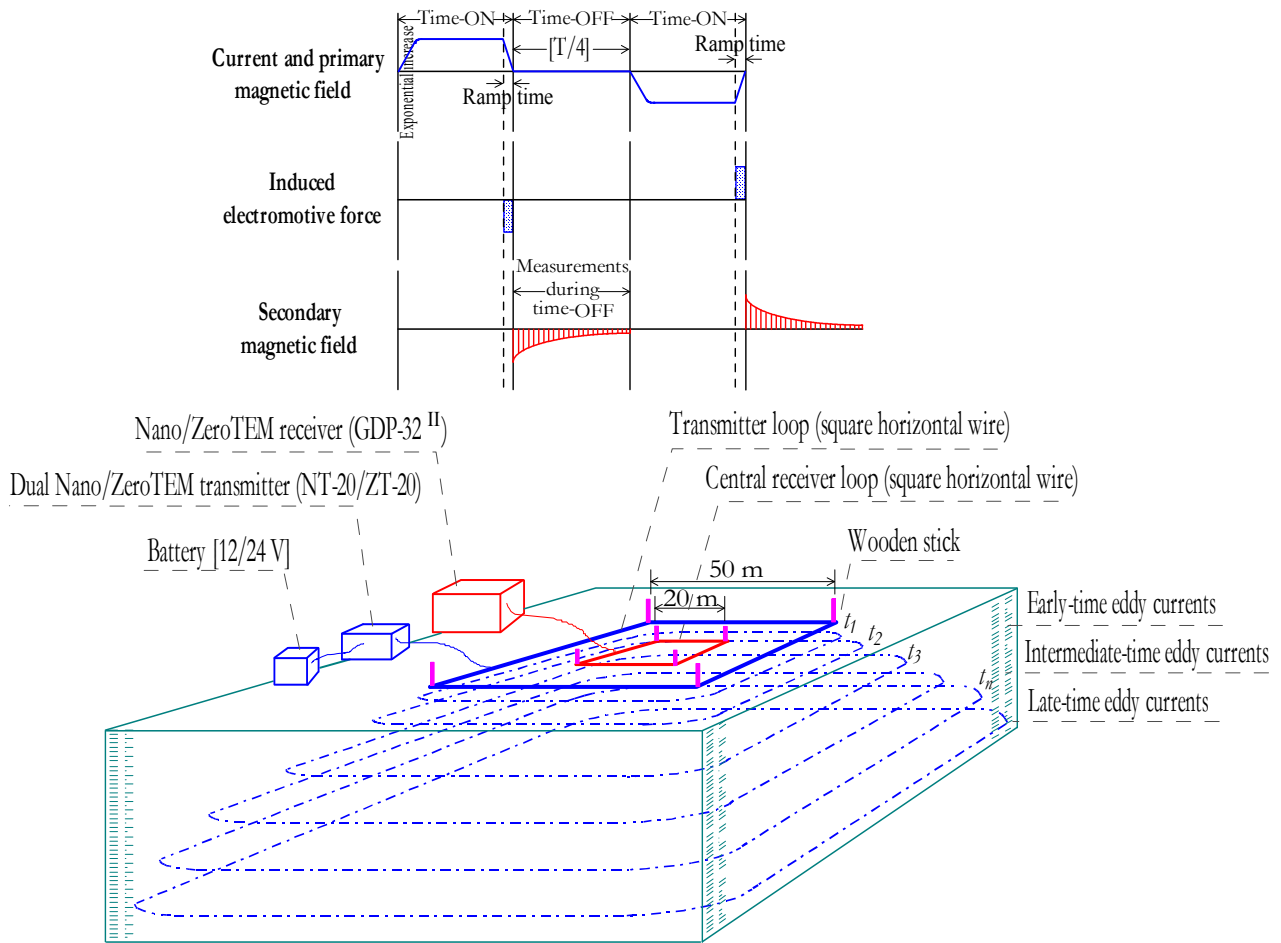


Figure 4.1: In-loop field setup of the Zonge Nano/ZeroTEM system. The downward and outward propagation of the eddy currents at successive time intervals over a homogeneous ground are displayed. In the upper part, the bipolar transmitter-current waveform, induced electromotive force in the receiver-loop, and secondary magnetic field measured during the time-off are illustrated.



Figure 4.2: Photograph showing the Zonge Nano/ZeroTEM system and other connections in the field.

Like any other TEM system, when a higher output-current is used, setting the gain to the highest possible range without producing blanking in the earliest time-windows is a crucial issue in the Nano/ZeroTEM system. The only remedy is to record the voltage by a special segmentation (or splicing) process on separate channels with different output-currents, gain-settings, bandwidths and sampling rates (Figure 4.3). First, the very fast turn-off NanoTEM measurements are taken from about 0.45 μs to 2.55 ms with low gain and output-current (about 0.5 A), and then with higher gain and output-current (about 3 A). A turn-off time (i.e. the ramp time at which transmitter-current takes to fall to zero) of approximately 3 μs , a moderate bandwidth of 64 Hz and a 1.6 μs sampling rate are used for both runs. In order to obtain a continuous transient in the NanoTEM time range, the data from the two runs should be combined to form one composite transient. Later on, the slow turn-off ZeroTEM measurements are taken from about 44.0 μs to around 6.15 ms with an automatic gain and a higher output-current (about 8.5 A). A turn-off time of about 50 to 55 μs , a narrower bandwidth of 32 Hz and a 30 μs sampling rate are used for this run. The proper choice of turn-off time is a complex-function of the dipole moment, self-inductance and damping resistance in the transmitter-loop as well as of the expected resistivity of the ground [Gaidetzka, 2002]. Background noise measurements should be carried out with the same recording scheme while the transmitter is turned-off. In such a way of recording, a real-time gain adjustment would be possible throughout the entire transient, and the available dynamic range of the GDP-32^{II} would be fully utilized.

Parameter	NanoTEM [Shallow investigation mode]	ZeroTEM [Deep investigation mode]
Configuration geometry	In-loop (Central loop)	In-loop (Central loop)
Transmitter (T_x)		
Area [m ²]	50×50	50×50
Type	12 V battery-powered NT-20	24 V battery-powered ZT-20
Current output [A]	0.5 (low gain) to 3 (high gain)	8.5 to 9
Number-of-turns	Zero-elevated single turn	Zero-elevated single turn
Waveform and duty cycle	Square bipolar current with 50% duty cycle*	Square bipolar current with 50% duty cycle
Turn-off (ramp) time [μs]	3	50 to 55
Receiver (R_x)		
Area [m ²]	20×20	20×20
Type	Multi-channel GDP-32 ^{II**}	Multi-channel GDP-32 ^{II}
Number-of-turns	Zero-elevated single turn	Zero-elevated single turn
Measured component(s)	($\partial h_z / \partial t$) ^{***} as voltage decay	($\partial h_z / \partial t$) as voltage decay
Time gates (windows)	31 gates covering approximately four decades at earlier-times	22 gates covering approximately two decades at later-times
Band-width (repetition rate) [Hz]	64	32
Sampling rate (window centers) [μs]	Manually set at 1.6	Automatically set at 30.5
Gain-setting	Manual low and high gain	Automatic gain
Number-of-cycles to be averaged	1024	1024
Number-of-stacks	10	10
Dumped data file	A 31 data-point binary file, easily transformed into ASCII text format	A 22 data-point binary file, easily transformed into ASCII text format

*50% of a constant period between successive cycles in which the transmitter current is delivered during a complete cycle (two signals of the same shape and polarity). **Multi-functional geophysical data processor, model 32^{II}. *** Other magnetic-field components, using a multiple receiver-loop system, are recently possible [e.g. Helwig et al., 2004].

Table 4.1: Summary of data acquisition parameters and specifications used in the Zonge Nano/ZeroTEM system.

The GDP-32^{II} applies a scheme of synchronous filtering, including anti-alias, digital powerline-notch and telluric filters, as well as SP buckout, to reject most of the broad-band natural EM and cultural noise. Furthermore, it sets a number of discrete time-windows, or gates, of finite width to measure the transient-decay amplitude after the applied current is turned-off. These gates are arranged logarithmically and controlled by changing the selected bandwidth. Normally, the transient-decay response changes rapidly at early times and more slowly at later times. To minimize the amplitude distortion, the early-time gates are set very narrow, later-time gates are set much wider [Zonge Engineering and Research Organization Inc., 2000]. Windowing is desirable since wider gates enhance the SNR at later-times.

Signals due to a positive pulse and the next negative pulse are then averaged, and considered to be one cycle. Signals can be averaged over as many as 1024 cycles to obtain an output-average for each gate. This is performed simultaneously over all gates so that the background noise is common to all gates at the time of measurement. Transient-decay data are stacked (statistically averaged) online to reduce the data quantity to a manageable size and to enhance the overall SNR. The standard deviations derived from the extensive stacking are usually used as weights in all inversion schemes. The acquisition software easily permits the data sets to be sampled, self-checked while recording and stored as time series in a solid-state memory. All data are in a block format and can be transferred digitally to any MS DOS-based PC via a serial interface. No further data processing is done in the field. Finally, the measured transients are automatically normalized at each sampling time from the output-current. Later on, they should also be normalized from the receiver-moment (the area times number-of-turns) to be given in units of V/Am².

In this recording fashion, the system has sufficiently early- to late-time information to be able to capture adequate TEM signals and to suppress instrumental and background noise problems. Sufficient early-time measurements usually result in a better resolution of shallow resistivity structures, and can be a determining factor in reducing the ambiguity caused by *model equivalence* in interpretation of geoelectric parameters for sufficiently-deep resistivity structures [Goldman *et al.*, 1994a].

Figure 4.3 shows the typical Nano/ZeroTEM transient-decay curves at the survey areas. Upon comparing the transients with their background noise amplitudes, it usually becomes clear that some data points need to be edited out to avoid erroneous resistivity models in the interpretation. Further quantitative data processing and interpretation can be carried in the time range between 2.03 μ s and 3.1 ms. Time-windows exceed this range are probably too noisy to use.

4.1.4 Data Deconvolution

As explained above, transient-decay Nano/ZeroTEM data are collected routinely using two different transmitter-current amplitudes and recording schemes. Although the composite-NanoTEM and ZeroTEM transients can be jointly interpreted [Helwig *et al.*, 2003], quantitative interpretation could be more efficiently undertaken if the whole data are converted to a unique form. This can be achieved by deconvolving the turn-off (ramp) time, i.e. system response, out of the measured signals.

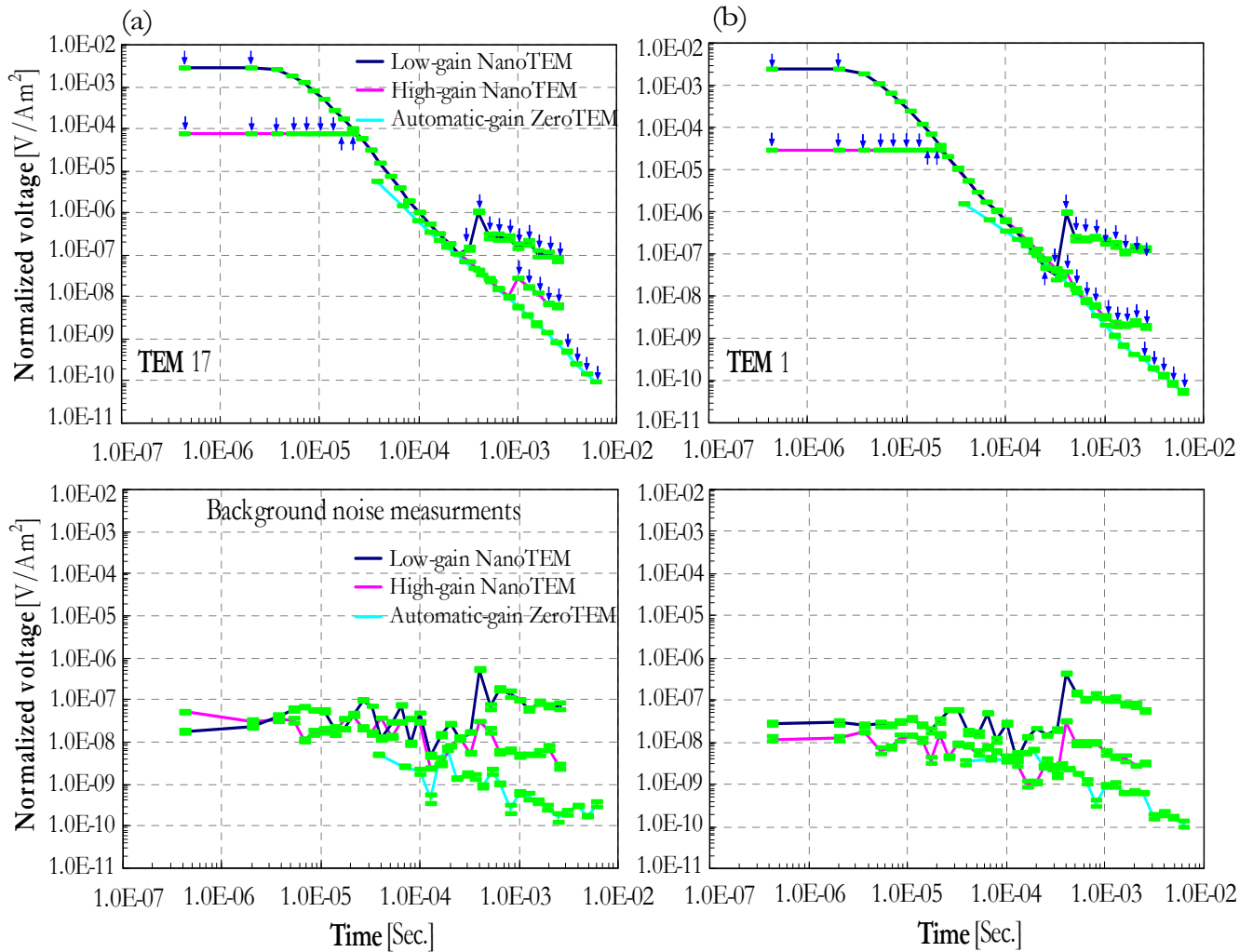


Figure 4.3: (Upper) Typical Nano/ZeroTEM transient-decay segments and (lower) their background noise measured at the survey areas: (a) 'Coal-covered Area', TEM 17 and (b) 'Sand-covered Area', TEM 1. The arrows mark the locations where the transient data are no longer reliable and must be edited out. The error bars describe the standard deviations derived from the extensive signal stacking.

Based on the simplifying assumption that the actual Nano/ZeroTEM ramp is fairly well-controlled, the transmitter-current waveform can then be approximated by a linear continuous-function. That means, the current is distributed uniformly over the intervening transition portion $-T \leq t \leq 0$ and has a time-derivative equals the negative reciprocal of T and zero elsewhere (Figure 4.4). In this case, the measured transient-decay (impulse) response can be represented as a convolution between the time-derivative of transmitter-current waveform $\partial I(t)/\partial t$ and pure-earth magnetic (step) response $h_z^*(t)$ [Nabighian and Macnae, 1991]. The process involves time-inversion (or folding) of $\partial I(t)/\partial t$ and its progressive sliding past $h_z^*(t)$. The individual terms in the convolution are then derived by summation of the cross-multiplication products over the overlapping parts of the two functions [Bracewell, 1978]. The convolution integral (filtered delta-function) can be given as

$$\partial h_z(t)/\partial t = \int_{-\infty}^{\infty} (\partial I(\tau)/\partial t) h_z^*(t-\tau) d\tau . \quad (4.6)$$

The pure-earth response can be given as the sum of decaying exponentials of discrete decay time-constants τ [Nabighian and Macnae, 1991], which may form suitable mathematical basis-functions for deconvolving TEM data to a standard form. Its series expansion is

$$h_z^*(t) = \sum_{k=1}^m a_k e^{-t/\tau_k}, \quad (4.7)$$

where a_k and τ_k are respectively the amplitude-coefficient and time-constant of k^{th} exponential basis-function. This characteristic constant is selected such as $\tau_1 < \tau_2 < \tau_3 < \tau_4 \dots < \tau_m$, $\tau_1 \ll t_1$ in logarithmic-domain and $\tau_m \approx t_n$ [Hanstein, 1992], where n is the maximum number of i^{th} time-window and m is the maximum number of the k^{th} pre-convolved base-function satisfying that $m < n$.

Substituting Equation (4.6) into (4.7), the integral which must be evaluated becomes thus

$$\partial h_z(t)/\partial t = 1/T \int_{-T}^0 \sum_{k=1}^m a_k e^{-(t-\tau)/\tau_k} d\tau'. \quad (4.8)$$

Equation (4.8) can be simplified further as

$$\underbrace{\partial h_z(t_i)/\partial t}_{y_i} = \sum_{k=1}^m a_k \underbrace{\left[\frac{\tau_k e^{-t_i/\tau_k} (e^{-T/\tau_k} - 1)}{T} \right]}_{G_{ki}} = \sum_{k=1}^m a_k G_{ki}, \quad (4.9)$$

where y_i is the measured transient-decay response at the i^{th} system time-window, G_{ki} is the amplitude of the k^{th} basis-function, corresponding to the k^{th} time-constant, sampled at the i^{th} system time-window. Here a_k is the amplitude-coefficient that the k^{th} basis-function is multiplied by to reconstruct the transient-decay response.

Equation (4.9) represents a linear-set of n equations in m unknowns (over-determined inverse problem, $n > m$), $\mathbf{y} = \mathbf{G}\mathbf{a}$. The left-hand side is the field transient-decay responses \mathbf{y} , which often includes a knowledge of measurement errors. In the right-hand side, \mathbf{G} is the sampled basis-functions constructed using the system waveform. Basis-function deconvolution involves solving the set of equations for the amplitude-coefficients \mathbf{a} , corresponding to each time-constant base, using the generalized inverse of \mathbf{G} , as $\mathbf{a} = (\mathbf{G}^T \mathbf{G}) \mathbf{G}^{-1} \mathbf{y}$. The pure-earth magnetic field is then calculated easily by substituting the a_k into equation (4.8). The deconvolution is non-unique because it depends on the range and number of time-constants pre-selected for the basis-functions [Helwig et al., 2003]. Noise amplification is also an additional fundamental problem in deconvolution. For numerical stability, the matrix \mathbf{G} is set to be tightly-scaled by two diagonal matrices such as $\mathbf{G}_n = \mathbf{W} \mathbf{G} \mathbf{D}^{-1}$, where \mathbf{W} whose elements $w_{ii} = 1/|y_i|$ to improve the condition-number of \mathbf{G} , and \mathbf{D}^{-1} whose elements $d_{jj} = (\sum_{i=1}^m g_{ij}^2)^{1/2}$ to guarantee equal data weighting. The mathematical-framework described above forms the basis of what may be described as *parameterized deconvolution* [Hanstein, 1992; Helwig et al., 2003].

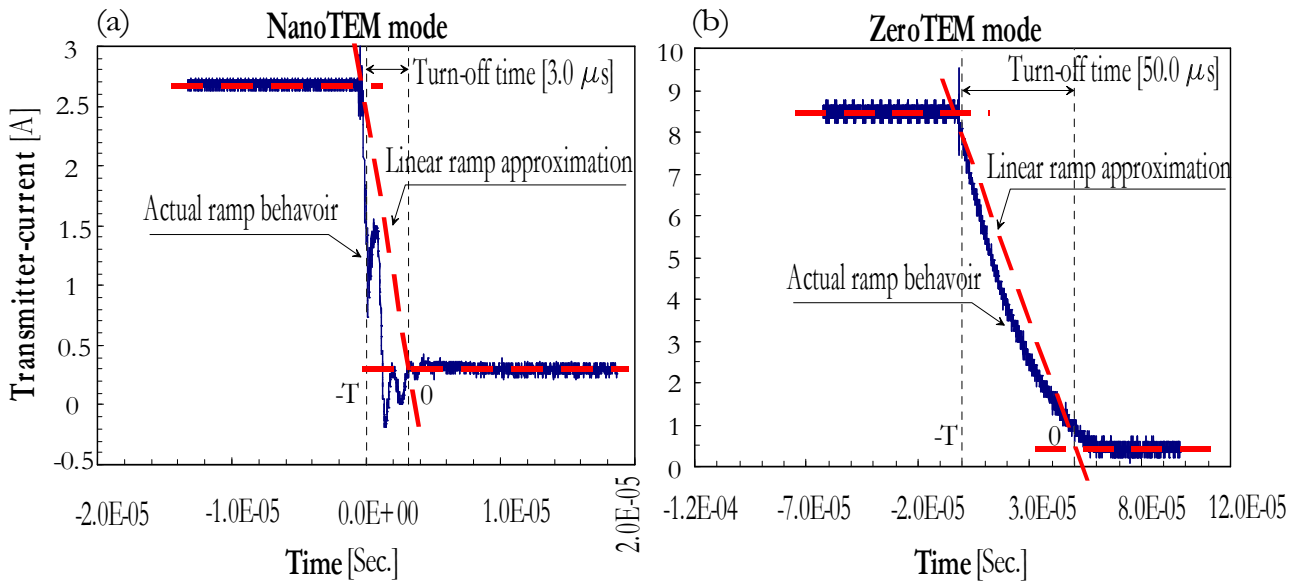


Figure 4.4: The actual transmitter-current waveforms of both (a) NanoTEM and (b) ZeroTEM investigation modes, which can be closely approximated by piecewise linear continuous-functions. Measurements are carried out at the sounding TEM 17, 'Coal-covered Area.'

Figure 4.5 shows the deconvolved TEM responses from its initial composite-NanoTEM and ZeroTEM transients for the control soundings at the survey areas. After carrying out the deconvolution, as explained above, restoring the pure-earth response is highly dependent on the earliest time-windows, and hence requires the transient-decay response to be finely sampled at earlier-time windows. Therefore, the first two or three ZeroTEM time-windows were usually not sufficiently perfect to restore the signal, and therefore should be edited out.

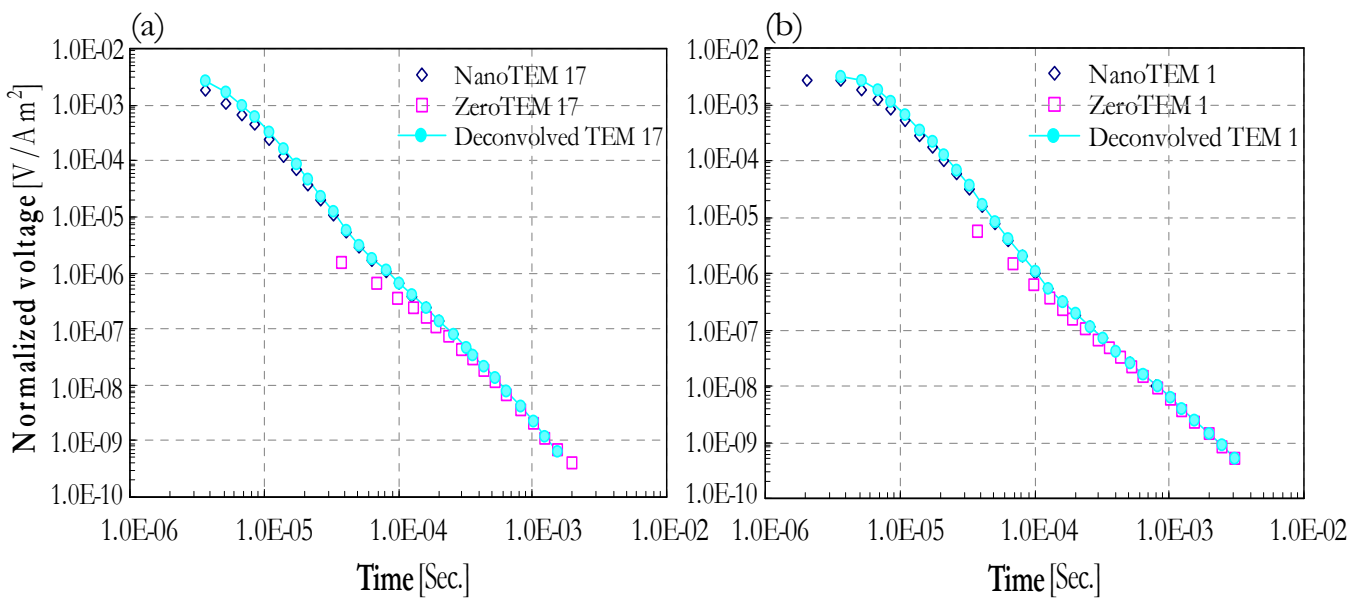


Figure 4.5: The deconvolved TEM responses from the initial composite-NanoTEM and ZeroTEM transients at the survey areas: (a) 'Coal-covered Area', TEM 17 and (b) 'Sand-covered Area', TEM 1. For better visualization the data are displayed without error bars.

4.1.5 Data Transformation

Quantitative interpretation of in-loop TEM soundings is often facilitated by transformation of the transient-decay response to apparent resistivity [Raiche, 1983]. It effectively normalizes for the theoretical variations in the response due to any dependent survey parameter over a fairly homogeneous half-space. The transformation is also well-behaved over an uniform horizontally layered-earth. Moreover, apparent resistivity transform parameterizes the response in units of an intrinsic rock property. Therefore, it can be used to obtain a qualitative indication of the ground-resistivity distribution [Nabighian, 1979], or may be used as reasonable starting model in the layered-earth inversion [Goldmann *et al.*, 1994a].

Apparent resistivity is traditionally defined as the resistivity of a homogeneous half-space which will produce the same transient-decay response $(\partial h_z / \partial t) / I$, over a broad time range, as that measured over the real earth with the same survey parameters [Spies and Eggers, 1986]. In other words, apparent resistivity is equal to the true ground resistivity only for the trivial case of a homogeneous half-space. If the ground is an uniform horizontally-layered earth, the apparent resistivity will vary with time in a distinctive manner, as is done for RMT soundings over a broad frequency range. The late-time apparent resistivity formulation [Ward and Hohmann, 1988] is defined as

$$\rho_a = \frac{I^{2/3} \mu_0 a^{4/3}}{20^{2/3} \pi^{1/3} t^{5/3}} \left[\frac{-\partial h_z}{\partial t} \right]^{-2/3} \quad (4.10)$$

Figure 4.6 (lower) shows the late-time apparent resistivity curves computed for the deconvolved transients, displayed on double-logarithmic axes along profile I for each survey area at the opencast mine 'Garzweiler I.' Because the definition of apparent resistivity is based mainly on the time behavior of the signal at late-time when it decays as $t^{-5/2}$. For this reason, all curves are characterized by a descending branch at earliest-times [Fitterman and Stewart, 1986], where the apparent resistivity is higher than the half-space resistivity. In the intermediate- and late-time stages this formulation behaves similarly. There are other apparent resistivity formulations which avoid this problem in the early-time stage [e.g. Spies and Eggers, 1986]. However, as long as the late-time apparent resistivity formulation is only applied to compare the field transients from different TEM soundings and to visualize their forward modeling or inversion responses, there would be no problem anymore.

4.2 Data Interpretation

4.2.1 Data Viewing

Coal-covered Area

The locations of all TEM sounding centers at the survey areas are accurately marked in Figure 1.3. Typical field transient-decay responses and the corresponding apparent resistivity curves at the survey areas are shown in Figure 4.6. At the 'Coal-covered Area', the transient-decay curves behave consistently. The small parallel differences in the apparent resistivity curves at early-time (Figure 4.6a) can be attributed to a gradual small thickness change of the shallow resistivity structures along the profiles from SW to NE.

Sand-covered Area

Here the transient-decay data contain the largest time range of approximately three decades. Their curve shapes are completely different from those at the 'Coal-covered Area.' The transient-decay responses for soundings TEM 1, 3 and 4 exhibit an abnormally upward shifting to higher amplitudes, particularly at earlier- and later-times (Figure 4.6b). A slight attenuation of their responses at intermediate-times can be seen. Note that their corresponding apparent resistivity curves approach 20 instead of 70 and 100 Ωm , as they should for the normal curves at earlier- and later-times respectively. Interestingly, highly-conductive surficial anomalies are already confirmed from the resultant 1D/2D RMT resistivity models, approximately underneath these abnormal soundings. Therefore, their odd-looking behavior is probably a result of corrupting the transient-decay data by highly-conductive surficial anomalies. On the other hand, the transient-decay responses of the rest soundings TEM 2, 5, 6, 7 and 8 (Figure 4.6b) decay with time smoothly, and show the typical curve shape at the area. *Newman* [1989] tried to explain the distorted transients which behaved differently, in a similar manner to the abnormal transients TEM 1, 3 and 4, when local near-surface conductors are present between the receiver- and transmitter-loops. He considered their enlarged amplitudes are a 3D EM effect.

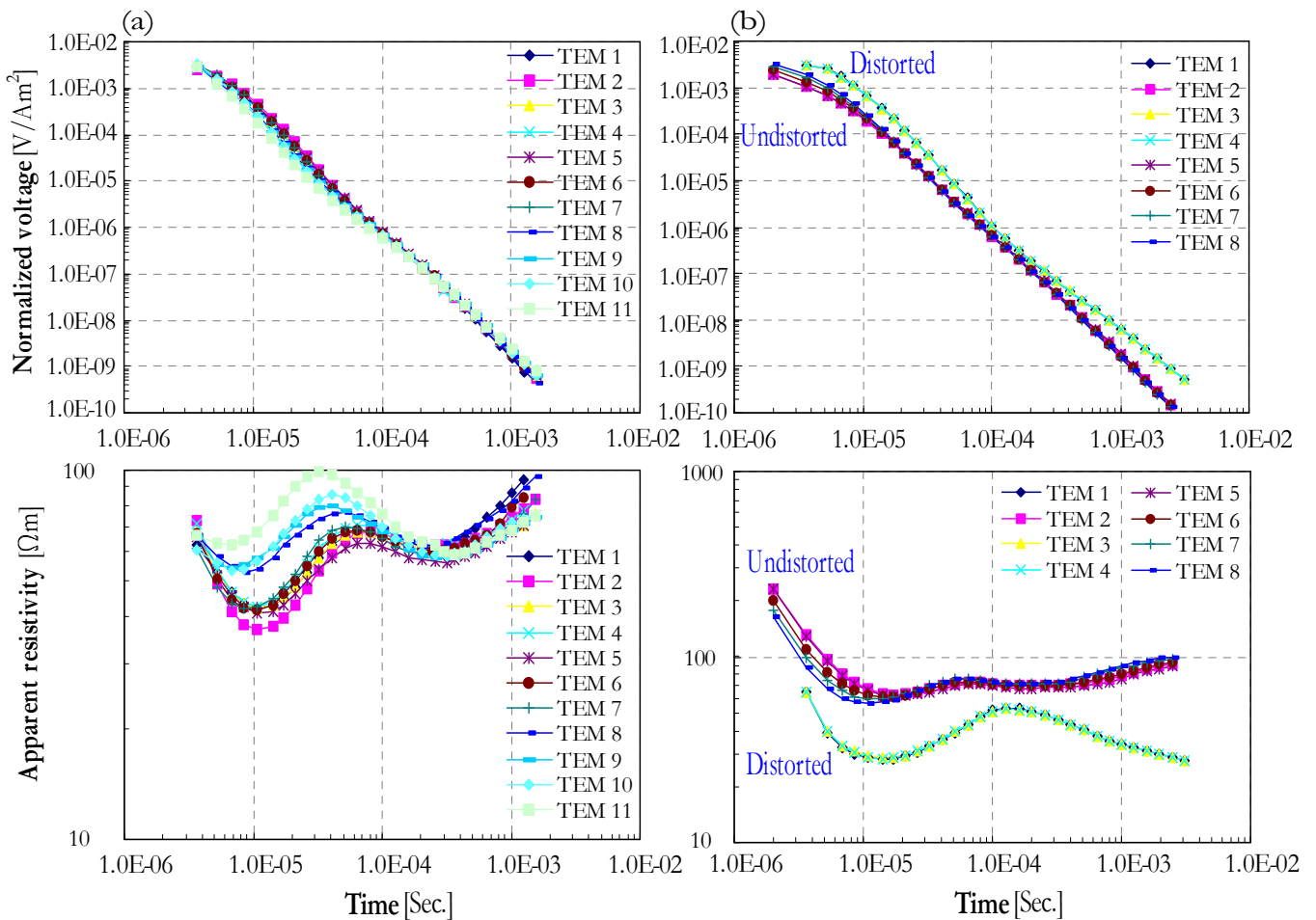


Figure 4.6: (Upper) A suite of transient-decay responses and (lower) the corresponding late-time apparent resistivity curves along profile I at each survey areas: (a) 'Coal-covered Area' and (b) 'Sand-covered Area.' For better visualization the data are displayed without error bars.

4.2.2 One-dimensional Inversion of Synthetic Data

In order to predict TEM responses at the survey areas and to determine how sensitive a real TEM survey would be for the target coal seams in some suggested earth models, forward calculations were performed over the reliable Nano/ZeroTEM time range. For each survey area, a detailed geoelectric model was first constructed based on layer thicknesses derived from the available stratigraphic-control boreholes (Figure 1.4) and average layer resistivities derived from the laboratory electrical measurements on rock samples (Table 5.2). The general model fashion comprises a layer-cake sequence, from top to bottom, of the conductive Garzweiler, Frimmersdorf and Morken Coals embedded in sufficiently resistive Surface, Neurath, Frimmersdorf and Morken Sands. The lowermost of the Neurath Sand between Garzweiler and Frimmersdorf Coals is less resistive, i.e. sand/silt, and Frimmersdorf Coal overlies a two-meter highly-conductive organic clay layer. The resistivities for the Morken Coal and Sand are being just a repeated image from the Frimmersdorf Coal and Sand respectively. Next, for the 'Sand-covered Area' model, a highly-conductive surficial clay layer was embedded within the Surface Sand and gradually replaced its thickness, from 0.0 to around 9.45 m, simulating the absence of clay to the complete sand-replacement by clay.

Starting from these models, three synthetic data sets were created by 1D forward calculations, and then inverted in terms of 1D smoothed-earth resistivity images [Constable, 1987]. 4% Gaussian noise that can be tolerated with the Nano/ZeroTEM system was added to the resulting synthetic data in order to artificially allow a realistic resolution assessment. The starting models chosen for all Occam's inversion runs were always average-apparent-resistivity homogeneous half-spaces, in which the number of layers is equal to the number of time-windows. Their thicknesses increase successively in the logarithmic-domain and were kept fixed during the inversion runs. In this model study, synthetic transients satisfy all data acquisition parameters and specifications for the Zonge Nano/ZeroTEM system.

Coal-covered Area

Figure 4.7 shows the smoothed-earth model and the responded apparent resistivities for the 'Coal-covered Area' synthetic data. The final inversion results fit the data within 0.99 RMS. We can see obviously that the only first four blocked-layers, i.e. Garzweiler Coal, Neurath Sand/Silt, Frimmersdorf Coal/Clay and Frimmersdorf Sand, are needed to explain the data. Distinguishing each blocked-layer into individual units would not be realized. The average resistivity for each blocked-layer was recovered fairly well by the inversion. The lower boundary of Frimmersdorf Coal/Clay is less well-determined, deviating more deeply, whereas Morken Coal is not recovered at all.

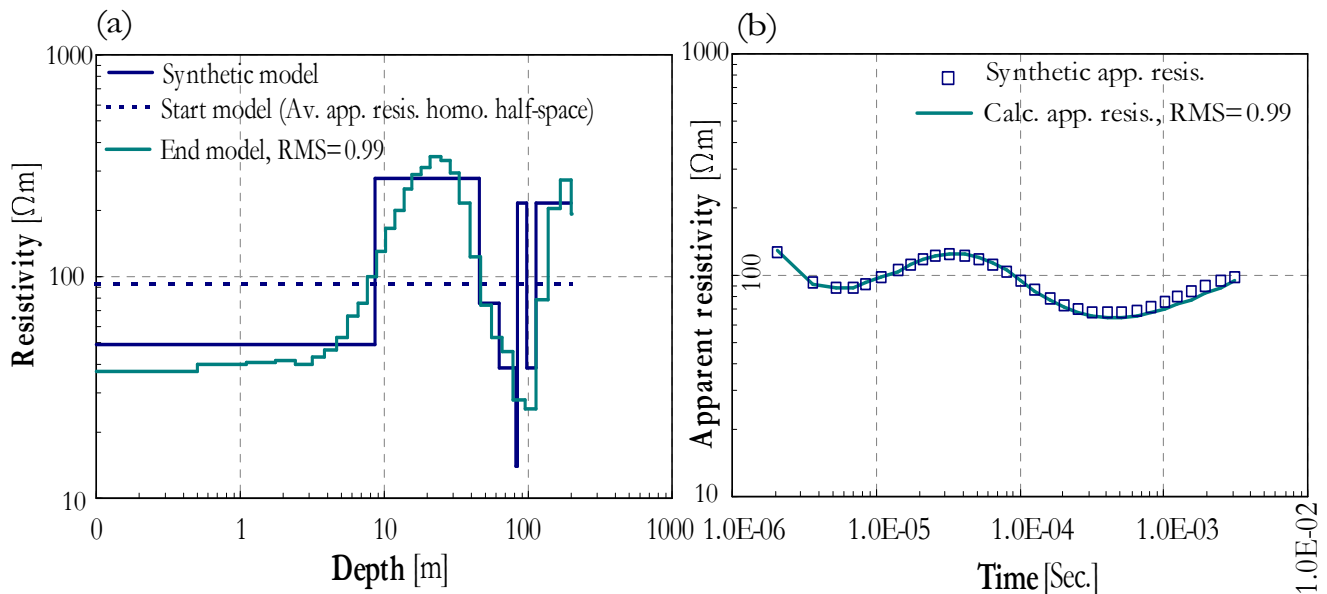


Figure 4.7: (a) 1D TEM smoothed-earth models and (b) the corresponding apparent resistivity curves of the 'Coal-covered Area' synthetic data.

Sand-covered Area

The apparent resistivity response of the smoothed-earth model fits the synthetic data with 2.12 RMS (Figure 4.8a). Similar to the 'Coal-covered Area', the data are quite sensitive to the previously-mentioned blocked-layers as well as to the Surface Sand. The recovered Surface Sand and Neurath Sand/Silt have essentially underestimated resistivities. The lower boundary of the Frimmersdorf Coal/Clay is less well-determined, deviating more deeply, whereas Morken Coal is not recovered at all.

The presence of a highly-conductive surficial clay layer within the clean Surface Sand, with a thickness of at least 2 m, drastically changes the smoothed-earth models at only the shallower depths (Figure 4.8b). The responded apparent resistivities, corresponding to different clay thicknesses, at earlier- to intermediate-times are all well-separated from each other and significantly different from that of undisturbed model. Whereas, the structures at deeper depths are almost the same, and their corresponding late-time branches of apparent resistivities are always ascending and closely following that of undisturbed model. This may indicate that the surficial clay layer can therefore be detected and resolved if a real TEM survey is conducted, but not uniquely because the shallower succession of the surficial clay and underlying Surface Sand and Garzweiler Coal appear as a moderately- to highly-conductive blocked-layer with increasing clay thickness. In other words, they are not resolved as individual units, but only as a whole.

It is worth mentioning that the minimum detectable clay thickness is within close proximity to the practical minimum diffusion-depths of the Nano/ZeroTEM time range. Surprisingly, the generated data are still rather sufficient to recover the underlying Neurath Sand/Silt and Frimmersdorf Coal fairly well. They have slightly underestimated and overestimated resistivities respectively, while their thicknesses are a little broadened. This also indicates that the negative contribution of the surficial clay layer gradually decreases with time and becomes insignificant at later-times and does not completely screen (or mask) the underlying conductive coal seams from being sounded. Furthermore, the model situation dictates that the resolution of TEM survey is poor for thin resistive layers, like the Surface Sand. Note that the data fit RMS decreases from 2.12 to 0.91 with increasing clay thickness.

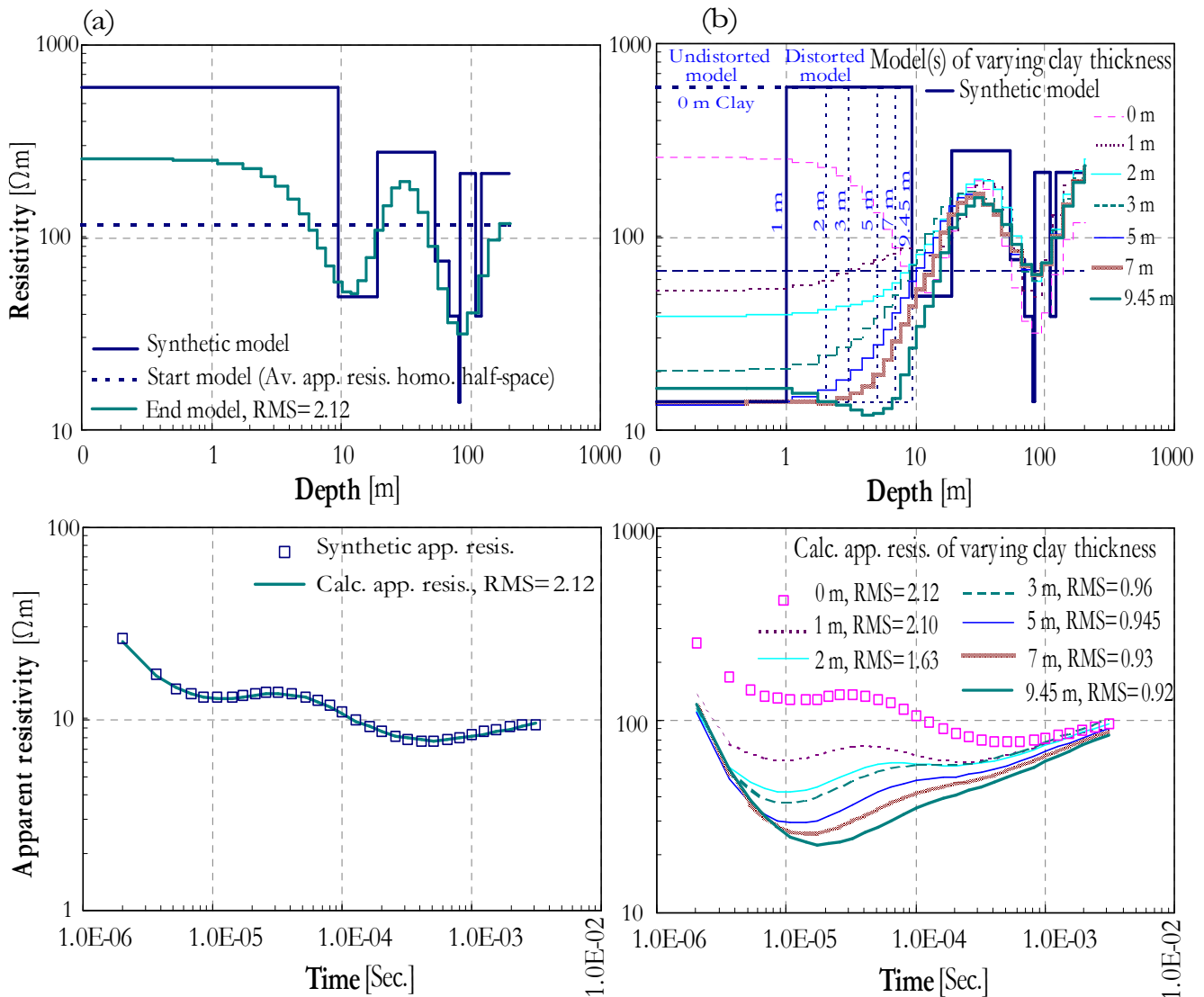


Figure 4.8: (Upper) 1D TEM smoothed-earth models and (lower) the corresponding apparent resistivity curves of the 'Sand-covered Area' synthetic data: (a) undisturbed model and (b) disturbed model(s) with a surficial clay layer of varying thickness.

4.2.3 One-dimensional Inversion of Field Data

The 1D inversion of the TEM data at each survey area was carried out using a standard scheme of successive techniques. No a-priori information was initially introduced. The data were first inverted in terms of 1D smoothed-earth models using average-apparent-resistivity homogeneous half-spaces as starting models, in which the number of layers is equal to the number of time-windows. Their thicknesses were increased successively in the logarithmic-domain, set to the average effective depth-of-investigation and kept fixed during the inversion. To drive a reasonable start model for further 1D full non-linear, layered-earth inversion [Inman, 1975; Jupp and Vozoff, 1975], Occam's inversion results were then blocked (or combined) such that a minimum structure is obtained. This least number of vertical layers is still well adapted to the intrinsic resolution capabilities of TEM data and preservative to the general trend of the borehole-geology. Applying the standard sensitivity (or resolution) analysis [Jupp and Vozoff, 1975; Jackson, 1972], typically for the best-fitted layered-earth model at each control sounding was very important, as it showed quantitatively how much confidence can be placed in that model.

Beginning from a control TEM sounding and using a kind of recursive starting modeling, which means that the output layered-inversion results of the previous sounding is used as starting model for the present sounding, the inverted section could be driven consistently and reasonably well with a resolution depth of approximately 100 m. This multi-sequential inversion is usually applicable where changes between soundings are gradational, but can grossly oversimplify the interpretation if these changes are abrupt [Hördt *et al.*, 1992b]. The individual inversion results from successive soundings, along each profile, were then assembled to create 2D pseudo-sections. These stitched sections were usually successful in determining any lateral resistivity variations present in the survey area. The final inversion statistics for the inverted layer parameters were used to cross-check their resolution in detail at each sounding. During all phases of the 1D inversion, one must make sure that the direct correlation to the borehole-geology was still reasonably maintained. However, the highly-conductive surficial anomalies at the 'Sand-covered Area', due to the presence of separate clay masses (or lenses) within the Surface Sand, broke down such interpretation scheme. In this case, to greatly improve the resistivity resolution for these surficial masses and for the underlying conductive coal seams, 3D modeling [Druskin and Knizhnerman, 1988] was additionally carried out.

Coal-covered Area

The smoothed-earth model obtained from Occam's inversion of measured data at the sounding TEM 17, close to the borehole 'WS1380', is shown in Figure 4.9. It clearly exhibits a distinct range of layer resistivities, corresponding to the Garzweiler Coal and Frimmersdorf Coal/Clay, which are responded as resistivity lows and known to be at these approximate depths. Their resistive background represents the Neurath Sand/Silt and Frimmersdorf Sand. The deepest Morcken Coal is beyond the depth-of-investigation of the present measurements and need not be considered. The final inversion results fit the data within 1.54 RMS.

Although the inversions were all carried out independently, Occam's results vary very little throughout each profile (Figure 4.10), with final data misfits ranged between 0.98 and 1.89 RMS. No remarkable local resistivity anomaly is encountered. This indicates that the 1D interpretation is very consistent and validated throughout the area and means that the general geoelectric model is essentially of 1D character. The two conductive coal seams are considered as marker layers within the whole vertical succession. Similar to the RMT inversion results, the Garzweiler Coal shows a gradual thickness decrease from SW to NE, while its resistivity is ranged from 15 to around 55 Ωm . Although the Frimmersdorf Coal seems somewhat too thick, its center is located reasonably well, as well as its resistivity is fairly homogenous and averaged approximately as 30 Ωm . The resistivity change from the Garzweiler Coal to Neurath Sand/Silt at about 10 m depth is more abrupt, whereas the resistivity contrast at the Frimmersdorf Coal–Sand interface at about 100 m depth is generally smooth. The Frimmersdorf Sand resistivity (from 60 to around 150 Ωm) is far less than the Neurath Sand/Silt resistivity (from 100 to around 450 Ωm), but still slightly greater than the Frimmersdorf Coal/Clay resistivity.

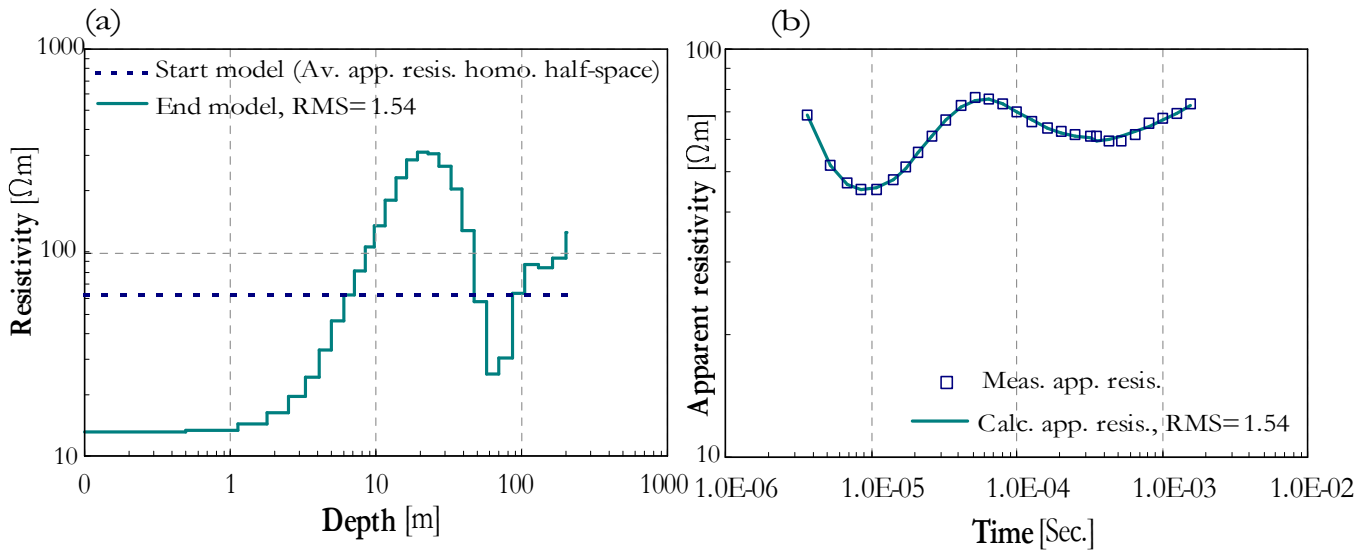


Figure 4.9: (a) 1D TEM smoothed-earth models and (b) the corresponding apparent resistivity curves of the sounding TEM 17 at the 'Coal-covered Area.'

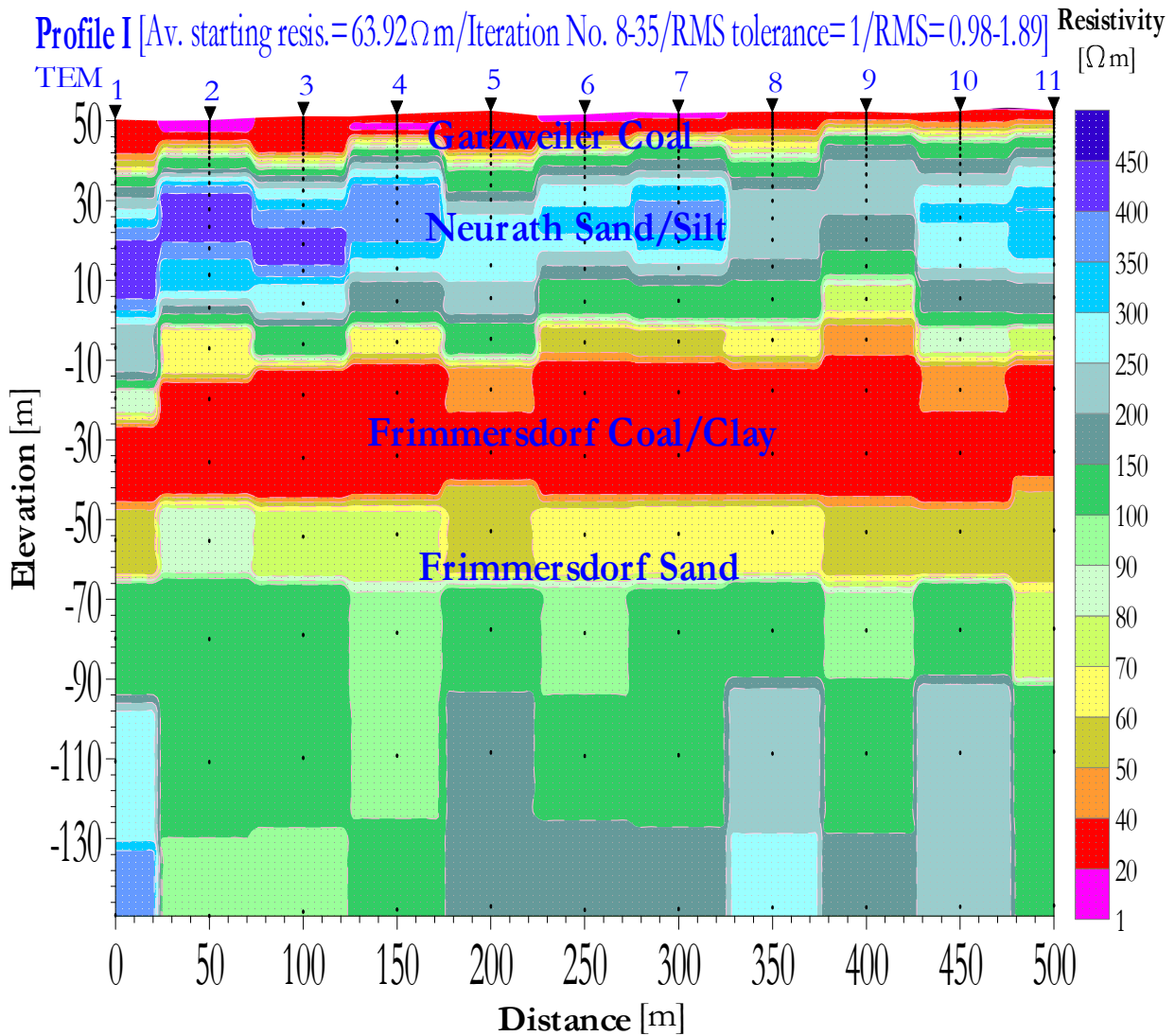


Figure 4.10: Stitched 1D TEM smoothed-earth inverted sections below profiles I, II, III and IV at the 'Coal-covered Area.' Warm colors indicate resistivity lows, while cold colors indicate resistivity highs.

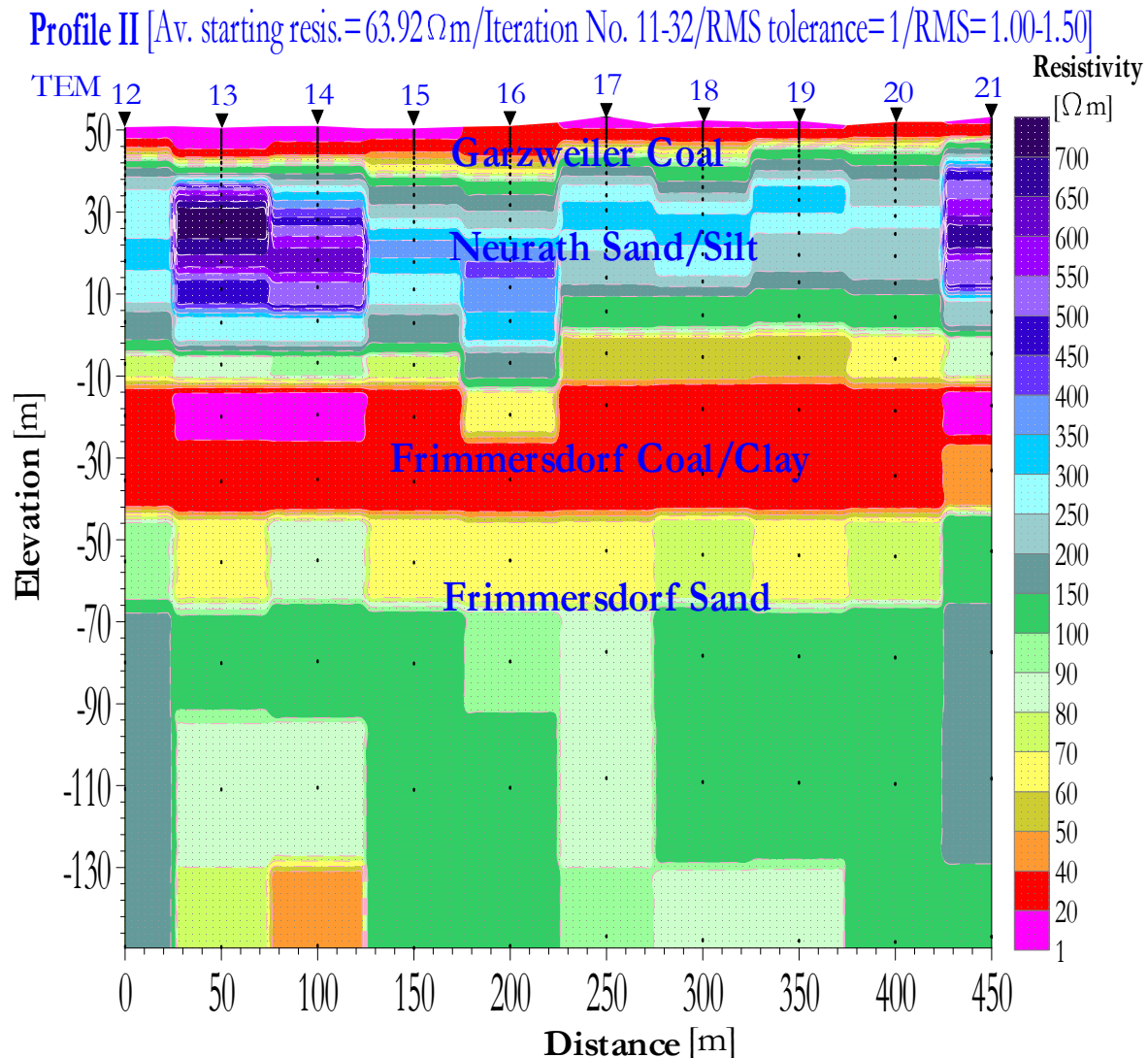


Figure 4.10: (Continued.)

The layered-earth inversion results at the sounding TEM 17 show that the least number of layers, which best represents the transient-decay data, are four blocked-layers with a final data fit of 1.44 RMS (Figure 4.11), while the correlation with the borehole-geology is still satisfied. It is obvious that the inversion closely maintained the starting model, which was derived from the Occam's blocked-layers. The estimated error bounds of the inverted model parameters are sufficiently small, and do not greatly increase with depth, indicating that the TEM signal is still able to accurately resolve the lower boundary of the Frimmersdorf Coal/Clay with increasing time.

Figure 4.12a displays the typical relative sensitivity behavior for the inverted layer parameters throughout the whole time range of the sounding TEM 17. The layer parameters of the Garzweiler Coal dominate the data strongest at the earlier-times and their influences decay sharply with time. The derivatives with respect to its resistivity and to its thickness change simultaneously in two different directions. This indicates a high negative correlation has to be expected and means that just a combination of the parameters could be resolved and neither of them independently. The layer parameters of the Neurath Sand/Silt are positively correlated, its thickness influences the TEM signal very well at the early- to intermediate-times. Beyond this, the derivative amplitudes of its resistivity are almost much smaller than all other amplitudes, and thus contribute to the data very little. Later on, from intermediate- to late-times, the layer parameters of the Frimmersdorf Coal/Clay dominate the data strongly with a

moderate negative correlation. Lastly, the Frimmersdorf Sand resistivity is resolved at the later-times with moderate derivative amplitudes.

When inspecting the damping factors, or importances, of the inverted layer parameters at all soundings, it becomes clear that none of the conductive coal seams are poorly resolved (Figure 4.12b). The derived values for almost all thicknesses and resistivities of the conductive coal seams, as well as of the resistive sand units, ranged between 0.88 and 0.53, indicating that they are well- to moderately-resolved. Only the Neurath Sand/Silt resistivity shows a poor to moderate resolution, its importance value is usually around 0.3.

Profile III [Av. starting resis.=63.92 Ω m/
Iteration No. 13-31/RMS tolerance=1/RMS=0.99-1.50] **Profile IV** [Av. starting resis.=63.92 Ω m/
Iteration No. 12-28/RMS tolerance=1/RMS=1.0-1.45]

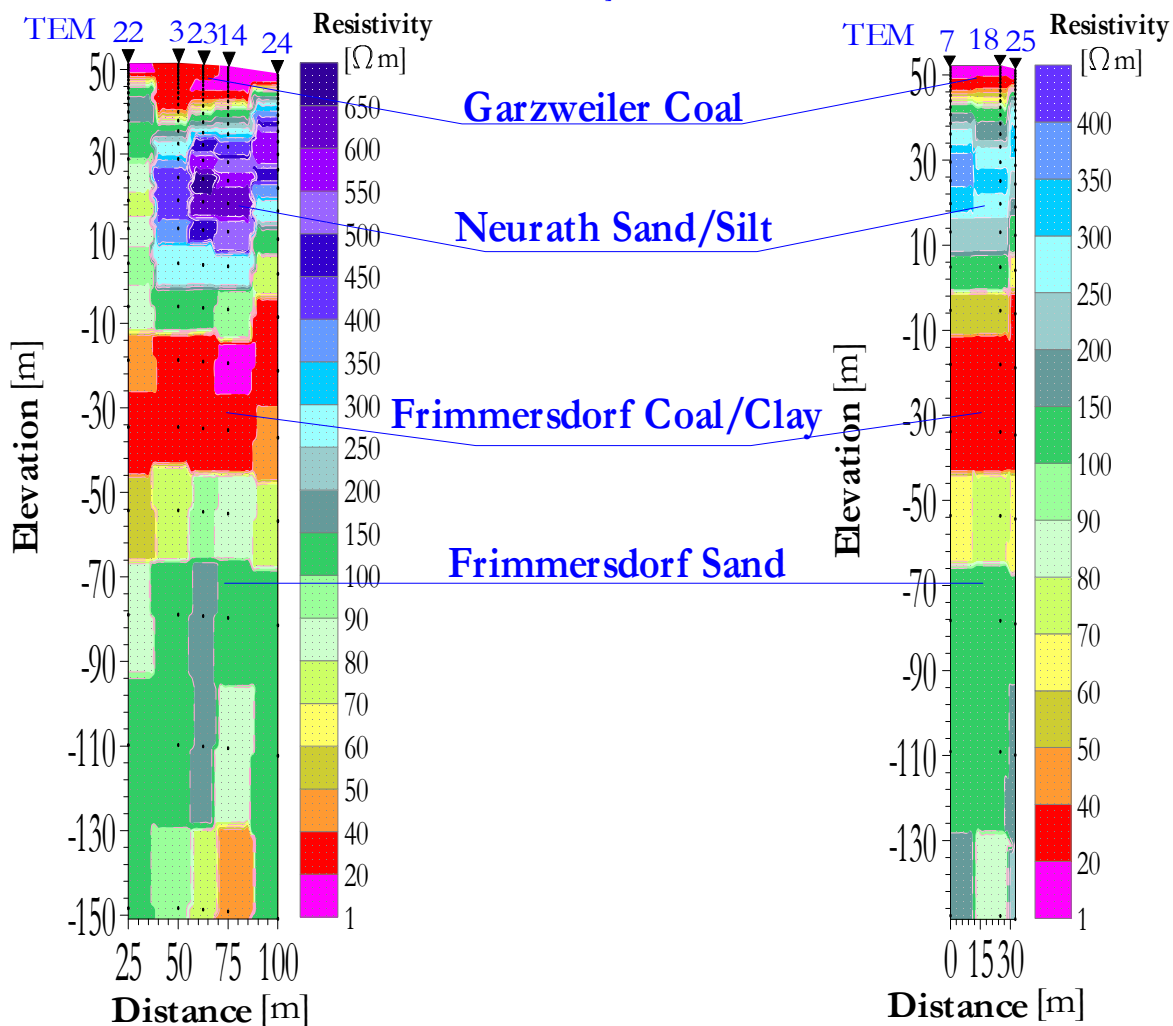


Figure 4.10: (Continued.)

The final 1D TEM layered-earth inverted sections at the 'Coal-covered Area' seem to be readily very consistent and geologically reasonable (Figure 4.13). The data misfits are ranged between 0.97 and 1.88 RMS respectively (Figure 4.12c). Both the Garzweiler Coal and Frimmersdorf Coal/Clay are normally responded as resistivity lows, their resistivities are averaged as 23 and 20 Ω m respectively. Whereas, their resistive background exhibits average resistivities of about 289 and 134 Ω m, corresponding to Neurath Sand/Silt and Frimmersdorf Sand respectively. Note that inverting with models having more (or less) than four layers resulted in a satisfactory data fit too, but the resulting models were justified neither by statistical analysis nor by correlation with the borehole-geology.

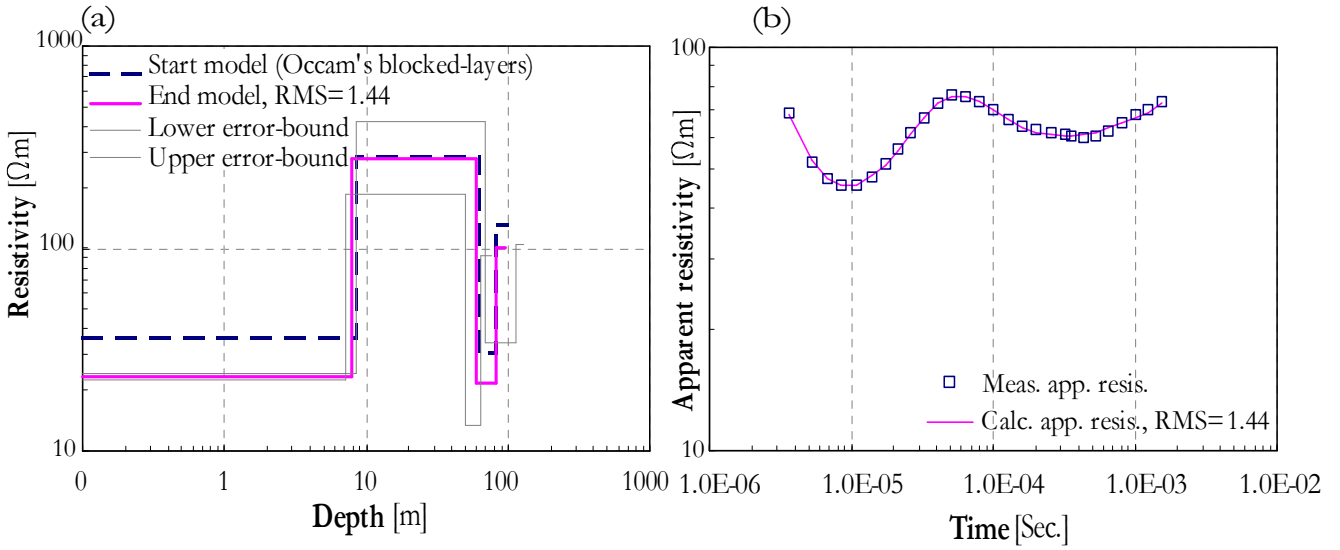


Figure 4.11: (a) 1D TEM layered-earth model and (b) the corresponding apparent resistivity curve of the sounding TEM 17 at the 'Coal-covered Area.'

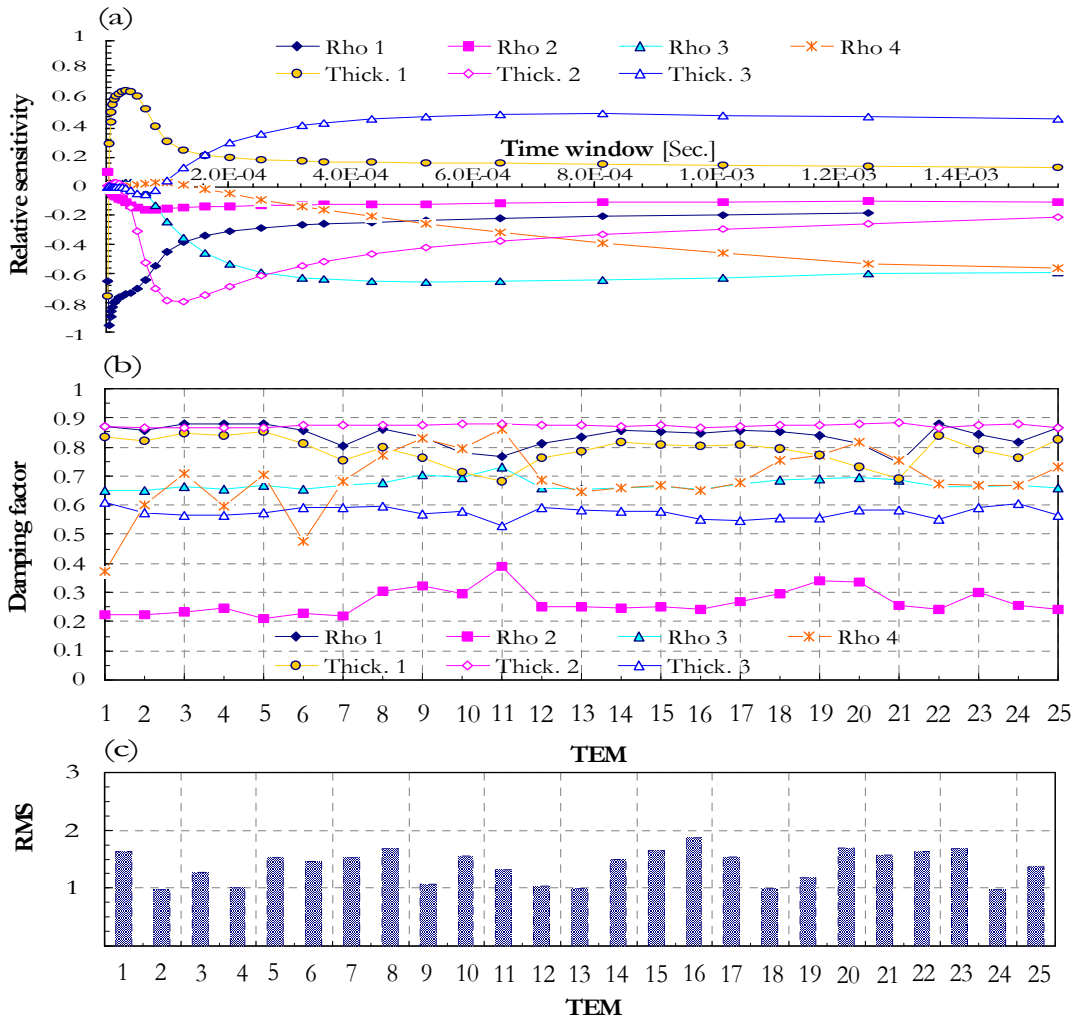


Figure 4.12: (a) Relative sensitivity for the inverted layer parameters throughout the whole time range of the sounding TEM 17, (b) the damping factors of these layer parameters at all soundings, and (c) a histogram of the RMS misfit values of all soundings at the 'Coal-covered Area.'

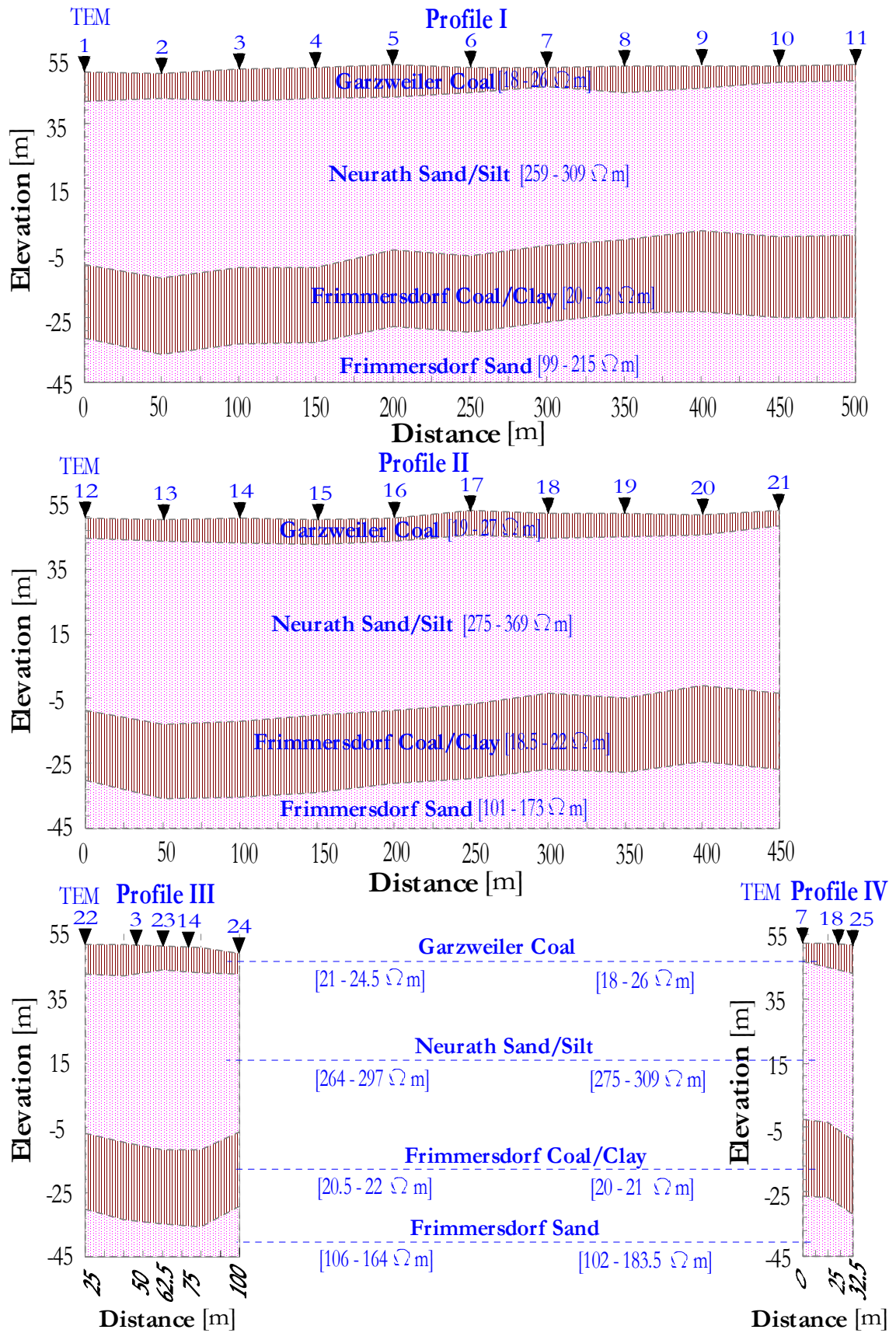


Figure 4.13: Stitched 1D TEM layered-earth inverted sections below profiles I, II, III and IV at the 'Coal-covered Area.'

Sand-covered Area

Models for different RMS thresholds obtained from Occam's inversion of transient-decay data at soundings TEM 1 and 2, close to the borehole 'WS 1452', are shown in Figure 4.14. The inversion results would be completely different at each sounding. Sounding TEM 2 clearly exhibit two conductors, interpreted as the Garzweiler Coal and Frimmersdorf Coal/Clay, which are known to be at these approximate depths. The fairly resistive sand background comprises the Surface Sand, Neurath Sand/Silt and Frimmersdorf Sand. The end inversion results fit the data within 1.10 RMS and, generally, the coal–sand boundary is not accurately resolved as the RMS threshold increases. Interesting is the appearance of an anomalously highly-conductive surficial layer in the end model of the sounding TEM 1, that is always necessary to obtain a reasonable data misfit of about 1.22 RMS. This surficial layer is interpreted as a separate clay mass within the clean Surface Sand. The model is changed drastically throughout the iterations, and greatly shifted downwards with almost constant throw between 18 and 20 m. The lower boundary of the Frimmersdorf Coal/Clay is not readily resolved, but it appears normally conductive.

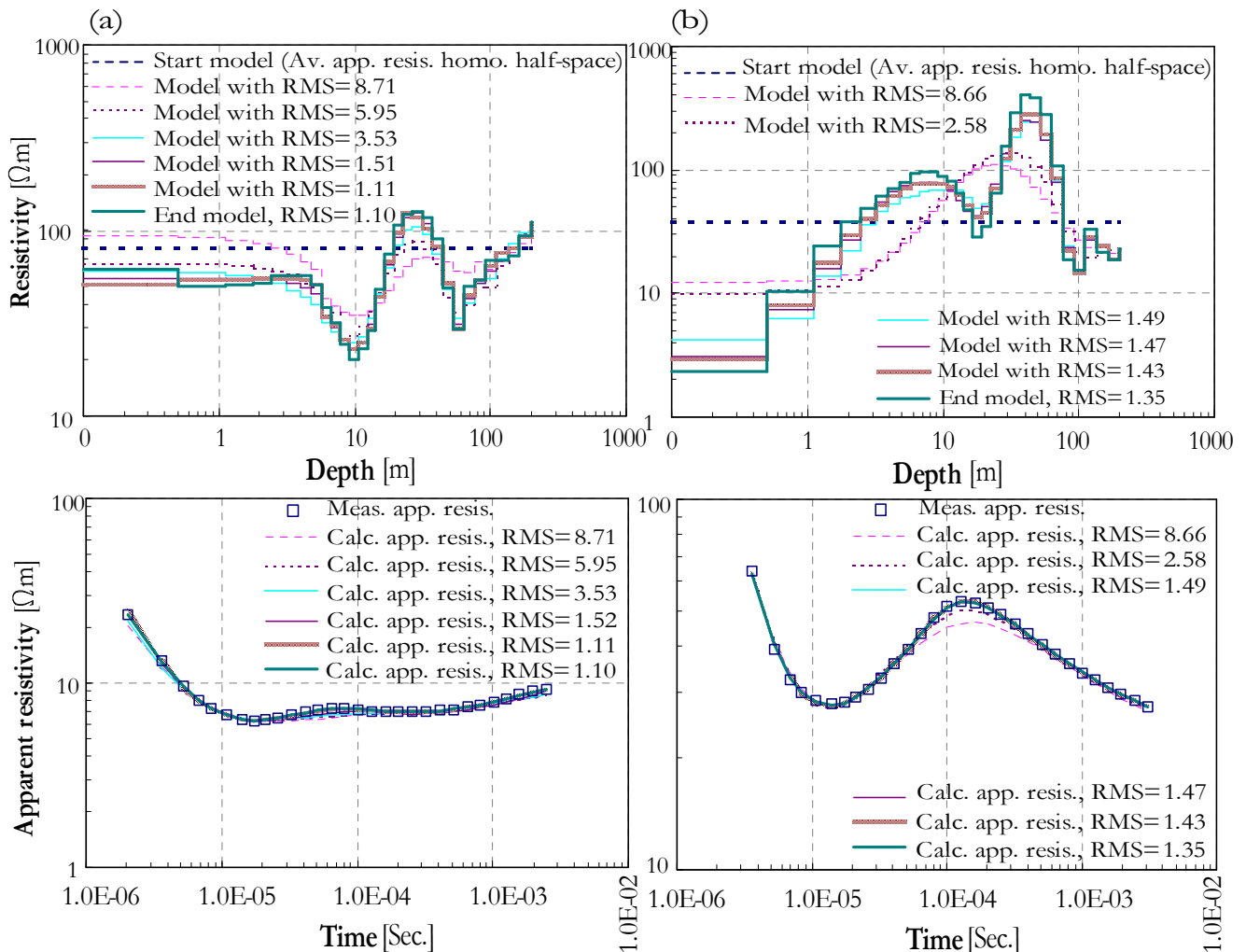


Figure 4.14: (Upper) 1D TEM smoothed-earth models and (lower) the corresponding apparent resistivity curves, at different RMS thresholds, of soundings (a) TEM 2 (undistorted) and (b) TEM 1 (distorted) at the 'Sand-covered Area.'

Collectively, the Occam's inversion results are not consistent along the whole profile (Figure 4.15). The results at soundings TEM 2, 5, 6, 7 and 8 belong to the consistent part of the profile, which still has almost 1D character and correlate satisfactory with the borehole-geology, with final data misfits ranged between 0.97 and 1.12 RMS. The Garzweiler Coal

gradually dips from east to west, while its resistivity is averaged as 25 Ωm . The boundaries of the Frimmersdorf Coal are as wide as the approximate thickness known for it, but its center is determined reasonably well. Its resistivity exhibits a limited range from 30 to 55 Ωm . The resistivity of the Frimmersdorf Sand is ranged from 55 to around 175 Ωm , while that of Neurath Sand/Silt is between 80 and 250 Ωm . Generally, the resistivity change from sand to coal is smooth. On the other hand, the inversion results from the soundings TEM 1, 3 and 4 neither agree with neighboring-sounding results nor correlate with the known borehole-geology. This supports that their data may be distorted by highly-conductive surficial anomalies.

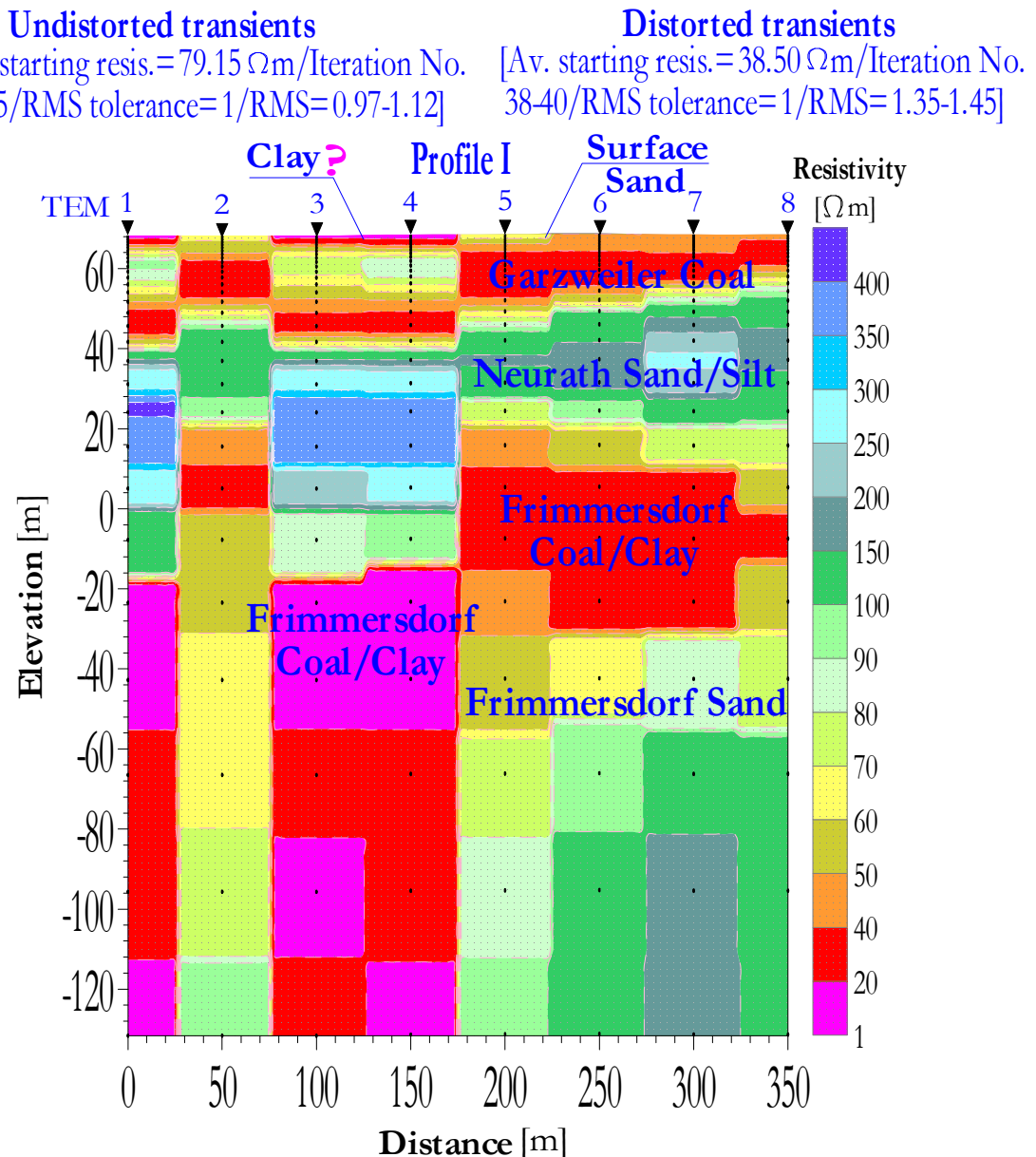


Figure 4.15: Stitched 1D TEM smoothed-earth inverted section below profiles I at the 'Sand-covered Area.' Warm colors indicate resistivity lows, while cold colors indicate resistivity highs.

Their final data fits are rather less worth than those of undistorted transients, ranged from 1.35 to 1.45 RMS, but still accepted. The earth model along this inconsistent part suffers from a significant bias to deeper depths probably due to the presence of these surficial clay masses, which have about 3 to 20 Ωm resistivity. The moderately-resistive Surface Sand has about 50 to 90 Ωm resistivity. The Frimmersdorf Coal seems to be somewhat thinner, while its average

resistivity is normally averaged as 25 Ωm . The resistivity change from sand to coal is generally more abrupt, particularly between Neurath Sand/Silt and Frimmersdorf Coal/Clay. A monotonic downward resistivity decrease is generally started from the upper boundary of Frimmersdorf Coal/Clay, leaving its lower boundary undefined.

Taking into account a surficial clay layer of about 3 m depth at the distorted soundings, the starting model thicknesses for further 1D layered-earth inversion were adjusted from the available borehole 'WS 1452.' The inversion results at soundings TEM 1 and 2 show that the least number of layers which best represents the transient data are five blocked-layers with final data misfits of 1.97 and 1.15 RMS respectively (Figure 4.16). The inversion closely maintained the starting model, which was derived mainly from the Occam's blocked-layers. For the sounding TEM 2, the error bounds of the inverted model parameters are sufficiently small and do not greatly increase with depth, indicating that the TEM signal is still able to accurately resolve the lower boundary of the Frimmersdorf Coal/Clay with increasing time. For the sounding TEM 1, the most inverted layer parameters are unbounded, particularly the layer thicknesses, yet the feeling of poor confidence in the 1D interpretation never left. The increased error bound size with depth is primarily due to decreasing the TEM signal resolution with increasing time.

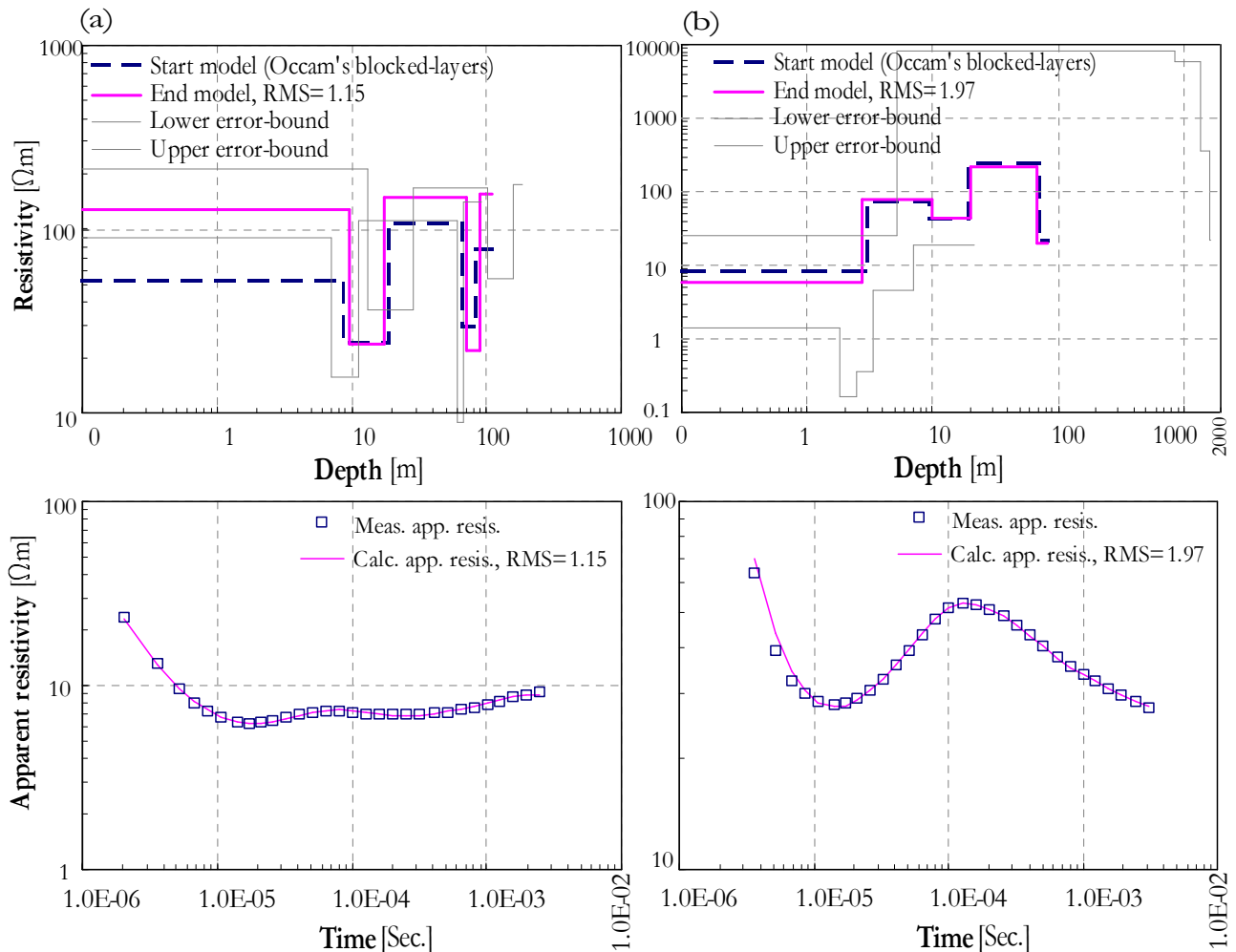


Figure 4.16: (Upper) 1D TEM layered-earth models and (lower) the corresponding apparent resistivity curves of the soundings (a) TEM 2 (undistorted transient) and (b) TEM 2 (distorted transient) at the 'Sand-covered Area.'

Figure 4.17a displays the typical relative sensitivity behaviors for the inverted layer parameters throughout the whole time ranges of soundings TEM 1 and 2. For the sounding TEM 2 (Figure 4.17a, upper), the layer parameters of Surface Sand dominate the data strongest in the very beginning, their influences decay sharply at the earliest time-windows. Immediately after their influences started to decay, the domination of Garzweiler Coal parameters starts strongly and decays slowly throughout the earlier- to intermediate-times. As both derivative curves have clearly different directions, the parameters should not be resolved independently. Simultaneously, the layer parameters of the Neurath Sand/Silt are positively correlated and influence the TEM signal moderately throughout the intermediate-times. Later on, from intermediate- to late-times, the Frimmersdorf Coal/Clay parameters dominate the data almost constantly with moderate derivative amplitudes. But, as both derivative curves have clearly different directions, just a combination of the parameters can be resolved and neither of them separately. Lastly, the Frimmersdorf Sand resistivity is resolved at the later-times and seems to be closely correlated to the Frimmersdorf Coal/Clay resistivity.

For the sounding TEM 1 (Figure 4.17a, lower), most of layer parameter pairs are negatively correlated, but by different degrees. The layer parameters of the surficial clay layer dominate the data strongest at the earlier-times and their influences decay sharply with time, whereas those of the Surface Sand show very low derivative amplitudes. This can be understood from the physical consideration, because the magnetic field only depends on the horizontal current flow, which penetrate into the ground through inductive coupling and is not strongly influenced by thin resistive layers like Surface Sand. The layer parameters of the Garzweiler Coal dominate the data moderately at earlier-times and their influences decay sharply with time too. Beyond this, the layer parameters of Neurath Sand/Silt are positively correlated, its thickness influences the TEM signal very well at the early- to intermediate-times, while its resistivity contributes to the data very little. This means again that the data have a little sensitivity to the changes of Neurath Sand/Silt resistivity. Later on, from intermediate- to late-times, the Frimmersdorf Coal/Clay resistivity strongly dominates the data with high derivative amplitudes.

Inspecting the damping factors of the inverted layer parameters along the consistent part showed clearly that none of the conductive coal seams are poorly resolved (Figure 4.17b). The derived values for almost all thicknesses and resistivities of the conductive coal seams, as well as for the resistive sand units, ranged between 0.88 and 0.40. This shows that they are well- to moderately-resolved. Along the inconsistent part, the resistivity of the surficial clay masses and underlying coal seams are fairly well-resolved, while their thicknesses are moderately-resolved. Both the Surface Sand and Neurath Sand/Silt resistivities showed an unusual poor resolution, their importance values are usually below 0.2. The thickness of the Surface Sand is poorly-resolved, while that of Neurath Sand/Silt exhibits high importance value.

The final 1D TEM layered-earth inverted section at the 'Sand-covered Area' (Figure 4.18) seems to be sufficiently consistent and geologically reasonable. The data misfits are ranged as 0.86 to 1.21 and 1.65 to 1.99 RMS for both the undistorted and distorted soundings respectively (Figure 4.17c). The earth model underneath the distorted soundings clearly shows the presence of highly-conductive surficial masses, with a thickness close to 3 m and resistivity of only about 6 Ωm . The model still bears a striking resemblance to the results from neighboring undistorted soundings. Both the Garzweiler Coal and Frimmersdorf Coal/Clay are responded as resistivity lows, their resistivities averaged as 33 and 23 Ωm respectively. The resistive background exhibits average resistivities of about 92, 199 and 149 Ωm , corresponding to Surface Sand, Neurath Sand/Silt and Frimmersdorf Sand respectively. Note that all attempts to invert the data in terms of models having more (or less) than five layers were statistically unsuccessful and not justified by correlation with the borehole-geology.

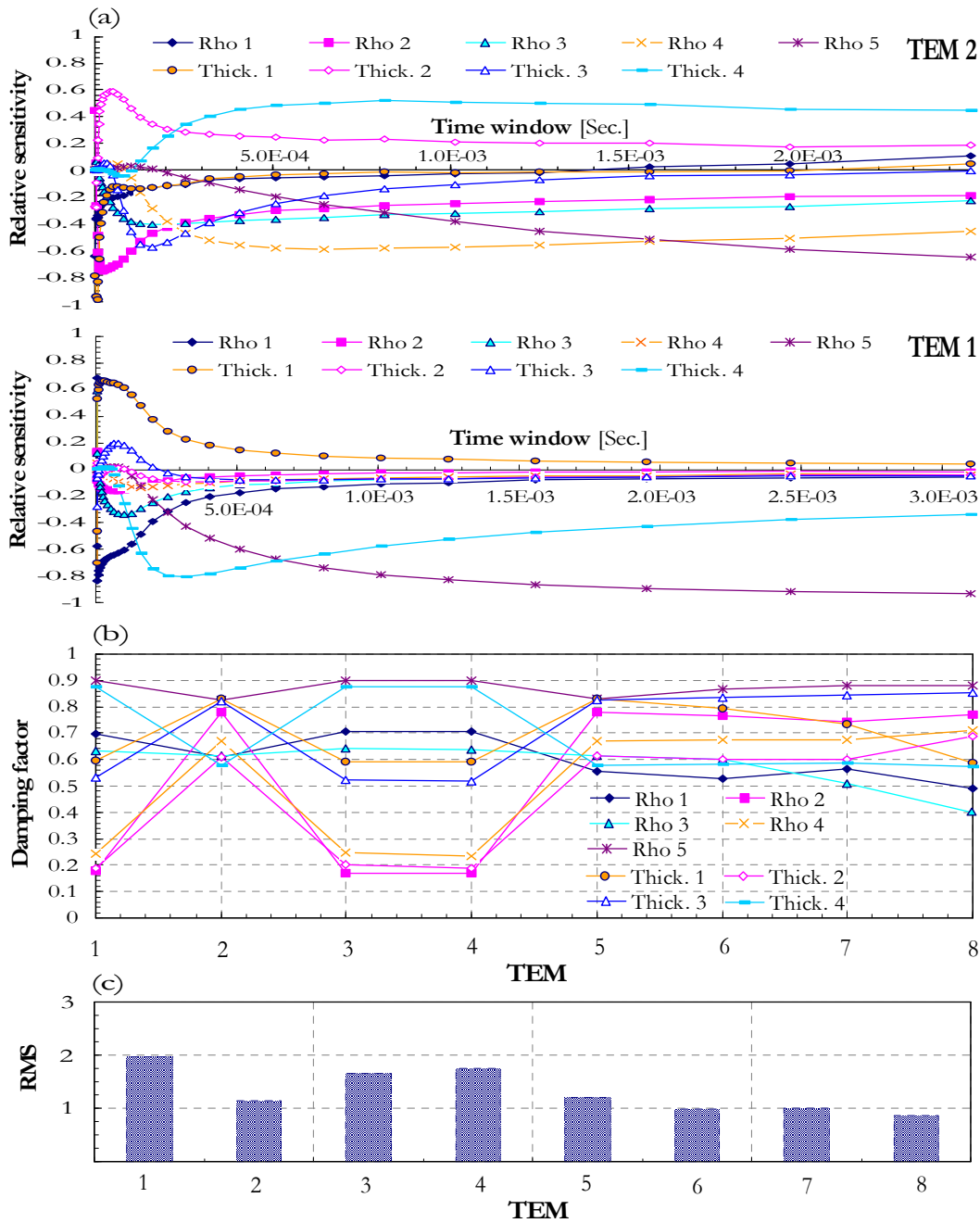


Figure 4.17: (a) Relative sensitivity for the inverted layer parameters throughout the whole time range of the sounding TEM 17, (b) the damping factors of these layer parameters at all soundings, and (c) a histogram of the RMS misfit values of all soundings at the 'Coal-covered Area.'

Contrary to the 1D inversion results from synthetic data, the presence of a real surficial clay layer (or mass) within the clear Surface Sand always results in a shifting of the deep-layering and delaying the transient at later-times. Therefore, the lower boundary of the Frimmersdorf Coal/Clay is clearly undefined at the distorted soundings. Moreover, most of layer parameters do not show sufficiently high importance values as usual. The main discrepancy between 1D inversion results from synthetic and field data will be declared in Section 4.2.5. During it, however, an important foremost question must be addressed: how deep the lower boundary of Frimmersdorf Coal/Clay may lie, and yet give a detectable EM anomaly on the ground surface?

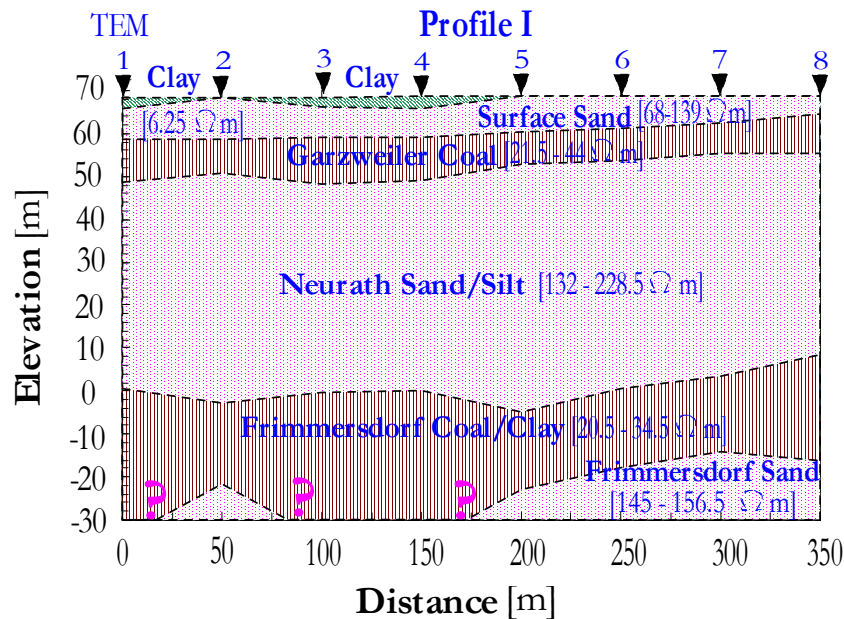


Figure 4.18: Stitched 1D TEM layered-earth inverted section below profiles I at the 'Coal-covered Area.'

4.2.4 One-dimensional Joint-inversion of RMT and TEM Field Data

Because the RMT data are usually skin-depth limited, they only provide information about the shallow resistivity structures. The TEM data still have sufficiently early- to late-time information, and therefore result in a flexible resolution of shallow to sufficiently-deep resistivity structures. A significant resolution improvement for the shallow resistivity structures would be expected when jointing both of them in the 1D layered-earth inversion scheme. Impressively, in most field cases [e.g. Hördt *et al.*, 1992b; Eckard, 1993; Tezkan *et al.*, 1996; Steuer, 2002], it was pointed out that the joint-inversion results of RMT and TEM data are usually unbiased and more reliable than those of individual inversions.

At the 'Coal-covered Area', the differences in the estimated Garzweiler Coal thickness, derived from individual RMT and TEM inversions at the same sounding centers, are generally ranged between 0.30 and 1.85 m. Only along profile III, they may approach 2.75 m. At the 'Sand-covered Area', where both the individual RMT and TEM models are agreed, the differences in the estimated thicknesses of surficial clay masses, Surface Sand and Garzweiler Coal are ranged between 0.30 and 2.05 m. Although these differences seem to be significant, their cause is not clearly known, but they could be attributed to the limited resolution of the TEM data themselves. Beyond this, the estimated RMT and TEM resistivities are quite comparable to each other and show a satisfied correlation with those typically obtained from the laboratory measurements (see Section 4.3).

Unfortunately the most promising way of inverting the RMT and TEM data jointly turned out to be unnecessary. This is either due to the close resemblance between the shallower skin- and diffusion-depths for the higher RMT frequencies and earlier TEM sampling times respectively or because the model inconsistency between both data sets. Thus, the joint-inverted layered-earth models at the 'Coal-covered Area' (Figures 4.19a) are almost similar, if not identical, to those obtained from the individual TEM inversion. They are slightly deviated from the individual TEM inversion models at the 'Sand-covered Area' (Figures 4.19b), particularly at shallower depths, where the correlation with the known borehole-geology becomes less satisfactory.

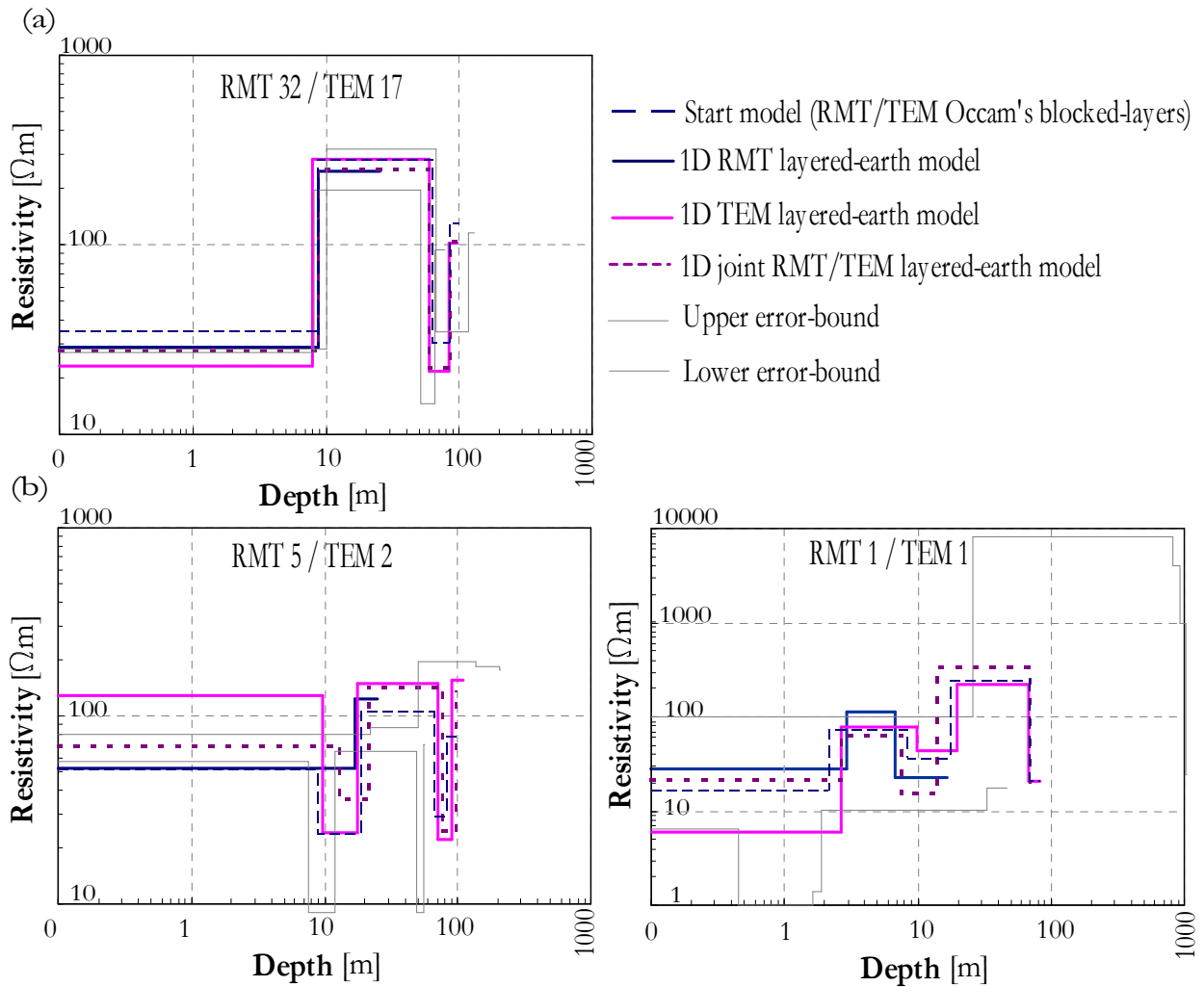


Figure 4.19: The 1D joint-inverted layered-earth models at the control soundings of the survey area: (a) RMT 32/TEM 17 at the 'Coal-covered Area', and (a) RMT 5/TEM 2 (undistorted) and RMT 1/TEM 1 (distorted) at the 'Sand-covered Area.'

Moreover, there is no significant resolution improvement achieved, where sensitivity analyses for the joint-inverted layer parameters at the control soundings and their importances at all soundings remain almost unchanged (compare Figures 4.12 and 4.17 with Figures 4.20 and 4.21 respectively). Although the use of 1D RMT–TEM joint-inversion slightly narrows the equivalent model ranges, it greatly worsens the final data fits. Not that the final correlation of surface EM with laboratory-based resistivity models shall only consider the individual 1D/2D RMT and 1D/3D TEM resistivity models, the 1D RMT–TEM joint-resistivity models need not be discussed (see Section 4.3).

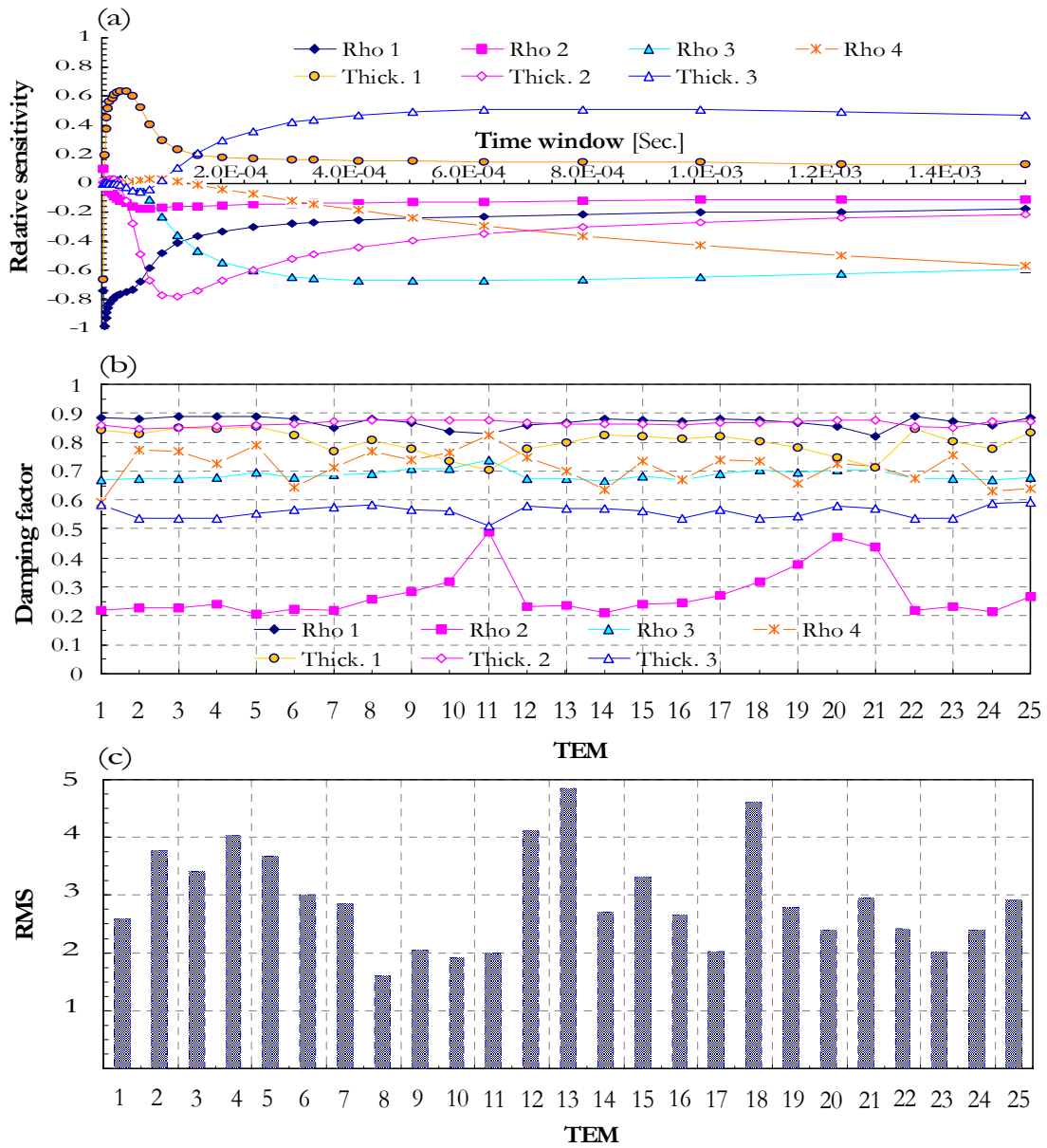


Figure 4.20: (a) Relative sensitivity for the inverted layer parameters throughout the whole time range of the sounding TEM 17, (b) the damping factors of these layer parameters at all soundings, and (c) a histogram of the RMS misfit values of all soundings at the 'Coal-covered Area.' Here the transient-decay data are jointly inverted with the corresponding RMT data.

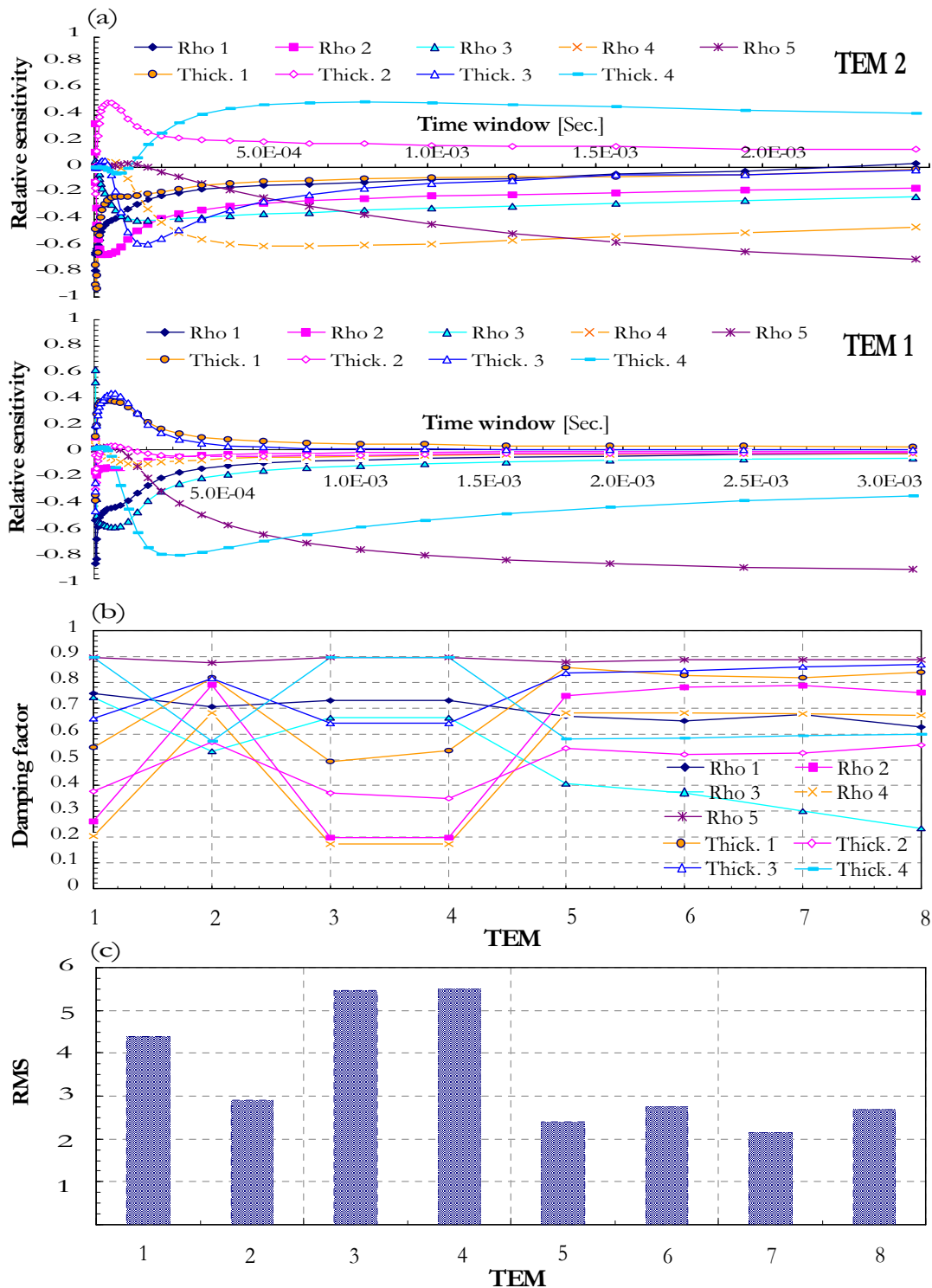


Figure 4.21: (a) Relative sensitivity for the inverted layer parameters throughout the whole time range of soundings (upper) TEM 2 (undistorted transient) and (lower) TEM 1 (distorted transient), (b) the damping factors of these layer parameters at all soundings, and (c) a histogram of the RMS misfit values of all soundings at the 'Coal-covered Area.' Here the transient-decay data are jointly inverted with the corresponding RMT data.

4.2.5 Three-dimensional Modeling of Synthetic Data

4.2.5.1 Grid Design and Verification

Analogous to the 2D RMT numerical solutions, the accuracy of the SLDM modeling results depends mainly on the 3D finite-difference gridding (or meshing). Carelessly designed grids can give independent users quite different results. Certain guidelines (or rules-of-thumb) are already exist, relating in principle to the physics of EM diffusion, and can be considered in designing a sensible 3D finite-difference grid [Weaver *et al.*, 1999; Koch *et al.*, 2004], but no simple formulas can be applied across different modeling problems. The most important empirical guidelines are:

- (1) The inner-grid nodes should be small around both the transmitter- and receiver-loop locations, to properly represent the gradients of the vertical and horizontal magnetic fields.
- (2) The outer-grid nodes should be far enough from the transmitter- and receiver-loop locations, almost logarithmically increased. This is because the scattered magnetic fields become predominantly horizontal, and hence are smoothly varying, away from any resistivity contrasts.
- (3) Finer grid nodes for early-time calculations and coarser nodes for late-time calculations, i.e. selective grid discretization. Their results are then jointed-together to form a composite 3D response for the whole time range of interest.
- (4) Finer grid nodes at each sharp vertical and horizontal resistivity-contrasts.
- (5) Finer grid nodes in any conductive region and coarser nodes in any resistive region within the model.
- (6) Model parameterization should be conformed to the grid discretization.

Normally, the diffusion-depth represents the extreme minimum and maximum diffusion cases of an EM wave in a homogeneous half-space or an uniform horizontally layered-earth [Spies, 1989]. Particularly for guidelines 1, 2 and 3, one can assume for practical purpose that realistic grid dimensions are usually starting at nodes few times shallower than the minimum diffusion-depth and terminating at nodes few-times deeper than the maximum diffusion-depth [Koch *et al.*, 2004].

Separately, the calculated 3D response for each guideline 3 to 6 was then verified with the corresponding 1D response over a 100 Ωm homogeneous half-space (models I) and two horizontally layered-earths (models I and II) (Figure 4.22). The results showed that the 3D solutions are in excellent agreement with the 1D solution over the three models, where both responses for each guideline are very similar, if not identical, indicating that the calculations satisfy the finite-difference analog of the governing differential-equations as well as all boundary and initial conditions. In all cases, guidelines 1 and 2 were found the most flexible and favorable strategies over other guidelines, and have been followed in designing the grid used in the present 3D forward calculations at the survey areas.

The final single grid (Figure 4.22) contains 72(X)×72(Y)×60(Z) nodes, corresponding to the whole time range of interest between 2.03 μs and 3.10 ms. The minimum and maximum grid-element sizes are about 3.5(X)×3.5(Y)×2.5(Z) cm^3 and 3.36(X)×3.36(Y)×3.33(Z) km^3 respectively. A real 50×50 m^2 transmitter-loop (T_X) was simulated by 30 equi-nodal electric-dipole elements, where the current is specified, and an arbitrarily located receiver-loop (R_X). The whole grid was always shifted horizontally, along the y-axis, over the earth model, while the calculations are performed at each sounding. Like the field transient-decay data, the output 3D response is readily normalized from any system parameter.

If, however, the models have topographic-air blocks, guidelines 3 is the only workable strategy, particularly on the conductive ground, where a high resistivity-contorts is present at the ground-air interface. This will be declared in the course of Section 4.2.6.

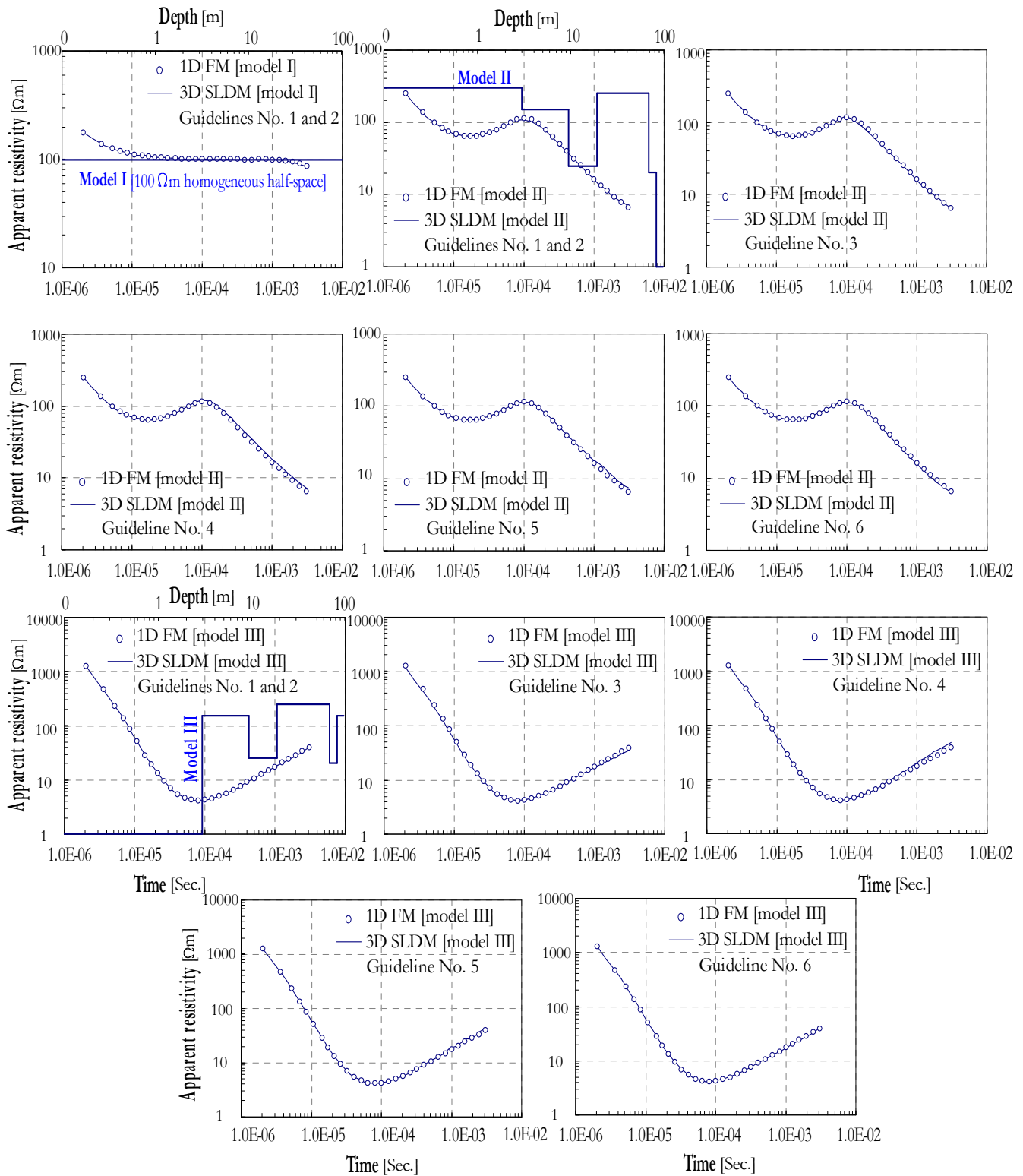


Figure 4.22: Grid verifications for different designing guidelines: comparison of the calculated 3D responses with the corresponding 1D responses over a homogeneous half-space (models I) and two horizontally layered-earths (models I and II).

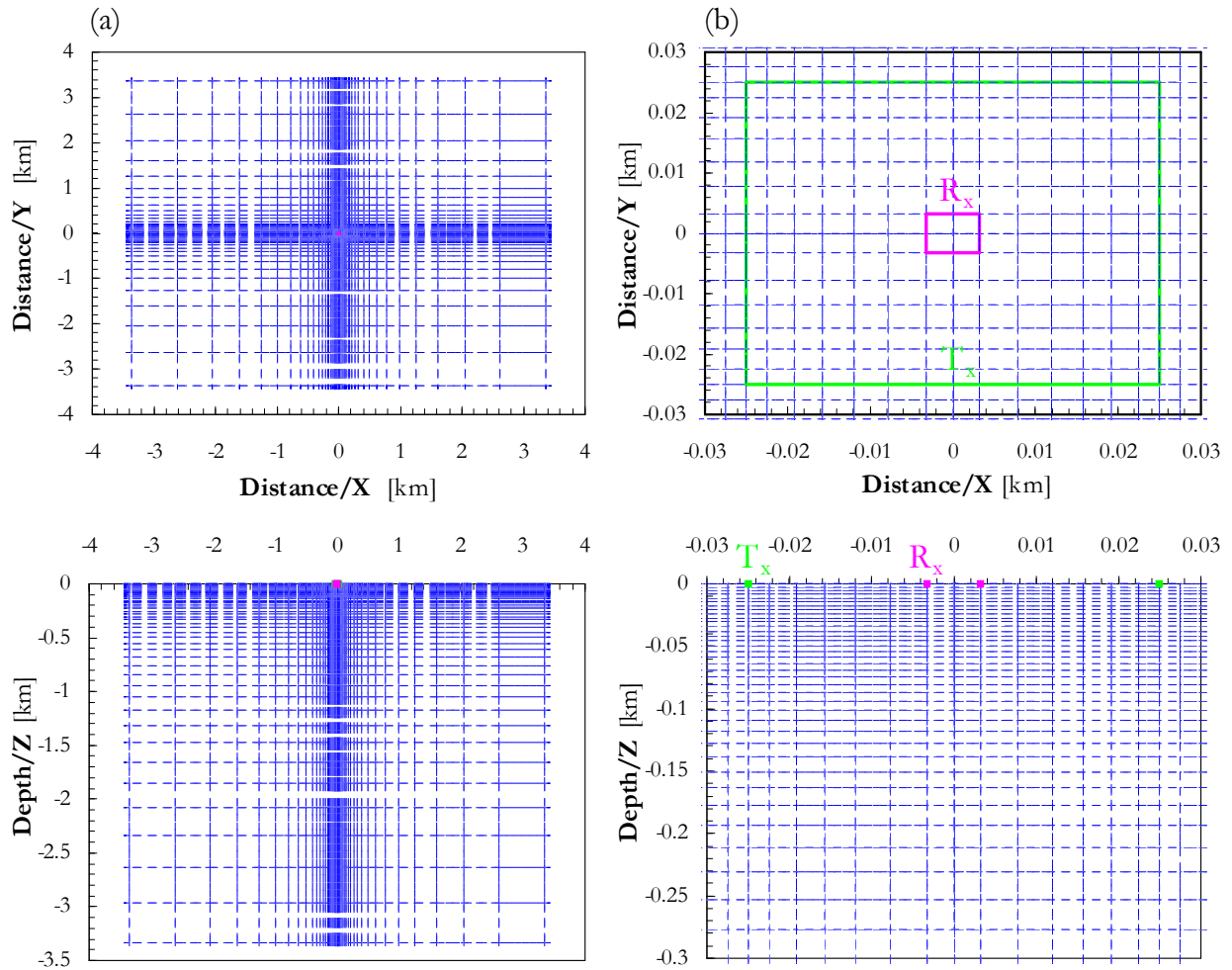


Figure 4.23: Final grid used for comparison of 3D forward calculations with field data at the survey areas. (Upper) Plan and (lower) section views for the (a) main and (b) core designs. Here the receiver-loop is arbitrarily designed.

4.2.5.2 Model Geometry and Results

Because the proper choice of starting model is the most significant effort- and time-consuming part in any 3D trial-and-error forward modeling, a prior knowledge of the model structure is essentially required. Initially, the 1D TEM inverted sections can be used as starting models for the present 3D forward calculations at the survey areas. A reference height begins at $Z=0$ m, which represents the top of layering at the survey areas, was taken as the averaged topographic-relief on the earth-ground. For the 'Coal-covered Area', the final model workspace consists of 75 rectangular resistivity-blocks (not shown here). Due to its secure 1D character, 3D modeling trials were only considered to cross-check the influence of nearby-topography on the TEM data and the results will be also discussed in Section 4.2.6.

For the 'Sand-covered Area', starting the 3D calculations with the 1D TEM inverted resistivity model incorporates a preliminary assumption that at soundings TEM 1, 3 and 4, the deep-layering does not change, but is disturbed by separate highly-conductive surficial masses. In this case, axially symmetrical structures can nicely simulate such surficial masses, without

adding any impractical complexity, and hence speed up the computations for the final 3D earth model. Thus, the resulting highly-conductive surficial anomaly underneath each distorted sounding, TEM 1, 3 and 4, was approximated by two vertically-coaxial surficial blocks. A highly-conductive inner block of 1 to 1.5 Ωm resistivity, $10(X)\times 10(Y)$ m^2 horizontal size and $3(Z)$ m thickness is embedded in a less conductive outer block of 65 Ωm resistivity, 50×50 m^2 horizontal size and about 9.5 m thickness. This composite-block is then located within a moderately-resistive horizontal host of resistivity 110 Ωm . An additional composite-block, with the same internal structure except that its outer block has a 50×45 m^2 horizontal size, is centrally-placed underneath the RMT sounding RMT 31, along profile II. The dimensions of each composite-block were chosen to meet approximately the sizes of highly-conductive surficial anomalies recovered by the 2D RMT inversion along profiles I and II (see Section 3.2.5.4) and to be as close as possible to the TEM loop geometry.

The corresponding resistivities of 1 to 1.5, 65 and 110 Ωm can be ideally representative of the surface clay, silty sand and sand respectively. The final model workspace consists of 55 rectangular resistivity-blocks (Figure 4.24). It should be mentioned that different resistivities and dimensions of the internal structure for each composite-block were also examined, during the numerous computation runs, before reaching such a refined form described above. The suggested earth model simulates one popular geological situation, where separate surficial clay masses (or lenses) are disturbed a clean sand, leaving a transitional zone of silty sand in-between. Moreover, it is almost ideal for SLDM scheme because the surficial anomaly zone is not confined to a small area and does not cause any high field gradients.

Figure 4.25 shows the results of 3D forward calculations compared with the respective field data sets along profile I. As would be expected, the calculated 3D responses of the undistorted soundings at the far end of the profile, i.e. TEM 6, 7 and 8, fit the field data very well. They do not show any anomalous behavior and are essentially similar to their 1D responses. When approaching TEM 2 or TEM 5, the fitting between the 3D response and field data at the early-to intermediate-times is slightly degraded, where the 3D effects are present, but significantly weaker. However, the whole layer sequence was used, where a resistive basement (or Frimmersdorf Sand) below the Frimmersdorf Coal/Clay is always needed (Figure 4.25a).

The distorted transients could not be modeled in the same manner. To model the data reasonably at soundings TEM 1, 3 and 4, a conductive basement must be introduced below the interpolated lower boundary of Frimmersdorf Coal/Clay (Figure 4.25b). In other words, the interpolated lower boundary of Frimmersdorf Coal/Clay needs to be infinitely extended to simulate how the transient decays much slower than it does over a resistive basement. Notably, the fitting between the 3D responses and field data at the earlier-times of soundings TEM 3 and 4 is not as perfect as that of TEM 1. The fitting can be improved further from changing only the block resistivities stepwise, reference to the resistivity values obtained from the laboratory measurements for each sediment type.

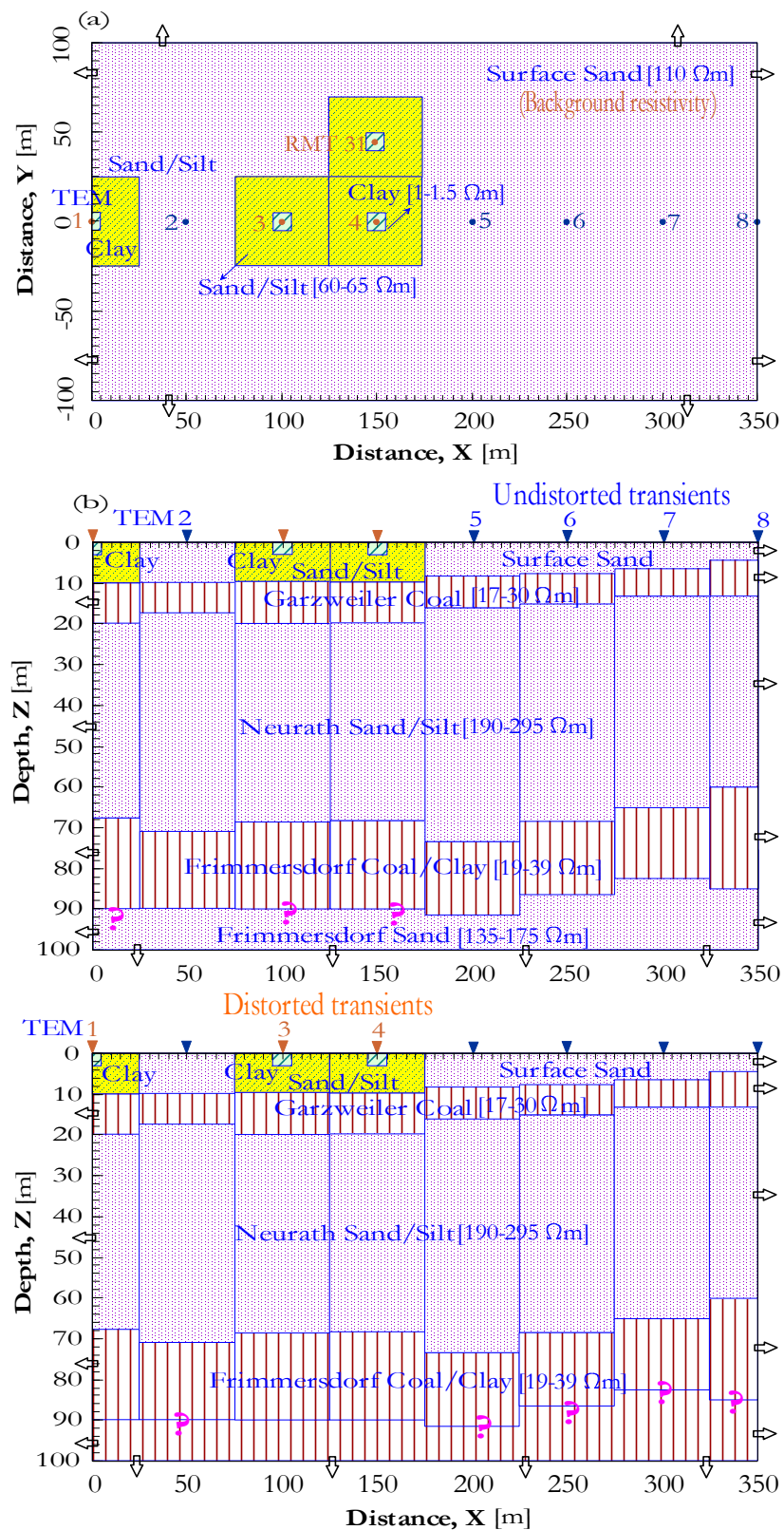


Figure 4.24: Final model geometry used for comparison of 3D forward calculations with field data along profile I at the 'Sand-covered Area': (a) plan view and (b) section views for the undistorted and distorted soundings. The corresponding locations of profiles I and II, and the surface projection of the surficial composite-blocks are also displayed in the plan view.

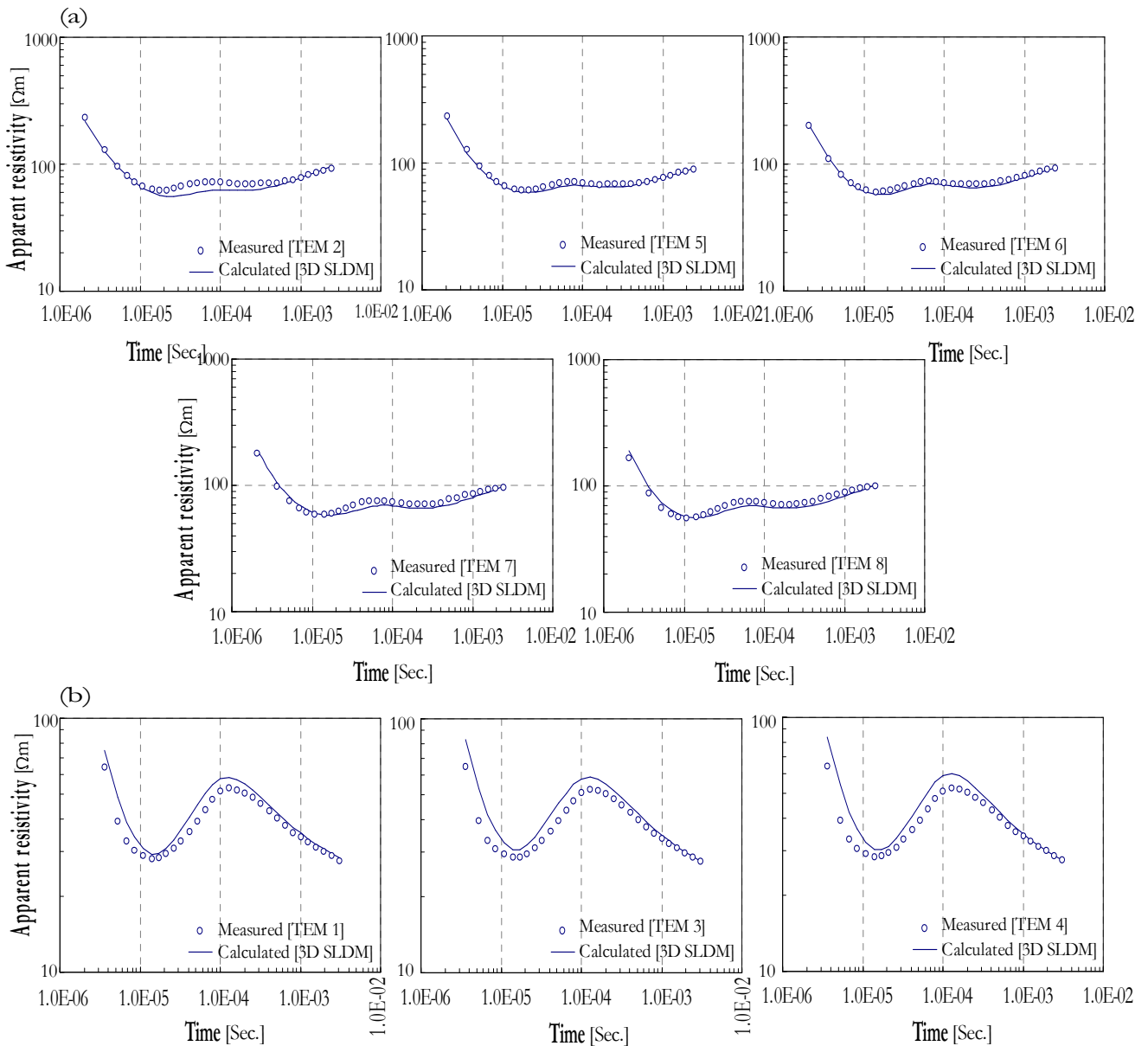


Figure 4.25: Comparison of the calculated 3D responses with field data at the (a) undistorted and (b) distorted soundings along profile I at the 'Sand-covered Area.'

In order to determine the model sensitivity to the presence of the highly-conductive surficial blocks and/or the conductive basement at the distorted soundings, some experiments were carried out. Figure 4.26 (a and b) shows the calculated 3D responses for the rest of the model, after removing only the inner and outer blocks successively, compared with the field data at the distorted sounding TEM 1. The misfit between the 3D responses and field data increases at the early-times as the surficial conductivities are inwardly reduced. In both cases the late-time match still very well. This obviously means that such surficial blocks are significantly needed to explain the early-time data and they effectively contribute to the total model conductance (thickness over resistivity).

As shown, the presence of the surficial blocks underneath each distorted sounding within the suggested model does not alter the late-time fitting, where the model essentially needs only to a conductive basement. Attempting to fit the field data without introducing a conductive basement within the 3D earth model was not successful at all. The calculated 3D response behavior is going over to an unacceptable divergence with the field data only at the later-times

(Figure 4.26c). This reveals that, in a distortion case, a conductive basement is urgently needed for the suggested model. Likewise, *Goldman et al.* [1994b] introduced an immediate practice to interpret transient data distorted by highly-conductive surficial anomalies that to consider an extremely-high conductive basement into the 1D layered-earth inversion, and then to exclude it from the final stitched resistivity section.

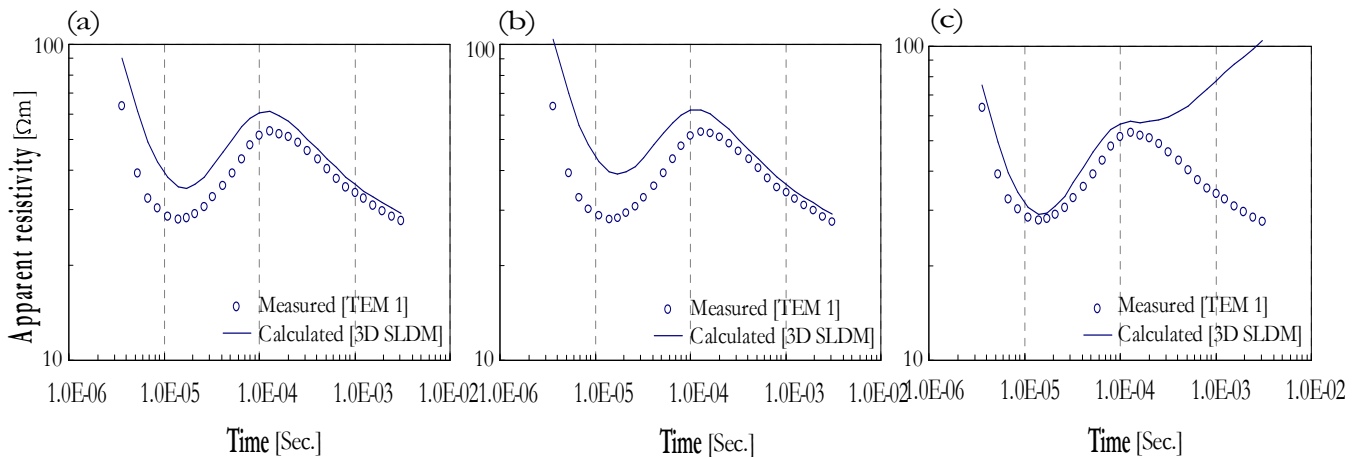


Figure 4.26: Comparison of the calculated 3D responses with filed data at the sounding TEM 1 after skipping only (a) the inner- and (b) outer-blocks successively or (c) the conductive basement from the 3D earth model, while other model structures are kept fixed.

One explanation for these abnormal transients at soundings TEM 1, 3 and 4 may be given as the highly-conductive surficial masses distort their data in such a way that they screen the underlying conductive coal seams, particularly the lower boundary of Frimmersdorf Coal/Clay, from being sounded. If this would be the case, the distortion must manifest itself as a much steeper downward inclination at later-times of apparent resistivity curve to approach a conductive basement than it would be in the case of the resistive basement. Contrary to that explanation, the calculated 1D late-time branches of apparent resistivity curves of a distorted transient, for model(s) of a varying clay thickness, were always ascending (see Figure 4. 8) and closely following that of undistorted transient for a model without surficial clay.

A favored physical explanation is that the initial currents at each distorted sounding, after transmitter turn-off, are partly channeled (gathered) through a centrally-placed surficial mass of high conductivity and flowing around the top of this mass. The currents do not remain longer within the mass, due to its small size, but probably caused a local anomalous current and an associated anomalous secondary magnetic field. This anomalous field curls around the current concentration and increases the total secondary magnetic field at earlier-times, as well as it delays and attenuates the energy a little in reaching the underlying conductive coal seams. This delay is in a proportional relation to the surficial mass conductance. At intermediate- to late-times, the field penetrates the surficial mass, and the response from the coal seams can be readily (and differently) identified. This response is actually an additive from the clay and coals responses. This superposition slightly modifies the intermediate-time asymptotic behavior of the transient. When it is molded, the estimated first coal appears more broadened. At later times, the transient behavior is greatly modified to decay slower than the power law $t^{-5/2}$ [Nabighian and Macnae, 1991], becoming no longer easy to be modeled or to be more representative for the second coal seam. However, the extensive 3D modeling in the present study could not confirm that the late time slowness was happened in such a way.

Certain qualitative conclusions can be readily drawn from the 3D forward simulations performed above. First, the results showed that the main 1D interpretation would not change too much. Thus, they support the foremost hypothesis that the cause of abnormal transients at soundings TEM 1, 3 and 4 is geological, where the deep-layering does not change, but is disturbed by separate surficial clay masses (or lenses). These masses are symmetrically located at, and thinning away from, the centers of the distorted soundings. This interpretation seems geologically reasonable. Second, the TEM signals are still able to detect the underlying coal seams at greater depths in the presence of such surficial clay masses, but with a partial screening, which is appeared as a kind of EM superposition from the responses of these masses and coal seams. Although the upper boundary of the Frimmersdorf Coal reasonably exists at reasonable depths at each distorted sounding, yet unclear is its lower boundary can be normally interpolated between the neighboring soundings or not. However, the 3D forward calculations reduced the inevitable non-uniqueness obtained by the 1D interpretation of the layered-earth parameters at the distorted soundings. Finally, the suggested earth model for the 3D forward simulations with such a dual resistive–conductive basement may represent the minimum working model (i.e. the least number of blocks that still honor the data sensitivity) at the 'Sand-covered Area.' Attempting to find a *single* basement, which may give a reasonable fit to all field data sets along the profile would not be realized.

No doubt there is still some ambiguity left in the 3D modeling procedure over a single-sounding fashion, which would not be present if the TEM data were collected, at least, on parallel profiles or even better on a survey grid to allow the best estimate of starting model. On the other hand, the sequential interpretation described above is not in complete accord with the borehole-geology of the local-mining industry (RWE-Power AG) (Figure 1.4a) at the 'Sand-covered Area', where these surficial clay masses are not well-documented. However, field inspections for the surface mining-exposures at the 'Sand-covered Area', where inorganic clay samples have been collected, obviously confirmed the presence of some separate clay masses (or lenses) within the Surface Sand (Figure 4.27).

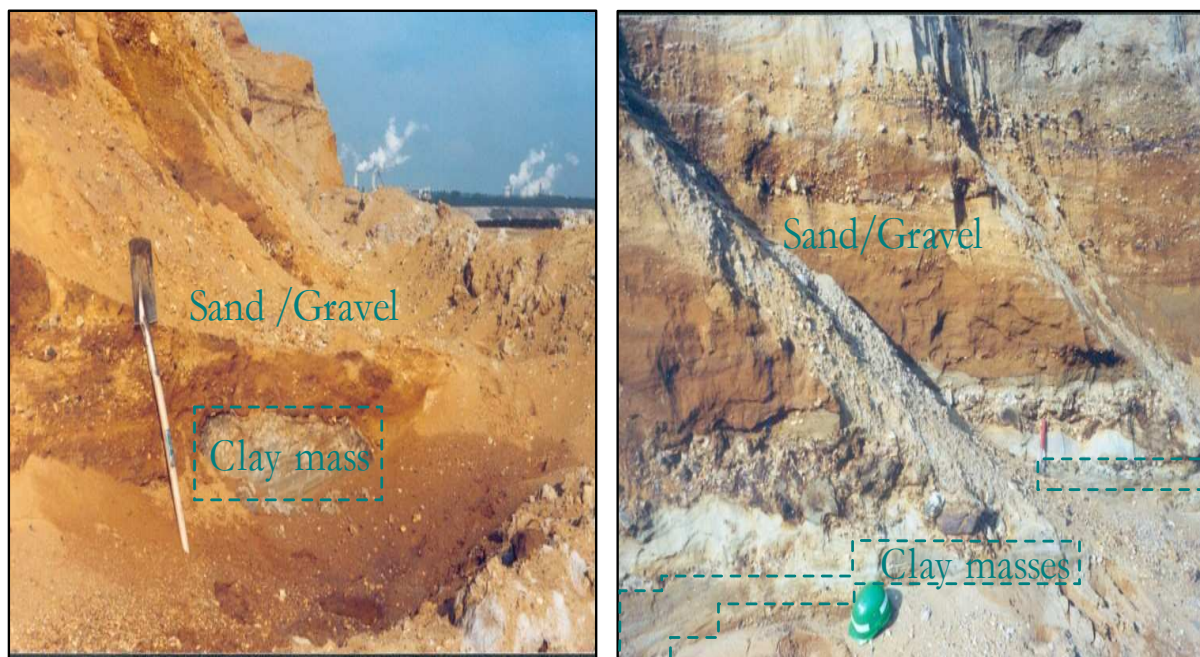


Figure 4.27: Photographs showing two selected surface mining-exposures, where the Surface Sand hosts some separate clay masses (or lenses), viewed close to the northern side at the 'Sand-covered Area.'

4.2.6 Nearby-topography Effect

To investigate whether the EM response of nearby-topography at the survey areas may be ignored or whether it should be incorporated into the modeling trials, a fair amount of topographic detail and air layers must be included without burdening the earth model too much. An additional topographic-block was added over the earth model at each survey area to approximate its hillock shape (Figure 4.28). In this case, the ground resistivities are averaged as 50 and 500 Ωm at the 'Coal-covered Area' and 'Sand-covered Area' respectively, while the resistivity of air is assumed to be $10^6 \Omega\text{m}$. In attempts to simulate data using the previous single grid, the calculated 3D responses, for a constant ground resistivity and continuously-reduced air resistivity, matched the field data very nicely until rather intermediate-times. For higher ground–air resistivity-contrasts, the late-time responses deviated very strongly from the field data and no convergence was achieved, whereas for lower contrasts the late-time responses still honor the data reasonably. Figure 4.29 exemplifies the dominant wrong late-time behaviors for the control soundings at the survey areas. Despite the clear nearby-topographic features present at the 'Sand-covered Area', it seems that nearby-topographic effect is not a concern at the undistorted soundings, although present. This is very clear at the sounding TEM 2, where the resistivity-contrast for all air values is relatively low.

Basically, the convergence characteristics of the SLDM scheme depends on the condition number (the ratio between largest and smallest eigenvalue) of the finite-difference matrix. In some cases, the single grid becomes too dense and the condition number of the finite-difference matrix becomes too large [Hördt and Müller, 2000; Commer, 2003]. Solving an 3D ill-conditioned differential-equation system is extremely difficult, so the fields in the scheme output do not converge and the responses at late-times are unstable and probably wrong. Similarly, the situation may be happened when applying high resistivity-contrasts at the ground–air interface.

To improve the accuracy of the solution at the late-times, one possible remedy is to apply a *selective grid discretization*. Two variable-expanding separate grids (not shown here) should be used and their results are then jointed-together to form a composite 3D response for the whole time range of interest: a finely-discretized grid for the early-times, between 2.03 μs and 51.6 μs , and another coarsely-discretized grid for the intermediate- to late-times, between 51.6 μs and 3.10 ms. The finer and coarser grid designs contain $80(X) \times 80(Y) \times 74(Z)$ and $68(X) \times 68(Y) \times 63(Z)$ nodes respectively. The minimum grid size, within the finer-grid, is about $0.75(X) \times 0.75(Y) \times 1.8(Z) \text{ cm}^3$, whereas the maximum grid size, within the coarser-grid, is $3.36(X) \times 3.36(Y) \times 3.33(Z) \text{ km}^3$. Other grid and model specifications are kept constant. The air resistivities are then approximated by values of 2.5×10^4 and $5 \times 10^4 \Omega\text{m}$ against the topographic-blocks at the 'Coal-covered Area' and 'Sand-covered Area' respectively. Additionally, to find the best compromise for Lanczos decomposition steps within the scheme itself, a value of 15000 is critically chosen, by iterating back and forth for values between 10000 and 20000. Collectively, these modifications are translated into about 2-fold running-time required to obtain the desired solution.

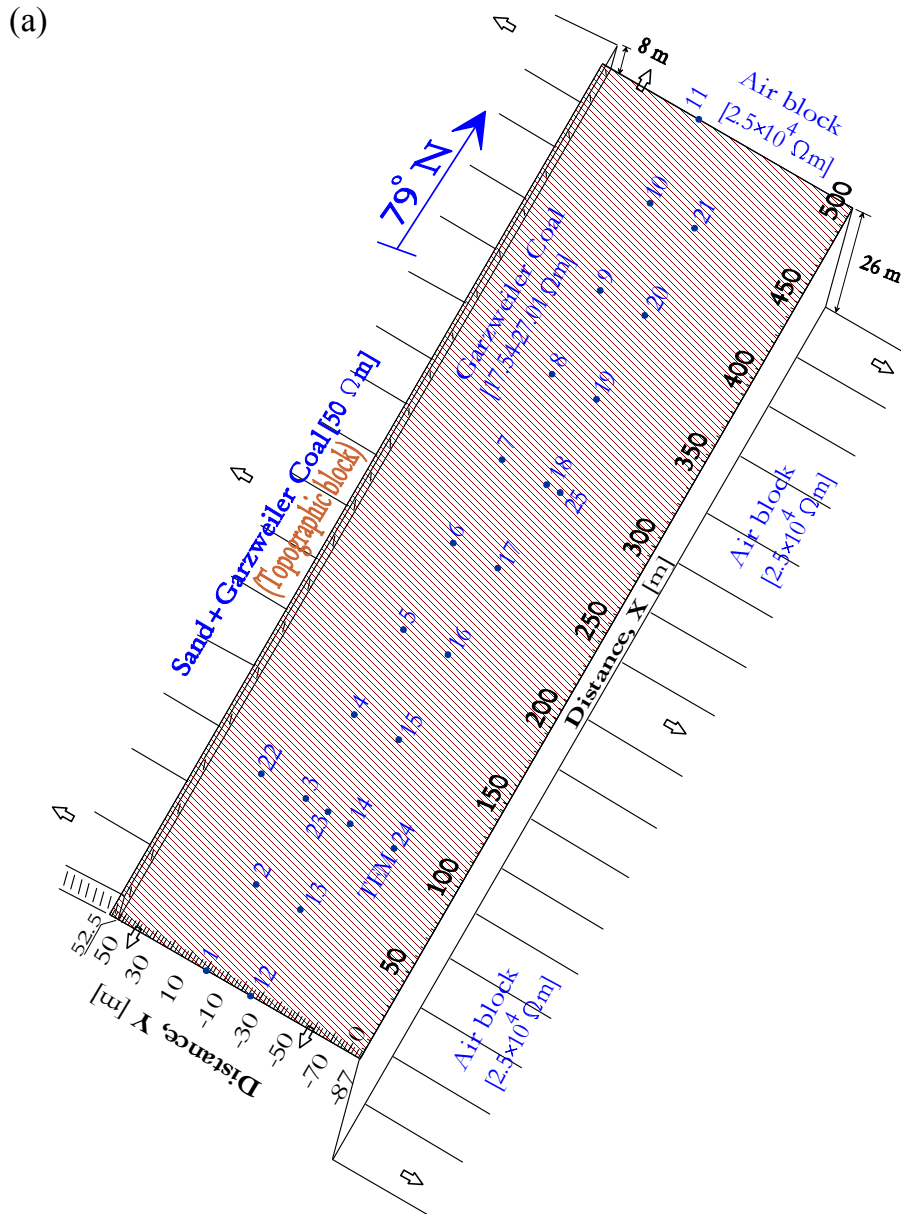


Figure 4.28: Approximate geometry of nearby-topography at the survey areas: (a) 'Coal-covered Area' and (b) 'Sand-covered Area.' The corresponding locations of the profiles at each survey area, as well as the surface projection of the surficial composite-blocks at the 'Sand-covered Area' are also displayed

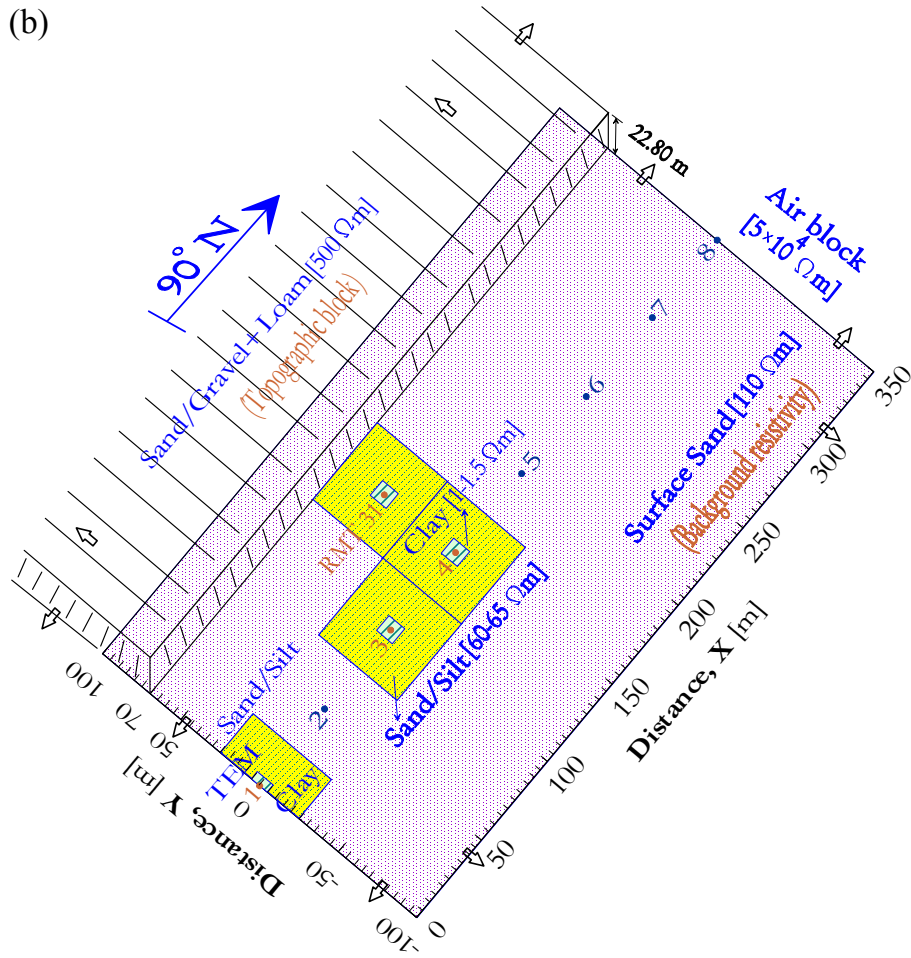


Figure 4.28: (Continued.)

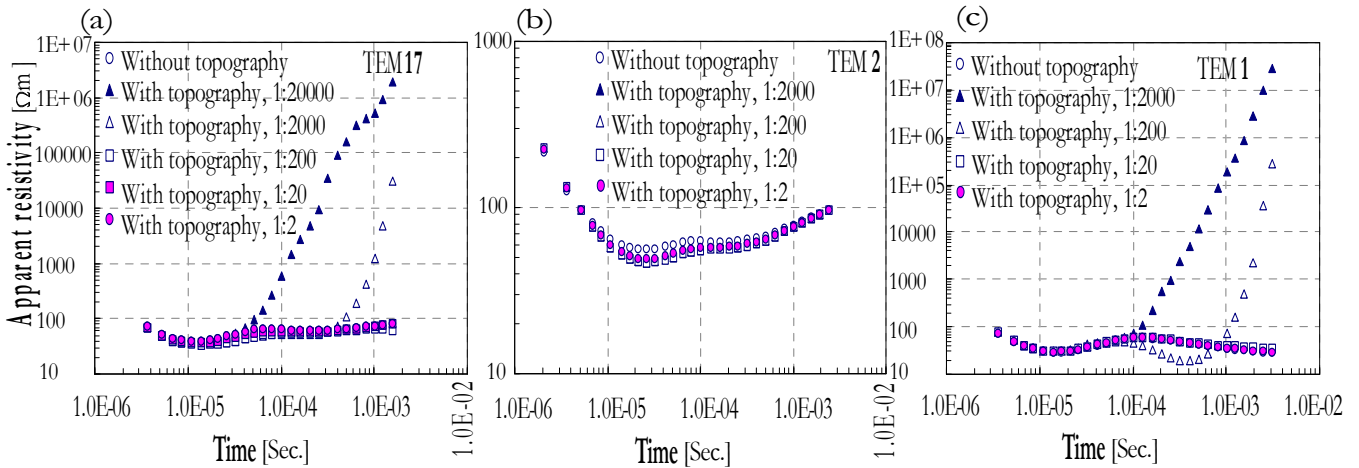


Figure 4.29: Modeling nearby-topography, for different ground-air resistivity-contrasts, using the well-verified grid shown in Figure 4.23 at the soundings: (a) TEM 17, 'Coal-covered Area' and (b) TEM 2 (undistorted transient) and (c) TEM 1 (distorted transient), 'Sand-covered Area.'

Now the responses are quite stable and converge very well at later-times (Figure 4.30). The data are modeled in a normal manner, with no need to add or remove any structure element or fictitious layer within the earth model. Generally, there is almost no significant difference between the calculated 3D responses obtained with and without including nearby-topography within the earth models at the survey areas. In particular, the topographic effect at the 'Coal-

covered Area' is relatively notable close to the very steep cliff located on the southern side (e.g. TEM 24), where a steep horizontal field gradient would be expected, than to the small hillock located on the northern side (e.g. TEM 22). However, these established differences are largely restricted to early-times and can be easily recovered from changing only the block resistivities stepwise, reference to the resistivity values obtained from the laboratory measurements for each sediment type. This strongly suggests that there is no any EM coupling between nearby-topographic features and the underlying conductive coal seams, and that the distances between the nearby-topography and main parallel profiles were chosen adequately enough to avoid its effect.

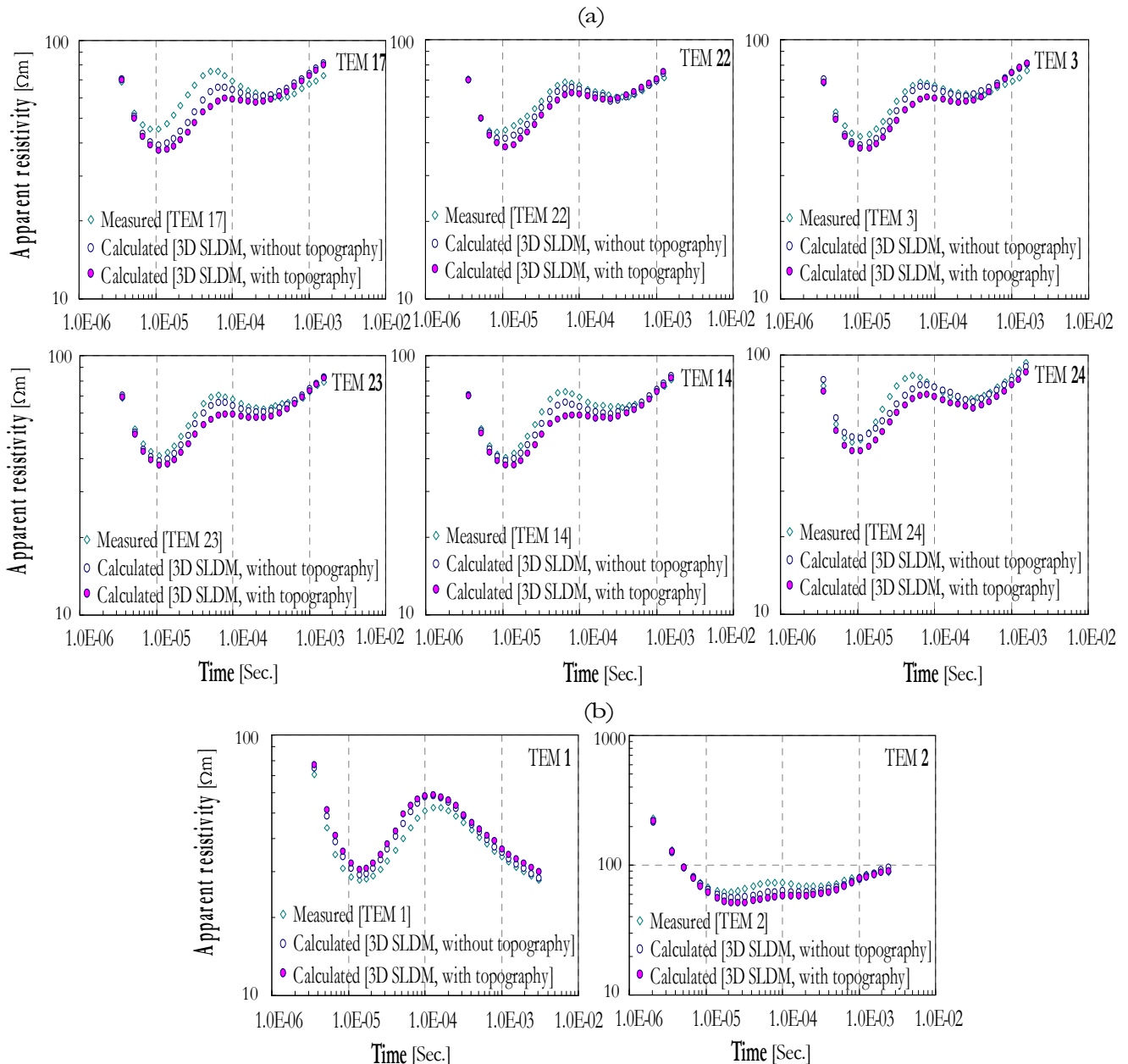


Figure 4.30: Modeling the nearby-topography correctly, for some selected transients, using appropriate air resistivities and selective grid discretization at the survey areas: (a) 'Coal-covered Area' and (b) 'Sand-covered Area.'

4.3 Correlation of Surface Electromagnetic with Laboratory-based Resistivity Models

Because the RMT data are usually skin-depth limited, they only provided a resolution depth between 25 and 30 m for the shallow resistivity structures. Whereas, the TEM data still have sufficiently early- to late-time information, and therefore resulted in a better resolution depth of about 100 m for the shallow to sufficiently-deep resistivity structures. At shallower depths, the 1D/2D RMT resistivity models agree fairly well with the 1D/3D TEM resistivity models. The deeper structures are adopted purely from the 1D/3D TEM resistivity models.

Comparing the different 1D/2D RMT and 1D/3D TEM resistivity models, gained from the control soundings at the survey areas, with the closely-spaced boreholes exhibits an obvious correlation (Figure 4.31). Generally, the RMT and TEM data are successful in identifying the major stratigraphic units, i.e. the shallowest Garzweiler Coal and Frimmersdorf Coal/Clay within their sand background which corresponds to the Surface Sand, Neurath Sand/Silt and Frimmersdorf Sand. They could not distinguish between Neurath Sand and the underlying sand/silt or between Frimmersdorf Coal and the underlying organic clay. In particular, the Frimmersdorf Coal/Clay seems somewhat too thick, but its center is located reasonably well. Furthermore, the deepest Morcken Coal or Sand are beyond the depth-of-investigation of the present measurements and need not be considered. Importantly, the 2D RMT and 3D TEM resistivity models demonstrate a very strong evidence for the presence of separate highly-conductive surficial clay masses (or lenses) at the 'Sand-covered Area.' As can be seen, the thickness of the surficial clay ties in well with the resistivity models (Figure 4.31b). At the distorted soundings, although the upper boundary of Frimmersdorf Coal/Clay exists at its known approximate depths, its lower boundary could not be readily resolved.

On the other hand, the estimated RMT and TEM resistivities are quite comparable to each other and show a satisfied correlation with those typically obtained from the laboratory measurements. The estimated TEM resistivities averaged well around the laboratory resistivities of Neurath Sand and the underlying Sand/Silt, and of Frimmersdorf Coal and the underlying organic clay. The estimated RMT and TEM resistivities of the Surface Sand, Garzweiler Coal and Frimmersdorf Sand are much lower than, but still not far beyond, the laboratory values.

The absolute laboratory values for the surficial clay mass lie almost halfway between the corresponding estimated RMT and TEM resistivities. Comparing to the 1D TEM resistivity models, the estimated resistivities from the 3D models usually try approaching the absolute laboratory values. The main conclusion can be drawn from such positive correlation is that the identification of the conductive coal seams from their resistive sand background, at the whole opencast mine 'Garzweiler I', seem to be possible solely on the basis of RMT and TEM sounding data.

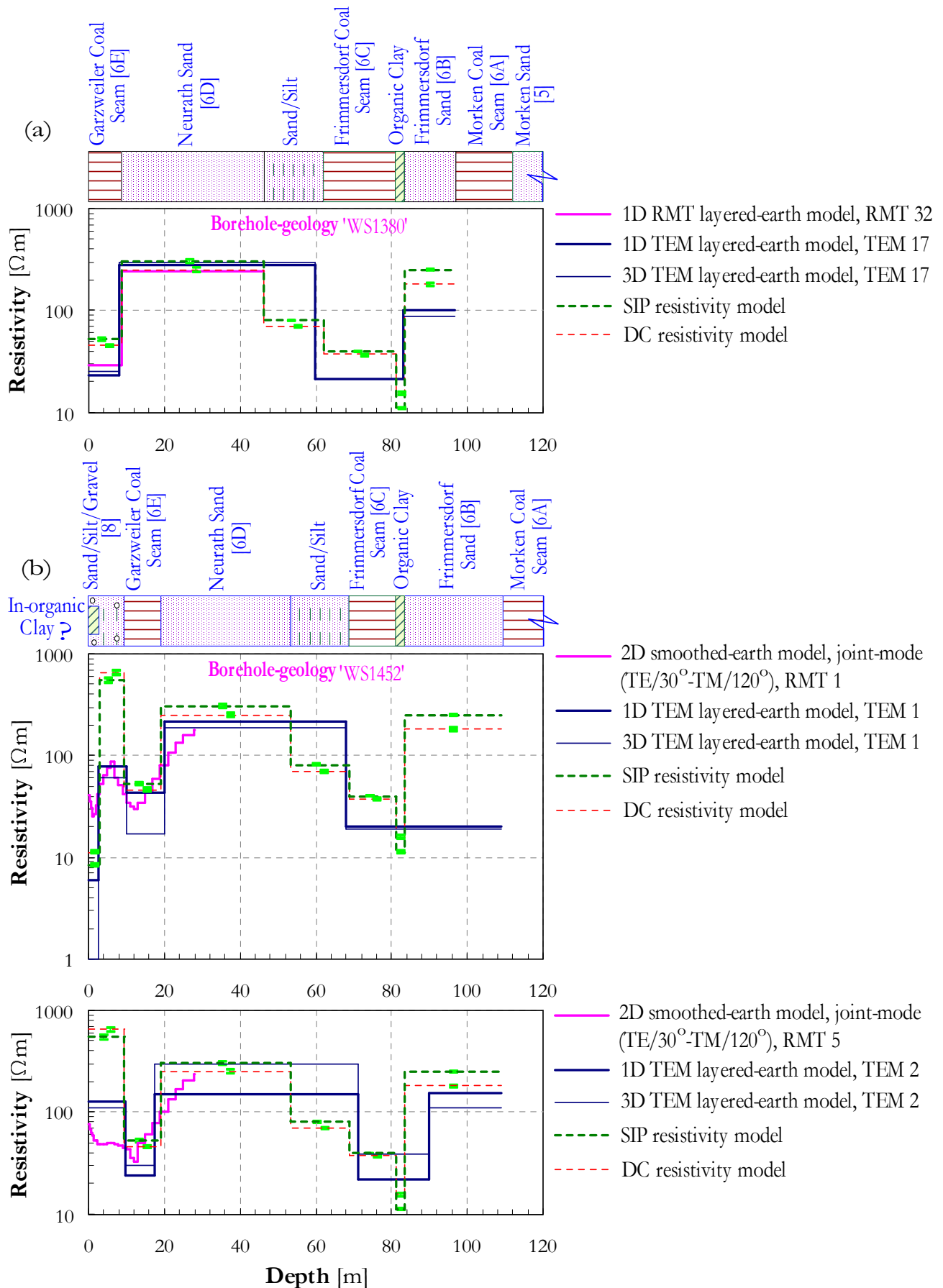


Figure 4.31: Correlation of the RMT and TEM earth models with laboratory-based resistivity models at the control soundings of each survey area: (a) RMT 32/TEM 17 at the 'Coal-covered Area', and (b) RMT 5/TEM 2 (undistorted) and RMT 1/TEM 1 (distorted) the 'Sand-covered Area.'

4.4 Geological Implications inferred from Surface Electromagnetic Resistivity Models

Geological surprises, like unexpected changes in the coal seam altitude or its thickness (faulting, dipping, thinning, etc.), can drastically alter the mining economics at the opencast mine 'Garzweiler I.' Therefore, it is perhaps worthwhile to introduce some useful geological implications from the present multi-dimensional RMT and TEM resistivity models at the survey areas. Contours joining points of equal seam altitude or thickness, inferred from these resistivity models, may serve as a guide to fix such problems, if present. Additionally, these implications can also enable the mining geologists or engineers at the opencast mine 'Garzweiler I' to quantitatively assess the most important mining estimates (reserve in-place, stripping ratio², etc.). Figure 4.32 shows depth-contour maps for the upper and lower boundaries of Garzweiler Coal, after recovering its uppermost part (about 5 m thick) which was already mined out prior to the field measurements at the 'Coal-covered Area', and Frimmersdorf Coal/Clay based on the 1/2D RMT and 1/3D TEM resistivity models.

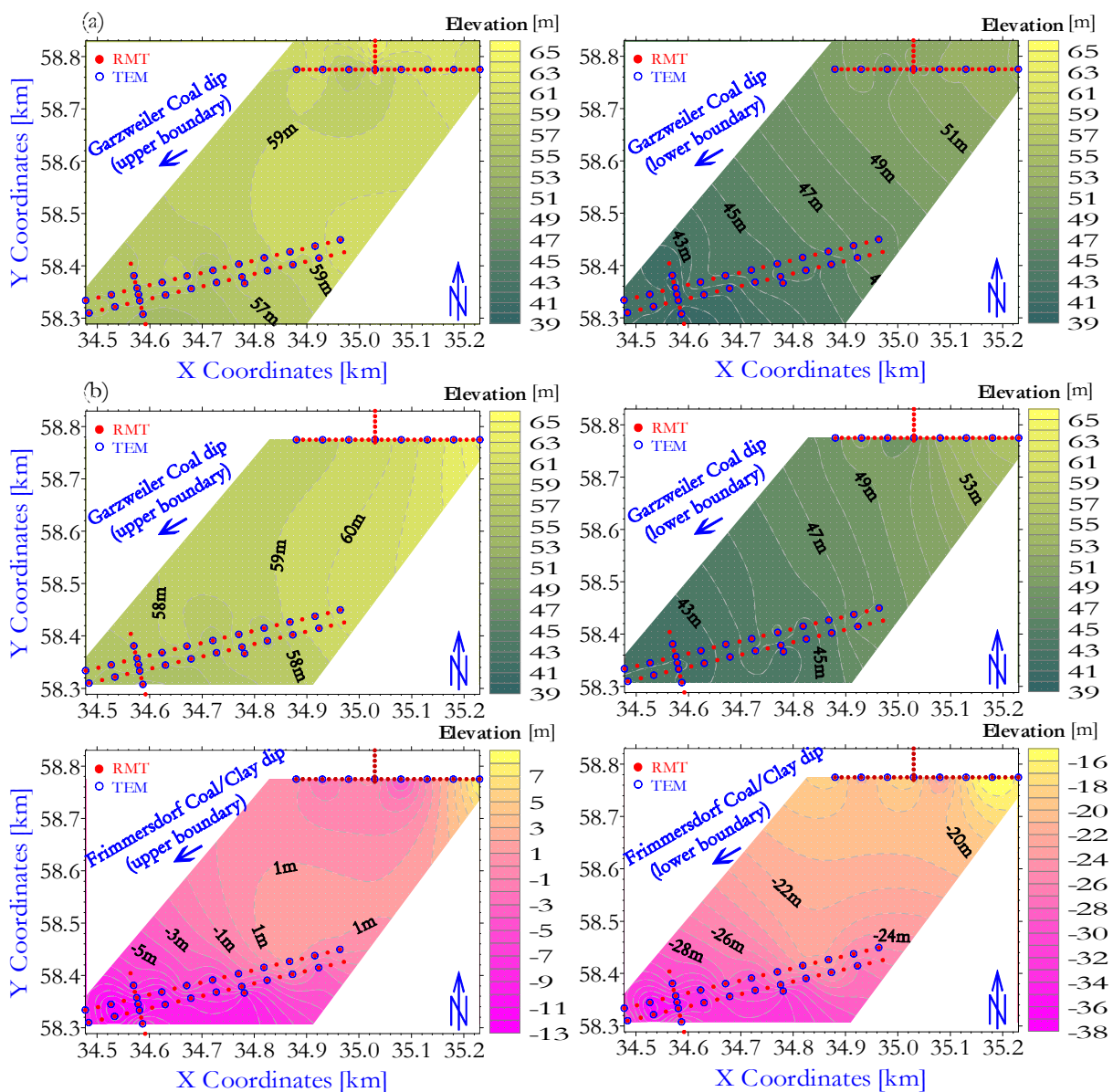


Figure 4.32: Depth contour maps for the (left column) upper and (right column) lower boundaries of the Garzweiler Coal and Frimmersdorf Coal/Clay inferred from (a) 1D/2D RMT and (b) 1D/3D TEM resistivity models at the survey areas.

²Ratio of the host material removed to the brown coal recovered [m^3/ton].

Generally, there is no indication of abnormal altitude or thickness changes for the Garzweiler Coal and Frimmersdorf Coal/Clay at the survey areas. As can be seen, both coal seams gently dip in the southwesterly direction. This should be in a fairly good agreement with the regional structural makeup of the Rhineland brown coal (see roughly Figure 1.2b). However, the Garzweiler Coal is gradually thinned northeastwards, while Frimmersdorf Coal/Clay still has almost a regular thickness.

Like any mining geophysical work, the uncertainty factor of both RMT and TEM interpretations, as measured by the actual brown coal finding (or brown coal elimination) information provided, is the most serious *limitation* in the present work, and in mining geophysics in general. Yet the final mining of Garzweiler Coal and Frimmersdorf Coal/Clay is a great challenge to both IGM-Cologne electromagnetists and RWE-Power geologists. To the former for improving their scientifically-based methodology and interpretation schemes, and to the latter for evolving the means for a narrower, more reliable localization of likely brown coal conditions. At the time of writing this dissertation, the only available mining results are provided for Garzweiler Coal at the 'Coal-covered Area.' Appendix B demonstrates these results, along profile I, in comparison to interpreted 1D/2D RMT resistivity models.

CHAPTER 5

LABORATORY-BASED RESISTIVITY MODELS

Near-surface electromagnetics like RMT and TEM methods make use of the property *electrical resistivity*. Therefore, the knowledge about this property in the laboratory is very important to assess such methods and to seriously interpret their results. Moreover, they often may require only laboratory data obtained at atmospheric pressure and room temperature (or at ambient temperature below 100 °C). If, however, we have in mind EM observations on the composition and state-of-matter deep in the Earth's crust and mantle, we must conduct laboratory experiments at high pressure and temperature. This chapter describes two direct methods, which are mostly used in the laboratory, for measuring the electrical resistivity of some rock samples of different lithologies. Because the samples represent approximately the whole vertical succession at the survey areas, the primary goal was to provide basic resistivity values, and characteristics, for use in performing all RMT and TEM forward modeling and, later on, in correlating their derived resistivity models.

5.1 Electrical Resistivity of Coal

Of all the physical properties of naturally occurring rocks and minerals, electrical resistivity shows the greatest variation. Metallic minerals (except sphalerite) conduct electricity fairly efficient by the flow of electrons. Most rock-forming minerals are, however, poor conductors (or insulators) and electrical current is carried through a rock mainly by the passage of ions in pore fluids. Many factors can influence the electrical resistivities of rocks in bulk. Such factors include porosity, nature and saturation of the pore fluids, nature and size of the grains making up the matrix and rock structure. The geologic age of a rock also is an important consideration. Isotropic materials have the same resistivity in all directions, while non-isotropic materials have a tensor resistivity. Most rocks are reasonably isotropic, but strongly laminated shales and slates are more resistive across the laminations than parallel to them. The amount of anisotropy is described by the *anisotropy coefficient* [Spies and Frischknecht, 1991], which is the ratio of maximum to minimum resistivity and generally lies in the range of 1 to 5. Resistivity ranges expected for the most common minerals and rocks are shown in Figure 5.1, significant uncertainties are associated with those ranges.

The range of electrical resistivity for coal is wide, even wider than the ranges of ores. The resistivity is a function of the degree of metamorphism (or carbonization), petrophysical character and mineral composition. Weakly metamorphosed coal, like *brown coal*, has a resistivity between 10 and 100 Ωm when moist (Figure 5.1). Further carbonization leads to the

formation of free carbon stringers and a reduction of the organic radicals in the coal, causing the resistivity to be lower [Parkhomenko, 1967]. However, the amount of decrease in resistivity with increasing metamorphism depends on the type of metamorphism. Highly metamorphosed coal, like *anthracite*, has a rather very low resistivity ranged from 0.001 and up to 10 Ωm .

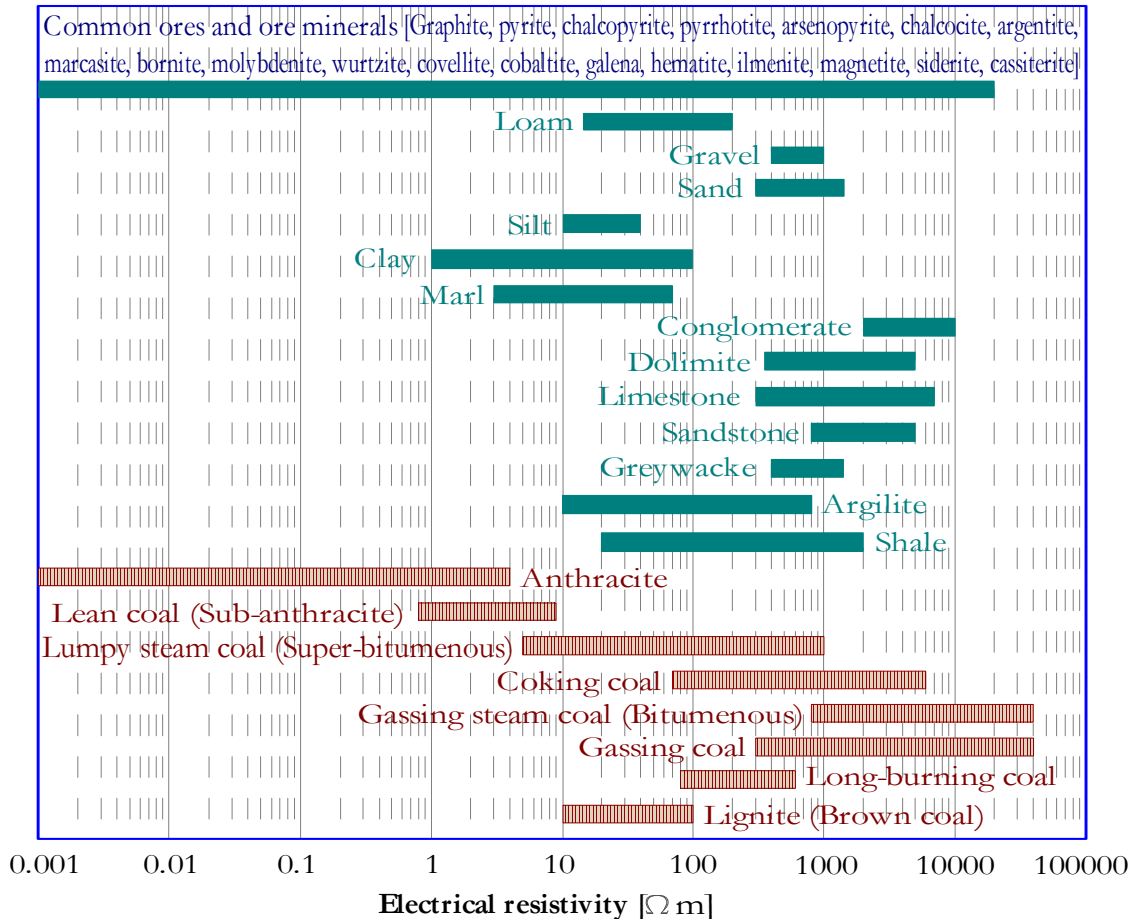


Figure 5.1: Approximate ranges of resistivity values of coal among the most common consolidated and unconsolidated sediments, ores and ore minerals. (Data compiled from different sources [Parkhomenko, 1967; Telford et al. 1990; Knödel et al. 1997].)

At the opencast mine 'Garzweiler I', the only available a-priori knowledge about the brown coal resistivity comes from a number of old borehole electrical resistivity and self-potential (SP) logs, being dated to 1949. The two logs were generally recorded as adjacent curves (Figure 5.2). Identification of coal seams, based on their logging resistivity values (30-35 Ωm), from the underlying and overlying clay (20 Ωm), sand (115-140 Ωm) and gravel/sand [375 Ωm] would be reasonably possible. The SP response occasionally is anomalous opposite the coal seams. Since the interstitial water is often the controlling factor on rock resistivity [Archie, 1942], at present the act of the extensive dewatering and flood control systems by local mining industry (RWE-Power AG) increased grossly the resistivity values for the permeable (sand/silt) and semi-permeable (brown coal) units. This will become evident below from the laboratory results and interpretation (see Section 5.3).

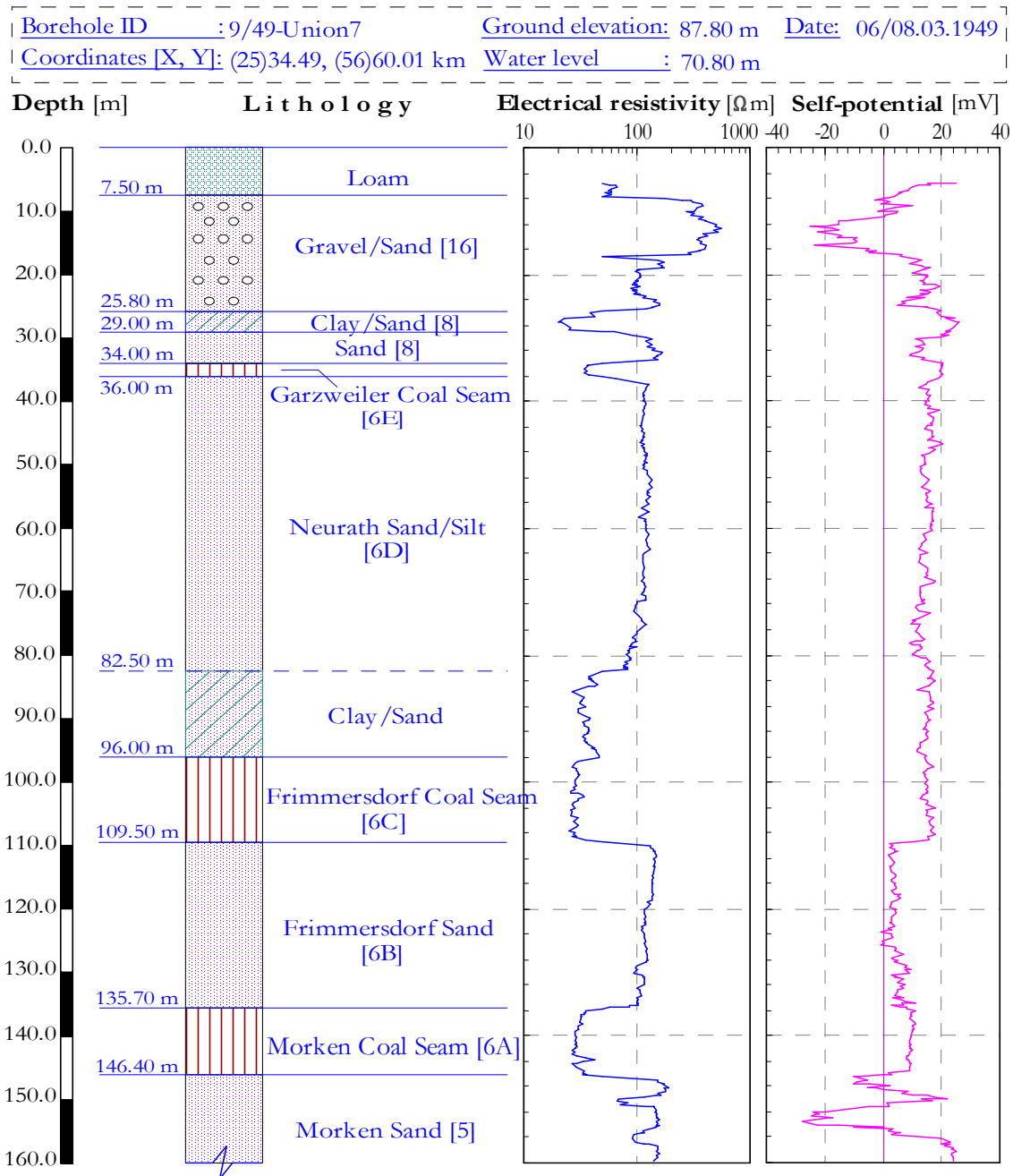


Figure 5.2: Electrical resistivity and self-potential (SP) logs at the opencast mine 'Garzweiler I.' The stratigraphical extent is from the Early/Middle Miocene Ville Formation (horizons 5, 6A, 6B, 6C, 6D and 6E) to the Early/Middle Pleistocene Hauptterrassen Series (horizon 16). (Data courtesy of RWE-Power AG, Cologne.)

5.2 Laboratory Methods for Measuring Resistivity

5.2.1 Conceptual Background

Virtually electrical resistivity of a rock sample, that has any geometrical form, can be measured in the laboratory by imposing an electric current I and measuring the resulting electric potential-difference or voltage V . If the excitation signal is constant in time, the method is known as direct-current (DC) measurement, while if the signal is alternating in time, the method is known as alternating-current (AC) measurement. During a DC

measurement, the resistance R is defined by the simple scalar form of *Ohm's law* as the ratio of the voltage to the current

$$R = \frac{V}{I} . \quad (5.1)$$

A parameter known as the *electrical resistivity* is derived from the measured resistance by applying a sample geometry correction

$$\rho = kR = \frac{1}{\sigma} , \quad (5.2)$$

where k is the geometrical factor (the ratio of sample cross-sectional area to its length). The units of resistivity are usually given as Ωm . Numerically, the reciprocal of resistivity is termed conductivity σ . Its dimensions are expressed as S/m.

For an AC measurement, the capacitance properties of the rock manifest themselves in addition to the pure resistance. In this case, *Ohm's law* is generalized to allow for the resulting frequency-dependent effects, and the ratio of the voltage to the current is defined as the impedance, rather than the resistance,

$$Z(\omega) = \frac{V(\omega)}{I(\omega)} \quad (5.3)$$

and the resistivity is given by

$$\rho^*(\omega) = kZ(\omega) = \frac{1}{\sigma^*(\omega)} , \quad (5.4)$$

where ω is the angular frequency ($=2\pi f$).

At any given frequency of excitation the measured voltage incurs a phase lag in time relative to the applied current (Figure 5.3a). To describe this effect, the output voltage can be expressed as the vector sum of both in-phase and quadrature components. Therefore, the electrical resistivity $\rho^*(\omega)$, or conductivity $\sigma^*(\omega)$, of the sample can be expressed as a complex quantity (Figure 5.3b). Both the magnitude and phase lag (or angle) of the voltage relative to the input current depend on the specific electrical properties of the liquid and/or the solid phases. This is the origin of the term *complex resistivity* (CR) [Cole and Cole, 1941; Pelton et al., 1978; Ruffet et al., 1991].

On a microscopic scale, the petrophysical character, electrochemical processes or a combination of both are likely responsible of the frequency-dependent effects for unconsolidated rocks when energized with an external AC current. The concept of the *ionic double layer*¹ forms the theoretical basis for understanding the main frequency-dependent (or dielectric) conduction mechanism [Ward, 1990]. The inner surfaces of rock-forming grains characteristically have an unbalanced layer of negative charges resulting from the continuous passing of the negative ions (or anions of small diameters) through the throats. Whereas, the positive ions (or cations of relatively large diameters) get held up. The negative charges attract a certain number of positive ions in the fluids, producing a highly viscous low-mobility layer in the fluid immediately adjacent to the grain-surfaces, and causing ionic concentration

¹The electrode (or grain) polarization is only occurred due to overvoltages resulting from the interchangeable ionic–electronic conduction at the interface between disseminated metallic particles (or grains) and fluids through narrow pore-throats inside the host rock.

gradient termed *membrane* (or *electrolytic*) *polarization*. Likewise, any observed change in resistivity with excitation frequency results from the inability of ions to move freely through the electrical obstruction formed by the double layer inside the throats (or ion-selective membranes). A common rule, but not always applicable [Marshall and Madden, 1959], membrane polarization tends to be pronounced in the presence of clay particles and less prevalent when the pore-fluids have high salinity.

Complex resistivity measurements have been performed for many years in mining geophysics [e.g. Zonge and Wynn, 1975; Pelton et al., 1978] and are widely known under the name of *spectral induced polarization* (SIP) methods. SIP measurements imply a frequency spectrum of the complex resistivity $\rho^*(\omega)$ components, such as in-phase or *resistive* component $\rho'(\omega)$ and quadrature or *reactive* component $\rho''(\omega)$, and hence the magnitude of complex resistivity $|\rho^*(\omega)|$ and phase angle $\theta(\omega)$ by which current and voltage are shifted. The resistive component is mainly related to the electronic (or ohmic) conduction, whereas the reactive one is associated with the dielectric conduction and varies over the frequency spectrum. In the series mode, the inter-relationship between these parameters is

$$|\rho^*(\omega)| = \sqrt{\rho'(\omega)^2 + \rho''(\omega)^2} \quad (5.5)$$

and

$$\theta(\omega) = \tan^{-1} \left[\frac{\rho''(\omega)}{\rho'(\omega)} \right], \quad (5.6)$$

where i is the complex operator ($=\sqrt{-1}$).

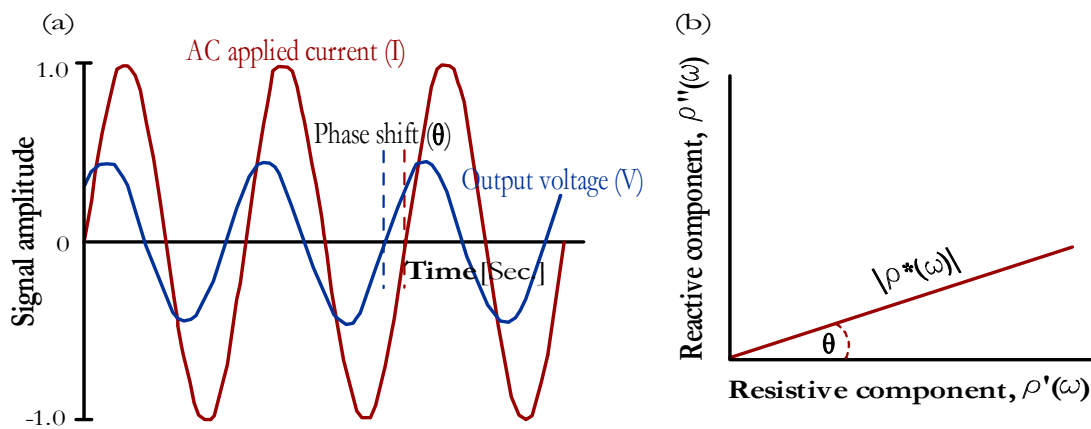


Figure 5.3: (a) Typical sinusoidal electric current and voltage amplitudes used to determine the complex resistivity and (b) relationship between resistive and reactive components of the complex resistivity.

5.2.2 Samples and Terminal-configurations

A total of 16 sedimentary blocks were collected from the surface and underground outcrops at the opencast mine 'Garzweiler I', avoiding the air-dried regions. Measurements of electrical properties were performed on a suite of 16 cylindrical samples (or plugs) prepared from such blocks in their natural state. Sample labels and descriptions are given in Table 5.1. Due to the fine-grained nature of the studied sediments, the dimensions for each sample are highly greater than the dimensions of the rock-forming grains. Therefore, all individual grains play an equal role in determining the electrical properties of the sample, and the results should be representative of the rock in bulk.

Normally, each sample is symmetrically clamped between two metal plates serve as current electrodes, C_1 and C_2 , inside a non-conducting cylindrical holder (about 60 mm in length and 36 mm in diameter), which supports a choice of two- or four-terminal configurations. In a four-terminal configuration, a separate pair of potential electrodes (small silver probes), P_1 and P_2 , is placed at a distance of more than 10 mm from the current electrodes along a line perpendicular to the sample faces. The voltage measurements are usually repeated four times with different potential electrode combinations to validate the results. Figure 5.4 shows the typical way in which current and potential electrodes may be attached to a rock sample in a four-terminal configuration. The two-terminal configuration uses the same metal plates as current and potential electrodes. Necessary requirement for applying such configurations is that good contact, i.e. a minimum amount of contact resistance, be obtained between electrodes and the sample.

Electrode configuration plays an important role in reducing the measurement errors, particularly for SIP methods. If the two-terminal configuration is used, there is no way to measure the resistance (or impedance) of the sample without including the resistance (or impedance) of the current electrodes. In addition, there may be localized electrical disturbances where the current is injected into the sample and consequently must be added to the sample polarization. This can lead to inaccuracies in the measurements, particularly at lower frequencies. In the four-terminal configuration, the potential electrodes are placed well away from current stimulus which means that no voltage is dropped across the current electrodes, leading to more accurate voltage measurements across the sample itself.

All laboratory measurements reported here were carried out, at laboratory temperature and pressure, utilizing the four-terminal configuration in order to minimize the electrode contact resistance and polarization problems inherent in two-terminal systems at lower frequencies.

Lithology	Sample label	Sample type	Visual inspection
Surface Sand [8]	S1, S2	Disturbed	Fine/medium, some gravel, traces iron oxides, light yellow
Clay masses [8]	S3, S4*	Undisturbed	In-organic, traces fine sand and iron oxides, yellowish green
Garzweiler Coal Seam [6E]	S5, S6	Undisturbed	Low dense, brownish black
Neurath Sand [6D]	S7, S8	Disturbed	Fine, traces mica, light/pale yellow
Neurath Sand/Silt [6D]	S9, S10	Disturbed	Fine, some silt, traces lignite and mica, pale/grayish yellow
Frimmersdorf Coal Seam [6C]	S11, S12	Undisturbed	Low dense, brownish black
Frimmersdorf Clay [6C]	S13, S14*	Undisturbed	Organic, traces fine sand, dark brown
Frimmersdorf Sand [6B]	S15, S16	Disturbed	Fine, traces mica, pale yellow

*Samples subjected only to DC measurements

Table 5.1: Description of the rock samples collected at the opencast mine 'Garzweiler I.' The stratigraphical extent is approximately from the Early/Middle Miocene Ville Formation (horizons 6B, 6C, 6D and 6E) to the Early Pliocene Hauptkies Series (horizon 8).

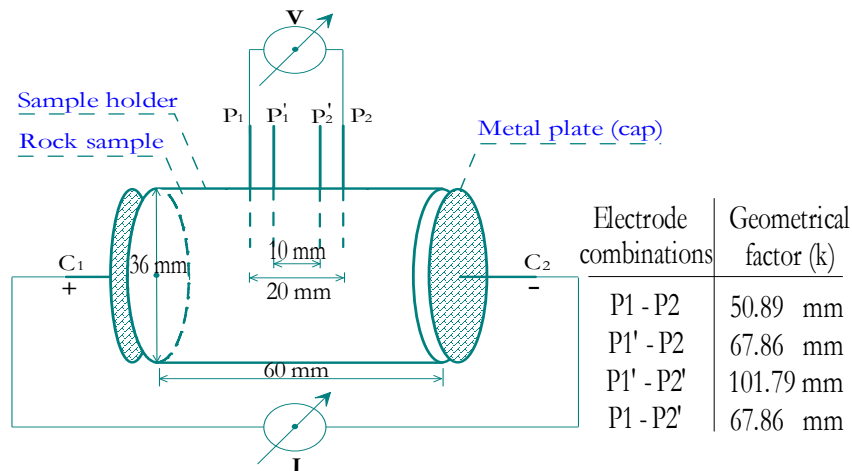


Figure 5.4: Simplified schematic of the four-terminal configuration used for measuring resistivity of a rock sample in the laboratory. The geometric factor k is calculated for different potential electrode combinations.

5.2.3 Direct-current Measurements

In practice, conventional DC (zero-frequency) measurements are infrequently carried out in the laboratory. If, however, direct-current was passed into a rock sample, microscopic polarization would be occurred from the bulk migration of charges in response to a constant applied electric field. As a result, the mobile ions are built up excessively around the electrodes and the electrode polarization effect would be increased. This would create an artificial DC extravoltage that would interfere with the resistivity measurements. Alternatively, geophysicists usually shield themselves from such unwanted capacitive behavior by alternating the polarity of the DC current over a limited very-low frequency range (typically from 1 to 20 Hz). Within this preferable range, the measured resistivity doesn't change very much. Here the method is still referred to as 'DC measurements' and *Ohm's law* (Equation (5.1)) can be directly applied to determine the sample resistance, and the corresponding bulk resistivity.

The present DC measurements were carried out on all studied rock samples using a '4-Punkt light μC ' resistivity meter (Lippman Geophysikalische Messgeräte, Germany) as illustrated in Figure 5.5. For fixed 4.16 Hz frequency, the strength of electrical current was usually variable between 10 and 100 μA , while the measured voltage at the potential electrodes was up to 200 mV.

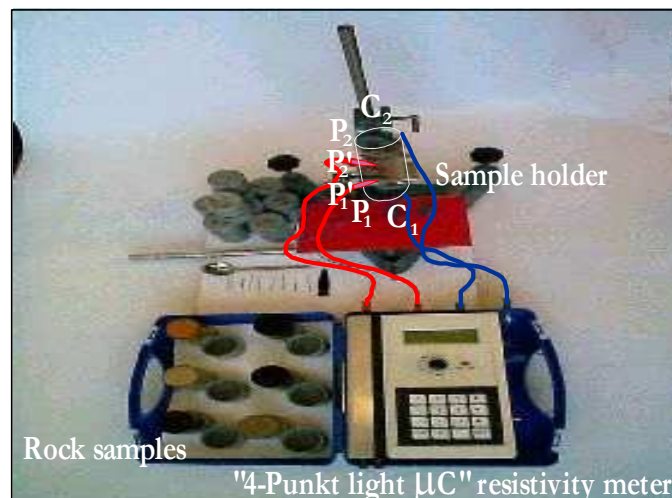


Figure 5.5: Photograph showing the experimental setup for the laboratory DC measurements.

5.2.4 Spectral Induced Polarization Measurements

Complex resistivity measurements were carried out only on 14 selected samples using 'Solartron 1260 impedance/gain-phase analyzer' (Solartron Analytical, UK) as pictured in Figure 5.6. Over a broad frequency range from 0.1 Hz to 1 MHz, the strength of electrical current ranged between 0.06 and 60 mA, while the measured voltage at the potential electrodes was up to 1V. The measuring system is interfaced with a logging PC, providing flexible software ('Z60W', Scribner Associates Inc., USA) that controls all experiments at the frequency range of interest and stimulus levels, and is able to plot results in a wide variety of formats. The method is an auto-balancing bridge with 0.1% measuring accuracy. The analyzer generates a variable AC sinusoidal signal which is applied to a series circuit consisting of the sample and a variable resistance–capacitance (RC) network. The voltage drop across the sample and the RC network is equal when the bulk resistivity of the RC network is adjusted to equal the sample resistivity.

At higher frequencies, accurate measurements are a specific problem due to errors introduced by fixturing and cabling (i.e. electromagnetic coupling due to mutual inductance between current and potential wires) in conjunction with the instrument inherent losses. All these parasitic effects are frequency-dependent and must be added to the sample polarization, and can be minimized either by an internal auto-compensation or suitable data correction. To ensure that the measuring system is operating correctly and to ensure that such unwanted spectral behavior is just limited to the higher frequencies, additional measurements were carried out over the same frequency span on two different dummy (synthetic) samples SX and SY (Figure 5.6). Their bulk resistivities of about 15 and 390 Ωm respectively [Bergers, 2002].

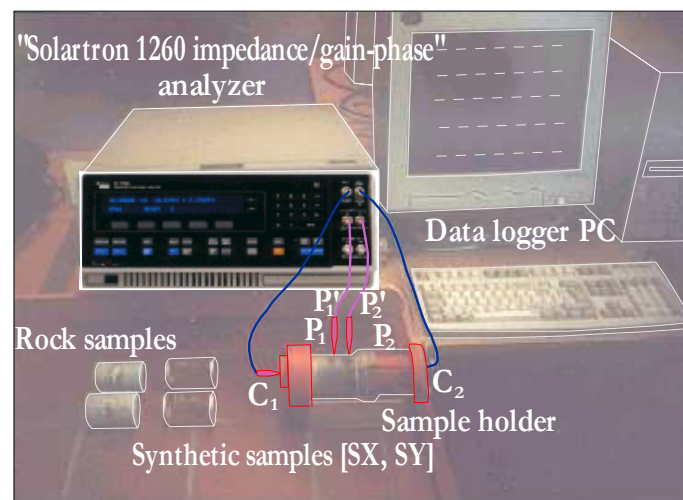


Figure 5.6: Photograph showing the experimental setup for the laboratory SIP measurements.

5.3 Results and Interpretation

5.3.1 Resistivity Magnitude and Phase Angle Spectra

Figure 5.7 demonstrates the typical measured *SIP spectra* (curves showing the variation of either resistivity magnitude or phase angle over seven decades of frequency) for two rock samples, Neurath Sand S8 and Frimmersdorf Coal S12. On a limited portion of the frequency range, below 1 Hz, signals are slightly noisy. From 1 to around 10^4 Hz, the measured phases show that no phase angle difference greater than 1 milliradians. This is in accordance with

approximately flat magnitude spectra or a slight frequency-dependence. This predominant behavior can be attributed to the bulk response for each sample. A frequency-dependence becomes obvious at higher frequencies: samples are characterized by magnitude and phase which change smoothly at approximately a constant rate with increasing frequency, whilst the measurement residual errors increase. A similar picture is obtained from the calibration tests on the synthetic samples SX and SY (Figure 5.8) at frequencies above 10^4 Hz, where the phase angles are smoothly deviated from zero milliradians, particularly for the more resistive sample SY. This spectral behavior is likely a result of an inductive coupling due to the fixturing and cabling, and unfortunately has not been compensated during the measurements.

5.3.2 Argand Diagrams

Three different regimes can also be identified on *Argand diagram* (a complex-plan plot consists of negative imaginary ordinate and positive real abscissa of the complex resistivity) for each sample (Figure 5.9). A very-low frequency noise regime is represented by clustered data points below 1 Hz. The bulk sample regime, i.e. a weak Cole-Cole polarization, is represented by a depressed arc (or semicircle) and is distinguishable from the high frequency regime, which appears as either a pseudo arc (sample S8) or an almost straight line (sample S12), at distinct point(s) close to a frequency of around 10^4 Hz. *Scromeda and Katsube [2001]* showed that the bulk sample resistivity can be determined on Argand diagram from the intersection point of the noise-free semicircle with the real abscissa at lower frequencies (i.e. DC level). This bulk resistivity is a function of the specific electrical properties of the liquid and/or the solid phases, and is understood to exclude effects such as electrode and dielectric polarizations.

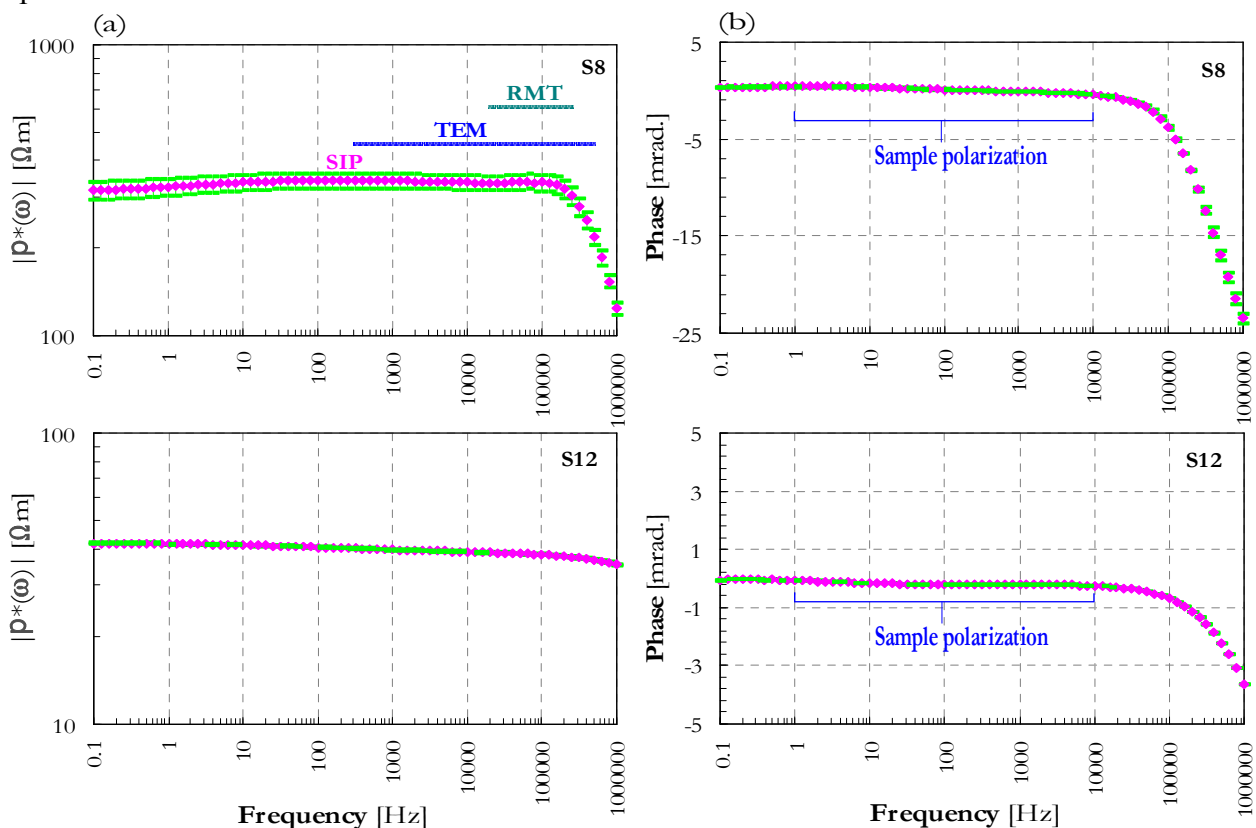


Figure 5.7: (a) Complex resistivity magnitude and (b) phase spectra of the rock samples S8 (Neurath Sand) and S12 (Frimmersdorf Coal). The error bars describe the standard deviations derived from the repeated measurements with different electrode combinations. Frequency ranges of interest for RMT and TEM surveys are also displayed.

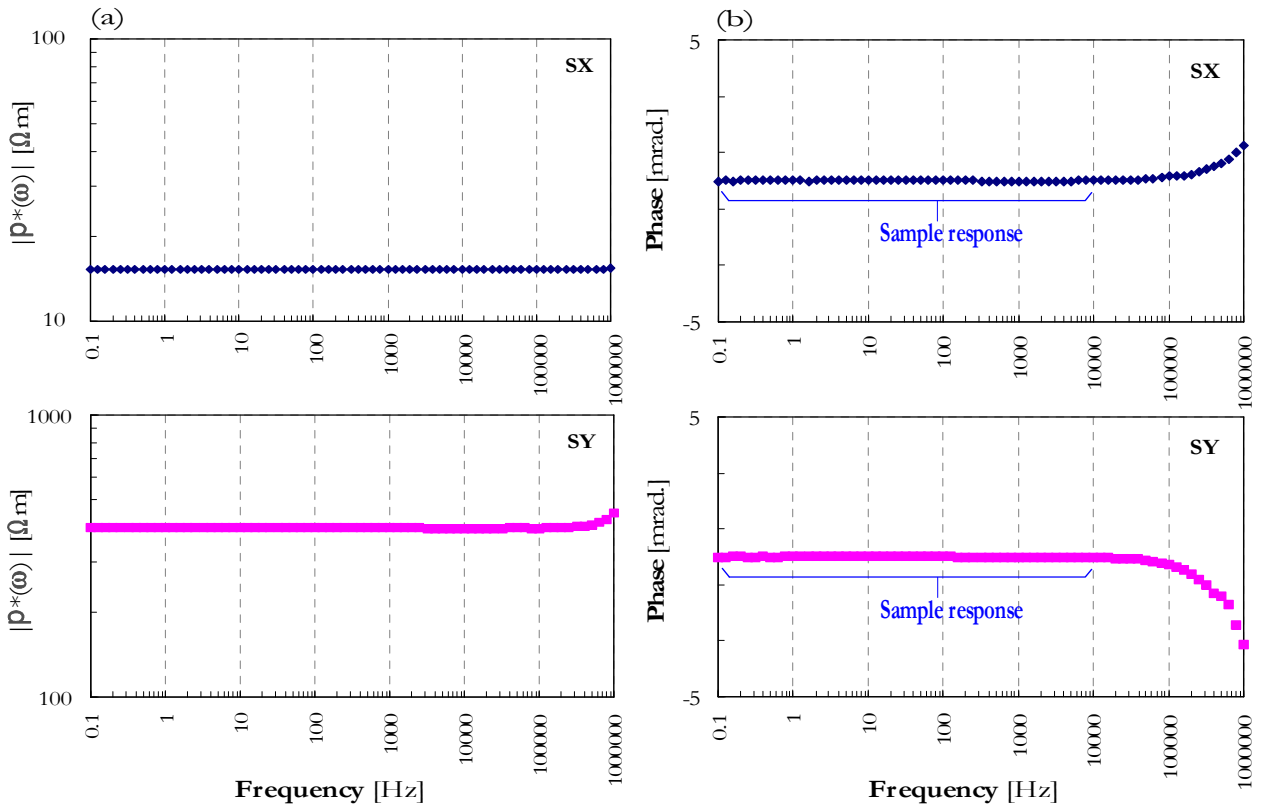


Figure 5.8: (a) Complex resistivity magnitude and (b) phase spectra of the synthetic samples SX and SY. The error bars are visually indistinguishable.

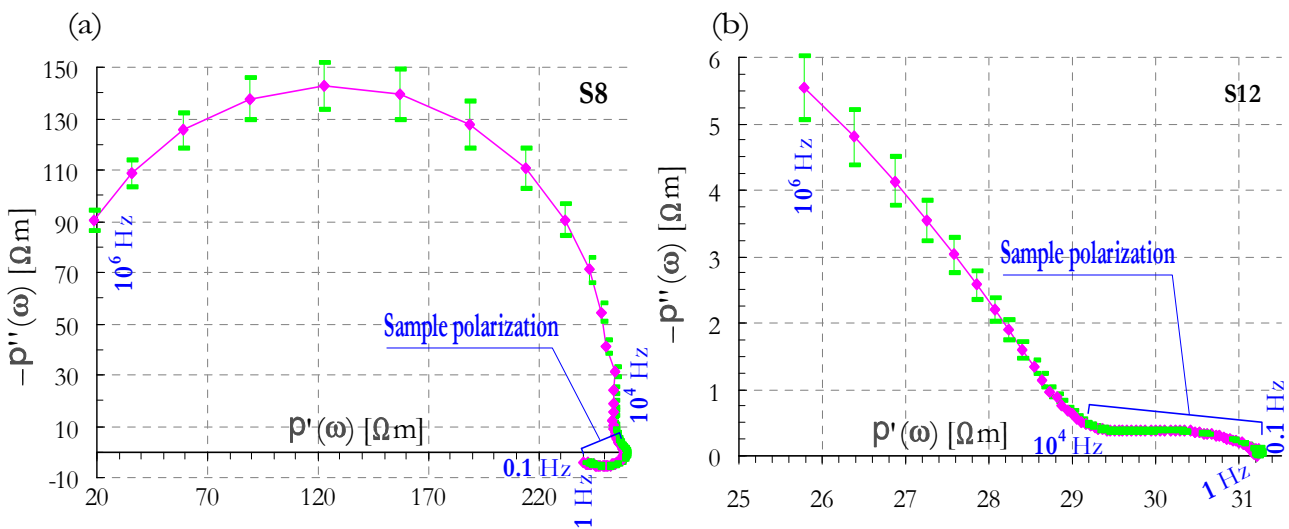


Figure 5.9: Argand diagrams for the rock samples (a) S8 (Neurath Sand) and (b) S12 (Frimmersdorf Coal). The real and negative imaginary parts of the complex resistivity are plotted against each other. The frequency increases from right to left along the trajectory. The error bars describe the standard deviations derived from the repeated measurements with different electrode combinations.

Upon completing all SIP measurements, the results confirmed that reliable data can be obtained neither below 1 Hz nor above 10^4 Hz. Furthermore, they indicated that all studied rock samples are weakly polarizable, as argued by the slight frequency-dependence of the measured magnitude and phase spectra (Figure 5.10). On a microscopic scale, this insignificant IP effect shows up as a depressed arc for brown coal and clay samples, and is almost variable for most sand samples. This presumably indicates that the samples have a limited internal electrochemical (or dielectric) activity, which may be returned to the extensive dewatering at the opencast mine 'Garzweiler I.'

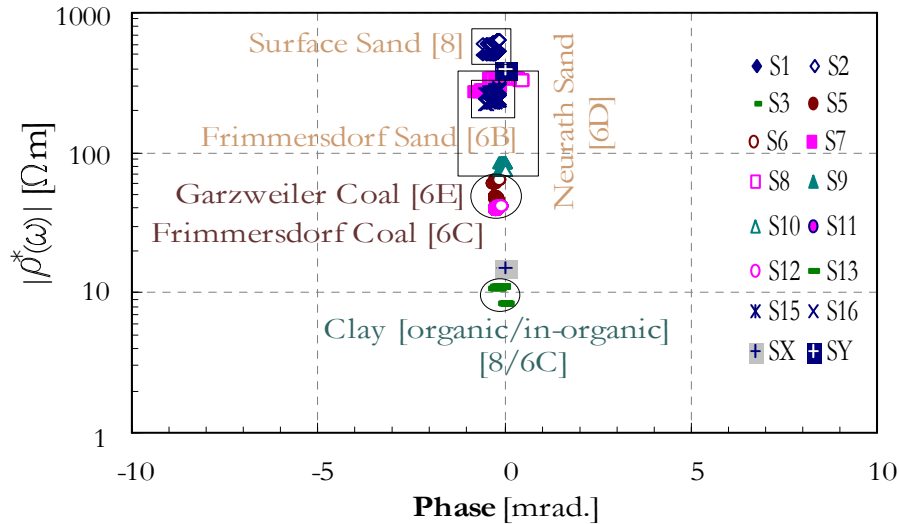


Figure 5.10: A cross-plot of SIP resistivity magnitudes versus phase angles over the reliable frequency range, from 1 Hz to around 10^4 Hz, for all studied rock samples at the opencast mine 'Garzweiler I.' Data from synthetic samples are also displayed.

5.3.3 IP Measures

Analogous to the frequency-domain IP field methods, SIP data can be represented by the *percent frequency effect* (PFE) parameter (the fractional rate of change in resistivity magnitude as a function of frequency) defined as

$$\text{PFE} = \frac{100[\rho_i^*(\omega) - \rho_{i+1}^*(\omega)]}{\rho_i^*(\omega)}, \quad (5.7)$$

where i and $i+1$ represent any two frequencies having a geometric-mean frequency in between against it a measured phase value can be found over only six decades, and $i=0.1, 0.32, 1.0, 3.20, 10, 3.20 \times 10, 10^2, 3.20 \times 10^2, 10^3, 3.20 \times 10^3, 10^4, 3.20 \times 10^4, 10^5, 3.20 \times 10^5$ Hz. This geometric progression works also well for the frequencies in between.

As might be expected, the resulting PFE spectra for the rock samples S8 and S12 (Fig. 5.11a) are approximately flat over the frequency range from 1 to around 10^4 Hz. At frequencies below 1 Hz, data points are slightly noisy. While at higher than 10^4 Hz, the PFE parameter is varied smoothly as a function of frequency.

Several authors ensured over the linear relation between the phase angle and PFE in the form

$$\theta(\omega) = k' \text{PFE}, \quad (5.8)$$

where k' is a proportional constant (or slope) which has an approximate range of -0.3 to -0.5 mrad./% for different grades of mineralization [Scott, 1971]. This constant is usually considered as a significant parameter in the frequency-domain IP methods. However, it was not clear whether this slope should be constant or vary slightly for different types of sediments. Van Voorhis *et al.* [1973] found that for phase angles which are slowly varying functions of frequency, if the PFE is computed between two low frequencies and the phase angle was measured near their geometric-mean frequency, the PFE is linearly proportional to the phase angle. They also showed that the PFE parameter is independent of particular measurement frequency, rather it depends on the spread between measurement frequencies

and a specific numerical exponent. Recently, *Bergers* [2002] extended this proportionality over the spectral coverage between 0.1 and 10^4 Hz to cross-check paths of slightly frequency-dependent SIP spectra for some contaminated and uncontaminated samples.

Figure 5.11b illustrates the relation between the computed PFE and measured phase angle for the rock samples S8 and S12. Here the lower and higher frequency regimes for each sample can be clearly identified and do not exhibit any linear behaviors. At the intermediate frequency range, from 1 to around 10^4 Hz, an almost excellent linear behavior can be observed and fitted using the least-squares fitting with slopes of -0.32 and -0.24 mrad./% for S8 and S12 respectively. The attractive feature of this display is the slope k' varies slightly for different types of sediments. It is also possible to correct for either the lower or higher frequency effects, reference to the obtained least-squares line for each data point outside the reliable intermediate range. In this case, and in accordance with the rough rule given by *Scromeda and Katsube* [2001], if the corrected arc for each rock sample is extrapolated back to intersect the real abscissa at lower frequencies on Argand diagram, we will meet a resistivity value approximately equal to the corresponding value measured by the DC system. However, this correction was not urgently needed and not performed on all studied samples, partly because the inductive coupling itself exhibited varying trends at higher frequencies.

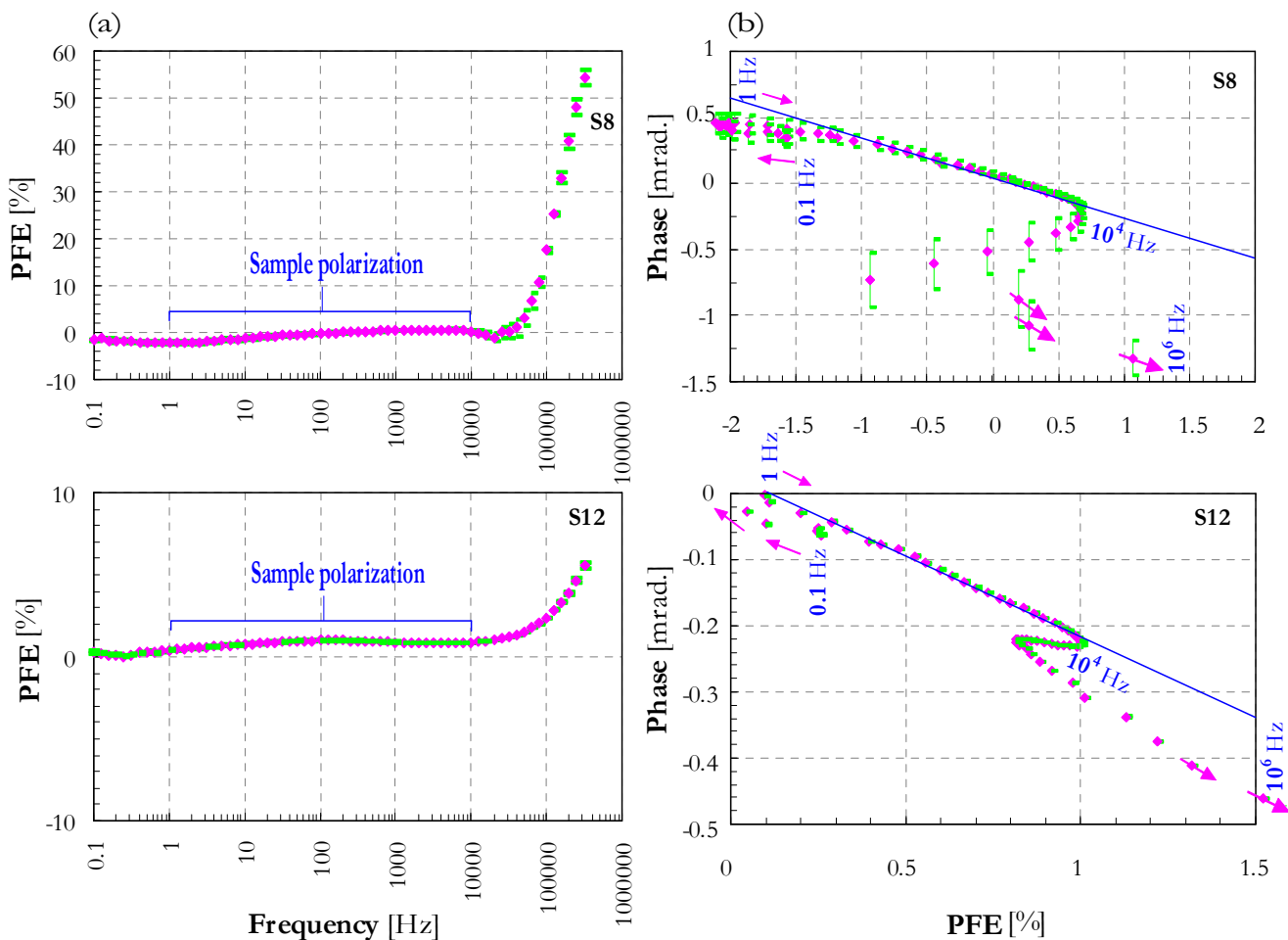


Figure 5.11: (a) Frequency-independence of the PFE parameter and (b) the linear relation between the PFE parameter and phase angle for the rock samples S8 (Neurath Sand) and S12 (Frimmersdorf Coal). The least-square lines (on right) are fitted through the center-of-gravity of each sample data with slopes k' of -0.32 and -0.24 mrad./% for S8 and S12 respectively.

Because all studied rock samples exhibit a slight frequency-dependence, the mean PFE for each sample tends to be a few percent, whereas it does not when IP effect is present. This makes categorization of the studied sediments in terms of IP signatures, only from PFE values, difficult. Alternatively, the *metal factor* or *metallic-conduction factor* (MF), originally suggested by *Marshall and Madden [1959]*, can be introduced instead. This can be computed for each data point by normalizing the PFE parameter with respect to the initial (or DC) resistivity $\rho_i^*(\omega)$ and multiplying by $2\pi \times 10^3$. The normalization compensates for the lower resistivity of obviously conductive sediments, such as brown coal and clay samples. Moreover, the multiplying factor simplifies calculations and gives convenient numbers which avoid the need of continually writing down a very small decimal fraction. Metal factor has units of conductivity.

Table 5.2 summarizes the arithmetic-mean DC and SIP bulk resistivities, together with measurement uncertainties, and the characteristic IP parameters for all studied rock samples. The obtained k' values were typically ranged from -0.30 to -0.48 mrad./% for sand, sand/silt and clay samples, while brown coal samples showed pronounced lower values averaged as 0.21 mrad./%. The brown coal and clay samples showed higher MF values than those obtained from sand and sand/silt samples. The clay ranges seemed to be a little wide. This clearly show that besides the standard frequency-domain IP measures, the constant k' can be successfully used in categorizing different types of sediments in terms of IP signatures. Therefore, it should be considered as one of the common IP measures.

Sample label	ρ_{DC} [Ωm]	σ_{sDC}^* [Ωm]	ρ_{SIP} [Ωm]	σ_{sSIP}^* [Ωm]	PFE [%]	k' [mrad./%]	MF [S/m]
S1	664.5	57.0	500.5	53.3	0.72–1.35	-0.48	7.6–15.5
S2	638.8	62.1	600.1	66.4	0.74–1.40	-0.47	6.5–13.1
S3	10.2	0.3	8.3	0.2	-0.01–0.63	-0.31	-6.3–472.9
S4	12.4	0.8	–	–	–	–	–
S5	50.0	2.1	45.5	2.1	0.82–1.22	-0.17	110.3–155.6
S6	42.0	3.1	60.1	4.1	0.62–1.34	-0.18	60.0–140.0
S7	222.4	16.3	270.3	5.9	0.52–2.30	-0.37	10.9–51.9
S8	282.2	28.0	340.5	40.5	-1.87–0.68	-0.32	-36.0–12.6
S9	60.6	1.4	85.8	2.2	-0.07–0.63	-0.31	-4.9–47.3
S10	79.7	5.4	75.6	1.9	-0.07–0.66	-0.30	-5.7–54.94
S11	36.1	1.2	40.8	0.4	0.42–1.06	-0.21	62.9–164.1
S12	37.9	1.8	39.2	0.4	0.20–1.01	-0.24	30.0–156.3
S13	14.8	1.1	11.3	0.4	0.27–1.08	-0.33	154.0–626.3
S14	16.6	1.1	–	–	–	–	–
S15	163.1	3.7	270.8	7.4	0.58–1.20	-0.41	12.7–27.4
S16	199.9	18.7	230.7	6.2	0.61–1.26	-0.42	15.9–34.5

*Standard deviation.

Table 5.2: Summary of the arithmetic-mean DC and SIP bulk resistivities, measurement uncertainties and the characteristic IP parameters for all studied rock samples at the opencast mine 'Garzweiler I.'

5.4 Discussion

The bulk resistivities obtained from both DC and SIP measurements on the same rock samples are approximately similar and fall between, if not identical to, the other published ranges for brown coal, sand/silt and clay (compare Table 5.2 with Figure 5.1). Moreover, they showed much higher values than those picked from resistivity logs, particularly for the permeable (sand/silt) and semi-permeable (brown coal) units (compare Table 5.2 with Figure 5.2). The

established resistivity differences within Neurath Sand can be attributed to the considerable amount of silt present in its lower part which contributes negatively to its bulk resistivity. This may suggest a kind of resistivity overlap can therefore be occurred between the lowermost Neurath Sand and Frimmersdorf Coal, if a real RMT/TEM survey was conducted. Although the resistivity values of the surficial clay masses and Frimmersdorf Clay are found to be apparently distinguishable from that of brown coal, it is still reasonable to combine them as a single conductive unit, having average resistivity of both.

Limited published results are available on the frequency-independent sediments and on the treatment of their bulk resistivities. The present SIP data analysis assumes that bulk resistivities obtained for all studied rock samples are sufficiently accurate, only if a slight frequency-dependence is considered. In many other respects, the SIP data for rock samples exhibit a significant frequency-dependence. Therefore, they should be modeled by using either equivalent RC networks, where series electrical circuits are dominant, [*Scromeda and Katsube, 2001; Scarlato et al., 2004*] or electrochemical formulas (i.e. Cole-Cole polarization) [*Pelton et al., 1978*]. That means, the resistivity and phase spectra should be reasonably fitted to the forward responses derived from each technique in a non-linear fashion to determine exactly their bulk resistivities. Additionally, this kind of modeling may yield useful direct information on pore wall morphology, hydraulic permeability and fluid saturation of the rock.

CHAPTER 6

SUMMARY AND CONCLUSIONS

The entire Cenozoic unconsolidated fill of the Lower Rhine Embayment in Germany hosts the largest single lignite, or brown coal, deposit in Europe which covers an area of some 2,500 km² to the northwest of Cologne. Cologne-based RWE-Power AG is responsible for mining of brown coal in Rhineland with an annual production of around 100 million metric tons. Rhineland brown coal accounts for around one-quarter of the public electricity supply in Germany. Growing competition from other energy sources in Germany, such as imported hard coal, made it essential for RWE-Power AG to minimize costs, especially in field-work functions like expensive drilling and direct-sampling. Here the geophysics enters the picture. The present study has been devoted to carrying out radiomagnetotelluric (RMT) and transient electromagnetic (TEM) investigations over the shallow coal seams at the opencast mine 'Garzweiler I.' The main objectives of the survey were to highlight the applicability and efficiency of RMT and TEM methods in an area like brown coal exploration, and to image the vertical electric resistivity structure of these seams.

Consequently, a total of 86 azimuthal RMT and 33 in-loop TEM soundings were carried out along six separate profiles over two opencast benches at the 'Garzweiler I' mine. These small-scale benching areas are referred to as 'Coal-covered Area' and 'Sand-covered Area.' The 'Sand-covered Area' is located at relatively higher altitude to the northeast of the 'Coal-covered Area' and bordered on the northerly side by a large hillock. The topography along the survey profiles is almost of very flat relief. The 'Coal-covered Area' is bordered on the northerly side by a small hillock and edged on the southerly side with a very steep cliff to another subjacent mining bench. The area displays a slightly rugged topographic relief. The local stratigraphy at the survey areas typically comprises a layer-cake sequence, from top to bottom, of Garzweiler, Frimmersdorf and Morken coal seams embedded in a sand background, consisting of Surface, Neurath, Frimmersdorf and Morken Sands. A considerable amount of clay and silt intervenes the whole succession.

In order to predict RMT/TEM responses at the survey areas and to determine how sensitive a real survey would be for the target coal seams, one-dimensional (1D) forward modeling was performed over the real RMT frequency range or the reliable Nano/ZeroTEM time range. The suggested geoelectric model fashions typically represented local stratigraphy at the survey areas. All synthetic data were then inverted in terms of 1D smoothed-earth models. A fairly well recovery and data fit were obtained only for the major stratigraphic units, including the shallowest conductive Garzweiler, Frimmersdorf Coals within their fairly resistive sand background. The results failed to reproduce the Morken Coal or Sand at all. They showed that distinguishing between Neurath Sand and the underlying sand/silt or between Frimmersdorf Coal and the underlying organic clay, solely from a real RMT/TEM survey would be difficult.

The presence of a highly-conductive surficial clay layer (or mass) within the Surface Sand, with a thickness of at least 2 to 3 m, drastically changed the smoothed-earth model at only shallower depths, where there is no resemblance with the undisturbed synthetic model. The responded apparent resistivities, corresponding to different clay thicknesses, either for the whole RMT frequency or for the TEM early- to intermediate-time ranges, were all well-separated from each other and significantly different from that of the synthetic model without the clay layer. This indicated that the surficial clay layer can therefore be detected and uniquely resolved if a real RMT survey was conducted. The underlying succession of the Surface Sand, Garzweiler Coal and Neurath Sand/Silt appeared as a moderately-conductive blocked-layer with increasing clay thickness, and could not be resolved as individual units, but only as a whole. Here the clay layer screened (or blanked) the underlying conductive coal seams from being accurately sounded. Whereas, the clay layer can also be detected and resolved if a real TEM survey was conducted, but not uniquely because the shallower succession of the surficial clay and underlying Surface Sand and Garzweiler Coal appeared as a moderately- to highly-conductive blocked-layer with increasing clay thickness. Because the negative contribution of the surficial clay layer (or mass) gradually decreased with time and became insignificant at later-times, it did not completely screen the underlying conductive coal seams from being sounded. Generally, these synthetic examples dictated that the resolution of a RMT/TEM survey is poor for thin resistive layers like Surface Sand.

Following the data viewing, deconvolution and transformation at each sounding, the RMT/TEM data were inverted in terms of 1D smoothed-earth models to drive a reasonable start guess for further 1D full non-linear inversion. No a-priori information was initially introduced. Beginning from a control RMT/TEM sounding and using a kind of recursive starting modeling, the final inverted sections at the 'Coal-covered Area' were readily very consistent. They showed a satisfactory data fit and well correlation with the borehole-geology, assuming that the general geoelectric model is essentially of 1D character. The final inversion statistics (estimated error bounds, relative sensitivities, importances, etc.) for the layer parameters were used to cross-check their resolution in detail at all soundings. They showed clearly that none of the conductive coal seams were poorly resolved. The resolution depths were up to 30 and 100 m for RMT and TEM soundings respectively. Collectively, the 1D RMT/TEM earth sections exhibited clearly the Garzweiler Coal and Frimmersdorf Coal/Clay within the Surface Sand, Neurath Sand/Silt and Frimmersdorf Sand. The deepest Morken Coal and Sand were beyond the depth-of-investigation of the present measurements.

Although the 1D RMT/TEM smoothed-earth sections at the 'Sand-covered Area' were quite inconsistent and not well-correlated with the bore-hole geology, the layered-earth sections were sufficiently consistent and showed a satisfactory data fit. The surficial clay masses and underlying coal seams were almost uniquely-determined as individual units. Nevertheless, at some considerable number of soundings the most of inverted layer parameters for themselves did not show regularly or sufficiently high importance values as usual, and not agreed well with the borehole-geology. Here the 1D interpretation had almost reached its limits to explain the validity of the 1D assumption. Unfortunately the most promising way of inverting the RMT and TEM data jointly turned out to be unnecessary, either due to the close resemblance between the shallower skin- and diffusion-depths for the higher frequencies and earlier sampling times respectively or because the model inconsistencies between both the data sets.

Systematic experiments, including 2D RMT inversion runs and corresponding sensitivity calculations, were performed for each measuring azimuth. The goals were to cross-check the effect of nearby-topography on the azimuthal RMT data at the survey areas, to derive reasonable estimates of the maximum depth-of-investigation for all soundings and to indicate whether increasing the number of operating frequencies at each sounding increases the resistivity resolution or not. The obtained smoothed-earth sections at the 'Coal-covered Area' for different measuring azimuths were almost very similar, revealing that the data have almost 1D character. Because the surface impedance is independent of the measuring azimuth, all frequency data could be used safely at each sounding, in both 1D and 2D inversion, to produce highly-resolved resistivity models. This also indicated that the nearby-topography has insignificant effect on the RMT data, and that the distances between the nearby-topography and main parallel profiles were chosen adequately enough to avoid its effect. The final smoothed-earth sections showed almost the same 1D coal-sand boundary, but less distinctive. Here one of the best uses of 2D inversion scheme was to confirm that the 1D character is reasonably valid.

At the 'Sand-covered Area', the most dramatic nearby-topography effect was occurred mainly at measuring azimuths perpendicular to the northern large hillock, where the entire current flow should round from this hillock to the ground of the area or vice versa. Whereas, the magnetic field remains uniform along the hillock. That means, the surface impedance is critically dependent of the measuring azimuth, and of course using all frequency data at each sounding, in either 1D or 2D inversion, would be impossible. On the other hand, the derived models for azimuths parallel and subparallel to the hillock showed all reliable resistivity anomalies which are not significantly affected by the nearby-topography. Adopting this view, the joint-inversion of both TE- and TM-mode data, for measuring azimuths 30° and 120° N respectively, was finally chosen and found to give much better resolution of smoothed-earth sections. The surficial clay masses and Garzweiler Coal were positioned reasonably well within their sand background, yet the feeling of more confidence in the interpretation ever left. Generally, the clay-coal-sand boundary was more sharp and well-resolved as the number of operating frequencies increased at each measuring azimuth. A maximum depth-of-investigation for the RMT soundings was averaged either around 30 m ($\approx 2.5z^*$) at the 'Coal-covered Area' or around 25 m ($\approx 2z^*$) at the 'Sand-covered Area.'

Trial-and-error 3D TEM forward simulations were performed at each survey area using initially its derived 1D TEM layered-earth section as starting model. At the 'Sand-covered Area', the resulting highly-conductive surficial anomaly underneath each distorted sounding was symmetrically approximated by vertically-coaxial surficial blocks, their bulk resistivity decreases inwards. This hypothesized that the cause of the abnormal transients is geological, where the deep-layering does not change, but is disturbed by separate surficial clay masses (or lenses), thinning away from the sounding centers. Expectedly, the whole layer sequence was used for modeling undistorted sounding data, where a resistive basement (or Frimmersdorf Sand) below the Frimmersdorf Coal/Clay was always needed. To model distorted transients reasonably, a conductive basement (or Frimmersdorf Coal/Clay) must be vertically extended to simulate how the field decays much slower than it does over a resistive basement. Therefore, the final earth model has a dual resistive-conductive basement. Attempting to find a single basement, which may give a reasonable fit to all field data sets along the profile, would not be realized. Experiments showed that the surficial blocks are significantly needed to explain the early-time data, and they effectively contribute to the total model conductance. Indeed, the presence of the surficial blocks underneath each distorted sounding within the suggested model did not alter the late-time fitting, where the model essentially needs only to a conductive basement. Therefore, the 3D forward calculations ascertained that the upper boundary of Frimmersdorf Coal reasonably exists at its normal depths at the distorted

soundings. Yet unclear is its lower boundary can be normally interpolated between the neighboring undistorted soundings or not. However, in all cases, they reduced the inevitable non-uniqueness obtained by the 1D interpretation of the layered-earth parameters at the distorted soundings.

Furthermore, the 3D TEM forward calculations showed clearly that there is almost no significant difference between the calculated 3D responses obtained with and without including nearby-topography within the earth models at the survey areas. This strongly suggested that there no any EM coupling between the topographic features and underlying conductive coal seams. In the extreme case, a slight marginal influence on the predicted data was relatively notable close to the very steep southern cliff at the 'Coal-covered-Area', where a steep horizontal field gradient would be expected. This influence was largely restricted to early-times and can be easily recovered from changing only block resistivities stepwise, reference to the resistivity values obtained from the laboratory measurements for each sediment type.

The final RMT and TEM resistivity models displayed a satisfied correlation with both thicknesses derived from the stratigraphic-control boreholes and resistivities measured from direct-current (DC) and spectral induced polarization (SIP) laboratory techniques on 16 rock samples. Generally, they could identify the major stratigraphic units at the survey areas, i.e. the shallowest conductive Garzweiler and Frimmersdorf Coals within their fairly resistive sand background, but they could not distinguish between Neurath Sand and the underlying sand/silt or between Frimmersdorf Coal and the underlying organic clay. They also revealed that both coal seams gently dip in the southwesterly direction. This should be in fairly good agreement with the regional structural makeup of the Rhineland brown coal. However, they showed that Garzweiler Coal is gradually thinned northeastwards, while Frimmersdorf Coal still has almost a regular thickness.

Outlook

The Garzweiler, Frimmersdorf and Morken coal seams join up in the center of the Rhineland basin to form one 'Main Seam', which reaches its maximum thickness and depth of about 100 and 500 m respectively. The present work encourages applying a specially-designed shallow LOTEM configuration to image the vertical resistivity structure of that Main Seam within its fairly resistive background.

ZUSAMMENFASSUNG (German Summary)

Die unverfestigten Ablagerungen des Känozoikums im unteren Rheingraben in Deutschland beherbergen das größte zusammenhängende Braunkohlevorkommen in Europa. Es befindet sich nord-westlich der Stadt Köln und umfasst eine Fläche von ca. 2.500 km². Der von der RWE-Power AG betriebene Braunkohle Abbau beträgt ca. 100 Millionen Tonnen pro Jahr. In Deutschland wird etwa ein Viertel des Bedarfes an elektrischer Energie durch Braunkohle aus dem Rheinland gedeckt. Wegen der zunehmenden Konkurrenz von anderen Energieträgern, wie beispielsweise importierter Steinkohle, strebt die RWE-Energie AG speziell bei kostspieligen Feldtechniken wie Bohrungen und Probennahmen eine Kostenminimierung an. Hier kommt die Geophysik ins Spiel. In der vorliegenden Arbeit wurden die Kohleflöze des Braunkohletagebaues „Garzweiler I“ mit den Methoden Radiomagnetotellurik (RMT) und Transientelektromagnetik (TEM) untersucht. Hauptziel der Messungen war es, die Anwendbarkeit und Effizienz der Methoden RMT und TEM in der Braunkohleexploration aufzuzeigen und die vertikale Verteilung der elektrischen Leitfähigkeit von Flözen abzubilden.

Infolgedessen wurden insgesamt 86 azimuthal RMT und 33 in-loop TEM Sondierung entlang sechs separater Profile auf zwei Strossen im Braunkohletagebau „Garzweiler I“ durchgeführt. Diese beiden Messgebiete werden im Weiteren als „Coal-covered Area“ und „Sand-covered Area“ bezeichnet. Die „Sand-covered Area“ befindet sich nordöstlich der höher liegenden „Coal-covered Area“ und wird auf der nördlichen Seite durch die nächst höher liegende Stufe begrenzt. Die Topographie entlang der Meßprofile ist sehr eben. Die „Coal-covered Area“ wird ebenfalls auf der nördlichen Seite durch die nächste Stufe bestehend eingefasst. An ihrem südlichen Ende bildet eine steile Stufe zur unteren Sprosse den Abschluss des Messgebietes, welches eine etwas unebene Topographie aufweist. Die lokale Stratigraphie am Ort der Meßgebiete entspricht gewöhnlich einer horizontalen Schichtung, bestehend aus den Garzweiler-, Frimmersdorf- und Morken-Kohlen, die in den Oberflächen-, Neurath-, Frimmersdorf- und Morken-Sand eingebettet sind und von unterschiedlich mächtigen Ton und Schlufflagen unterbrochen werden.

Um die vorrausichtlichen RMT/TEM Antworten an den Messgebieten abschätzen zu können und festzustellen, wie empfindlich eine reale Messung für das Ziel, der Bestimmung Flözmächtigkeiten ist, wurden für verschiedene geoelektrische Modelle eindimensionale (1D) Vorwärtsmodellierungen für den realen RMT Frequenzbereich und für die vorrausichtlichen Nano/ZeroTEM Zeitfenster durchgeführt und mit realistischem Rauschen versehen. Die gewählten Modelle sollten dabei für die Messgebiete typische Leitfähigkeitsverteilungen repräsentieren. Alle synthetischen Daten wurden dann unter Berücksichtigung einer Occam Glättungsbedingung 1D invertiert. Eine gute Modellwiedergabe und Datenreproduktion wurde nur für die wichtigsten stratigraphischen Schichten, den in elektrisch schlecht leitenden Sand eingebetteten gut leitenden und hoch liegenden Garzweiler und Frimmersdorf Kohleflöze erreicht. Die Morken Kohle und Morken Sand konnten die Ergebnisse nicht reproduzieren. Sie zeigten, dass eine Unterscheidung nur Anhand der realen RMT/TEM-Messungen des Neurath Sandes von dem darunter liegenden Sand/Schluff oder der Frimmersdorf Kohle vom darunter liegenden organischem Ton schwierig sein würde.

Das Vorhandensein einer elektrisch sehr gut leitenden Tonschicht innerhalb des Oberflächensandes, mit einer Mächtigkeit zwischen zwei bis drei Metern, änderte das aus der Inversion erhaltene geglättete Erdmodell nur für die oberen, vom ungestörten Modell abweichende, Schichten deutlich. Für verschiedene Tonschichtdicken ergaben sich deutlich von einander unterscheidbare scheinbaren Widerstände (und Phasen), für den vollständigen RMT Frequenzbereich und für die frühen und mittleren TEM Zeitbereichen, die sich zudem deutlich von denen des ungestörten Modells unterschieden. Dies zeigte an, daß die Oberflächen nahe Tonschicht durch eine RMT Messung gut detektiert und eindeutig aufgelöst werden kann. Mit zunehmender Dicke des Tones können die darunter liegenden Schichten schlechter aufgelöst werden. Die unter dem Ton liegende Schichtfolge von Oberflächensande, Garzweiler Kohle und Neurath Sand/Schluff taucht als ein einziger mäßig leitender Block in den Inversionsergebnissen auf, wobei die einzelnen Schichten nicht aufgelöst werden. In diesem Fall verhindert die Tonschicht die Detektion der darunter liegenden Kohleflöze. Im Fall einer TEM-Messung kann die obere Tonschicht ebenfalls gut detektiert werden. Mit zunehmender Dicke der Tonschicht verschmilzt diese in den Inversionsergebnissen mit den darunter liegenden Oberflächen Sanden und Garzweiler Kohlen zu einem einzigen mittel bis gut leitenden Block. Zu späteren Zeiten verschwindet jedoch der negative Einfluss der Tonschicht, so dass die Tieferen Schichtfolgen wieder gut aufgelöst werden können. Im Allgemeinen zeigen diese Beispiele mit synthetischen Daten, dass das Auflösungsvermögen einer RMT/TEM Messung für dünne hochohmige Schichten wie Oberflächensand schlecht ist.

Nach der Sichtung, Dekonvolution und Transformation der Daten jeder Sondierung, wurden die RMT/TEM Daten der 1D mit einer Occam-Inversion ausgewertet, um sinnvolle Startmodelle für weitere nicht-lineare 1D-Inversionen zu erhalten. Hierbei wurden keine Vorinformationen für die Inversion benutzt. Beginnend mit einer Kontroll- RMT/TEM-Sondierung und unter Anwendung einer rekursivem Startmodellwahl, zeigte das aus den Inversionsergebnisse erhaltene Profil für die „Coal-covered Area“ bereits eine sehr gleich bleibend Struktur. Bei zufrieden stellender Datenanpassung ergab sich eine gute Korrelation der Ergebnisse mit der aus den Bohrlöchern bekannten Geologie, die die Annahme einer 1D Geologie nahe legen. Anhand der Inversionsstatistik (geschätzte Fehlergrenzen, relative Sensitivitäten, Importances, etc.) für die Modellparameter wurde die Auflösung für alle Sondierungen überprüft. Sie zeigte, dass alle Kohleflöze gut aufgelöst werden können. Die Aussagetiefen für RMT betragen 30 m und für die TEM-Sondierungen 100 m. Die Inversionsergebnisse beide Methoden zeigen deutlich die Garzweiler Kohle und die/den Frimmersdorf Kohle/Ton innerhalb des Oberflächensandes, des Neurath Sand/Sluffes und des Frimmersdorf Sandes. Die Morken Kohle und der Morken Sand lagen unterhalb der Aussagetiefe der Sondierungen.

Obwohl die 1D RMT/TEM Inversionsmodelle der „Sand-covered Area“ inkonsistent mit der Bohrlochgeologie waren und schlecht mit ihr korrelierten, waren die Schichtdicken der einzelnen 1D-Modelle gleich bleibend und zeigten eine zufrieden stellende Datenanpassung. Die Oberflächen nahen Tone und darunter liegenden Kohlenflöze konnte nahezu alle von einander unterschieden werden. Dennoch gab es eine beträchtlicher Zahl von Sondierungen deren Inversionsmodellparameter niedrige und unterdurchschnittliche Importances und eine schlechte Übereinstimmung mit der Bohrlochgeologie zeigten. An diesen Punkte verlor die Annahme einer eindimensionalen Geologie und somit einen 1D Inversion ihre Gültigkeit. Leider konnte die eigentlich viel versprechende Joint-Inversion von RMT- und TEM-Daten nicht durchgeführt werden, da sich zum die Diffusions- und Eindringtiefe beider Methoden zu wenig überschneiden und sich die Modelle der einzelnen Methoden zu sehr unterschieden.

Systematische Untersuchungen (einschließlich 2D RMT Inversionen und Sensitivitätsuntersuchungen) wurde für jede gemessene Senderrichtung durchgeführt. Das Ziel der Untersuchungen war es den Effekt der nahegelegenen Topographie auf die Daten in Abhängigkeit von der Senderrichtung zu untersuchen und Abschätzungen für die maximale Aussagetiefe durchzuführen. Zusätzlich wurde untersucht, ob die Verwendung zusätzlicher Frequenzen für die einzelnen Sondierungen eine verbesserte Auflösung der Widerstände ermöglicht. Die geglätteten Erdmodelle im Bereich der „Coal-covered Area“ zeigten für unterschiedliche Senderrichtungen kaum Unterschiede, woraus man ableiten kann, daß die Daten näherungsweise eindimensional sind. Da die Impedanz an der Oberfläche näherungsweise unabhängig von der Senderrichtung ist, wurden die Daten für alle Frequenzen an jedem Sondierungspunkt sowohl bei den 1D als auch bei den 2D Inversionen gemeinsam invertiert, um hoch aufgelöste Widerstandsmodelle zu erzeugen. Die Unabhängigkeit von der Senderrichtung bedeutet auch, dass der Effekt der nahegelegenen Topographie vernachlässigbar klein ist. Die parallelen Haupt-Profile wurden also in hinreichend großem Abstand der Topographie gemessen. Das geglättete Erdmodell zeigt für 1D und 2D Inversionen ungefähr die gleiche Kohle-Sand-Grenze, wobei die Grenze für die 2D Inversionen weniger klar aufgelöst ist.

Im Bereich der „Sand-covered Area“ wurde der stärkste Effekt der Topographie für Senderrichtungen im rechten Winkel zum nördlich gelegenen Hügel. Hier hilft die Vorstellung, daß der gesamte Strom vom Hügel zum Boden oder in Gegenrichtung fließt, während das magnetische Feld entlang des Hügels konstant bleibt. Dies bedeutet, daß der scheinbare Widerstand an der Oberfläche von der Senderrichtung abhängt und man nicht alle Daten gleichzeitig in 1D oder 2D Inversionen verwenden kann. Andererseits zeigen die Modelle für Senderrichtungen parallel und antiparallel zum Hügel zuverlässige Widerstandsanomalien, die nicht von der nahegelegenen Topographie beeinflusst werden. In Anschluss an die Überlegungen wurde die Joint-Inversion der TE- und TM-Mode (30° und 120° N) ausgewählt, was eine verbesserte Auflösung der Erdmodells ermöglicht. Die oberflächennahen Tonschichten und die Garzweiler Kohle konnten sehr genau lokalisiert werden. Generell gilt: Die Ton-Sand-Grenze konnte besser aufgelöst werden je mehr Frequenzen für jede Senderrichtung verwendet wurden. Die maximale Aussagetiefe wurde entweder mit 30 m ($\approx 2.5z^*$) für den Bereich der „Coal-covered Area“ mit 25 m ($\approx 2z^*$) im Bereich der „Sand-covered Area“ abgeschätzt.

3D TEM Vorwärts Modellierungen wurden für jedes der Messgebiete durchgeführt, wobei jeweils das 1D Schicht-Modell als Startmodell verwendet wurde. Im Bereich der „Sand-covered Area“ wurden die gestörten Transienten mit Hilfe vertikaler koaxialer Blöcke im Untergrund, deren Widerstand nach innen abnimmt, angenähert. Dies geschah unter der Annahme, daß die geologische Ursache der anomalen Transienten, in die tiefe Schichtung eingelagerte Tonlinsen sind, die zu den Rändern hin dünner werden. Eine Schichtabfolge aus einem schlecht-leitendem Basement (Frimmersdorf Sand) unterhalb der Frimmersdorf Kohle/Ton Schicht wurde verwendet, um die ungestörten Transienten zu modellieren. Um die gestörten Transienten zu modellieren, muss ein leitfähiges Basement (oder Frimmersdorf Kohle/Ton) vertikal stark ausgedehnt sein, da das Feld viel langsamer als über einem schlecht leitfähigen Basement abfällt. Daher hat das endgültige Erdmodell eine Basis aus gut und schlecht leitenden Teilen. Es erscheint unmöglich, ein Basement, das alle Datensätze entlang eines Profils erklärt, zu finden. Experiment haben gezeigt, dass die oberflächen Blöcke gebraucht werden, um die Frühzeit Daten zu erklären und sie einen signifikanten Beitrag zur Gesamtleitigkeit des Modells leisten. Die Präsenz von oberflächennahen Blöcken unterhalb der gestörten Transienten verändert das Spätzeit-Verhalten der Kurve nicht. Hier benötigt das Modell nur ein leitfähiges Basement. Daher kann gefolgert werden, dass die Obergrenze der

Frimmersdorf Kohle in der normalen Tiefe existiert. Unklar ist allerdings, ob die untere Grenze abgeleitet werden kann, indem einfach zwischen den ungestörten Sondierungen interpoliert. Für alle Fälle hat die 3D Modellierung die Nicht-Eindeutigkeit der aus den 1D Interpretationen abgeleiteten Erdparameter an den gestörten Sondierungen reduziert. „Sand-covered Area“

Desweiteren haben die 3D TEM Modellierungen mit und ohne Topographie gezeigt, dass nahegelegene Topographie keinen signifikanten Einfluss auf die Modellantwort hat. Dies impliziert, dass es keine elektromagnetische Kopplung zwischen topographischen Merkmalen und den Kohleflözen im Untergrund gibt. Im extremsten Fall in der Nähe der steilen Südkante des Bereichs der „Coal-covered Area“, wo ein steiler horizontaler Feldgradient erwartet wurde, konnte nur ein marginaler Unterschied in den Modellantworten beobachtet werden. Dieser Unterschied beschränkte sich auf die Antwort zu frühen Zeiten und kann leicht behoben werden, indem man die Modellwiderstände schrittweise an die auf Grund von Labormessungen erwarteten Widerstandswerte anpasst.

Die Mächtigkeiten der Schichten, die aus den Widerstandsmodelle für RMT und TEM abgeleitet werden können, stimmen mit den aus Bohrlöchern abgeleiteten Mächtigkeiten überein. Eine ähnlich gute Korrelation existiert mit den Widerstandswerten, die man aus Labor Messungen mit Gleichstrom Geoelektrik (DC) und spektraler induzierte Polarisation (SIP) für 16 Gesteinsproben abgeleitet hat. Die größten stratigraphischen Einheiten im Messgebiet konnten identifiziert werden. Insbesondere konnten die flachen gut leitfähigen Garzweiler und Frimmersdorf Kohle identifiziert werden. Der Neurath Sand konnte nicht vom den tieferen Sand und Sluffe Schichten unterschieden werden. Die Frimmersdorf Kohle konnte nicht von tiefer gelegenen organischen Kohle Schichten unterschieden werden. Es konnte gezeigt werden, dass beide Kohleflöze leicht in Richtung SW abfallen. Dies ist in guter Übereinstimmung mit der regionalen Geologie für die Braunkohle des Rheinlandes. Außerdem konnte gezeigt werden, dass die Mächtigkeit der Garzweiler Kohle in Richtung NE leicht abnimmt, während die Frimmersdorf Kohle eine konstante Mächtigkeit zeigt.

APPENDIX A

PROGRAMS

The most frequently used programs in the present work are given as follows:

CalcView-XL

The collected RMT/TEM data were manually fed into or automatically dumped, viewed, averaged and transformed by the specially-designed Spreadsheet package 'CalcView-XL.' The package contains all calculations and statistics needed for RMT/TEM data, as well as very quick and easy-to-use plotting templates. The program is by no means a competition to commercial software.

EMIX-MT 2.0

The synthetic and field RMT data were interpreted in terms of 1D smoothed and layered resistivity models using the program 'EMIX-MT 2.0' [Interpex Limited, 1989]. It is a commercially available software package which allows for single-site forward/inverse modeling of RMT data. Both Occam's and Marquardt-Levenberg schemes are available for non-linear least squares curve fitting of an earth with up to 19 or 10 uniform horizontally-layers respectively.

eadec

The FORTRAN code 'eadec' [Helwig *et al.*, 2003] was used to convert both the composite-NanoTEM and ZeroTEM transients to an unique form by deconvolving their turn-off (or ramp) time out of the measured signals. The program is by no means a competition to commercial software.

emoplus, rmttem

The synthetic and field TEM data were interpreted in terms of 1D smoothed and layered resistivity models using updated versions of the FORTRAN codes 'emoplus' [Commer, 1999] and 'rmttem' [Eckard, 1993] respectively. They allows for single-site forward/inverse modeling of TEM data. Both Occam's and Marquardt-Levenberg schemes are available for either individual or joint inversion of RMT and TEM Data. Both programs are by no means a competition to commercial software.

mt2dinv-NLCG, mt2dinv-GN

The field RMT data were interpreted in terms of 2D smoothed resistivity models using an updated version of the FORTRAN code 'mt2dinv-NLCG' based on the non-linear conjugate gradients algorithm [Mackie *et al.*, 1997]. The corresponding sensitivity calculations were performed using an older version of the FORTRAN code 'mt2dinv-GN' based on the Gauss-Newton algorithm [Mackie *et al.*, 1997; Schwalenberg *et al.*, 2002]. Both programs are by no means a competition to commercial software.

Maxwell, calogri

The synthetic TEM data were interpreted in terms of 3D layered resistivity models using an updated version of the FORTRAN code 'Maxwell' [Druskin and Knizhnerman, 1988]. It allows for single/multi-site trail-and-error forward modeling of TEM data and is based on the spectral Lanczos matrix decomposition algorithm. The FORTRAN code 'calogri' [Koch *et al.*, 2004] was used to automatically generate the 3D finite-difference grid and START/MODEL-namelists data file. Both programs are by no means a competition to commercial software.

SURFER[®] 7.0

All topographic models and transformed/smoothed resistivity models were contoured using the commercially available software package 'SURFER 7.0'(Golden software, Inc., USA).

APPENDIX B

MINING RESULTS

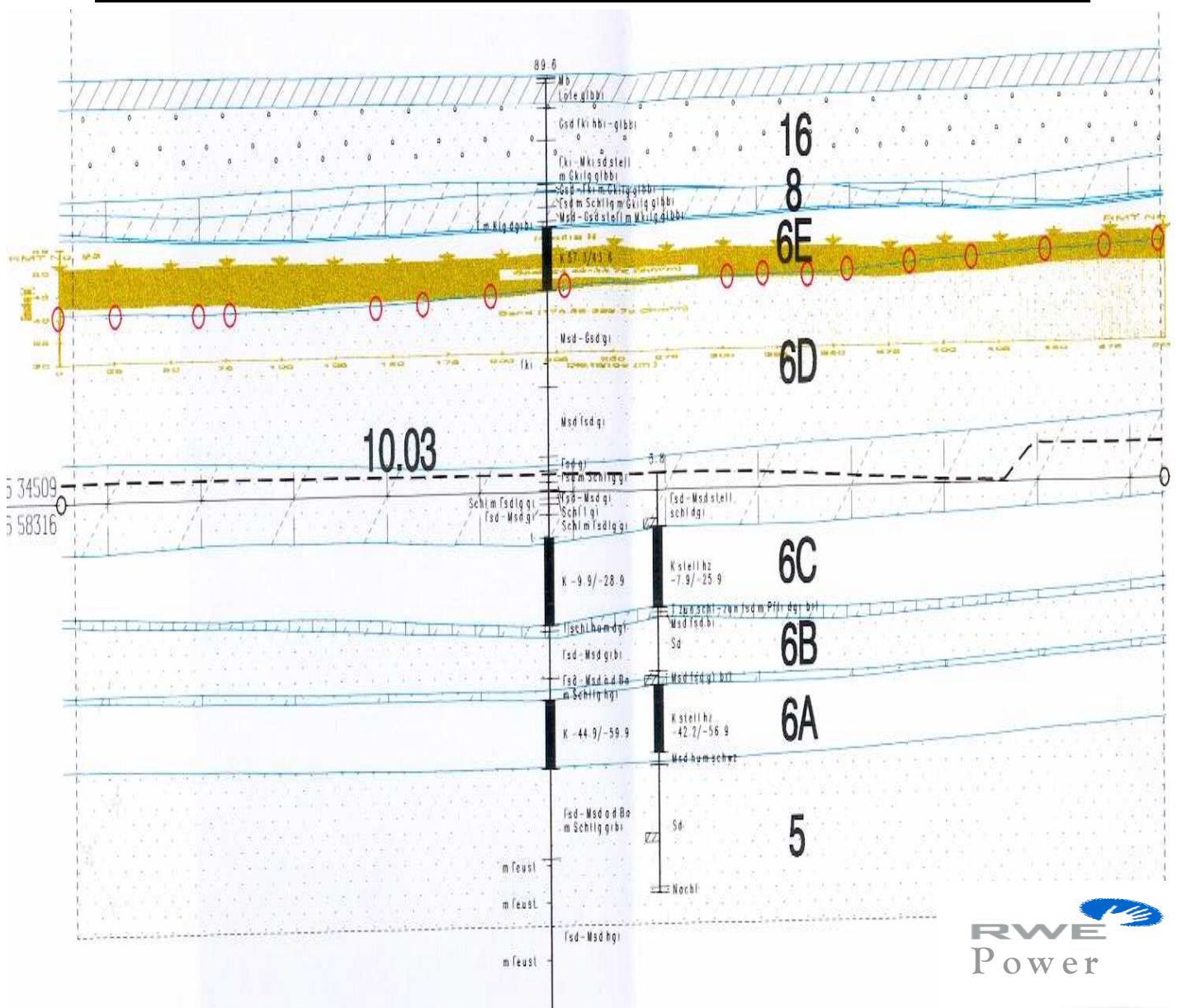


Figure B.1: (Open red ellipses) Mining results of the Garzweiler Coal base versus (light brown) the interpreted 1D/2D RMT resistivity model along profile I at the 'Coal-covered Area.' (Data courtesy of RWE-Power AG, Cologne.)

REFERENCES

- Archie, G. E., 1942.** The electrical resistivity log as an aid in determining some reservoir characteristics. *Trans. Am. Inst. Min. Metall. Pet. Eng.*, 146, 54–62.
- Asten, M. W., 1987.** Full transmitter waveform transient electromagnetic modeling and inversion for soundings over coal measures. *Geophysics*, 52, 279–288.
- Bastani, M., 2001.** EnviroMT—a new controlled source/radio magnetotelluric system. Ph.D. thesis, Department of Earth Sciences, Uppsala University.
- Bastani, M. and Pedersen, L. B., 2001.** Estimation of magnetotelluric transfer functions from radio transmitters. *Geophysics*, 66, 1038–1051.
- Bergers, R., 2002.** Untersuchung von oberflächennahen Klärschlämmen mit elektrischen und elektromagnetischen Methoden der Angewandten Geophysik. Diplomarbeit, Institut für Geophysik und Meteorologie, Universität zu Köln.
- Bosch, F. P. and Gurk, M., 2000.** Comparison of RF–EM, RMT and SP measurements on a karstic terrain in the Jura Mountains (Switzerland). In: Hördt, A. and Stoll, J. B. (Eds.), *Protokoll über das 18. Kolloquium Elektromagnetische Tiefenforschung*, Altenberg, DGG, 51–59.
- Bosch, F. P. and Müller, I., 2001.** Continuous gradient VLF measurements: A new possibility for high resolution mapping of karst structures. *First break*, 19, 343–350.
- Bosch, F. P. and Müller, I., 2002.** Contribution to karst ground vulnerability mapping by VLF–Gradient survey: Comparison with other Geophysical methods. *European Journal of Environmental and Engineering Geophysics*, submitted.
- Bracewell, R. N., 1978.** *The Fourier Transform and its Applications, Second Edition.* McGraw-Hill, New York.
- Cagniard, L., 1953.** Basic theory of the magnetotelluric method of Geophysical prospecting. *Geophysics*, 18, 605–635.
- Chen, P. F. and Fung, P. C. W., 1989.** A mesh convergence test for the finite-difference method in three-dimensional electromagnetic modeling. *Chinese J. Geophys.*, 32, 569–573.
- Christensen, N. B. and Sørensen, K. I., 1998.** Surface and borehole electric and electromagnetic methods for hydrogeological investigations. *European Journal of Environmental and Engineering Geophysics*, 3, 75–90.
- Cole, K. S. and Cole, R. H., 1941.** Dispersion and absorption in dielectrics. *J. Chem. Phys.*, 9, 341–209.
- Commer, M., 1999.** Ein spezielles Verfahren der eindimensionalen kombinierten Inversion von Long–Offset Transient Electromagnetic (LOTEM) – und Magnetotellurik (MT) – Daten. Diplomarbeit, Institut für Geophysik und Meteorologie, Universität zu Köln.

- Commer, M., 2003.** Three-dimensional inversion of transient electromagnetic data: A comparative study. Doktorarbeit, Institut für Geophysik und Meteorologie, Universität zu Köln.
- Constable, S. C., Parker, R. L. and Constable, C. G., 1987.** Occam's Inversion: A practical algorithm for generating smooth models from EM sounding data. *Geophysics*, 52, 289–300.
- deGroot-Hedlin, C. and Constable, S. C., 1990.** Occam's Inversion to generate smoothed, two-dimensional models for magnetotelluric data. *Geophysics*, 55, 1613–1624.
- Druskin, V. L. and Knizhnerman, L. A., 1988.** A spectral semi-discrete method for the numerical solution of 3-D non-stationary problems in electrical prospecting. *Physics of the Solid Earth*, 24, 641–648.
- Druskin, V. L. and Knizhnerman, L. A., 1994.** Spectral approach to solving three-dimensional Maxwell's diffusion equations in the time and frequency domains. *Radio Science*, 29, 937–953.
- Eckard, M., 1993.** Joint Inversion von Gleichstromgeoelektrik und Transientenelektromagnetik. Diplomarbeit, Institut für Geophysik und Meteorologie, Universität zu Köln.
- Edwards, R. N. and Nabighian, M. N., 1991.** The magnetometric resistivity method. In: Nabighian, M. N. (Ed.), *Electromagnetic Methods in Applied Geophysics, Vol. 2A*, Society of Exploration Geophysicists, Tulsa, 47–104.
- Farquharson, C. G. and Oldenburg, D. W., 1996.** Approximate sensitivities for electromagnetic inverse problem. *Geophys. J. Int.*, 126, 235–252.
- Fischer, G., 1989.** A strong topographic valley effect in AMT and VLF–R measurements. *Geophysical Journal*, 96, 469–475.
- Fischer, G., Le Quang, B. V. and Müller, I., 1983.** VLF ground survey, a powerful tool for the study of shallow two-dimensional structure. *Geophysical Prospecting*, 31, 977–991.
- Fitterman, D. V. and Stewart, M. T., 1986.** Transient electromagnetic sounding for groundwater. *Geophysics*, 51, 995–1055.
- Fletcher, R. and Reeves, C. M., 1964.** Function minimization by conjugate gradients. *Computer J.*, 7, 149–154.
- Frischknecht, F. C., Labson, V. F., Spies, B. R. and Anderson, W. L., 1991.** Profiling methods using small sources. In: Nabighian, M. N. (Ed.), *Electromagnetic Methods in Applied Geophysics, Vol. 2A*, Society of Exploration Geophysicists, Tulsa, 105–270.
- Gaidetzka, A., 2002.** Erste Erfahrungen mit der NanoTEM–Apparatur. Diplomarbeit, Institut für Geophysik und Meteorologie, Universität zu Köln.
- Goldman, M., du Plooy, A. and Eckard, M., 1994a.** On reducing ambiguity in the interpretation of transient electromagnetic sounding data. *Geophysical Prospecting*, 42, 3–25.
- Goldman, M., Tabarovsky, L. and Rabinovich, M., 1994b.** On the influence of 3-D structures in the interpretation of transient electromagnetic sounding data. *Geophysics*, 59, 889–901.
- Hansen, P. C., 1992.** Analysis of discrete ill-posed problems by means of the L-curve. *SIAM Review*, 34, 561–580.

- Hansen, P. C., 1999.** The L-curve and its use in the numerical treatment of inverse problems. Technical Report (IMM-REP 99-15), Department of Mathematical Modeling, Technical University of Denmark.
- Hanstein, T., 1992.** Iterative und parametrisierte Dekonvolution für LOTEM Daten. In: Haak, V. and Rodemann, H. (Eds.), *Protokoll über das 14. Kolloquium Elektromagnetische Tiefenforschung*, Borkheide, DGG, 163–172.
- Harrell, J. A., 2002.** Archaeological geology in Egypt: Ancient oil wells and mummy bitumen, earliest geological map, first paved road, pyramid temple pavements, and the Sphinx age controversy. In: *2001–2002 AAPG Distinguished Lecture Program*.
- Helwig, S. L., Bergers, R. and Koch, O., 2004.** Entwicklung einer Drei-Komponenten-Empfangsspule für oberflächennahe TEM-Messungen. In: *Protokoll über die 64. Jahrestagung der Deutschen Geophysikalischen Gesellschaft*, Berlin, DGG, EMP10.
- Helwig, S. L., Goldman, M. and Hördt, A., 1994.** Multidimensional interpretation of TDEM data collected for mineral exploration in Israel. In: *56th Annual International Meeting of European Association of Exploration Geophysics, Expanded Abstracts*, Zeist, EAGE.
- Helwig, S. L., Lange, J. and Hanstein, T., 2003.** Kombination dekonvolvierter Messkurven zu einem langen Transienten. In: *Protokoll über die 63. Jahrestagung der Deutschen Geophysikalischen Gesellschaft*, Hannover, DGG, EMP04.
- Hördt, A., Druskin, V. L. and Knizhnerman, L. A., 1992a.** Interpretation of 3-D effects in long-offset transient electromagnetic (LOTEM) soundings in the Münsterland area/Germany. *Geophysics*, 57, 1127–1137.
- Hördt, A., Greinwald, S., Hoheisel, A., Neubauer, F. M., Schaumann, G. and Tezkan, B., 1999.** Joint 3D interpretation of radiomagnetotelluric (RMT) and transient electromagnetic (TEM) data from an industrial waste deposit in Mellendorf, Germany. *European Journal of Environmental and Engineering Geophysics*, 4, 151–170.
- Hördt, A., Strack, K. -M., Vozoff, K. and Wolfgram, P. A., 1992b.** Resolving resistive layers using joint inversion of LOTEM and MT data. In: Vogel, A., Sarwar, A. K. M., Gorenflo, R. and Kounchev, O. I. (Eds.), *Theory and Practice of Geophysical Data Inversion, Vol. 5*, Vieweg, 147–158.
- Hördt, A. and Müller, M., 2000.** Understanding LOTEM data from mountainous terrain. *Geophysics*, 65, 1113–1123.
- Inman, J. R., 1975.** Resistivity inversion with ridge regression. *Geophysics*, 40, 798–817.
- Interpex Limited, 1989.** *User's Manual*. Interpex Ltd., Golden, Colorado.
- Jackson, D. D., 1972.** Interpretation of inaccurate, insufficient, and inconsistent data. *Geophys. J. Roy. Astr. Soc.*, 28, 97–109.
- Junge, A., 1988.** Analytical presentation of statistically estimated magnetotelluric transfer functions by a set of polynomials. *J. Geophys.*, 62, 193–197.
- Jupp, D. L. B. and Vozoff, K., 1975.** Stable iterative methods for the inversion of Geophysical data. *Geophys. J. Roy. Astr. Soc.*, 42, 957–976.
- Kaufman, A. A. and Keller, G. V., 1983.** *Frequency and transient soundings*. Elsevier, Amsterdam.

- Klawitter, G., 1998.** *100 Jahre Funktechnik in Deutschland–Funksendestellen rund um Berlin. Band 1*, Wissenschaft und Technik, Berlin.
- Klett, M., Eichhorst, F. and Schäfer, A., 2002.** Facies interpretation from well logs applied to the Tertiary Lower Rhine Basin fill. *Netherlands Journal of Geosciences*, 81, 167–176.
- Knödel, K., Krummel, H. and Lange, G., 1997.** *Handbuch zur Erkundung des Untergrundes von Deponien und Altlasten–Geophysik. Band 3*, Springer, Berlin.
- Koch, O., Helwig, S. L., Meqbel, N. and The Desert Group, 2004.** Vertical near surface conductivity-anomaly detected at the Dead-Sea-Transform. In: *17th International Workshop on Electromagnetic Induction in the Earth, Extended Abstracts*, Hyderabad, NGRI–IIG, S.6–P.8.
- Levenberg, K., 1944.** A method for the solution of certain non-linear problems in least-squares. *Quart. Appl. Math.*, 2, 164–168.
- Li, X., and Pedersen, L. B., 1991.** The electromagnetic response of an azimuthally anisotropic half-space. *Geophysics*, 56, 1462–1473.
- Linde, N. and Pedersen, L. B., 2004.** Evidence of electrical anisotropy in limestone formations using the RMT technique. *Geophysics*, 69, 909–916.
- Lines, L. R. and Treitel, S., 1984.** Tutorial: A review of least-squares inversion and its application to Geophysical problems. *Geophysical Prospecting*, 32, 159–186.
- Mackie, R. L. and Madden, T. R., 1993.** Three-dimensional magnetotelluric inversion using conjugate gradients. *Geophys. J. Int.*, 115, 215–229.
- Mackie, R., Rieven, S. and Rodi, W., 1997.** *Users Manual and Software Documentation for Two-dimensional Inversion of Magnetotelluric Data*. GSY-USA Inc., San Francisco, California.
- Macnae, J. C., Lamontagne, Y., and West, G. F., 1984.** Noise processing techniques for time-domain EM systems. *Geophysics*, 49, 934–948.
- Madden, T. R. and Mackie, R. L., 1989.** Three-dimensional magnetotelluric modeling and inversion. *Proceedings of the IEEE*, 77, 318–333.
- Marquardt, D. W., 1963.** An algorithm for least-squares estimation of non-linear parameters. *SIAM J.*, 11, 431–441.
- Marshall, D. J. and Madden, T. R., 1959.** Induced polarization: A study of its causes. *Geophysics*, 24, 790–816.
- Matthes, S., 1990.** *Mineralogie*. Springer, Berlin.
- McGillivray, P. R. and Oldenburg, D. W., 1990.** Methods for calculating Frechet derivatives and sensitivities for the non-linear inverse problem: A comparative study. *Geophysical Prospecting*, 38, 499–524.
- McNeill, J. D. 1980.** Electromagnetic terrain conductivity measurement at low induction numbers. Technical Note TN-6, Geonics Ltd., Ontario.
- McNeill, J. D. and Labson, V. F., 1991.** Geological mapping using VLF radio fields. In: Nabighian, M. N. (Ed.), *Electromagnetic Methods in Applied Geophysics, Vol. 2B*, Society of Exploration Geophysicists, Tulsa, 521–640.

- Mehanee, S. and Zhdanov, M., 2002.** Two-dimensional magnetotelluric inversion of blocky geoelectrical structures. *Journal of Geophysical Research*, 107, EPM1–11.
- Moskow, S., Druskin, V. L., Habashy, T., Lee, P. and Davydycheva, S., 1999.** A finite difference scheme for elliptic equations with rough coefficients using a Cartesian grid nonconforming to interfaces. *SIAM J. Numerical Analysis*, 36, 442–464.
- Nabighian, M. N., 1979.** Quasi-static transient response of a conducting half-space an approximate representation. *Geophysics*, 44, 1700–1705.
- Nabighian, M. N., 1988.** *Electromagnetic Methods in Applied Geophysics. Vol. 1*, Society of Exploration Geophysicists, Tulsa.
- Nabighian M. N. and Asten, M. W., 2002.** Metalliferous mining Geophysics—State of the art in the last decade of the 20th century and the beginning of the new millennium. *Geophysics*, 67, 964–978.
- Nabighian, M. N. and Macnae, J. C., 1991.** Time domain electromagnetic prospecting methods. In: Nabighian, M. N. (Ed.), *Electromagnetic Methods in Applied Geophysics, Vol. 2A*, Society of Exploration Geophysicists, Tulsa, 427–520.
- Newman, G. A., 1989.** Deep transient electromagnetic soundings with a grounded source over near-surface conductors. *Geophys. J. Int.*, 89, 889–914.
- Newman, G. A., Recher, S., Tezkan, B. and Neubauer, F. M., 2003.** 3D inversion of a scalar radio magnetotelluric field data set. *Geophysics*, 68, 791–802.
- Oristaglio, M. L. and Hohmann, G. W., 1984.** Diffusion of electromagnetic fields into two-dimensional earth. *Geophysics*, 49, 870–894.
- Paal, G., 1965.** Ore prospecting based on VLF-radio signals. *Geoexploration*, 3, 139–147.
- Palacky, G. J., 1983.** Tutorial: Research, application and publications in electrical and electromagnetic methods. *Geophysical Prospecting*, 31, 861–872.
- Parasnis, D. S., 1973.** *Mining Geophysics*. Elsevier, Amsterdam.
- Parasnis, D. S., 1991.** Large-layout harmonic field systems. In: Nabighian, M. N. (Ed.), *Electromagnetic Methods in Applied Geophysics, Vol. 2A*, Society of Exploration Geophysicists, Tulsa, 271–283.
- Parkhomenko, E. I., 1967.** *Electrical Properties of Rocks*. Plenum, New York. (Keller, G. V., English translation.)
- Parlett, F., B., 1980.** *The symmetric eigenvalue problem*. Prentice-Hall, Inc.
- Pedersen, L. B., Bastani, M. and Dynesius, L., 2003.** Radiotransmitters in Europe to be used in high resolution Geophysical exploration of near-surface geology. *Geophysical Prospecting*, submitted.
- Pelton, W. H., Ward, S. H., Hallof, P. G., Sill, W. R. and Nelson, P. Hi., 1978.** Mineral discrimination and removal of inductive coupling with multifrequency IP. *Geophysics*, 43, 588–609.
- Polak, E., 1971.** *Computational Methods in Optimization: A unified Approach*. Academic Press.

- Raiche, A. P., 1983.** Comparison of apparent resistivity functions for transient electromagnetic methods. *Geophysics*, 48, 787–789.
- Raiche, A. P., Jupp, D. L. B. and Vozoff, K., 1985.** The joint use of coincident loop transient electromagnetic and Schlumberger sounding to resolve resistive layers. *Geophysics*, 50, 1618–1627.
- Recher, S., 1998.** Untersuchung der Anwendbarkeit der Radiomagnetotellurik-Methode auf die Lokalisierung von Kontaminiertem Boden. Diplomarbeit, Institut für Geophysik und Meteorologie, Universität zu Köln.
- Recher, S., 2002.** Dreidimensionale Erkundung von Altlasten mit Radio-Magnetotellurik. Doktorarbeit, Institut für Geophysik und Meteorologie, Universität zu Köln.
- Rodi, W. and Mackie, R. L., 2001.** Nonlinear conjugate gradients algorithm for 2-D magnetotelluric inversion. *Geophysics*, 66, 174–187.
- Ruffet, C., Gueguen, Y. and Darot, M., 1991.** Complex resistivity measurements and fractal nature of porosity. *Geophysics*, 56, 758–768.
- RWE AG Group, 1998.** RWE environmental report–1998. (Online at URL http://www.rwe.com/genertor.aspx/property=data/id=5628/archive_2pdf.pdf.)
- Scarlato, P., Poe, B., T., Freda, C. and Gaeta, M., 2004.** High-pressure and high-temperature measurements of electrical conductivity in basaltic rocks from Mount Etna, Sicily, Italy. *Journal of Geophysical Research*, 109, 1–11.
- Schäfer, A., Hilger, D., Gross, G. and von der Hocht, F., 1996.** Cyclic sedimentation in Tertiary Lower-Rhine Basin (Germany)–the 'Liegendrücken' of brown coal open-cast Fortuna mine. *Sedimentary Geology*, 103, 229–247.
- Schmucker, U., 1970.** Anomalies of geomagnetic variations in southwestern United States. *Scripps Institute of Oceanography Bulletin*, 13, University of California Press.
- Schmucker, U., 1987.** Substitute conductors for electromagnetic response estimates. *PAGEOPH*, 125, 341–367.
- Schröder, R., 1994.** Gültigkeitsbereich der 'Ebenen-Wellen-Theorie' unter Berücksichtigung der Verschiebungsströme bezogen auf die geoelektrischen Meßmethoden VLF–R, LF–R, CSAMT und Short Wave Loop-Loop. Diplomarbeit, Institut für Geophysik und Meteorologie, Universität zu Köln.
- Schwalenberg, K., Rath, V. and Haak, V., 2002.** Sensitivity studies applied to a two-dimensional resistivity model from the Central Andes. *Geophys. J. Int.*, 150, 673–686.
- Scott, W. J., 1971.** Phase angle measurements in the IP method of Geophysical prospecting. Ph.D. thesis, McGill University (Montreal).
- Scott, W. J., 1975.** VLF resistivity (Radio-ohm) survey, Agricola Lake area, district of Mackenzie. *Geol. Surv. Can.*, 75-A, 223–225.
- Scromeda, N. and Katsube, T. J., 2001.** Spectral induced measurements of sericite schist and ore samples from the Yellowknife mining district, Northwest Territories. Geological Survey of Canada, Current Research, 2001–E2. (Online at URL <http://www.nrcan.gc.ca/gsc/bookstore>.)
- Siebel, W., 1991.** *Spezial-Frequenzliste 9 kHz–30 MHz*. Siebel, Meckenheim.

- Smith, J. T. and Booker, J. R., 1991.** Rapid inversion of two- and three-dimensional magnetotelluric data. *Journal of Geophysical Research*, 96, 3905–3922.
- Spies, B. R. and Eggers, D. E., 1986.** The use and misuse of apparent resistivity in electromagnetic methods. *Geophysics*, 51, 1462–1471.
- Spies, B. R. and Frischknecht, F. C., 1991.** Electromagnetic sounding. In: Nabighian, M. N. (Ed.), *Electromagnetic Methods in Applied Geophysics, Vol. 2A*, Society of Exploration Geophysicists, Tulsa, 285–425.
- Spies, B. R., 1989.** Depth of investigation in electromagnetic sounding methods. *Geophysics*, 54, 872–888.
- Steuer, A., 2002.** Kombinierte Auswertung von Messungen mit Transientelektromagnetik und Radiomagnetotellurik zur Grundwassererkundung im Becken von Ouarzazate (Marokko). Diplomarbeit, Institut für Geophysik und Meteorologie, Universität zu Köln.
- Strack, K. -M., 1992.** *Exploration with Deep Transient Electromagnetics*. Elsevier, Amsterdam.
- Swift, C. M., 1971.** Theoretical magnetotelluric and turam response from two-dimensional inhomogenities. *Geophysics*, 36, 38–52.
- Tabarovski, L. A., 1982.** Boundary conditions for vector potential at interface between conductor and isolator. *Electromagnitniye metody geofizicheskikh issledovaniy, Novosibirsk*, 36–50. (In Russian.)
- Telford, W. M., Geldart, L. P., and Sheriff, R. E., 1990.** *Applied Geophysics, Second Edition*. Cambridge University Press, Cambridge.
- Tezkan, B., Goldman, M., Greinwald, S., Hördt, A., Müller, I., Neubauer, F. M. and Zacher, G., 1996.** Joint application of radiomagnetotellurics and transient electromagnetics to the investigation of a waste deposit in Cologne (Germany). *Journal of Applied Geophysics*, 34, 199–212.
- Tikhonov, A. N., 1950.** On determining electrical characteristics of the deep layers of the Earth's crust. *Dokl. Akad. Nauk SSSR*, 73, 295–297. (In Russian.)
- Tikhonov, A. N. and Arsenin, V. Y., 1977.** *Solutions of Ill-posed Problems*. John Wiley, New York.
- Turberg, P. and Barker, R., 1996.** Joint application of radio-magnetotelluric and electrical imaging surveys in complex subsurface environments. *First Break*, 14, 105–112.
- Turberg, P. and Müller, I. and Flury, B., 1994.** Hydrogeological investigation of porous environments by radio magnetotelluric-resistivity (RMT–R 12–240 kHz). *Journal of Applied Geophysics*, 31, 113–143.
- Van Voorhis, G. D., Nelson, P. H. and Drake, T. L., 1973.** Complex resistivity spectra of porphyry copper mineralization. *Geophysics*, 38, 49–60.
- Vozoff, K. and Jupp, D. L. B., 1975.** Joint inversion of Geophysical data. *Geophys. J. Roy. Astr. Soc.*, 42, 977–991.
- Wait, J. R., 1954.** On the relation between telluric currents and the earth's magnetic field. *Geophysics*, 19, 281–289.
- Wannamaker, P. E., Stodt, J. A. and Rijo, L., 1987a.** A stable finite element solution for two-dimensional magnetotelluric modeling. *Geophys. J. Roy. Astr. Soc.*, 88, 277–296.

- Wannamaker, P. E., Stodt, J. A. and Rijo, L., 1987b.** *PW2D—Finite Element Program for Solution of Magnetotelluric Responses of Two-dimensional Earth Resistivity Structure, User Documentation*. Earth Sciences Laboratory, University of Utah.
- Ward, S. H., 1990.** *Geotechnical and Environmental Geophysics*. Society of Exploration Geophysicists, Tulsa.
- Ward, S. H. and Hohmann, G. W., 1988.** Electromagnetic theory for Geophysical applications. In: Nabighian, M. N. (Ed.), *Electromagnetic Methods in Applied Geophysics, Vol. 1*, Society of Exploration Geophysicists, Tulsa, 131–250.
- Ward, S. H., O'Brien, D. P., Parry, J. R. and McKnight, B. K., 1968.** Afmag interpretation. *Geophysics*, 33, 621–644.
- Watson, K. A. and Barker, R. D., 1999.** Differentiating anisotropy and lateral effects using azimuthal resistivity offset Wenner soundings. *Geophysics*, 64, 739–745.
- Watt, A. D., 1967.** *VLF radio engineering*. Pergamon Press, New York.
- Weaver, J., Agarwal, A. K., and Pu, X. H., 1999.** 3-D finite-difference modeling of the magnetic field in geoelectromagnetic induction. In: Oristaglio, M., and Spies, B. (Eds.), *Three dimensional Electromagnetics*. Society of Exploration Geophysicists.
- West, G. F. and Macnae, J. C., 1991.** Physics of the electromagnetic induction exploration method. In: Nabighian, M. N. (Ed.), *Electromagnetic Methods in Applied Geophysics, Vol. 2A*, Society of Exploration Geophysicists, Tulsa, 5–45.
- Wong, Th. E., Parker, N. and Horst, P., 2001.** Tertiary sedimentary development of the Board Fourteens area, the Netherlands. *Netherlands Journal of Geosciences*, 80, 85–94.
- Yee, K. S., 1966.** Numerical solution of initial boundary value problems involving Maxwell's equations in isotropic media. *IEEE Trans. Ant. Prop.*, AP-14, 302–309.
- Zacher, G., Tezkan, B., Neubauer, F. M., Hördt, A. and Müller, I., 1996.** Radiomagnetotellurics: A powerful tool for waste-site exploration. *European Journal of Environmental and Engineering Geophysics*, 1, 139–159.
- Zagwijn, W. H., 1989.** The Netherlands during the Tertiary and Quaternary: A case history of coastal lowland evolution. *Netherlands Journal of Geosciences*, 68, 107–120.
- Ziebell, M., 1998.** Untersuchung einer Altlast in Köln-Holweide mit Hilfe von RMT und Vergleich der Ergebnisse verschiedener Interpretationssoftware. Diplomarbeit, Institut für Geophysik und Meteorologie, Universität zu Köln.
- Zonge Engineering and Research Organization Inc., 2000.** *Zonge GDP32^{II} Multifunction Receiver Operation Manual*. Zonge Engineering and Research Organization Inc., Tucson, Arizona.
- Zonge, K. L. and Wynne, J. C., 1975.** Recent advances in complex resistivity measurements. *Geophysics*, 40, 851–864.

ACKNOWLEDGMENT

The work in the front of you is the main part of my research studies at the 'Institut für Geophysik und Meteorologie–Universität zu Köln.' It would not have been possible to complete it without the following people and authorities.

Before I came to Cologne I knew very little of EM's. I would like to express my hearty thanks to my supervisor Prof. Dr. **Bülent Tezkan** who patiently taught me more about EM's. I deeply appreciate his valuable discussion, comments and supports during the whole time of this work. I am also grateful to Prof. Dr. **Andreas Junge** for appraising this thesis.

I appreciate the valuable support of **Rainer Bergers** during the field work at the opencast mine 'Garzweiler I.' Without you I would not have achieved the RMT and TEM measurements there. I am indebted to **Gerhard Zacher** who has introduced us to the RWE-Power AG and discussed with me very important issues related to the RMT's. **Michael Lohmer**, many thanks for your hard field work.

I am indebted to **RWE-Power AG** for access to their opencast mine 'Garzweiler I', generous loans of cars and material in the field. Special thanks should be go to Mr. **B. Asmus**, Mr. **B. Becker** and Mr. **K. Schneider** for allowing us to use the stratigraphical, topographical and well logging data.

I would particularly like to acknowledge the supports of **Stephan Recher** and **Katrin Schwalenberg** during all RMT data processing and inversion stages.

I express my gratitude to **Olaf Koch** and **Jörn Lange** for providing supports during all TEM data processing and inversion stages. The same goes to **Stefan L. Helwig**, **Carsten Scholl**, **Rainer Bergers** and **Roland Martin** for their critical reviews the manuscript. **Mohammed Helmy**, I thank you for checking the English. **Jörn Lange** and **Tim Seher** were more than helpful while German-translating Chapter 6: Summary and Conclusions, thanks.

I would also like to thank **Martin Müller** who let me use the facilities in TU–Berlin's Laboratory to perform all the SIP measurements on my rock samples.

Without a list of names I want to acknowledge all the members of the **Institut für Geophysik und Meteorologie–Universität zu Köln**. My roommate **Markus Perk**, thanks.

I am grateful to the **Egyptian government** for the Ph.D. scholarship award.

Lastly, I deeply appreciate my wife's support and devotion. She paused her study and career to come with me to Cologne and always encouraged me. Thank you **Marwa**, without you I would never have made it. Hello **Toka!** You have suffered like us too.

Ich versichere, dass ich die von mir vorgelegte Dissertation selbständig angefertigt, die benutzten Quellen und Hilfsmittel vollständig angegeben und die Stellen der Arbeit– einschließlich Abbildungen und Tabellen–, die anderen Werken im Wortlaut oder dem Sinn nach entnommen sind, in jedem Einzelfall als Entlehnung kenntlich gemacht habe; dass diese Dissertation noch keiner anderen Fakultät oder Universität zur Prüfung vorgelegen hat; dass sie– abgesehen von unten angegebenen Teilpublikationen– noch nicht veröffentlicht worden ist sowie, dass ich eine solche Veröffentlichung vor Abschluß des Promotionsverfahrens nicht vornehmen werde.

Die Bestimmungen dieser Promotionsordnung sind mir bekannt. Die von mir vorgelegte Dissertation ist von Prof. Dr. B. Tezkan betreut worden.

Köln, Dezember 2004

Karam S. I. Farag

Teilpublikationen

List of publications and extended abstracts (listed in chronological order) while at the Institute of Geophysics and Meteorology (IGM), University of Cologne:

Farag, K. S. I. and Tezkan, B., 2003. RMT signature of the Rhineland brown coal. In: Hördt, A. and Stoll, J. B. (Eds.), *Protokoll über das 20. Kolloquium Elektromagnetische Tiefenforschung*, Königstein, DGG, 47–54.

Farag, K. S. I. and Tezkan, B., 2003. Vertical electrical resistivity structure of the Garzweiler and Frimmersdorf coal seams inferred from transient electromagnetic data. In: Hördt, A. and Stoll, J. B. (Eds.), *Protokoll über das 20. Kolloquium Elektromagnetische Tiefenforschung*, Königstein, DGG, 55–62.

Farag, K. S. I. and Tezkan, B., 2004. Mutli-dimensional radiomagnetotelluric and transient electromagnetic interpretation for the shallow coal seams at the Garzweiler mine, west of Cologne. In: *Protokoll über die 64. Jahrestagung der Deutschen Geophysikalischen Gesellschaft*, Berlin, DGG, EM09.

Farag, K. S. I. and Tezkan, B., 2004. Near-surface electromagnetics for imaging the shallow coal seams at the Garzweiler mine, west of Cologne. In: *10th European Meeting of Environmental and Engineering Geophysics–Near Surface 2004, Extended Abstracts*, Utrecht, EAGE, B024.

Farag, K. S. I. and Tezkan, B., 2004. Coal exploration using electromagnetic methods. In: *17th International Workshop on Electromagnetic Induction in the Earth, Extended Abstracts*, Hyderabad, NGRI–IIG, S.3–O.7.

Farag, K. S. I. and Tezkan, B., 2005. Influence of highly-conductive surficial masses on the detection of deep conductors: A field TEM example. In: *Protokoll über die 65. Jahrestagung der Deutschen Geophysikalischen Gesellschaft*, Graz, DGG, EMP02.

Farag, K. S. I. and Tezkan, B., 2005. Resistivity models of the shallow coal seams at the 'Garzweiler I' mine, Northwest of Cologne. *Geophysical Prospecting*, in preparation.

Farag, K. S. I. and Tezkan, B., 2002. Report on the resistivity structure of the Garzweiler and Frimmersdorf Coal Seams inferred from radiomagnetotelluric and transient electromagnetic data at the mining bench 'SB2', opencast mine 'Garzweiler I.' Internal Report (submitted to RWE-Power AG), Institut für Geophysik und Meteorologie, Universität zu Köln.

LEBENS LAUF

Name Karam Samir Ibrahim FARAG

Anschrift Kalscheurenerstraße 63
50354 Hürth

Geburtsdatum 04. 01. 1973

Geburtsort Kairo (Ägypten)

Familienstand Verheiratet (1 Kind)

Schulbildung

1979 – 1985 Primary School in El-Sharabia – Kairo

1985 – 1988 Preparatory School in El-Sharabia – Kairo

1988 – 1991 Secondary School in El-Abbassia – Kairo
Abschluß: Egyptian General Secondary School of Education
(*High School Success Statement, Math Branch*)

Universität

1991 – 1995 Ain Shams University, Kairo
Abschluß: Bachelor of Science (B.Sc.) in Geology – Geophysics

1995 – 1996 Ain Shams University, Kairo
Abschluß: Pre-master courses in Geophysics
(*Potential-field Section*)

1996 – 1999 Ain Shams University, Kairo
Abschluß: Master of Science (M.Sc.) in Geophysics
(*Title: A paleomagnetic study of some basaltic rocks in Baharyia – Beni Suef sector, Egypt*)

Seit SS 2001 Universität zu Köln
Institut für Geophysik und Meteorologie
Wissenschaftlicher Mitarbeiter
Studienfach: *Geophysik – Promotion*